


1992

The global potential energy surfaces of the lowest two $1A'$ states of the ozone molecule: theoretical determination and analysis

Gregory John Atchity
Iowa State University

Follow this and additional works at: <https://lib.dr.iastate.edu/rtd>

 Part of the [Atomic, Molecular and Optical Physics Commons](#), and the [Physical Chemistry Commons](#)

Recommended Citation

Atchity, Gregory John, "The global potential energy surfaces of the lowest two $1A'$ states of the ozone molecule: theoretical determination and analysis " (1992). *Retrospective Theses and Dissertations*. 10093.
<https://lib.dr.iastate.edu/rtd/10093>

This Dissertation is brought to you for free and open access by the Iowa State University Capstones, Theses and Dissertations at Iowa State University Digital Repository. It has been accepted for inclusion in Retrospective Theses and Dissertations by an authorized administrator of Iowa State University Digital Repository. For more information, please contact digirep@iastate.edu.

INFORMATION TO USERS

This manuscript has been reproduced from the microfilm master. UMI films the text directly from the original or copy submitted. Thus, some thesis and dissertation copies are in typewriter face, while others may be from any type of computer printer.

The quality of this reproduction is dependent upon the quality of the copy submitted. Broken or indistinct print, colored or poor quality illustrations and photographs, print bleedthrough, substandard margins, and improper alignment can adversely affect reproduction.

In the unlikely event that the author did not send UMI a complete manuscript and there are missing pages, these will be noted. Also, if unauthorized copyright material had to be removed, a note will indicate the deletion.

Oversize materials (e.g., maps, drawings, charts) are reproduced by sectioning the original, beginning at the upper left-hand corner and continuing from left to right in equal sections with small overlaps. Each original is also photographed in one exposure and is included in reduced form at the back of the book.

Photographs included in the original manuscript have been reproduced xerographically in this copy. Higher quality 6" x 9" black and white photographic prints are available for any photographs or illustrations appearing in this copy for an additional charge. Contact UMI directly to order.

U·M·I

University Microfilms International
A Bell & Howell Information Company
300 North Zeeb Road, Ann Arbor, MI 48106-1346 USA
313/761-4700 800/521-0600

Order Number 9311473

**The global potential energy surfaces of the lowest two $^1A'$ states
of the ozone molecule: Theoretical determination and analysis**

Atchity, Gregory John, Ph.D.

Iowa State University, 1992

U·M·I

300 N. Zeeb Rd.
Ann Arbor, MI 48106

The global potential energy surfaces of the lowest two $^1A'$ states of the
ozone molecule: Theoretical determination and analysis

by

Gregory John Atchity

A Dissertation Submitted to the
Graduate Faculty in Partial Fulfillment of the
Requirements for the Degree of
DOCTOR OF PHILOSOPHY

Department: Chemistry
Major: Physical Chemistry

Approved: _____

Signature was redacted for privacy.

In Charge of Major Work _____

Signature was redacted for privacy.

For the Major Department

Signature was redacted for privacy.

For the Graduate College

Iowa State University
Ames, Iowa

1992

TABLE OF CONTENTS

GENERAL OVERVIEW	1
1. Ozone	1
2. Potential Energy Surfaces (PES)	3
3. Present Investigation	5
PAPER I. PERIMETRIC SCALE-SHAPE COORDINATES FOR TRIATOMIC MOLECULES	9
ABSTRACT	11
1. INTRODUCTION	12
2. PERIMETRIC COORDINATES	14
2.1 Definition	14
2.2 Scale and Shape	15
2.3 Parameter Space	16
3. SEPARATION OF SCALE AND SHAPE COORDINATES	17
3.1 Rotation of Coordinate Basis	17
3.2 Scale-Independent Shape Coordinates	19
4. RELATION BETWEEN COORDINATE POINTS AND MOLECULAR SHAPES	21
4.1 General Relationships	21
4.2 Illustrative Examples	23

4.3	Symmetry	24
5.	EXTENDED SHAPE COORDINATE SPACE	27
	REFERENCES	30
	PAPER II. POTENTIAL ENERGY SURFACES NEAR INTERSECTIONS	44
	ABSTRACT	46
1.	INTRODUCTION	47
2.	THEORETICAL BACKGROUND	49
2.1	The Crossing Conditions	49
2.2	The Intersection Space (ICS)	51
2.3	The Branching Space	60
3.	TOPOGRAPHY OF THE LOWER SURFACE IN THE TANGENT BRANCHING SPACE	66
3.1	Expression for a PES in terms of Mass-Weighted Cartesian coordinates	66
3.2	Case of a Circular Difference Cone	68
3.3	The case of an Elliptic Difference Cone with Principal Axes Lined Up Along the Linear Term	73
3.4.	The General Case ($c \neq 1$ and $a, b \neq 0$)	77
4.	TOPOGRAPHY OF THE UPPER SURFACE	87
5.	CONCLUSIONS	90
	ACKNOWLEDGMENT	92

REFERENCES	93
------------------	----

PAPER III. A QUANTUM CHEMICAL CONSTRUCTION OF DIABATIC STATES	104
---	-----

ABSTRACT	106
----------------	-----

1. INTRODUCTION	107
-----------------------	-----

2. CONSTRUCTION OF DIABATIC STATES	110
--	-----

2.1 Premises	110
--------------------	-----

2.2 Diabatic states	111
---------------------------	-----

2.3 Diabaticity Criterion	114
---------------------------------	-----

2.4 The Transformation Matrix	115
-------------------------------------	-----

3. CALCULATION OF ΔH AND H_{12}	117
---	-----

4. COMMENT	118
------------------	-----

REFERENCES	120
------------------	-----

PAPER IV. ELECTRONIC STRUCTURE BASIS FOR THE CONICAL INTERSECTION BETWEEN THE LOWEST TWO 1A_1 STATES OF OZONE	121
--	-----

ABSTRACT	123
----------------	-----

1. INTRODUCTION	124
-----------------------	-----

2. THE ADIABATIC AND DIABATIC POTENTIAL ENERGY SURFACES	127
---	-----

2.1 Coordinate Space	127
----------------------------	-----

2.2	Orbital Space	127
2.3	Configuration Space	128
2.4	Potential Energy Surfaces	131
3.	QUANTITATIVE ANALYSIS OF THE INTERSECTION	134
3.1	The Surfaces of $\Delta H(x,y)$ and $H_{12}(x,y)$	134
3.2	The Wavefunctions	135
3.3	Configurational Analysis of ΔH and H_{12} along the line connecting the two minima	138
4.	CONCLUSION	143
	REFERENCES	144
	 PAPER V. THE INTERSECTION SEAM BETWEEN THE $1^1A'$ AND $2^1A'$ STATES OF OZONE	158
	ABSTRACT	160
1.	INTRODUCTION	161
2.	ENERGY FUNCTIONS IN TERMS OF PERIMETRIC COORDINATES	162
2.1	Coordinate Space	162
2.2	Energy Surfaces for Homonuclear Triatomic Molecules	164
3.	DETERMINATION OF THE SEAM	166
3.1	Point to Point Extrapolation	166
3.2	Planar Search by Minimizing $(E_2 - E_1)^2$	168

3.3	Corralling an Intersection Point	169
4.	THE INTERSECTION SEAM OF THE $1^1A'$ AND THE $2^1A'$ STATES	174
4.1	Ab-Initio Procedure	174
4.2	The Intersection Seam in C_s Symmetry	174
4.3	The Intersection Seam in C_{2v} Symmetry	176
4.4	Orbital Interpretation of the Symmetry Change	178
4.5	Another Intersection Seam of the 1^1A_1 state	181
5.	CONCLUSIONS	182
	REFERENCES	183

PAPER VI. GLOBAL POTENTIAL ENERGY SURFACES
FOR THE LOWEST TWO $^1A'$ STATES OF OZONE . . . 197

ABSTRACT	199
1. INTRODUCTION	201
2. METHOD	204
2.1 Wavefunctions	204
2.2 Energy Surface in Coordinate Space	206
3. CRITICAL FEATURES OF THE POTENTIAL ENERGY SURFACES	212
4. GLOBAL FEATURES OF THE $1^1A'$ AND THE $2^1A'$ POTENTIAL ENERGY SURFACES	216
4.1 PES of the $1^1A'$ state	216
4.2 PES of the $2^1A'$ state	223

4.3 Energy difference between the two states	228
5. CONCLUSIONS	231
REFERENCES	233
SUMMARY AND CONCLUSIONS	257
REFERENCES	265
ACKNOWLEDGEMENTS	266

GENERAL OVERVIEW

1. Ozone

In recent years the ozone molecule has received considerable attention in the public eye. Its importance in atmospheric chemistry, especially its absorption of ultraviolet radiation, has been studied for some time by chemists and physicists. On the one hand, excessive generation of ozone in exhaust gases of combustion processes in metropolitan areas is considered a health hazard, on the other hand, the layer of ozone in the upper atmosphere is known to be responsible for shielding the surface of our planet from levels of ultraviolet radiation which would be fatal to many forms of life. The discovery that the amount of the ozone in the upper atmosphere is decreasing, due in great part to the emissions of our technological society, has therefore stimulated ozone research.

The need for *theoretical* studies of ozone is fueled by the fact that experimental methods have so far been unable to provide more than basic information about the electronic and vibrational structures of ozone. Moreover, experiments only yield information about near-equilibrium structures, vibrational energies, and excitation energies, but little to no information about geometries far from equilibrium or about excited states. Most of the information gained from experiment about the excited states of

ozone is based on extensive measurements of the four observed vibronic bands (named Wulf, Chappuis, Huggins, and Hartley)[1].

Even the experimental picture of the *ground state* is far from complete. Although the equilibrium geometry, bent at an angle of 116° , was elucidated many years ago, the second minimum, a ring structure predicted by theoretical calculations for over two decades, has yet to be experimentally observed. Furthermore, Xantheas et. al. [2], in a detailed theoretical study of the ground state of ozone in the C_{2v} constrained coordinate space, recently uncovered new and unexpected features. While determining the ring-opening transition state, they found that the ground state surface intersects the first excited state surface of the same symmetry in the region of the transition state. This is one of the first documented cases of an intersection of two states of like symmetry in a common molecule. Furthermore, not only does the intersection lie within 0.1\AA of the ring-opening transition state, it also lies within 0.1\AA of the global minimum of the excited state within C_{2v} .

The mentioned observations imply that the ground state and the lowest excited state of like symmetry strongly interact in certain regions of coordinate space. It is therefore apparent that a clearer understanding of the situation can only be given by a global examination of the respective potential energy surfaces.

2. Potential Energy Surfaces (PES)

The concept of the Potential Energy Surface (PES) is central to chemical physics. It arises naturally from the insight of Born and Oppenheimer [3] that the motion of the nuclei and that of the electrons within a molecule can be treated separately because the electrons move much more quickly than the nuclei. Therefore, the equations describing the motion of the electrons can be solved within the constant field of motionless nuclei. The solution of this problem yields a set of electronic wavefunctions $\psi_n(\mathbf{r}, \mathbf{q})$ which are functions of the electronic coordinates \mathbf{r} and the fixed nuclear coordinates \mathbf{q} . The corresponding electronic energies $E_n(\mathbf{q})$ are functions of the nuclear coordinates. These electronic wavefunctions can then be used to solve the equations for the nuclear motions by expressing the total wavefunction in the form $\Psi(\mathbf{r}, \mathbf{q}) = \sum_n \chi_n(\mathbf{q}) \psi_n(\mathbf{r}, \mathbf{q})$. This approach leads to coupled differential equations for the nuclear wavefunctions $\chi_n(\mathbf{q})$ in which the electronic energies $E_n(\mathbf{q})$ play the roles of potential energies. The determination of the electronic wavefunctions $\psi_n(\mathbf{r}, \mathbf{q})$ traditionally lies in the field of quantum chemistry while that of the nuclear wavefunctions $\chi_n(\mathbf{q})$ traditionally lies in the field of dynamics. In recent years the two fields have begun to merge, with quantum chemists performing dynamics calculations, and dynamicists using quantum chemical results.

The potential energies, $E_n(\mathbf{q})$, of the molecule are functions of the nuclear

coordinates and are therefore called potential energy surfaces (PES). The PES are multi-dimensional hyper-surfaces in the coordinate space of the nuclei. The molecule (or molecular ensemble) can be visualized as "moving on its potential energy surface". The lowest points on a PES, its minima, correspond to stable equilibrium structures, whereas the highest points correspond to unstable, high energy structures. The low energy channels connecting the minima are reaction paths, with the highest energy points along such paths, the transition states, being saddlepoints with one negative eigenvalue. The difference in height between a minimum on a PES and the transition state between it and another minimum provides an approximation to the activation energy for that reaction.

Acquisition of accurate knowledge about PES is still in its infancy. The experimental approach is limited to areas of PES near the minima and activation energies of reactions. The theoretical approach is limited, too, in that it requires demanding *ab-initio* calculations which, not only must be quite accurate but, moreover, must be carried out at many points in the space of the molecular internal coordinates. However, with the advent of high-speed computers and advances in quantum chemical methods it is now possible to get fairly accurate potential energy surfaces for small molecules, such as those obtained by the present work.

3. Present Investigation

The theoretical observations mentioned in the first subsection, coupled with the experimental importance of ozone, provide the impetus for the present theoretical study of the two lowest $^1A'$ potential energy surfaces of this molecule. The goal of this work is twofold. A large part of it involves various aspects of the intersection of the two states, which is one of the remarkable features of these potential energy surfaces. Also of interest, however, are the global characteristics of the two potential energy surfaces: the location of all minima, transition states, the dissociative pathways, and rearrangement pathways of the molecule. This involves not only the formidable task of accurately mapping out the surfaces in the full three-dimensional coordinate space of C_s symmetry, but the equally formidable task of interpreting all of this three-dimensional information.

This dissertation consists of six investigations presented as papers ready for submission to scholarly publications. One paper (Paper II) has already been published in the *Journal of Chemical Physics*, the rest will be submitted subsequently. These six papers are presented as published or submitted, with the references and figures for each paper included. The papers are preceded by a general overview, and are followed by a general summary and a list of references cited in the overview and general summary.

The dissertation consists of two sets of investigations. The first set consists of three formal theoretical developments which provide a necessary basis for the three investigations of ozone in the second part.

In the first paper, the problem of the internal coordinates of a triatomic molecule is addressed. In view of the equivalence of the atoms, the *perimetric* scale-shape coordinates are chosen. Their definition and relation to other triatomic coordinates is presented. Furthermore, the important relations between these coordinates and the corresponding molecular geometries are discussed in detail. These coordinates are used later in papers V and VI.

Paper II contains a review of the relevant theory of intersections between potential energy surfaces and, in particular, an in depth analysis of the behavior of potential energy surfaces near an intersection. The theory in this paper is referred to throughout the rest of the dissertation.

Paper III presents a novel, "quantum chemical" method for constructing diabatic states from adiabatic states. The eigenstates of the electronic hamiltonian, produced by the *ab-initio* methods used to determine the potential energy surfaces of this study are *adiabatic* states which, near real or avoided crossings, have large coupling terms with respect to nuclear motion. By transforming to *diabatic* states, this coupling can be greatly reduced and, moreover, the electronic aspects of their crossing can be

elucidated. In the next paper, IV, this approach is shown to be effective in analyzing the causes of the intersection between the two lowest 1A_1 states of ozone in C_{2v} symmetry.

The second part of this dissertation consists of investigations into the actual potential energy surfaces of ozone.

Paper IV raises the question "Why do these two states of like symmetry cross?". It provides an in-depth analysis and discussion of the causes for the intersection in C_{2v} . By transforming the adiabatic states to diabatic states, one is able to determine the interaction matrix H_{ij} between them. Careful examination of the matrix elements and relating them to the electronic structures of the two states leads to an understanding of the reasons for the conical intersection between them.

This point of intersection of the two surfaces in C_{2v} (a two-dimensional coordinate subspace), as determined by Xantheas et. al. [2], is actually part of a one-dimensional intersection *seam* in the full three-dimensional coordinate space which has C_s symmetry. This seam is determined in Paper V. A novel method for determining an intersection point in a two-dimensional coordinate space is also presented.

Paper VI, finally, deals with the *global* shapes of the potential energy surfaces of the two states. Global mappings of the two potential energy surfaces over large parts of the full coordinate space are determined. The

various critical points of the two surfaces are found. Dissociation and rearrangement pathways are discussed.

PAPER I. PERIMETRIC SCALE-SHAPE COORDINATES FOR
TRIATOMIC MOLECULES

PERIMETRIC SCALE-SHAPE COORDINATES FOR
TRIATOMIC MOLECULES

Ames Laboratory USDOE and Department of Chemistry

Iowa State University

Ames, IA 50011

ABSTRACT

Perimetric nuclear coordinates of a triatomic molecule treat all three nuclei equivalently and are not subject to the triangle conditions. Through an appropriate orthogonal transformation they can be separated into one scale coordinate, viz. the circumference, and two shape coordinates, which are determined by the angles. The parameter space of the shape coordinates is an equilateral triangle. The basic formulas are given and the relationship between points in coordinate space and molecular shapes are elucidated.

1. INTRODUCTION

Many features of polyatomic potential energy surfaces (PES) do not appear in the paradigm of diatomic potential energy curves. Moreover, because of our inability to "see" in more than three dimensions, their visualization is difficult. Triatomic molecules, being the smallest molecules with multi-dimensional PES, represent the necessary next step in understanding PES depending on more than one internal coordinate. They have three internal coordinates and furnish the simplest material on which to study and become familiar with features of general PES. Yet, already in this case, an effort is required in order to relate the points in the internal coordinate space to the actual molecular shapes. We encountered this problem in the accompanying study of ozone [1] which lead to the account presented below.

In discussions of triatomic molecules, it is desirable to be able to express and visualize potential energy surfaces or other properties as functions of the three internal coordinates in a way that treats all three atoms on an equal footing. A relatively simple parametrization which satisfies this requirement is given by the so-called perimetric coordinates. They were introduced in quantum chemistry by James and Coolidge [2] in the thirties and used later by Pekeris [3], in both instances for electronic calculations on the He atom.

Davidson [4] seems to have been the first to use and discuss them for the nuclear coordinates of triatomics. We shall examine these coordinates here in some detail. We shall show how they can be separated into scale and shape coordinates and establish the relationship between them and the so-called "symmetric coordinates" of Murrel et.al. [5]. We shall furthermore discuss the meaning of various aspects of the parameter space for the molecular geometries.

2. PERIMETRIC COORDINATES

2.1 Definition

The three distances r_{12} , r_{23} , r_{13} between the nuclei N_1 , N_2 , N_3 are the most natural independent coordinates that treat the three nuclei equivalently.

They have, however, the drawback of being subject to the triangle conditions $r_{ij} + r_{jk} \leq r_{ik}$. This shortcoming is eliminated by the perimetric coordinates which are defined as

$$s_i = (r_{ij} + r_{ik} - r_{jk})/2 \quad (1)$$

where (i,j,k) represents every permutation of (1,2,3). Inversion of Eq. (1)

yields

$$s_i + s_j = r_{ij} \quad (2)$$

and Eqs. (1), (2) are equivalent to the equations

$$s_i + r_{jk} = s = r/2, \quad (3)$$

where

$$s = (s_1 + s_1 + s_3), \quad (4)$$

$$r = (r_{12} + r_{23} + r_{13}). \quad (5)$$

The geometric meanings of s_1 , s_2 , s_3 are illustrated by Figure 1 which is self-evident in view of Eq. (2). The points which separate the two segments s_i and s_j on the side r_{ij} are, in fact, the points where the *inscribed circle touches* the three sides of the molecular triangle [6]. The lines connecting the corners to the center of the inscribed circle bisect the respective angles.

2.2 Scale and Shape

The relation of the lengths s_i and r_{ij} to the angles can be derived from the formula

$$r_{ij} = 2R\sin\phi_k \quad (6)$$

where R is the radius of the *circumscribed* circle [6]. From Eq. (6) follows

$$r_{ij}/r = \sin\phi_k / \sum_1 \sin\phi_i \quad (7)$$

and

$$s_i = sf_i \quad (8)$$

with

$$f_i = f_i(\phi_1, \phi_2, \phi_3) = 1 - 2\sin\phi_i / \sum_k \sin\phi_k. \quad (9)$$

Manifestly,

$$\sum_i f_i = 1. \quad (10)$$

It is apparent that, in Eq. (8), the parameter s determines the overall size of the molecule, it is a *scale factor*. The angular functions $f_i(\phi_1, \phi_2, \phi_3)$ on the other hand determine the angular appearance of the molecule, they are *shape factors*. By virtue of the relation $\phi_1 + \phi_2 + \phi_3 = \pi$, the right-hand side of Eq. (9) can be recast in the form

$$f_i = \tan\frac{1}{2}\phi_j \cdot \tan\frac{1}{2}\phi_k. \quad (11)$$

2.3 Parameter Space

Let the parameter space be spanned by a cartesian axis system along which the (s_1, s_2, s_3) are taken as coordinates. The three perimetric coordinates vary independently from zero to infinity. Hence, only the first octant is used. In this parameter space, molecules of the same angular shape are given by the coordinates of Eq. (8) with constant factors f_i , i.e. by points which fall on straight rays through the origin, their distances being proportional to s . The points along the diagonal of the first octant, for which $s_1=s_2=s_3$ correspond to equilateral molecules for which $f_1=f_2=f_3=1/3$.

Isosceles molecules correspond to points on the planes $s_i=s_j$; for example, the plane $s_1=s_2$ contains all isosceles triangles with the apex at the nucleus N_3 .

The three coordinate planes $s_i=0$ contain the points representing linear molecules. For example, the s_1-s_2 plane, corresponding to $s_3=0$ contains the linear molecules with nucleus N_3 in between nuclei N_1 and N_2 and with the internuclear distances $r_{13}=s_1$, $r_{23}=s_2$, $r_{12}=r_{13}+r_{23}=s_1+s_2$ so that all molecules with $r_{12}=\text{constant}$ lie on the straight line intersecting the s_1 and s_2 axis at 45° .

The three coordinate axes correspond to the coincidence of two nuclei. E.g. the s_1 axis corresponds to $s_2=s_3=0$ and the coincidence of nuclei N_2 and N_3 , with $r_{12}=r_{13}=s_1$. The origin corresponds to the coincidence of all three nuclei.

3. SEPARATION OF SCALE AND SHAPE COORDINATES

3.1 Rotation of Coordinate Basis

A separation of scale and shape coordinates is obtained by considering all molecules with a given circumference $r=2s$. By virtue of Eq. (8) they are given by the points lying in the plane

$$s_1 + s_2 + s_3 = s = \text{constant} \quad (12)$$

i.e. in a plane perpendicular to the diagonal of the first octant and intercepting all three axes at a distance $s=r/2$ from the origin. Accordingly, we introduce a new right handed set of basis vectors $\mathbf{d}_1, \mathbf{d}_2, \mathbf{d}_3$ by the orthogonal transformation

	\mathbf{d}_1	\mathbf{d}_2	\mathbf{d}_3	
\mathbf{e}_1	-1/2	-1/√6	1/√6	
\mathbf{e}_2	1/√2	-1/√6	1/√6	(13)
\mathbf{e}_3	0	2/√6	1/√6	

where $\mathbf{e}_1, \mathbf{e}_2, \mathbf{e}_3$ denote the unit basis vectors along the axis s_1, s_2, s_3 . Since \mathbf{d}_3 points along the first octant diagonal, the vectors $(\mathbf{d}_1, \mathbf{d}_2)$ span a plane passing through the origin which is parallel to all planes $s=\text{constant}$. The orientation of these basis vectors is shown in Figure 2. If x_1, x_2, x_3 denote the new coordinates along the vectors $(\mathbf{d}_1, \mathbf{d}_2, \mathbf{d}_3)$, then

$$\sum_i \mathbf{e}_i s_i = \sum_k \mathbf{d}_k x_k, \quad (14)$$

and the transformation between (s_1, s_2, s_3) and (x_1, x_2, x_3) is given by the same

orthogonal transformation:

$$\begin{array}{c|ccc}
 & x_1 & x_2 & x_3 \\
\hline
s_1 & -1/\sqrt{2} & -1/\sqrt{6} & 1/\sqrt{3} \\
s_2 & 1/\sqrt{2} & -1/\sqrt{6} & 1/\sqrt{3} \\
s_3 & 0 & 2/\sqrt{6} & 1/\sqrt{3}
\end{array} \quad (15)$$

It entails

$$x_3 = (s_1 + s_2 + s_3)/\sqrt{3} = s/\sqrt{3} = r/2\sqrt{3}, \quad (16)$$

confirming that the plane $s=\text{constant}$ is the plane $x_3=\text{constant}$ and spanned by the coordinates (x_1, x_2) .

Since the three-dimensional parameter space is limited to the first octant, the two-dimensional parameter plane for $x_3=\text{constant}$ is limited to an equilateral triangle as illustrated perspectively in Figure 3. The first octant diagonal penetrates this triangle in its origin $x_1=x_2=0$ at a distance x_3 from the origin of the s_1, s_2, s_3 coordinate system. The coordinates (s_1, s_2, s_3) of a number of points on the triangle $s = \text{constant}$ are also given on Figure 3. From these coordinates the dimensions of the triangle are found to be as follows:

$$\begin{array}{l}
 \text{Side} = s/\sqrt{2}, \quad \text{Height} = s/\sqrt{3}/2. \text{ The origin lies } 2/3 \\
 \text{of the way from the corner to the opposite side.}
 \end{array} \quad (17)$$

Figure 4 provides a plane view of this triangle with the coordinate axis x_1, x_2 on it. The corners are numbered by the axes s_1, s_2, s_3 penetrating the plane at those points. Also indicated are the coordinates (x_1, x_2) of a number of

points, calculated from Eq. (15) and scaled by s .

3.2 Scale-Independent Shape Coordinates

The *linear size* of the parameter triangle spanned by x_1, x_2 is proportional to the molecular scale parameter s . The *shape* of the molecule is given by the *relative* position of the representative point inside the triangle, i.e. by the two scale-independent parameters

$$\xi_1 = x_1/s, \quad \xi_2 = x_2/s. \quad (18)$$

These *two* independent shape coordinates are equivalent to the *three* angles ϕ_1, ϕ_2, ϕ_3 , which are subject to the constraint $\phi_1 + \phi_2 + \phi_3 = \pi$. By virtue of the relations $s_i = s f_i$ [See Eq. (8)] and the orthogonal transformation, Eq. (15), between the x_i and the s_j , the two independent shape coordinates ξ_1, ξ_2 are related to the three dependent shape factors of Eqs. (9) and (11) by the orthogonal transformation

	ξ_1	ξ_2	$\xi_3 = 1/\sqrt{3}$	
f_1	$-1/\sqrt{2}$	$-1/\sqrt{6}$	$1/\sqrt{3}$	(19)
f_2	$1/\sqrt{2}$	$-1/\sqrt{6}$	$1/\sqrt{3}$	
f_3	0	$2/\sqrt{6}$	$1/\sqrt{3}$	

where we formally introduced $\xi_3 = x_3/s = 1/\sqrt{3}$ [See Eq. (16)]. Manifestly, the parameter space of the scale-independent shape coordinates (ξ_1, ξ_2) also forms an equilateral triangle. It is, in fact, the one shown in Figure 4. The side of this triangle has a length of $\sqrt{2}$ and its height is $\sqrt{3/2} = 3/\sqrt{6}$.

From Eq. (19) one obtains for the s_i the following expression in terms of the independent scale-shape coordinates (s, ξ_1, ξ_2):

$$\begin{aligned}
 s_1 &= s(-\xi_1/\sqrt{2} - \xi_2/\sqrt{6} + 1/3) \\
 s_2 &= s(\xi_1/\sqrt{2} - \xi_2/\sqrt{6} + 1/3) \\
 s_3 &= s(2\xi_2/\sqrt{6} + 1/3),
 \end{aligned} \tag{20}$$

from which follows, by virtue of Eq. (2),

$$\begin{aligned}
 r_{13} &= s(-\xi_1/\sqrt{2} + \xi_2/\sqrt{6} + 2/3) \\
 r_{23} &= s(\xi_1/\sqrt{2} + \xi_2/\sqrt{6} + 2/3) \\
 r_{12} &= s(-2\xi_2/\sqrt{6} + 2/3).
 \end{aligned} \tag{21}$$

4. RELATION BETWEEN COORDINATE POINTS AND MOLECULAR SHAPES

4.1 General Relationships

The visualization of molecules represented by arbitrary points in the triangle of the parameters x_1, x_2 is facilitated by the following theorem [which is readily proved in the three dimensional coordinate space of (s_1, s_2, s_3) depicted in Figure 3]:

The perpendicular distance D_j between an arbitrary point in the parameter triangle and its side opposite to the corner j , is related to the coordinate s_j by

$$D_j = s_j \sqrt{3/2}. \quad (22)$$

From it follows the corollary

$$D_1 + D_2 + D_3 = s \sqrt{3/2} = \text{Height} = \text{const}, \quad (23)$$

in agreement with a geometrical theorem about equilateral triangles. Figure 5 depicts the distances D_k as well as the distances D_k' to the *circumscribed equilateral triangle*. By virtue of Eq. (22), the distances D_k' are given by

$$D_k' = (\text{Height of original triangle}) - D_k = (s - s_k) \sqrt{3/2}$$

$$D_k' = (s_i + s_j) \sqrt{3/2} = r_{ij} \sqrt{3/2}. \quad (24)$$

Figure 5 and Eq. (24) establish contact with the "symmetry coordinates" of

Murrel et. al. [4]. It is easily seen that the limitation of the representative points to the original, shaded triangle in Figure 5 is equivalent to the triangle conditions on the distances r_{ij} .

Let $\delta_j = D_j/s$ denote the distance corresponding to D_j in the triangle of the scale-independent shape coordinates (ξ_1, ξ_2) . Then they satisfy the corresponding identities

$$\delta_j = f_j \sqrt{3/2}, \quad (25)$$

$$\delta_1 + \delta_2 + \delta_3 = \sqrt{3/2} = \text{Height}. \quad (26)$$

For the distances δ'_i to the circumscribed triangle, corresponding to the distances D'_i one obtains

$$\delta'_i = (1-f_i) \sqrt{3/2} = (r_{jk}/r) \sqrt{6}. \quad (27)$$

Of interest are also the lines along which any one of the angles of the molecule is constant. If one angle is fixed, say ϕ_3 , then ϕ_2 is given by ϕ_1 because the sum of all three is π . A parametric representation of the curves $\{\xi_1(\phi_1), \xi_2(\phi_1)\}$ for constant ϕ_3 is then obtained by substituting the expression of Eqs. (9) or (11), with $\phi_3 = \text{const.}$ and $\phi_2 = \pi - \phi_3 - \phi_1$, in the equations

$$\begin{aligned} \xi_1 &= (f_2 - f_1) / \sqrt{2} \\ \xi_2 &= (2f_3 - f_1 - f_2) / \sqrt{6} \end{aligned} \quad (28)$$

which follow from Eq. (19). Figure 6 displays the curvilinear grid of the curves

$$\phi_j = 15^\circ, 30^\circ, 45^\circ, 60^\circ, 75^\circ, 90^\circ, 105^\circ, 120^\circ, 135^\circ, 150^\circ, 180^\circ$$

for $j=1,2,3$. The plot shows that all acute molecules lie inside the shaded area enclosed by the lines $\phi_1=90^\circ$, $\phi_2=90^\circ$, $\phi_3=90^\circ$ which become tangent at the corners where two nuclei coincide. The three unshaded areas correspond to the three types of obtuse molecules.

4.2 Illustrative Examples

Since the first octant diagonal of the (s_1, s_2, s_3) space penetrates the shape coordinate triangle at the origin $\xi_1=\xi_2=0$, this point corresponds to the equilateral molecule with sides $s/3$. From what has been said earlier, it is also apparent that the isosceles molecules correspond to points on the lines from the three corners through the origin to the mid-points of the opposite sides. E.g., the ξ_2 -axis contains the isosceles molecules with the nucleus N_3 at the apex. From the discussion of the three-dimensional parameter space, it is also seen that the three sides of the shape-coordinate triangle correspond to linear molecules, the points on the side connecting the corners i and j representing the linear molecules with the nucleus N_k lying between the nuclei N_i and N_j .

Some illustrative examples of oblique triangles are displayed in Figure 7.

Of importance is the case of linear molecules. If nucleus N_3 lies between nuclei N_1 and N_2 , then one has

$$\phi_1 = 0, \quad \phi_2 = 0, \quad \phi_3 = \pi, \quad r_{12} = r_{13} + r_{23}, \quad (29)$$

$$s_3 = 0, \quad s_1 = r_{13}, \quad s_2 = r_{23}, \quad s = s_1 + s_2,$$

and the shape factors become

$$\begin{aligned} f_1 &= s_1/(s_1 + s_2) = r_{13}/(r_{13} + r_{23}), \\ f_2 &= s_2/(s_1 + s_2) = r_{23}/(r_{13} + r_{23}), \\ f_3 &= 0. \end{aligned} \quad (30)$$

By virtue of Eqs. (30) and (25), we have $\delta_3=0$ so that the parameter point lies indeed on the (1-2) side of the shape coordinate triangle. Such a point is shown in Figure 8. Since the corner angle is 60° , one obtains for the segments σ_1, σ_2 on the triangle side [note Eq.(25)]

$$\sigma_1 = \delta_2 2/\sqrt{3} = f_2 \sqrt{2} = \sqrt{2} r_{23}/(r_{13} + r_{23}), \quad \sigma_2 = \delta_1 2/\sqrt{3} = f_1 \sqrt{2} = \sqrt{2} r_{13}/(r_{13} + r_{23}) \quad (31)$$

which add indeed up to the side length $\sqrt{2}$. The coordinates of this point are therefore found to be

$$\xi_1 = \sigma_1 - \sqrt{2}/2 = \sqrt{2}(r_{23} - r_{13})/r, \quad \xi_2 = -1/\sqrt{6}. \quad (32)$$

4.3 Symmetry

The C_s symmetry, possessed by all triatomic molecules, is intrinsic to the entire perimetric parameter space. The latter is invariant with respect to the molecular C_s group.

If the nuclei N_1 and N_2 are identical, then all points on the plane spanned by the x_3 and $x_2 = s\xi_2$ axes correspond to molecules with C_{2v} symmetry. I.e., the plane $x_1=0$ is " C_{2v} restricted". Moreover, any two points in the remainder

of the coordinate space obtained from each other by reflection through this plane describe two molecules which are each other's mirror image with respect to any plane perpendicular to the N_1 - N_2 bond. Consequently, any molecular function which is invariant with respect to the interchange of N_1 and N_2 will have C_s symmetry in the (x_1, x_2, x_3) coordinate space, with $x_1=0$ defining the C_s plane.

If all three atoms are identical, then analogous considerations show that not only the plane of $x_1=0$, but also the two planes obtained from it by rotation through $\pm 120^\circ$ around the x_3 axis are (i) C_{2v} restricted and (ii) symmetry planes for any function which is invariant under the permutation of any of the nuclei. In fact, any such function possesses C_{3v} symmetry in coordinate space. The x_3 axis corresponds to molecules with D_{3h} symmetry.

In the subspace defined by $x_1=0$ which, when N_1 and N_2 are identical nuclei, corresponds to C_{2v} symmetry, i.e. isosceles molecules, it is often convenient to make use of the coordinates x and y defined in Figure 9. It is therefore useful to know the coordinate grid defined by the lines $s=\text{constant}$ and $x_2=\text{constant}$ in the (x,y) plane.

From the definitions of s and x_2 [See Eqs. (3), (4), (5),(15)] and from Figure 9, one readily derives

$$s = s(x,y) = (x^2 + y^2)^{1/2} + x, \quad (33)$$

$$x_2 = x_2(x,y) = [(x^2+y^2)^{1/2} - 2x] \sqrt{2/3}. \quad (34)$$

The inversion of these equations yields

$$x = x(s,x_2) = s/3 - x_2/\sqrt{6}, \quad (35)$$

$$y = y(s,x_2) = s[(1 + \sqrt{6}x_2/s)/3]^{1/2}. \quad (36)$$

From Eqs. (33) to (36), one readily finds the lines of constant s and x_2 .

The lines $s=\text{constant}$ are given by the parabolas

$$y^2 - sx = s^2, \quad (s=\text{const}). \quad (37)$$

The lines $x_2 = \text{constant}$ are given by the hyperbola branches

$$6(x + x_2\sqrt{2/3})^2 - 2y^2 = x_2^2, \quad (x_2=\text{const.}) \quad (38a)$$

$$x \geq \max\{0, -x_2\sqrt{3/8}\} \quad (38b)$$

The sections of these curves in the first quadrant are displayed in Figure

10a. The points on the two axes correspond to the limits of x_2 for given s .

The points on the x -axis correspond to the lower limits $x_2 = -s/\sqrt{6}$; the points on the y -axis correspond to the upper limits $x_2 = 2s/\sqrt{6}$. This is illustrated in Figure 10b which also indicates the values of x and y at these limits.

The lines corresponding to the shape coordinates $\xi_2 = x_2/s = \text{constant}$ are obtained by dividing Eq. (35) into Eq. (36) which yields the straight lines

$$[3(1+\sqrt{6}\xi_2)]^{1/2}x - (1-\frac{1}{2}\sqrt{6}\xi_2)y = 0, \quad (\xi_2=\text{const.}) \quad (39)$$

They are displayed in Eq. (10c).

5. EXTENDED SHAPE COORDINATE SPACE

Certain continuous deformations of the molecule are not accounted for by continuous coordinate changes in the discussed coordinate space, namely the in-plane inversions of a triatomic molecule through the linear structures. If, in the spirit of considering only internal coordinate variations, out-of-plane motions are excluded then these inversions change a clockwise ordering of the three atoms into a counterclockwise ordering. Such deformations can be accounted for by suitably enlarging the coordinate space, as illustrated in Figure 11: The consecutive deformations exhibited in Figure 11A are represented by the sequence of points in the coordinate space of Figure 11B where a second coordinate triangle has been attached to the original one through reflection with respect to the line connecting corners 2 and 3. Further thought shows that this kind of enlargement has to be repeated in all directions over the entire x_1 - x_2 plane in order to cover all possible molecular in-plane inversions by continuous coordinate curves. The entire x_1 - x_2 plane is thus divided into coordinate triangles, half of them with clockwise ordering, the other half with counterclockwise ordering of atoms, as shown in Figure 11C. They are related by the translational grid of symmetry elements also shown on that figure: a set of trigonal rotation axes and three sets of reflection axes. Such translational symmetry grids are typical for internal

shape coordinates. (Another such translational grid for another set of internal coordinates has been discussed in an investigation of another PES [7].)

The enlargement of the coordinate triangle is not a purely academic exercise, but also serves a very practical purpose. Since one can only afford to calculate energy values at a limited number of coordinate points, it is necessary to interpolate these pristine energy values in order to obtain an intelligible picture of the energy surface. However, near the borders of the original coordinate triangle, successful interpolation would not be possible without taking into account the reflected values in the adjacent coordinate triangles. We found it therefore useful to generate, by reflection and rotation of the original, pristine energy values, the corresponding values in an extended shape coordinate region such as displayed in Figure 12A, which contains the section of the infinite grid that surrounds the original coordinate triangle (Figure 12B illustrates molecular deformations corresponding to twelve points A to N on a coordinate path circling corner No. 3 on Figure 12A). Interpolation was then performed in the entire space shown in Figure 12A. This procedure gave good energy contours in the original triangle near its borders. Figure 13 displays an interpolation of the groundstate of ozone [1] in the enlarged parameter space. The interpolation near the outside borders is clearly inferior to that near the inside borders. Ozone has, of

course, an additional C_{3v} symmetry within each triangle, as discussed in Section 4.3. The white areas near the triangle corners are the areas where two atoms come so close that the energy becomes extremely high and is not calculated. This would not be the case, of course, if the purely electronic PES would be plotted (i.e. without nuclear repulsions). It is apparent that, for the purpose of interpolating the PES in the original central triangle, one really requires only energy values within the dashed line of Figure 13.

The discussed coordinate space extension may also be useful for dynamic calculations. In this context, it may be noted that, for very small values of s , all three atoms come very close to each other, the PES tends to infinity and becomes highly repulsive. Hence, these regions of coordinate space are in fact inaccessible and there is no need to deal with very small and negative values of the coordinate x_3 .

REFERENCES

1. G. Atchity and K. Rudenberg, to be submitted.
2. A. S. Coolidge and H. M. James, *Phys. Rev.* **51** 855 (1937)
3. C. L. Pekeris, *Phys. Rev.* **112** 1649 (1958)
4. E. R. Davidson, *J. Am. Chem. Soc.* **99** 397 (1977)
5. J. N. Murrell, S. Carter, S. C. Farantos, P. Huxley, and A. J. C. Varandas
Molecular Potential Energy Functions (Wiley, New York 1984) Figure 7.8.
6. The radius of the inscribed circle is given by $\rho = s_i \tan(\phi_i/2) =$
 $s \tan(\phi_1/2) \tan(\phi_2/2) \tan(\phi_3/2) = (s_1 s_2 s_3 / s)^{1/2}$. The triangle area is $A = \rho s$.
The circumscribed-circle radius R is related to ρ by $\rho/R =$
 $4 \sin(\phi_1/2) \sin(\phi_2/2) \sin(\phi_3/2)$.
7. P. Valtazanos, S. T. Elbert, S. Xantheas, K. Ruedenberg, *Theor. Chim. Acta* **78**, 287 (1991).

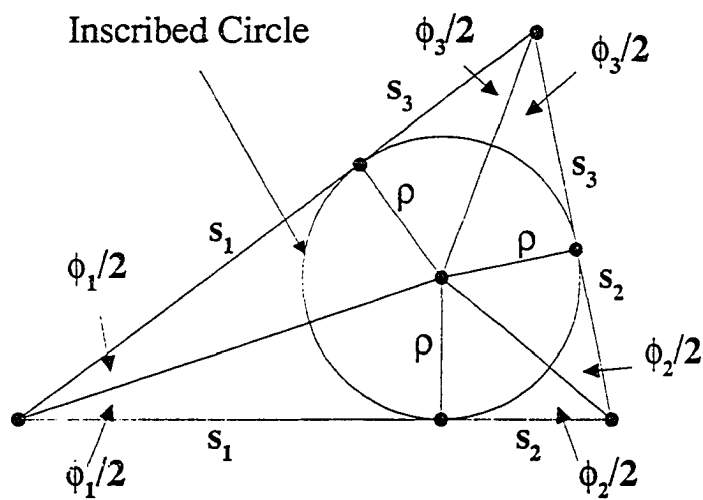
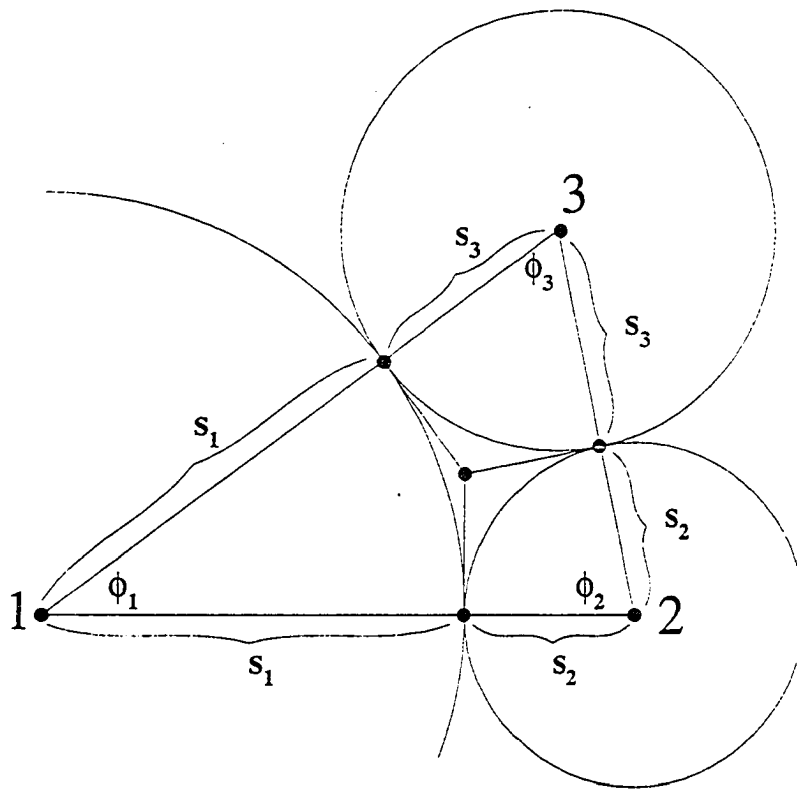


Figure 1. Geometric meaning of the perimetric coordinates s_1, s_2, s_3

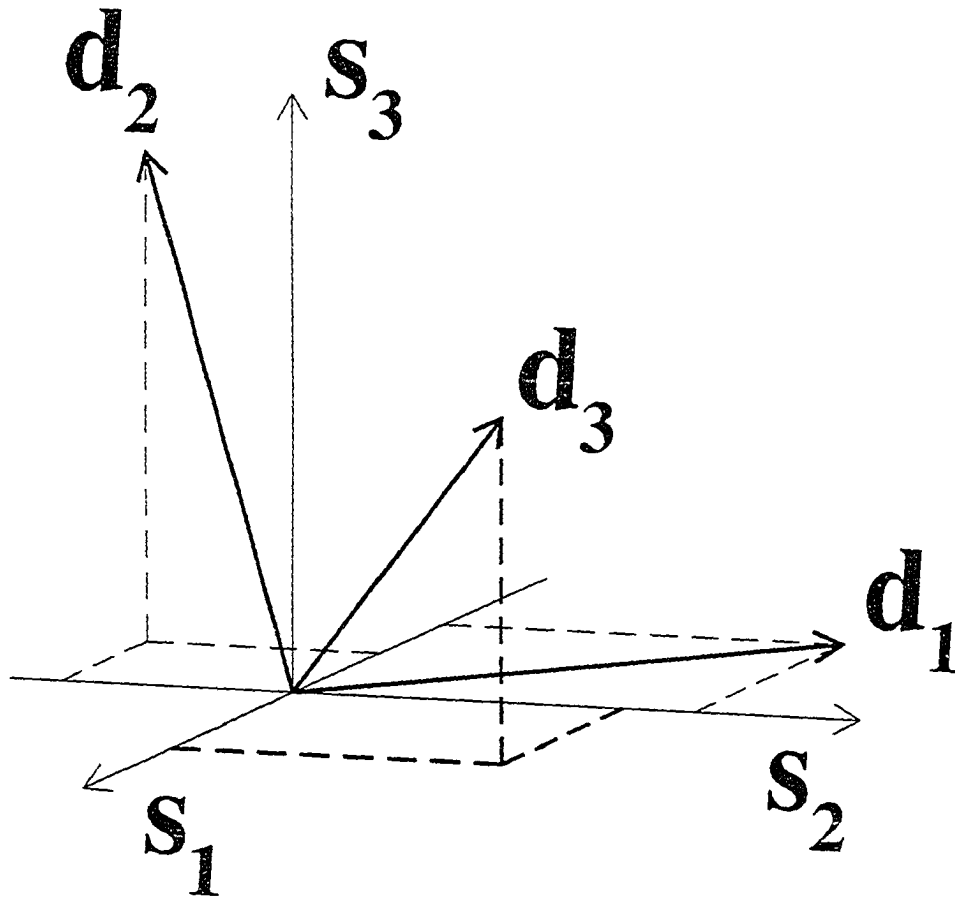


Figure 2. Basis vectors for perimetric scale-shape coordinates

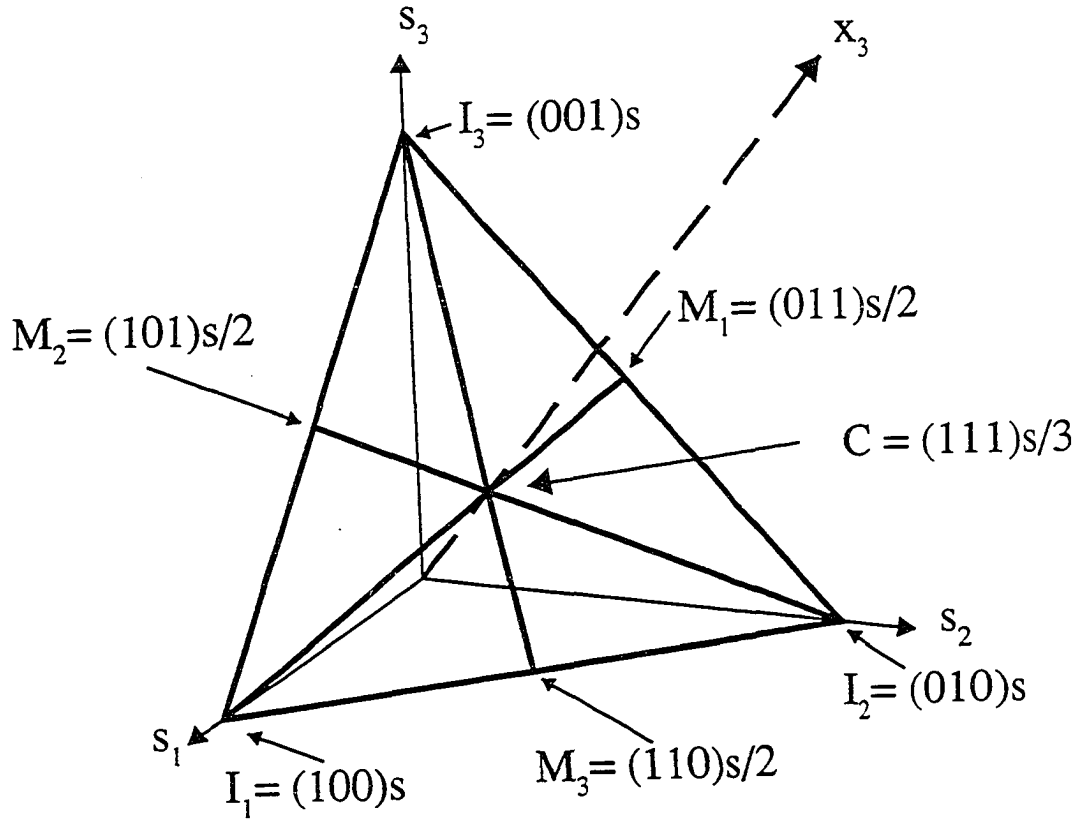


Figure 3. Perspective view of two-dimensional parameter plane for shape coordinates

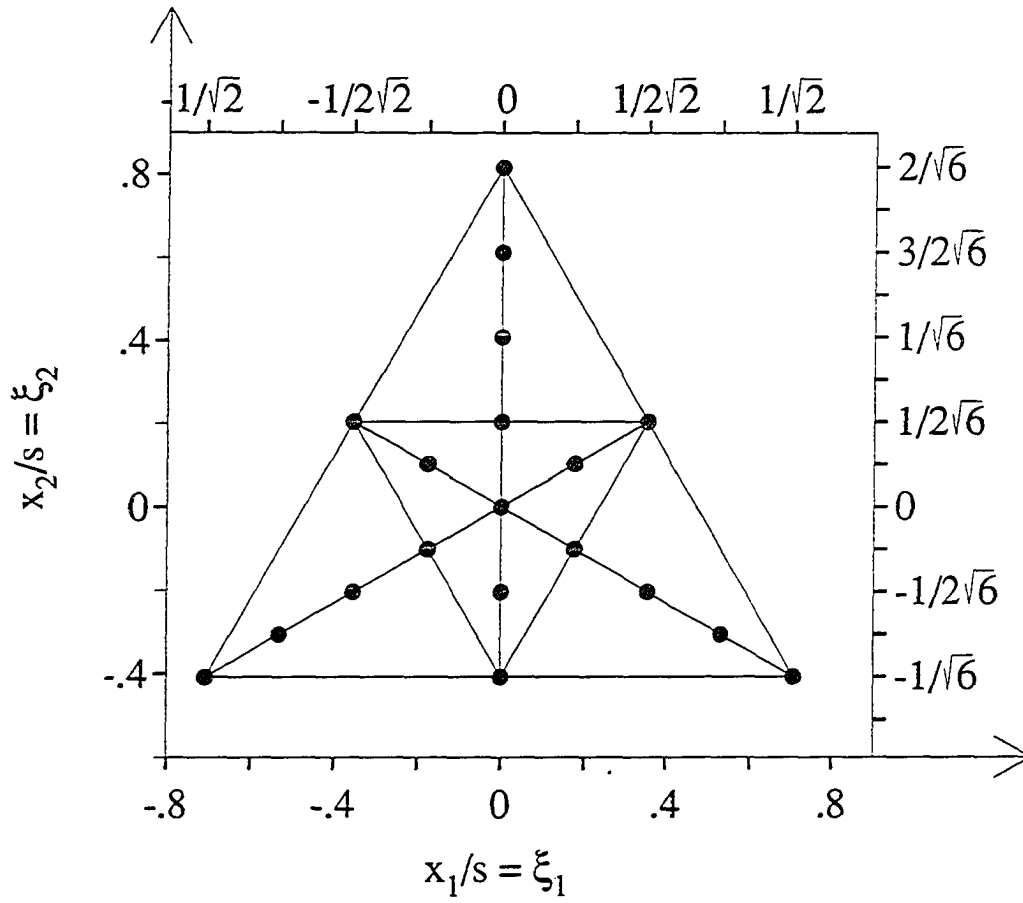
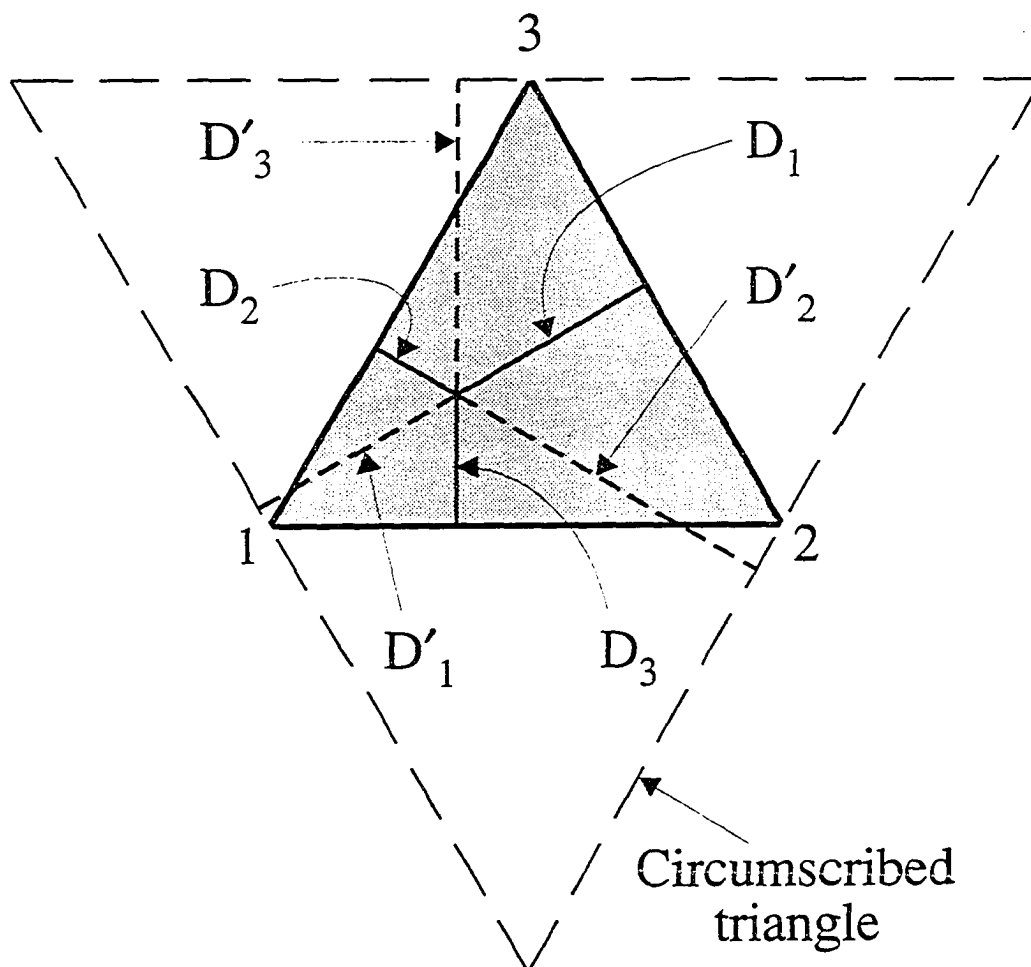


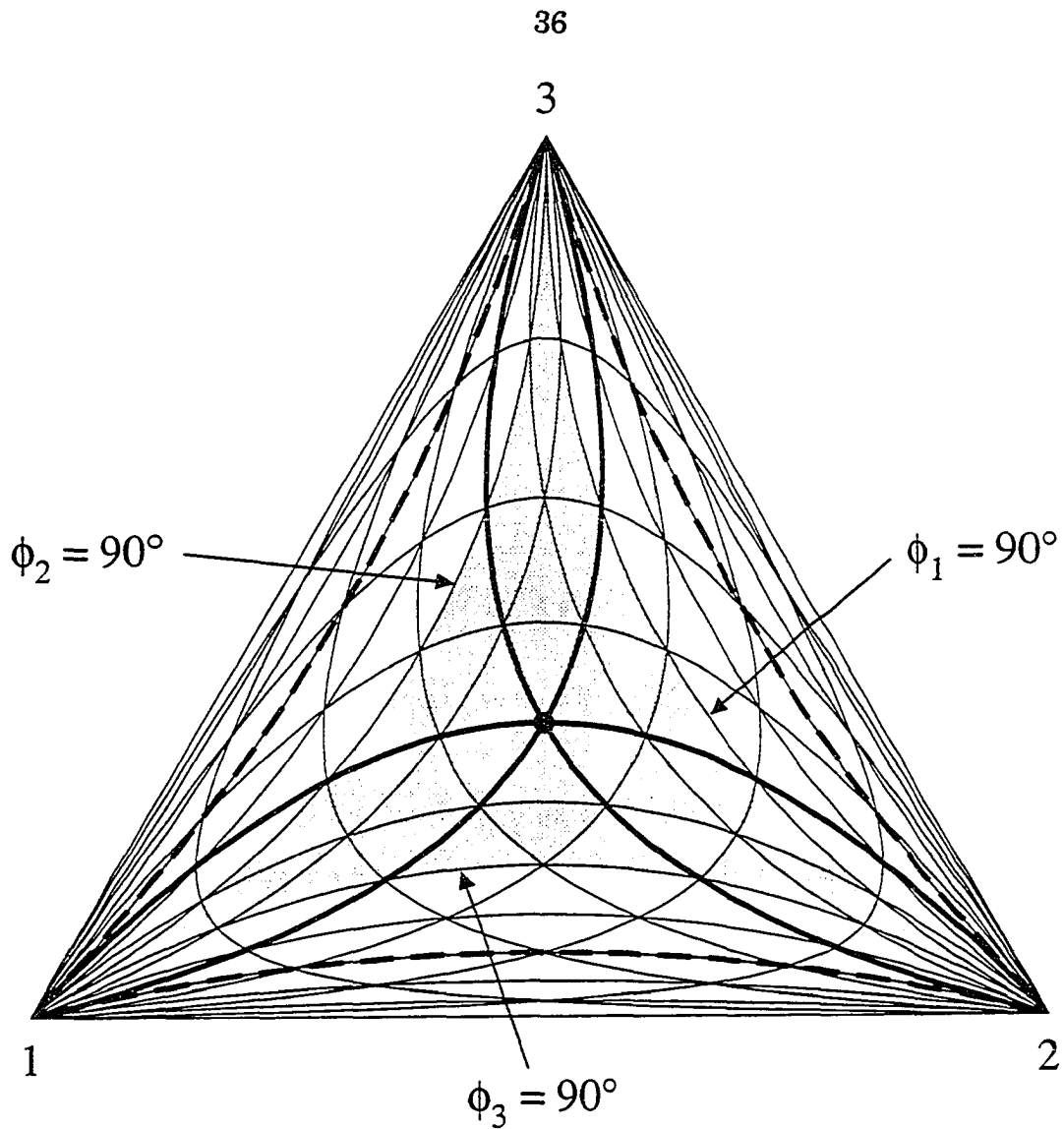
Figure 4. Coordinates on parameter plane of the shape coordinates



$$D_i = s_i \sqrt{3/2},$$

$$D'_i = r_{jk} \sqrt{3/2}$$

Figure 5. Definition of D_1 , D_2 , D_3 and D'_1 , D'_2 , D'_3 for Eqs. (22) and (24)



Constant angle grid on the shape coordinate triangle.
 The curves $\phi_j = \text{constant}$ are convex towards corner j .
 Increments: $\Delta\phi_j = 15^\circ$, Bold: 60° , Dashed: 120° .
 Shaded area: ϕ_1, ϕ_2, ϕ_3 all $\leq 90^\circ$

Figure 6. Curves of constant angle in scale-independent shape coordinate space

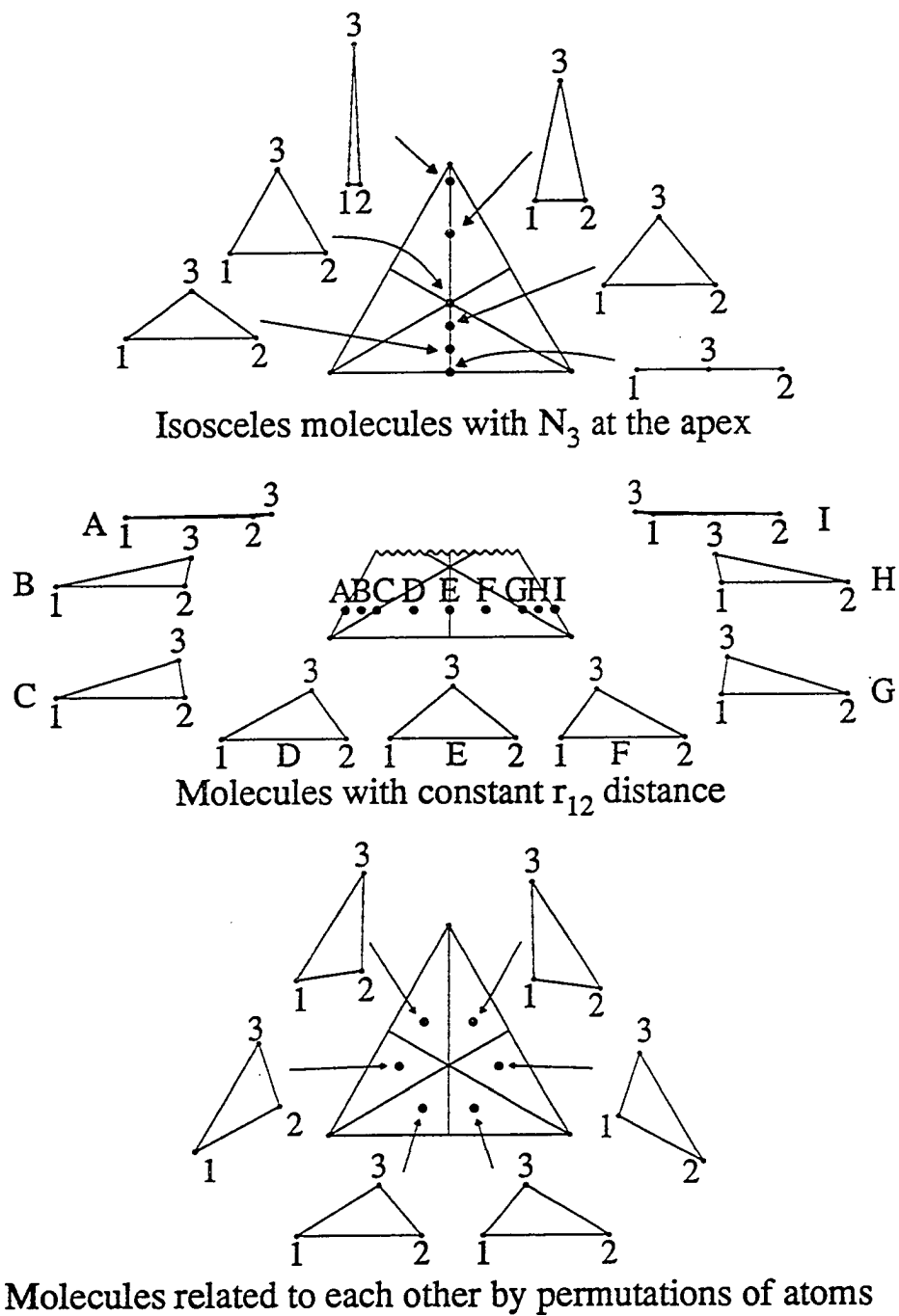


Figure 7. Examples of molecular shapes for selected points in the scale-independent shape coordinate plane

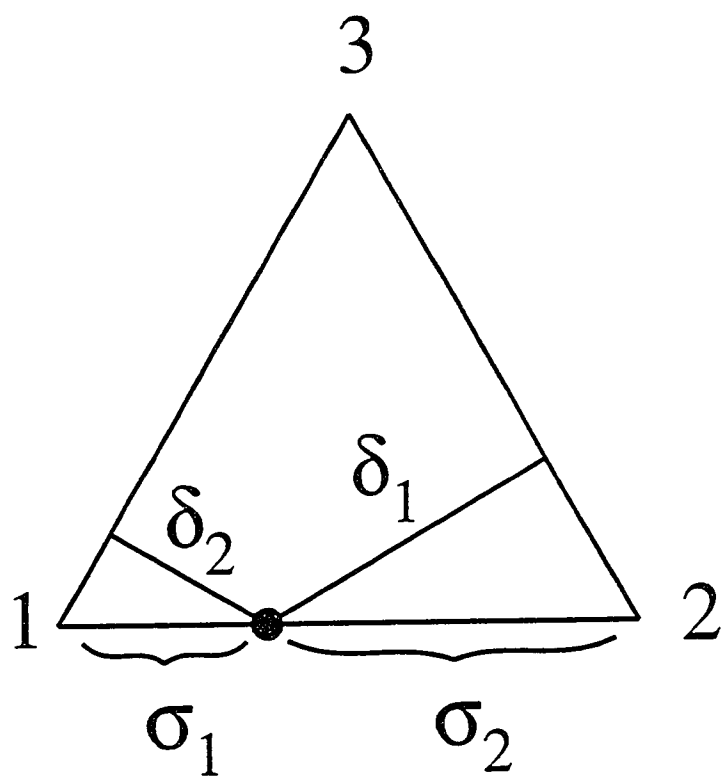


Figure 8. Coordinate point of a linear molecule $N_1N_3N_2$

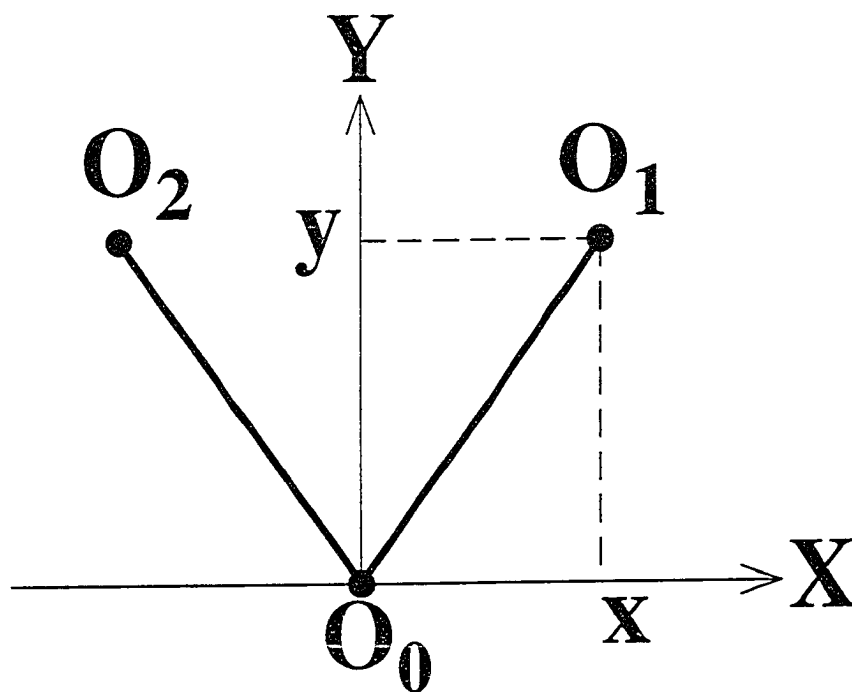


Figure 9. Coordinates x and y for isosceles molecules

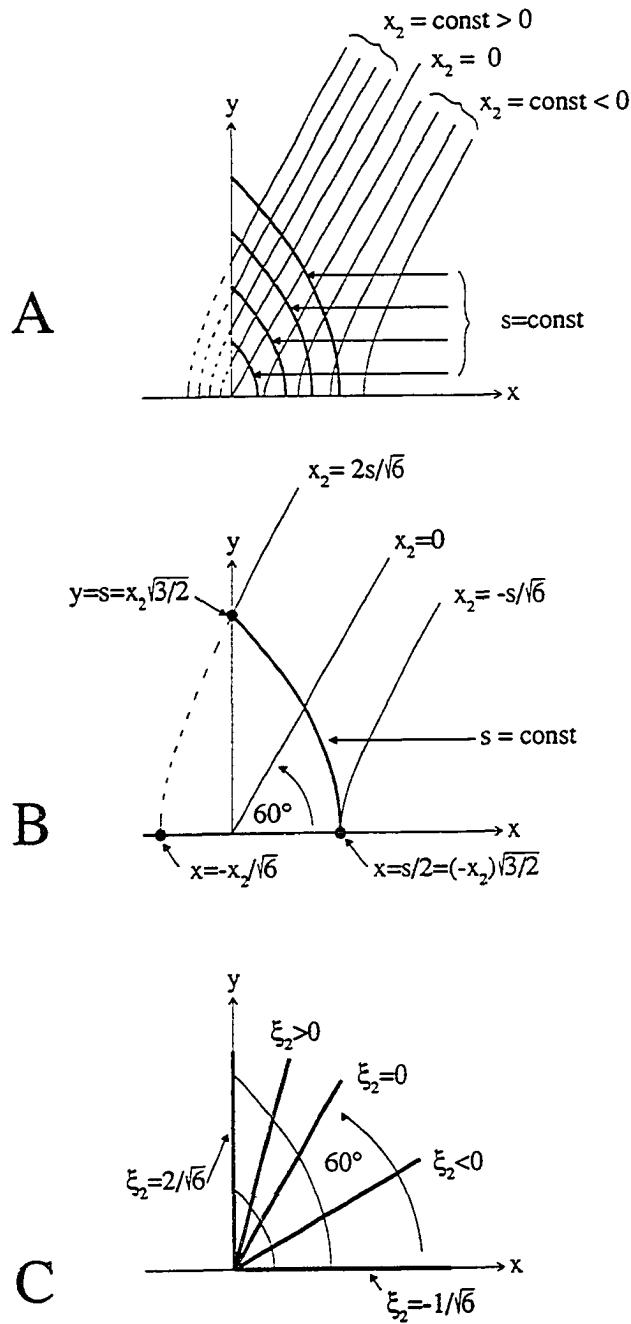
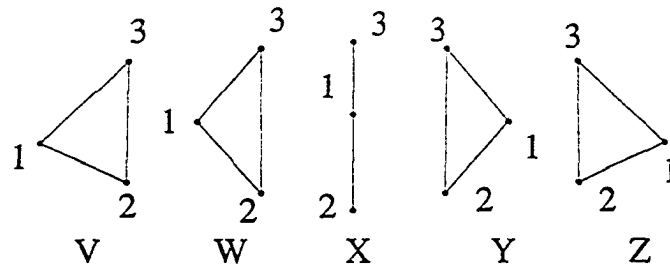
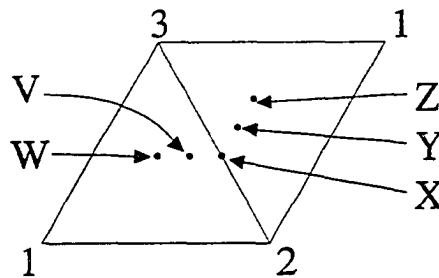


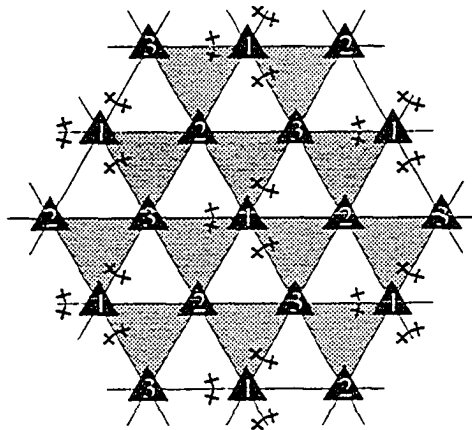
Figure 10. Lines $s=\text{constant}$, $x_2=\text{constant}$, and $\xi_2=\text{constant}$ on the (x,y) plane



A. In-plane molecule inversions keeping $r_{12} = \text{const.}$ and $r_{12} + r_{23} + r_{13} = \text{const.}$

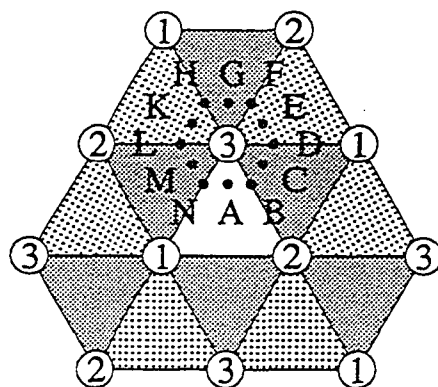


B. Extended shape coordinates for deformations of A.

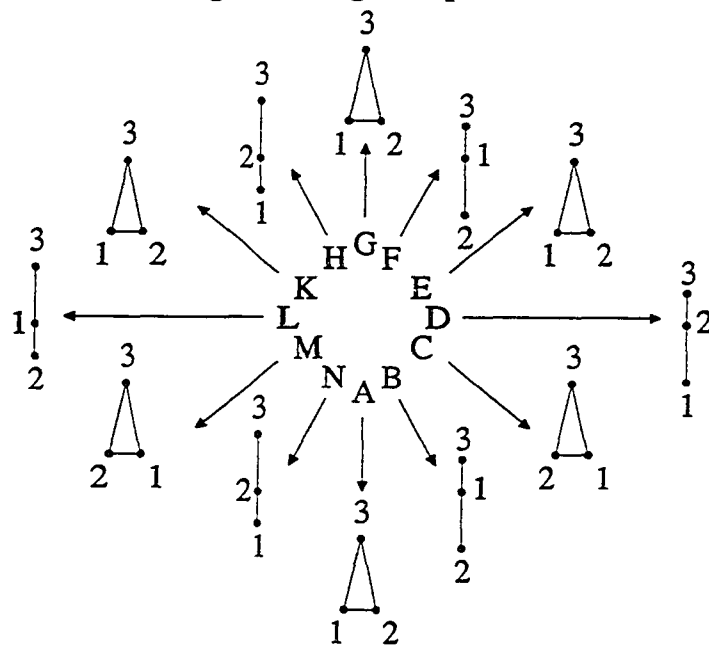


C. Complete extended shape coordinate space. 1,2,3: Triangle corners. Shaded: Clockwise order. White: Anticlockwise order of atoms. ▲: Trigonal axes. Solid lines: mirror planes. Crosses: Equivalent coordinate points.

Figure 11. Complete extended shape coordinate space



- A. Shape coordinate space for interpolation.
 Shaded triangles: clockwise atom order.
 Dotted triangles: anti-clockwise atom order.
 Center triangle: original space (anti-clockwise).



- B. Molecular shapes corresponding to points A to N above.

Figure 12. Shape coordinate space extended for interpolation

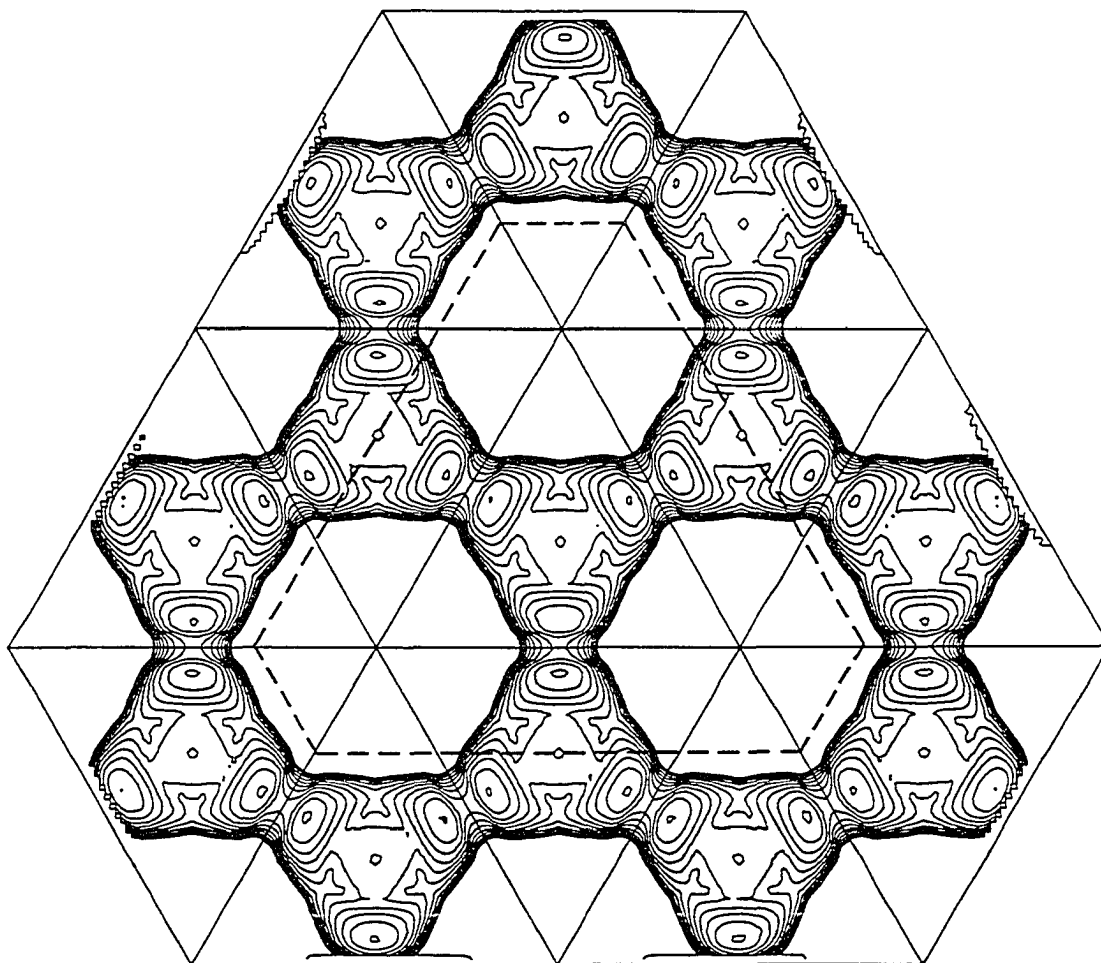


Figure 13. Extended potential energy surface of ozone ground state for $s=2.4\text{\AA}$

PAPER II. POTENTIAL ENERGY SURFACES NEAR INTERSECTIONS

POTENTIAL ENERGY SURFACES NEAR INTERSECTIONS

Ames Laboratory USDOE and Department of Chemistry

Iowa State University

Ames, IA 50011

ABSTRACT

The topographies of two potential energy surfaces are examined in the vicinity of their intersection. A brief account of the basic theory is given and the possible surface types are discussed explicitly. Two main patterns are found. One of these ("peaked") has the character of a tilted double cone in that the lower (upper) surface decreases (increases) in all directions from the intersection which is a point where an infinite number, in fact, all orthogonal trajectories emanate. The other pattern ("sloped") results when both surfaces are monotonically sloped and touch each other along the slope, with most orthogonal trajectories bypassing the intersection. When the latter pattern prevails, the intersection can lie on a steepest descent line which originates at a transition state and hence may qualify as a reaction path model. An intermediate pattern, involving a horizontal slope on both surfaces, is also possible. The topographical patterns also differ markedly with respect to the bunching of the steepest descent lines. In general, the latter tend to veer away from the intersection on the lower surface favoring bifurcations but are funneled towards the intersection on the upper surface, making the vicinity of the intersection a region favoring radiationless transitions. The various cases are classified and illustrated through quantitative graphs of contours and orthogonal trajectories.

1. INTRODUCTION

Radiationless transitions among potential energy surfaces play essential roles in photophysical phenomena and photochemical reactions. They occur preferentially when potential energy surfaces (PES's) approach each other closely and, in particular, when they cross. Such crossings represent therefore an important aspect of potential energy surfaces. Although quantitative *ab initio* information about them is still limited, it has become apparent that intersections occur frequently. The results reported in previous papers furthermore show that they can lie close to transition states [1] as well as on steepest descent curves connecting transition states and minima [2], i.e., on curves which are often viewed as models for reaction paths.

Fundamental theorems regarding PES intersections have been known since 1927 [3] and have been discussed in further detail in recent years [4,5,6]. However, we are not aware of any quantitative presentation of the variety of shapes which PES's can assume around intersections nor of any discussion of their orthogonal trajectories. Since the difference between two PES's near an intersection is an elliptical cone, and since the two surfaces *together* form a double cone when the energy is plotted against the internal coordinate plane, it is customary to talk about "conical" intersections.

However, this double cone may be arbitrarily tilted against the energy axis so that, in general, it is not too helpful for visualizing the energy contours on any one surface.

In the neighborhood of a point where two states cross, the first-order approximations to the two PES's depend essentially on three parameters, and their values strongly affect the topographical features of the surfaces. In the present note, we analyze and exhibit graphically contours as well as orthogonal trajectories for the various possible cases in this approximation. Since the values of these parameters can be readily determined in any specific case, the classification given provides adequate information for recognizing the character of a particular crossing.

2. THEORETICAL BACKGROUND

In the present section some basic relationships are summarized, which are spread over the literature, and certain specific aspects are discussed in greater detail.

2.1 The Crossing Conditions

The intersection of two potential energy surfaces, $E_1(\mathbf{q})$ and $E_2(\mathbf{q})$, implies that, for certain values of the internal coordinates $\mathbf{q} = (q_1, q_2 \dots q_M)$ of the molecule, the two energies are equal. The locus of all points in the internal coordinate space where the identity $E_1(\mathbf{q})=E_2(\mathbf{q})$ holds, is a curvilinear coordinate *subspace* which we denote as the *intersection coordinate subspace* (ICS). If E_1 and E_2 were two *arbitrary* surfaces, then one would expect the condition $E_1 = E_2$ to determine an ICS of dimension $(M - 1)$. However, E_1 and E_2 are not independent of each other, rather they are two solutions of the same eigenvalue problem of *one* Hamiltonian H . This circumstance leads to an additional condition, as was first recognized by von Neuman, Wigner, and Teller [3].

Without loss of generality, the two intersecting adiabatic states, ψ_1 and ψ_2 , can be expressed as linear combinations of two *arbitrary*, e.g., diabatic orthogonal states, ϕ_1 and ϕ_2 , in the function space that is complementary to

the space spanned by all *other* eigenstates ψ_n ($n \geq 3$) of the relevant electronic Hamiltonian operator H whose energies $E_3, E_4 \dots$ are assumed to be non-degenerate with E_1 and E_2 :

$$\psi_1 = \phi_1 c_{11} + \phi_2 c_{21}, \quad \psi_2 = \phi_1 c_{12} + \phi_2 c_{22}. \quad (2.1)$$

The expansion coefficients c_{ij} and the corresponding energies E_1, E_2 are determined by the eigenvalue problem of the 2x2 matrix $H_{ij} = \langle \phi_i | H | \phi_j \rangle$. We consider here the practically important case that all H_{ij} are real. The variation of the E_j and c_{ij} with the nuclear motions is a result of the dependence of the H_{ij} upon the M internal coordinates $\mathbf{q} = (q_1, q_2, \dots, q_M)$ which describe the geometry of the nuclear framework: $H_{ij} = H_{ij}(\mathbf{q})$. The phase-consistent discussion of the solutions is made transparent by writing the matrix $\mathbf{H} = \{H_{ij}\}$ in the form

$$\mathbf{H} = \bar{H} \mathbf{I} + R \mathbf{U}, \quad (2.2)$$

with \mathbf{I} denoting the identity matrix and \mathbf{U} denoting the matrix

$$\mathbf{U} = \begin{pmatrix} \cos\alpha & \sin\alpha \\ \sin\alpha & -\cos\alpha \end{pmatrix}, \quad (2.3)$$

where the quantities \bar{H} , R and α are defined by

$$\bar{H} = (H_{11} + H_{22})/2, \quad \Delta H = (H_{11} - H_{22})/2, \quad R = (\Delta H^2 + H_{12}^2)^{1/2}, \quad (2.4)$$

$$\cos\alpha = \Delta H/R, \quad \sin\alpha = H_{12}/R. \quad (2.5)$$

From Eqs. (2.2) and (2.3), the expectation value of an *arbitrary* linear combination $\psi = (\phi_1 \cos\gamma + \phi_2 \sin\gamma)$ is found

to be

$$\langle \psi | H | \psi \rangle = \bar{H} + R \cos(2\gamma - \alpha). \quad (2.6)$$

The manifest extrema of this function with respect to γ yield the two eigenstates

$$\psi_1 = \phi_1 \cos\alpha/2 + \phi_2 \sin\alpha/2 \quad (2.7)$$

with

$$E_1 = \bar{H} + R, \quad (2.8)$$

and

$$\psi_2 = \phi_1 \cos(\alpha+\pi)/2 + \phi_2 \sin(\alpha+\pi)/2 = -\phi_1 \sin\alpha/2 + \phi_2 \cos\alpha/2 \quad (2.9)$$

with

$$E_2 = \bar{H} - R. \quad (2.10)$$

According to Eqs. (2.8) and (2.10), an intersection occurs whenever R vanishes which, according to Eq. (2.4), requires that the *two* quantities ΔH and H_{12} *both* vanish. The intersection coordinate subspace (ICS) is therefore defined by the two crossing conditions

$$\Delta H(\mathbf{q}) = 0, \quad \text{i.e.} \quad H_{11}(\mathbf{q}) = H_{22}(\mathbf{q}), \quad (2.11)$$

$$H_{12}(\mathbf{q}) = 0. \quad (2.12)$$

2.2 The Intersection Space (ICS)

Dimension and Symmetry

It is possible that the equation system (2.11), (2.12) has no real solutions,

in which case the two states do not cross. However, *if* a real solution exists for one particular point \mathbf{q}° , *then* it is to be expected (i.e., the opposite is unlikely) that this point is part of a contiguous (M-2) dimensional region in which this remains true. This inference is based on the premise that the matrix elements H_{ij} are piecewise continuous functions in all coordinates. Thus, *if* there exists an ICS, *then* it is expected to be of dimension (M-2).

This conclusion has to be modified in those cases where, for some reason, the off-diagonal element H_{12} vanishes *identically for all* values of the nuclear coordinates q_1, q_2, \dots, q_M . In such a case, ϕ_1 and ϕ_2 clearly are the eigenfunctions ψ_1, ψ_2 for all values of \mathbf{q} and Eq. (2.11) is the only remaining condition for a crossing. Thus, the ICS, if it exists, is expected to be of dimension (M-1). The most common reason for this to happen is that the two states ψ_1, ψ_2 belong to different irreducible representations of the symmetry group of the molecule. In such a case, the space spanned by ϕ_1 and ϕ_2 spans a reducible representation and the reduction, by purely group theoretical means, yields two states belonging to different irreps between which the off-diagonal element H_{12} vanishes identically for all (q_1, q_2, \dots, q_M) . Hence, they are in fact the eigenstates ψ_1, ψ_2 and Eq. (2.11) remains as only condition for crossing so that the ICS is of dimension (M-1).

Often a situation is found which combines aspects of the two cases just discussed. It occurs in molecules where a certain restricted class of nuclear

arrangements belong to a higher symmetry group than other geometries. For example, a molecule XY_2 belongs to the symmetry group C_s when all internuclear distances are different, but it belongs to the higher group C_{2v} when the two (XY) bond lengths are the same. In such molecules, there usually exist states which belong to the same irreducible representation in the lower symmetry (e.g., A' in C_s) but to different irreps of the higher symmetry (e.g., A_1 and B_1 in C_{2v}) for the restricted class of geometries. There are many examples for two such states to cross for a geometry that has the higher symmetry. In the space of higher symmetry, the upper state belongs to one irrep (e.g., A_1) on one side of the intersection and to the other irrep (e.g., B_1) on the other side of the intersection. The reverse is true for the lower state. If the restricted coordinate space of higher symmetry is of dimension R , then the M coordinates can be chosen in such a manner that all variations in (q_1, q_2, \dots, q_R) maintain the higher symmetry and $(q_{R+1}, q_{R+2}, \dots, q_M)$ break that symmetry unless they all vanish. It can then be concluded that the intersection space of the two states is of dimension $(M-2)$ in the *total* space and of dimension $(R-1)$ in the *restricted* space of higher symmetry. The intersection space is therefore of dimension $(R-1)$ in the coordinates (q_1, \dots, q_R) , and has $[(M-2)-(R-1)] = (M-R-1)$ additional degrees of freedom when the coordinates (q_{R+1}, \dots, q_M) are allowed to vary as well. If it so happens that $R = M - 1$, then it is thus possible that the intersection space lies entirely in the

restricted coordinate space of higher symmetry.

The discussed case of two states belonging to the same irrep in the larger space of low symmetry and to different irreps in the restricted space of high symmetry is not the only possibility for the intersection of two PES's in a space of higher symmetry. It can also happen that two PES's which intersect in the space of higher symmetry, belong to the same irrep in the space of higher symmetry as well as in the space of lower symmetry. An example of such a crossings has recently been found through *ab initio* calculations for the lowest two 1A_1 states of ozone [1]. In terms of the coordinates chosen at the end of the last paragraph, the ICS is, in such cases, of dimension $(M-2)$ in the total space, of dimension $(R-2)$ in the coordinates (q_1, q_2, \dots, q_R) and has $(M-2)-(R-2) = (M-R)$ additional degrees of freedom when the coordinates $(q_{R+1}, q_{R+2}, \dots, q_M)$ are added to the coordinates (q_1, q_2, \dots, q_R) . That is, the intersection space corresponds to a subspace of dimension $(R-2)$ in the restricted coordinate space of q_1, \dots, q_R , complemented by the full variation in the coordinates q_{R+1}, \dots, q_M .

Still another situation is found in the cases of the Jahn-Teller and the Renner-Teller effects. Here two states, which belong to *different* irreps in the larger space of low symmetry, become two partner functions spanning *one* two-dimensional irrep in a restricted space where a higher, non-Abelian symmetry group applies. For the Renner-Teller effect, this group is $C_{\infty v}$; for

the Jahn-Teller effect, it is another point group.

Diatomic and triatomic molecules are special in that, for them, the lowest possible symmetry is not C_1 as it is for all other molecules. In triatomic molecules, it is C_s , so that, for *any* molecular geometry, there exist two kinds of states, those belonging to the irrep A' and those belonging to A'' . Since there are three internal coordinates, the intersection "seam" between two surfaces is a line (dimension 3-2) if they belong to the same irrep and a two-dimensional sheet (dimension 3-1) if they belong to different irreps. Furthermore, within the full three-dimensional coordinate space, there always exists a two-dimensional subspace, corresponding to the linear conformations of the molecule, where it belongs to $C_{\infty h}$ symmetry. Since most of its irreps are two-dimensional, there exists then the possibility for a Renner-Teller effect. When two atoms are of the same element, then there also exists a two-dimensional coordinate subspace where the molecule has C_{2v} symmetry. One then has three possible cases: (i) both states belong to the *same* irrep in C_s and C_{2v} : (in this case, the ICS seam is a line in the full C_s space and penetrates the C_{2v} coordinate plane in a point); (ii) both states belong to *different* irreps in C_s and C_{2v} : (in this case the ICS is a two-dimensional sheet in C_s and penetrates the C_{2v} coordinate plane in a line); (iii) the two states belong to the *same* irrep in C_s , but to *different* irreps in C_{2v} : in this case the ICS seam is a line in C_s and in C_{2v} ; it is therefore

possible that it is a line which lies *entirely* in the C_{2v} -preserving coordinate space without extending in the full C_s space. If all three atoms are of the same element, then there exists a one-dimensional coordinate subspace of equilateral triangles with D_{3h} symmetry. Since this group has two-dimensional irreps, one has here the possibility of a Jahn-Teller effect for two states belonging to different symmetry in C_{2v} .

Diatomic molecules are special in that they have only one internal coordinate, i.e., the internuclear distance, and in that they belong to the symmetry groups $C_{\infty v}$ or $D_{\infty h}$. The states may therefore belong to many different irreps. Two states belonging to different irreps intersect in a point (dimension $1-1=0$). However, for two states of the same symmetry, the *two* conditions (2.11) and (2.12) cannot, in general, be satisfied by adjusting the one available variable R and hence they cannot be expected to intersect. This "non-crossing rule" is, however, strictly limited to diatomic molecules. Attempts to establish a wider validity for it have failed [5].

Intersection Space and Reaction Paths

At a transition state, orthogonal trajectories of PES contours emanate in the directions of the M normal modes. One of them, the intrinsic reaction path, is a steepest descent line. The $(M-1)$ others are steepest ascent lines and define the barrier ridge. If the transition state lies in an R dimensional

coordinate subspace of higher symmetry, then its normal modes either lie entirely in the space of higher symmetry or are perpendicular to it. It can then be shown that the orthogonal trajectories starting out *in* the space of higher symmetry maintain that symmetry until they come to a point where the gradient vanishes or is discontinuous. For example, if the transition state of a triatomic molecule lies in the C_{2v} preserving subspace, then two of the orthogonal trajectories emanating from the transition state stay in the C_{2v} subspace and the third one starts out along the C_{2v} symmetry breaking coordinate.

If now, in the subspace of higher symmetry, this PES also has an intersection with another PES belonging to a *different* irreducible representation, then the intersection space is of dimension (R-1) within the higher symmetry space. It is therefore not unlikely that any one of the R one-dimensional orthogonal trajectories originating at the transition state in the high-symmetry subspace (be it the reaction path or one of the ridge lines) crosses the ICS. Indeed, we have shown elsewhere [2] that the reaction path of the cyclopropylidene ring opening goes through an intersection after having passed the transition state under the described conditions.

If the PES intersects a surface belonging to the *same* irreducible representation then the ICS is of dimension (R-2) within the high-symmetry subspace and one would think that it is unlikely to be crossed by a specific

one-dimensional orthogonal trajectory in that subspace. For example, in the C_{2v} preserving subspace of a triatomic molecule, such an intersection is a *point* in a two-dimensional plane and it would seem improbable that an orthogonal trajectory in that plane would go through exactly that point. Nonetheless, we have found [1] that in the ozone molecule, such an intersection point does in fact lie on the orthogonal trajectory emanating from a transition state along a barrier ridge. In addition, this intersection point lies within 0.04Å and 1 kcal/mol of a transition state on one PES and a minimum on the other PES. These "coincidences" are clearly consequences of an intrinsic relation between the lowest two eigenvalues of this particular Hamiltonian, so that purely probabilistic reasoning is inappropriate.

Intersection Adapted Coordinates

The discussion of an intersection is simplified by choosing, in a certain domain around the intersection, curvilinear coordinates which are particularly suited to the problem. Such intersection adapted coordinates

$p_1, p_2, p_3, \dots, p_M$ can be defined as follows:

$$p_1 = H_{12}(\mathbf{q}) \tag{2.13a}$$

$$p_2 = \Delta H(\mathbf{q}) = [H_{11}(\mathbf{q}) - H_{22}(\mathbf{q})]/2, \tag{2.13b}$$

$$p_j = p_j(\mathbf{q}), \quad j = 3, 4, \dots, M \tag{2.13c}$$

where the p_j for $j \geq 3$ are chosen orthogonal to p_1, p_2 in the sense that

$$\sum_{t=1}^M (\partial p_j / \partial q_t) (\partial p_n / \partial q_t) = 0 \quad (2.14)$$

for $n = 1, 2$ and $j = 3, 4, \dots, M$. In the domain where these definitions are valid, the two energy surfaces are given by

$$E_{1,2} = \bar{H}(\mathbf{p}) \pm \{p_1^2 + p_2^2\}^{1/2} \quad (2.15)$$

and the intersection space is then given by the conditions $p_1 = p_2 = 0$. It is therefore spanned by the coordinates p_3, p_4, \dots, p_M .

Tangent Intersection Space

It is useful to examine the ICS within a small neighborhood of a point $\mathbf{q}^\circ = (q_1^\circ, q_2^\circ, \dots, q_M^\circ)$. In such a domain, the ICS is approximated by the $(M-2)$ dimensional *linear* space which is tangential to the ICS at \mathbf{q}° , the *tangent* ICS. It is obtained by expanding the matrix elements $H_{ij}(\mathbf{q})$ to first order in terms of the displacements \mathbf{x} from the point \mathbf{q}° , i.e.,

$$\mathbf{x} = \mathbf{q} - \mathbf{q}^\circ = (x_1, x_2, \dots, x_M). \quad (2.16)$$

Writing

$$\bar{H}(\mathbf{q}) = \bar{H}^\circ + \sum_{t=1}^M U_t x_t, \quad \bar{H}^\circ = \bar{H}(\mathbf{q}^\circ); \quad U_t = [\partial \bar{H} / \partial q_t]^\circ, \quad (2.17a)$$

$$\Delta H = 0 + \sum_{t=1}^M V_t x_t, \quad V_t = [\partial(\Delta H) / \partial q_t]^\circ, \quad (2.17b)$$

$$H_{12} = 0 + \sum_{t=1}^M W_t x_t, \quad W_t = [\partial H_{12} / \partial q_t]^\circ, \quad (2.17c)$$

we can express the two energy surfaces near \mathbf{q}_0 as

$$E_{1,2} = \sum_t U_t x_t \pm \{ (\sum_t V_t x_t)^2 + (\sum_t W_t x_t)^2 \}^{1/2}. \quad (2.18)$$

The tangent ICS is then determined by

$$\sum_t V_t x_t = \sum_t W_t x_t = 0, \quad (2.19)$$

i.e., it is the plane orthogonal to the gradients of $H_{1,2}$ and ΔH .

2.3 The Branching Space

Energies

While the degeneracy $E_1=E_2$ is *preserved* in the $(M-2)$ dimensional ICS spanned by the coordinates p_3, \dots, p_M , it is *lifted* in the two-dimensional *branching space* spanned by the coordinates p_1, p_2 . On this sheet, defined by $p_3=p_4=\dots=p_M=0$, the energies are given by

$$E_{1,2} = \bar{H}(p_1, p_2) \pm (p_1^2 + p_2^2)^{1/2} \quad (2.20)$$

Near a point \mathbf{q}_0 on the ICS, this branching sheet is approximated by the *tangent branching plane* spanned by the gradients of $H_{1,2}$ and ΔH at \mathbf{q}_0 , i.e., by the coordinates

$$y_1 = \sum_t V_t x_t \approx p_1, \quad y_2 = \sum_t W_t x_t \approx p_2. \quad (2.21)$$

In this tangent branching space the energies become

$$E_{1,2} \approx A_1 y_1 + A_2 y_2 \pm (y_1^2 + y_2^2)^{1/2}. \quad (2.22)$$

On any given, fixed straight line through the intersection in the tangent branching space, say $y_1=B_1 t$, $y_2=B_2 t$, one finds

$$E_1 = (A_1 B_1 + A_2 B_2)t + (B_1^2 + B_2^2)|t| \quad \text{for the upper state}$$

$$E_2 = (A_1 B_1 + A_2 B_2)t - (B_1^2 + B_2^2)|t| \quad \text{for the lower state}$$

so that one has the identities

$$(\partial E_1 / \partial t)^{\circ} = (\partial E_2 / \partial t)^{\circ}_{+}, \quad (2.23a)$$

$$(\partial E_2 / \partial t)^{\circ} = (\partial E_2 / \partial t)^{\circ}_{+}. \quad (2.23b)$$

They are illustrated by Figure 1 which also explains the somewhat confusing terms "intersection" and "crossing". They are based on the picture that on any line through the intersection, $(E_1)_{+}$ and $(E_2)_{-}$ form a continuously varying state with a continuous slope [see also the remarks after Eq.(2.25) regarding the continuity of the wave functions] as do $(E_1)_{-}$ and $(E_2)_{+}$. In fact, $(E_1)_{+}$ and $(E_1)_{-}$ are of course connected by going around the crossing in an additional dimension as are $(E_2)_{+}$ and $(E_2)_{-}$. Figure 1 also shows that the two surfaces can connect in three possible ways, namely, according to a "peaked" pattern, a "sloped" pattern, and an intermediate, "semi-level" pattern, a distinction which will turn out to be useful for the classification of intersections to be developed in Sec. 2. The stated conclusions remain valid if the straight line also has components with respect to the additional coordinates p_3, p_4, \dots, p_M .

Wave Functions

The quantities R and α which were introduced in Eqs. (2.4) and (2.5) have a simple meaning in the branching space. From the definitions (2.13), it

follows that

$$R = (p_1^2 + p_2^2)^{1/2}, \quad \cos\alpha = p_1/R, \quad \sin\alpha = p_2/R \quad (2.24)$$

and it is apparent that (R, α) are the polar coordinates corresponding to the intersection- adapted coordinates (p_1, p_2) if the latter are plotted as a Cartesian axis system. On the other hand, the states ψ_1, ψ_2 can be considered as unit vectors in the function space spanned by the orthogonal functions ϕ_1, ϕ_2 . According to Eqs. (2.7) and (2.9), the polar angles in this function space are $(\alpha/2)$ for ψ_1 and $(\alpha+\pi)/2$ for ψ_2 . Consequently, if one moves along a continuous sequence of coordinates (p_1, p_2) describing a loop around the intersection point q° in the coordinate branching space, then the two corresponding eigenstates rotate continuously around the origin in the (ϕ_1, ϕ_2) function space, but "at half the speed." This is illustrated in Figure 2. Since ϕ_1 and ϕ_2 can be assumed to be univalued everywhere, the following two inferences can therefore be drawn.

First, if one travels halfway around q° , corresponding to an increase in α by π , then one would have

$$\psi_1(\alpha+\pi) = \psi_2(\alpha), \quad \psi_2(\alpha+\pi) = -\psi_1(\alpha) \quad (2.25)$$

if the functions ϕ_1 and ϕ_2 were the same. This becomes in fact the case at the intersection. Thus, Eq.(2.25) holds when ψ_1 is the limiting wave function immediately "before" and ψ_2 is the limiting wave function immediately "after" passing through q° on a straight line ("before" corresponding to α and "after"

corresponding to $\alpha+\pi$). At the intersection point, the wave function of the lower PES connects thus with that of the higher PES, and vice versa, except for possible changes in sign. Consequently, in passing through the intersection along any fixed direction, the wave functions of both, the lower as well as the higher PES, change their character abruptly because, in fact, they *exchange characters* at \mathbf{q} . (At the intersection, *any* linear combination of ψ_1 and ψ_2 is of course an eigenfunction.) This behavior of the wave function is related to the behavior of the gradients of E_1 and E_2 expressed by Eq.(2.23) and depicted in Figure 1 and is the limiting case of the behavior found for wave functions near avoided crossings.

The sudden change in the character of the wave function of the lower PES and that of the higher PES is very obvious for the intersection of two surfaces of different symmetries because, if the PES belonging to irrep A lies above that for irrep B "before" the intersection, then the reverse is true "after" the intersection in such a case. Consequently, both the upper as well as the lower PES change from one irrep to the other when one moves through the intersection.

There exists some inconsistency in the use of the concept of a "state" in such situations. In general and in the case of two PES's of the same symmetry, one state is usually defined as comprising all wave functions with the lower energy, the other state is defined as comprising all wave functions

with the higher energy. However, when the two states belong to different irreducible representations of a group, then it is customary to consider all energies corresponding to wave functions *belonging to the same irreducible representation* as one state and one PES. The second convention contradicts the first one. The contradiction leads to a conceptual conflict in cases, such as discussed above, when the two surfaces belong to the same irrep in the lower symmetry group, which is valid in the entire coordinate space, but to different irreps in a restricted coordinate subspace where a higher symmetry holds. In such cases, it seems appropriate to stick with the first convention and to admit that, in the high symmetry subspace, each state belongs to one irrep in one domain and to another irrep in another domain.

The second inference of Figure 2 is the theorem of Herzberg and Longuet-Higgins [4] which states: if one follows the continuous deformations of the wave functions ψ_1 , ψ_2 along a *closed* path looping around the intersection point q° , then both wave functions return to their original form multiplied by (-1), i.e.,

$$\psi_1(\alpha+2\pi) = -\psi_1(\alpha), \quad \psi_2(\alpha+2\pi) = -\psi_2(\alpha) . \quad (2.26)$$

This theorem permits the determination of the existence of an intersection in a certain domain without having to find its location or when the equality of the energies of the two states has only been approximately established [1].

It is evident that the two discussed inferences remain valid (i) if one

follows the straight line through \mathbf{q}_0 or the continuous loop around \mathbf{q}_0 , respectively, in terms of any other coordinates which are related to p_1, p_2 by a one-to-one topological mapping and (ii) if one extends the path followed by allowing the variables p_3, p_4, \dots, p_M to become different from zero and letting them vary at the same time, as long as the variables p_1, p_2 remain sufficiently well defined along the chosen path. It is also apparent that the validity of the phase theorem is limited to the domain in which the functions $H_{12}(q)$ and $\Delta H(q)$ are sufficiently regular and where a one-to-one correspondence exists between the intersection adapted coordinates \mathbf{p} and the original coordinates \mathbf{q} .

3. TOPOGRAPHY OF THE LOWER SURFACE IN THE TANGENT BRANCHING SPACE

If the branching space is of dimension 1, then the three patterns of Figure 1 cover all possibilities and there is not much to discuss. In the present section we consider PES's in a two-dimensional branching space, which is the general case.

3.1 Expression for a PES in Terms of Mass-Weighted Cartesian Coordinates

While the difference between the two potential energy surfaces in the tangent branching space,

$$E_1 - E_2 = 2(y_1^2 + y_2^2)^{1/2} . \quad (3.1)$$

is a cone, the individual PES's of Eq. (2.22) are superpositions of a plane and a cone. In the present section we shall examine the basic topography of such functions. We shall also examine their steepest descent lines which furnish additional information and are often considered as model curves for reaction paths. Since orthogonal trajectory patterns depend markedly upon coordinate scaling, it is relevant that reaction paths are generally believed to be most appropriately modeled by steepest descent lines in the space of mass-weighted Cartesian coordinates or coordinates obtained from them by orthogonal transformations. The coordinates which led to the simple Eq.

(2.22) were, however, obtained by a very specific scaling which, in general, is not orthonormal. In terms of displacements x_1, x_2, \dots, x_M of mass-weighted Cartesian coordinates, the expressions for the two PES's have therefore the more general form

$$E_{1,2} - E^0 = B_1 x_1 + B_2 x_2 \pm (C_1 x_1^2 + C_2 x_2^2 + 2C_{12} x_1 x_2)^{1/2}, \quad (3.2)$$

where the quadratic under the radical sign is positive definite. It can be brought into diagonal form by an orthogonal transformation and, in terms of these new coordinates, one has

$$E_{1,2} - E^0 = b_1 x + b_2 y \pm (c_1^2 x^2 + c_2^2 y^2)^{1/2}. \quad (3.3)$$

Without loss of generality, we can divide through by c_1 , which can be assumed positive, and obtain

$$E_2 - E^0 = c_1 f(x,y) \quad \text{for the lower PES} \quad (3.4a)$$

$$E_1 - E^0 = -c_1 f(-x,-y) \quad \text{for the upper PES}, \quad (3.4b)$$

where

$$f(x,y) = -ax - by - (x^2 + c^2 y^2)^{1/2}. \quad (3.5)$$

Since both the upper and the lower PES's can be obtained from the function $f(x,y)$, we shall discuss this function, i.e. the lower surface, in this section in detail. It is apparent that the surfaces obtained for the parameters a and $(-a)$ are each others' mirror images with respect to the y -axis and that the surfaces obtained for b and $(-b)$ are each others mirror images with respect to the x axis. We therefore limit the parameters a and b to positive values.

This has the effect that in those cases where f is monotonic, it *decreases* with increasing values of x and y .

The energy of the lower surface, plotted as a function of x and y , is an elliptical cone tipped over. The contour curves of constant energy [$f(x,y)=\text{constant}$] are intersections of planes with this cone, i.e., they are conic sections. Depending on the ellipticity and how the cone is tipped, they may be ellipses, parabolas, hyperbolas, or limiting cases like circles or straight lines.

3.2 Case of a Circular Difference Cone

General Considerations

We begin by examining the special case of a circular difference cone because it is simple and yet exhibits important characteristic features. According to Eq.(3.5), a circular difference cone results when the parameter c is unity. Since the radicand (x^2+y^2) is invariant under orthogonal transformations, it is apparent that the expression for $f(x,y)$ can be brought into the form

$$f(x,y) = -ax - (x^2+y^2)^{1/2} \quad (3.6)$$

while still maintaining orthogonally transformed mass-weighted Cartesian coordinates. Thus, we can assume $b=0$ without loss of generality. [When *arbitrary* scaling is admitted, as in Eq.(2.22), *all* surfaces reduce to this

form.]

Contour plots of the function (3.6) are exhibited in Figure 3. Nine panels are shown corresponding to nine values of the parameter a . In all panels, both coordinates, x and y , go from -2.5 to $+2.5$. The origin, indicated by a bold-faced dot at the center, is the intersection point. Solid lines depict the contours $f=0.3n$ (n =integer). Bold-faced solid lines are contours where $f=0$. The functions $f(x,y)$ are positive in the shaded areas and negative in the unshaded areas. Dashed lines depict orthogonal trajectories. Bold-faced dashed lines indicate orthogonal trajectories that are straight lines. They separate orthogonal trajectories of opposite curvatures from each other.

Sloped patterns

It is apparent from Eq.(3.6) that there are always regions where f is negative. If there also exist areas where f is positive, then there must be contours for which $f(x,y)=0$. According to Eq.(3.6), they are given by

$$ax = -(x^2+y^2)^{1/2}. \quad (3.7a)$$

When $a>1$, then Eq.(3.7a) yields the two straight lines

$$y = \pm(a^2-1)^{1/2}x. \quad (3.7b)$$

Since a is assumed to be positive, Eq.(3.7a) also shows, however, that x must be negative. Equation (3.7b) defines therefore two straight *half-lines* which meet at the origin, as indeed shown in Figure 3 on the four panels for $a>1$.

The two bold-faced half-lines corresponding to $f=0$ form *one* contour separating the shaded domain at the left where $f>0$ from the domain at the right where $f<0$.

These panels are labelled by the symbol S indicating that all of these surfaces are "sloped" in the sense that they descend monotonically from left to right, i.e., with increasing values of x . The slope of this descent is much steeper in the region of negative f than in the region of positive f , i.e., the surfaces decrease gently coming from the left and rapidly to the right of $f=0$. From Eq.(3.6), one obtains for the orthogonal trajectories the differential equation

$$dy/dx = y/[x+a(x^2+y^2)^{1/2}] \quad (3.8)$$

whose numerical integration yields the dashed steepest descent lines in Figure 3. All of them originate in the region to the left where f is positive and, for large negative x values, start out parallel to the x axis. As x approaches zero, the orthogonal trajectories turn away from the x axis so as to cut through the bold-faced straight line contours $f = 0$ at right angles. The closer to the negative x axis the steepest descent lines start out, the more abruptly they turn away from the x axis at the appropriate points.

The x axis itself is a steepest descent line which rides downhill on a ridge from left to right straight through the intersection point, where its slope abruptly increases in absolute value. It is readily confirmed that $y=0$ is in

fact the only straight line which satisfies the differential equation (3.8).

Since the slope changes discontinuously at the origin, we consider it as two half-lines, one ending and the other beginning at the origin. The existence of two straight-line orthogonal trajectories is indicated by the number 2 in the symbol S2 labeling these panels. By virtue of Eq.(3.4), it is apparent that the steepest descent lines of E_1 and E_2 going through the intersection form the sloped pattern of Figure 1.

We have discussed the pattern for $c=1$, $a>1$ in some detail since, in a previous investigation [1] we found that a reaction path descending from a transition state was modeled by a steepest descent line passing through an intersection in exactly the same manner as the x axis does in the "S2" panels of Figure 3. Immediately after the transition state this steepest descent line followed the floor of a valley. Then, at a *valley-ridge inflection point* [7], it turned into the crest of a ridge which then passed through the intersection as illustrated in Figure 3. Upon approaching the intersection point on such a reaction path, the system will become subject to random dynamic instabilities when it arrives on the ridge and will fall off it. The orthogonal trajectory pattern exhibited in Figure 3 implies that the system, once off the ridge will be subject to forces which will push it more and more away from the ridge and more and more strongly so. It is thus apparent that in the region around an intersection point with the discussed topography, *the PES has a*

strong bifurcating effect on the reaction path, and particularly so when the parameter a is close to 1.

Peaked Patterns

When $a < 1$, then Eq.(3.7) has only one solution, namely $x=y=0$. Thus, the function $f(x,y)$ vanishes only at the origin and descends in all directions towards negative values. This peaked pattern is therefore labelled by the symbol P. The positive as well as the negative x axis both are again the only straight-line orthogonal trajectories and the panels are therefore labelled as P2. All other steepest descent lines start out at the origin in the direction of the *negative* x axis and, then, turn around towards increasing x values. The contours are ellipses. The steepest descent lines on E_1 and E_2 form the peaked pattern of Figure 1.

When $a=0$, these contours become circles and *all* orthogonal trajectories become straight lines. The function $f(x,y)$ is a circular cone and the panel is therefore labelled as PC in Figure 3.

Intermediate Patterns

For $a > 1$, the inclination of the bold-faced contours $f=0$ with respect to the x axis becomes progressively smaller as the parameter a approaches 1. Concomitantly, the region of positive f -values becomes progressively narrower

and the steepest descent lines start out as a progressively narrower bundle to the left, which upon approaching the origin, suddenly splits by veering to one side on the other. For $a=1$, we have the limiting case between the patterns P and S, and we denote this intermediate pattern as R. In this case, the two bold-faced straight-line contours $f=0$ of the S pattern have collapsed into the negative x axis and the region with $f>0$ has been squeezed out. The function f descends downhill from all points on the negative x axis, which is now the contour $f=0$. Hence, only the positive x axis is a straight-line orthogonal trajectory and the panel symbol is therefore R1. All steepest descent lines, except the $+x$ axis, start out perpendicular to the $-x$ axis and are mirror images (with respect to the y -axis) of certain contour lines of $f(x,y)$. The steepest descent lines on E_1 and E_2 form the intermediate pattern of Figure 1.

3.3 The case of an Elliptic Difference Cone with Principal Axes Lined Up Along the Linear Term

General Considerations

For c different from unity, the difference cone (E_1-E_2) is elliptical and, in general, its principal axes are unrelated to the vector (a,b) which determines the linear term. However, when $b=0$, then

$$f(x,y) = -ax - (x^2 + c^2y^2)^{1/2} \quad (3.9)$$

and the vector $(a,b) = (a,0)$ is lined up with one of the axes of the difference cone. It is unnecessary to consider the case $(a=0, b \neq 0)$ as well, if we consider $c > 1$ and $c < 1$ for the case $(a \neq 0, b=0)$. This is because rotation by 90° will map each pattern $(a=0, b \neq 0, c > 1)$ into a pattern $(a \neq 0, b=0, c < 1)$ and each pattern $(a=0, b \neq 0, c < 1)$ into a pattern $(a \neq 0, b=0, c > 1)$.

As in the case of a circular difference cone, we have regions where $f > 0$ only if there exist contours $f=0$. From Eq.(3.9) follows that they are given by

$$y = \pm[(a^2-1)^{1/2}/c]x, \quad x < 0 \quad (3.10)$$

provided that $a \geq 1$, as before. A region $f > 0$ exists when $a > 1$ and it lies between the two straight half-lines defined by Eq.(3.10), as illustrated by the bold-faced solid lines in Figure 4. For $a=1$, the negative x axis with $f=0$ is the crest of the surface. For $a < 1$, the origin is the only point where $f=0$.

Accordingly, the three cases $a > 1$, $a=1$, $a < 1$ are again characterized by the symbols P, R, and S introduced in the last section.

The orthogonal trajectories are now given by the differential equation

$$dy/dx = c^2y/[x+a(x^2+c^2y^2)^{1/2}]. \quad (3.11)$$

As before, the dashed lines in Figure 4 represent some of them, obtained by numerical integration, and the bold-faced dashed lines are straight-line orthogonal trajectories. The equations for the latter are obtained by substituting $y=kx$ into Eq.(3.11):

$$k = c^2kx/[x+a(x^2+c^2k^2x^2)^{1/2}]$$

$$k[1+\text{sign}(x)a(1+c^2k^2)^{1/2} - c^2] = 0$$

which factors into the two equations

$$k = 0 \tag{3.12}$$

$$(1+c^2k^2)^{1/2} = [(c^2-1)/a]\text{sign}(x). \tag{3.13}$$

Thus, we have again the orthogonal trajectories $y=0$ for $x>0$ and for $x<0$ (except in the case $a=1$, where $x>0$ is the only one). However, in addition we find now from Eq.(3.13) the two straight-line orthogonal trajectories given by

$$k = \pm[(c^2-1)^2-a^2]^{1/2}/ac \tag{3.14a}$$

$$\text{sign}(x) = \text{sign}(c^2-1) \tag{3.14b}$$

provided that $|c^2-1|>a$.

The x-axis is the Shorter Principal Axis of the Difference Cone ($c<1$).

The case $c<1$ is illustrated in Figure 4 for $c=0.5$. As discussed after Eq.(3.10), regions with $f>0$ exist for $a>1$ (panels S), but not for $a<1$ (panels P). Panel R is the limiting case.

All panels S and P exhibit the two straight-line orthogonal trajectories ($y=0, x>0$) and ($y=0, x<0$). However, it is readily verified that for the panel R, corresponding to $a=1$, only ($y=0, x>0$) is an orthogonal trajectory.

In addition, there exist, however, the additional straight-line orthogonal trajectories corresponding to Eq.(3.14), as long as $a < |c^2-1| = 1-c^2 = 0.75$. In agreement with Eq.(3.14b), they are half-lines with $\text{sign}(x) = \text{sign}(c^2-1) < 0$.

Thus, there are four straight-line orthogonal trajectories for $a < 1 - c^2 = 0.75$ and two straight-line orthogonal trajectories for $a \geq 0.75$, except only one such orthogonal trajectory exists for $a = 1$. Correspondingly, the patterns are labelled by the symbols P4, P2, R1, S2. In contrast to the situation in Sec. 3.2, the case $a = 0$ is also of type P4 here.

The x axis is the Longer Principal Axis of the Difference Cone ($c < 1$).

Consider first the case $1 < c < \sqrt{2}$. This case differs from the preceding case in two respects. First, for $a = 0$, the long axis of the elliptical cone is now along the x axis. Second, Eq.(3.14b) now yields $\text{sign}(x) > 0$, so that the two straight-line orthogonal trajectories with $k \neq 0$ are inclined to the right. These features are illustrated in Figure 5, depicting the case $c = 1.25$, which otherwise is entirely analogous to Figure 4 for $c < 1$. According to Eq.(3.14a), the two straight-line orthogonal trajectories collapse into the positive x axis for $a = |c^2 - 1| = c^2 - 1 = 0.5625$.

Next, consider the case $c > \sqrt{2}$. It is illustrated in Figure 6 for $c = 1.7$. This case has an interesting further feature in addition to those shown on Figure 5. It arises from the fact that, according to Eq.(3.14a), the two straight-line orthogonal trajectories with $k \neq 0$ will collapse into the positive x axis only for $a = |c^2 - 1| = (c^2 - 1) > 2 - 1 = 1$, in the present example for $a = 1.89$. Thus, there exist now patterns where $1 < a < |c^2 - 1|$, i.e., where the surface has a region

with $f > 0$ and, *also*, two straight-line orthogonal trajectories with $k \neq 0$. These surfaces are illustrated on the three panels labelled S4 on Figure 6. For $a=1$, the negative x axis is no longer an orthogonal trajectory and it is therefore labelled R3.

The surface patterns of type S4 exhibit thus the following new pattern: *One* downhill steepest-descent line enters the intersection point from the left along the negative x axis, but *infinitely many* steepest-descent lines leave the intersection point towards the right, initially parallel to the positive x axis, but quickly fanning out between the two bold-faced straight-line orthogonal trajectories with $k \neq 0$ as indicated by the lightly shaded area in Figure 6. This pattern presents then a situation where a steepest descent line that could model a reaction path can fan out into an infinite number of steepest descent lines upon passing through an intersection point. This possibility further emphasizes the bifurcating character of the intersection region should the intersection point lie on a reaction path.

3.4 The General Case ($c \neq 1$ and $a, b \neq 0$)

In general, the surface pattern of $f(x,y)$ has no symmetry and a more complicated structure than in the two special cases considered in Secs. 3.2 and 3.3. Nonetheless, it remains true that the chief criteria characterizing the various topographies are (i) whether there exist straight-line contours

through the origin on which $f(x,y)$ vanishes and (ii) how many straight-line orthogonal trajectories through the origin there are. We shall examine the analytic conditions pertaining to these two criteria.

Straight-Line Contours $f=0$ Through the Origin

From Eq. (3.5), it is apparent that $f(x,y)$ always vanishes at the origin and that there is always a region where $f(x,y)$ is negative. Two fundamentally different general patterns are therefore possible, namely, *regions where $f(x,y)$ is positive do exist or such regions do not exist*. The former case can be identified by observing that there must exist *contour curves* which separate the domain where $f > 0$ from the domain where $f < 0$. Along such curves, $f(x,y)$ vanishes which implies that

$$-ax - by = (x^2 + c^2y^2)^{1/2} . \quad (3.15)$$

Since this equation is of the form $F(y/x) = 0$, it determines one or several straight lines $y/x = m = \text{constant}$. The function f vanishes therefore *always* on straight lines passing through the origin. Their slopes m are obtained as solutions of the quadratic equation

$$(c^2 - b^2)m^2 - 2abm - (a^2 - 1) = 0 \quad (3.16)$$

whence

$$m = (ab \pm \sqrt{D})/(c^2 - b^2) , \quad D = b^2 + c^2(a^2 - 1) . \quad (3.17)$$

The coefficients a , b , and c and the discriminant D are thus related by

$$a^2 + b^2/c^2 = 1 + D/c^2 \quad (3.18)$$

and three cases are possible:

$D > 0$, $a^2 + b^2/c^2 > 1$. There exist two different solutions m_1 and m_2 and, hence, two straight lines. However, because of Eq. (3.15), the inequality

$$ax + by = (a + bm) x < 0 \quad (3.19)$$

must also be satisfied. It implies that, for given values of a , b , and m , the values which x may assume are limited to having the opposite sign as $(a + bm)$. Hence m_1 and m_2 generate only two half-lines, both of which end at the origin. Together, they form the contour $f = 0$ which separates the domain where $f > 0$ from that where $f < 0$. As before, we shall use again the symbol S to label such patterns.

$D = 0$, $a^2 + b^2/c^2 = 1$. The two lines of the previous case coalesce into one line with $m = ab/(c^2 - b^2) = b/ac^2$. The condition (3.19) yields therefore the result $x/a < 0$, i.e., that x must have the opposite sign as a . Since a is assumed to be positive, we thus always have one half-line with $x < 0$ which ends at the origin. The region where $f > 0$ has again been squeezed out. The function $f(x,y)$ assumes its maximum value $f = 0$ on the mentioned half-line. As before, we shall use the label R for this pattern.

$D < 0$, $a^2 + b^2/c^2 < 1$. In this case $f(x,y)$ vanishes only at the origin and this is the point where $f(x,y)$ reaches its maximum. $f(x,y)$ is negative everywhere else. As before, we shall label this pattern by the symbol P .

Straight-Line Orthogonal Trajectories Through the Origin.

From Eq. (3.5) it follows that the orthogonal trajectories of $f(x,y)$ are functions $y(x)$ which are defined by the differential equation

$$dy/dx = f_y/f_x = (br + c^2y)/(ar + x) \quad (3.20a)$$

with

$$r = (x^2 + c^2y^2)^{1/2}. \quad (3.20b)$$

This differential equation is of the homogeneous form

$$dy/dx = f(t), \quad t = y/x \quad (3.21)$$

$$f(t) = [b(1 + c^2t^2)^{1/2} + c^2t]/[a(1 + c^2t^2)^{1/2} + 1], \quad (3.22)$$

which can be reduced to a quadrature in t . The latter yields the parametric representation

$$x = K \exp\{ \int dt[f(t)-t]^{-1} \}, \quad y=xt, \quad (3.23)$$

where different values of the integration constant K determine different orthogonal trajectories.

In general, the orthogonal trajectories are curvilinear and, with appropriate changes of the parameter values a , b , and c , their curvatures can invert. Whenever this happens, a separating orthogonal trajectory is found which is a straight line passing through the origin: $y = kx$. The condition for this to happen is obtained by inserting $y=kx$ into Eq.(3.20). This yields

$$[b(x^2 + c^2k^2x^2)^{1/2} + c^2 kx]/[a(x^2 + c^2k^2x^2)^{1/2} + x] = k = \text{constant}$$

from which follows

$$ak - b = \sigma g(k), \quad (3.24a)$$

where

$$\sigma = \text{sign}\{x(c^2-1)\}, \quad (3.24b)$$

$$g(k) = |c^2-1|k/(1+k^2c^2)^{1/2}, \quad (3.25)$$

i.e.,

$$ak - b = g(k), \quad \text{when } \text{sign}(x) = \text{sign}(c^2-1), \quad (3.26)$$

$$-ak + b = g(k), \quad \text{when } \text{sign}(x) = -\text{sign}(c^2-1). \quad (3.27)$$

Equations (3.26) and (3.27) show that the straight lines $y=kx$ end at the origin, i.e. they are again half-lines. Equations (3.24) - (3.27) are equations of the fourth degree for the slope k . The nature of their solutions can be recognized from the graphic representation in Figure 7 which exhibits a plot of the function $g(k)$ of Eq(3.25) vs. k for some arbitrary value of $c(\neq 1)$ as well as graphs of three straight lines $(ak-b)$, denoted by A,B, and C, and three straight lines $(-ak+b)$, denoted by A', B', and C'. The abscissas of the intersections of any one of these straight lines with the function $g(k)$ are the solutions of Eq.(3.24) for the pertinent values of a , b , and c . The lines A',B', and C' yield the solutions of Eq.(3.27) and it is apparent that there always exists one such solution. The lines A, B, and C yield the solutions of Eq.(3.26) and there can be manifestly one, two, or three such solutions. Since we have $b \neq 0$, the following conclusions can be drawn.

First, there always exist two solutions with $k > 0$. In most cases, they

correspond to two straight-line orthogonal trajectories with positive slopes, one being a half-line with $\text{sign}(x)=\text{sign}(c^2-1)$, the other being a half-line with $\text{sign}(x)=-\text{sign}(c^2-1)$. The only exception is the case when a , b , and c satisfy the condition $a^2+b^2/c^2=1$, which leads to the pattern R, discussed after Eq.(3.19), when the two straight-line contours $f=0$ collapse into one such contour with $x<0$ and the slope $m=b/ac^2$. It turns out that this limiting straight-line contour in fact satisfies Eq.(3.24). Indeed, replacing k by $m=b/ac^2$ and $\text{sign}(x)$ by (-1) in Eq.(3.24), one finds

$$a(b/ac^2) - b = \text{sign}(1-c^2) |1-c^2| (b/ac^2) / (1+c^2b^2/a^2c^4)^{1/2}$$

which simplifies to

$$1 = 1/(a^2+b^2/c^2)^{1/2},$$

an identity that is in fact satisfied. This result implies that, in this case, the solution $k>0$ of Eq.(3.24) with $\sigma=\text{sign}(1-c^2)$ is a contour $f=\text{constant}$ and, hence, *not a steepest descent line*. It is also readily verified that f_x/f_x is no longer given by Eq.(3.20) in this case. Thus, the pattern R always has one straight-line orthogonal trajectory less than the corresponding patterns P and S. The same result had been found for the specific cases considered in Secs. 3.2 and 3.3.

Secondly, there can exist two, one, or no solutions with $k<0$. They yield straight-line orthogonal trajectories with negative slopes, all of which are half-lines with $\text{sign}(x)=\text{sign}(c^2-1)$. The condition for having two, one or no

such trajectories is obtained as follows. According to Figure 7, the limiting case of *one* solution with $k < 0$ corresponds to the line B which is tangent to the curve $g(k)$. Equating the slopes of $(ak-b)$ and $g(k)$ yields

$$a = |c^2 - 1| / (1 + k^2 c^2)^{3/2}, \quad (3.28)$$

and this equation, together with Eq.(3.26) embodies the requirements for tangency. It is possible to eliminate the variable k between Eqs.(3.26) and (3.28) and, thereby, one obtains the condition

$$(a^2)^{1/3} + (b^2 c^2)^{1/3} = [(1 - c^2)^2]^{1/3} \quad (3.29)$$

between a , b , and c . By reference to the intercept b in Figure 7, it is readily seen that

$$\text{No solution } k < 0 \text{ exists when } |a/(c^2 - 1)^{2/3} + |bc/(c^2 - 1)|^{2/3} < 1 \quad (3.30a)$$

$$\text{One solution } k < 0 \text{ exists when } |a/(c^2 - 1)|^{2/3} + |bc/(c^2 - 1)|^{2/3} = 1 \quad (3.30b)$$

$$\text{Two solutions } k < 0 \text{ exist where } |a/(c^2 - 1)|^{2/3} + |bc/(c^2 - 1)|^{2/3} > 1. \quad (3.30c)$$

Classification of Patterns

The distinctions made in the preceding subsections are combined graphically in Figure 8 which displays plots of

$$a^2 + b^2/c^2 = 1 \quad (\text{dashed curves}) \quad (3.31)$$

as well as plots of

$$|a/(c^2 - 1)|^{2/3} + |bc/(c^2 - 1)|^{2/3} = 1, \quad (\text{solid curves}) \quad (3.32)$$

in the a - b plane for various values of the parameter c . Four panels are

shown corresponding to the four cases $0 < c < 1/\sqrt{2}$, $1/\sqrt{2} < c < 1$, $1 < c < \sqrt{2}$, $\sqrt{2} < c$. Depending on the value of c , the two curves divide the first quadrant into five or nine regions which are labeled by the symbols introduced earlier to denote the various surface patterns that can result from the corresponding parameter choices. The characteristics of the nine different types are listed in Table 1. On the panels of Figure 8, the patterns P2, P4, S2, S4 obtain in two-dimensional regions, the patterns P3, S3, R1, R3 obtain on curves, and the pattern R2 obtains at points. It is apparent from Eq. (3.5) that the

Table 1. Patterns for the function $f(x,y)$ of Eq. (3.5) when $c \neq 1$, $a \neq 0$, $b \neq 0$.

	$a^2 + b^2/c^2$	$ a/(c^2-1) ^{2/3} + bc/(c^2-1) ^{2/3}$	Dimension of region where $f > 0$	Number of straight line orthogonal trajectories		
				$k > 0, x < 0$	$k > 0, x > 0$	$k < 0, x(c^2-1) > 0$
P2	<1	>1	0	1	1	0
P3	<1	=1	0	1	1	1
P4	<1	<1	0	1	1	2
R1	=1	>1	1	0	1	0
R2	=1	=1	1	0	1	1
R3	=1	<1	1	0	1	2
S2	>1	>1	2	1	1	0
S3	>1	=1	2	1	1	1
S4	>1	<1	2	1	1	2

function $f(x,y)$ for $(a = u, b = v, c = w)$ can be obtained from the function for $(a = v/w, b = u/w, c = 1/w)$ by interchanging x and y and multiplying the entire function by w . Thus, for every point with $a/b = \alpha$ on a panel for c , there exists a point with $a/b = \alpha^{-1}$ on the panel for c^{-1} in Figure 9 such that the corresponding surfaces differ essentially only in the interchange of x and y . Therefore, if we consider $c > 1$ as well as $c < 1$ then we have to discuss only the patterns for $a > b$. Conversely, if we consider all values a and b of the panel for c , we do not have to discuss the panel for c^{-1} .

Figure 9 depicts nine PES contour plots for $c=2.29$, corresponding to the nine patterns listed on the panel for $c > \sqrt{2}$ in Figure 8. The panels on Figure 9 are arranged relative to each other in the same order as the regions corresponding to these patterns on the $c > \sqrt{2}$ panel of Figure 8. As before, solid bold-faced lines are contours $f=0$, and dashed bold-faced lines are straight-line orthogonal trajectories. The dark shaded areas to the left of the intersection on the S panels are regions where $f > 0$. The light shaded areas to the right of the intersection on the panels S3, S4, R2, R3 are regions where infinitely many orthogonal trajectories leave the origin towards the right and fan out between the bold-faced dashed lines. It is apparent that the bunching of the orthogonal trajectories near the origin differs qualitatively for the three cases characterized by the Eqs.(3.30a), (3.30b), (3.30c).

The patterns which one obtains for $c < 1$ differ from those of Figure 9 in

that the relative positions of the long and the short axis of the difference cone are interchanged with respect to the bold-faced contours and trajectories.

4. TOPOGRAPHY OF THE UPPER SURFACE

From Eq.(3.5), we know that near an intersection the surface of the upper state can be obtained from that of the lower state by the relation

$$E_{\text{upper}}(x,y) = -E_{\text{lower}}(-x,-y). \quad (3.33)$$

In the case of S patterns, it is seen that both states have the same overall direction of their slopes and, at the intersection, merely exchange the steepness of their slopes. It is also apparent from Eq.(3.33) that the upper state has a valley floor wherever the lower state has a ridge. Consequently, whereas downhill reaction paths on E_{lower} will tend to veer away from the crossing, such reaction paths on E_{upper} will be funneled towards the crossing. As an example, Figure 10 displays contours and orthogonal trajectories of both states for the case S4 discussed in Sec. 3.3. The plot of the lower surface is identical with that for $a=1.05$ on Figure 6 except that the contour increment has been increased. The plot of the higher surface is obtained from it by Eq.(3.33). On both panels, the shaded area indicates where the energy is higher than the intersection energy, as before. For clarity, only steepest descent lines passing through the intersection are drawn (dashed lines).

The negative x-axis is seen to be the floor of a valley on the upper surface descending to the intersection, whereas the positive x-axis is the crest

of a ridge on the lower surface descending from the intersection. It is apparent that on the upper surface, there exists a funnel of steepest-descent lines (shown in Figure 10) that are focussing toward the intersection and emerge on the lower surface where they fan out in a diverging pattern. On each of these steepest-descent lines the wavefunction of the one state goes continuously into that of the other state, as discussed in Sec. 2.3, and for these *adiabatic* paths, the intersection is a diabatic valley-ridge inflection point [7]. It is apparent that these conditions strongly favor radiationless transitions from the upper surface to the lower surface. Outside the funnel of steepest descent lines shown in Figure 10, the steepest descent lines of the upper surface do not reach the intersection and stay on the upper surface.

On the other hand, on the lower surface, the negative x-axis is a ridge descending towards the intersection and the steepest-descent line on this ridge emerges on the upper surface as the floor of a valley along the positive x-axis. All other steepest-descent lines on the lower surface veer, however, away from the intersection and stay on the lower surface.

In the case of P patterns, the lower state has a pointed maximum at the intersection whereas the upper state has a pointed minimum. Thus *all* steepest descent lines of the upper surface lead to the intersection and emerge on the lower surface. There will be an even stronger tendency to funnel reaction paths (should there be one) towards the crossing with a

resultant radiationless transition to the lower state.

In some of the cases considered, radiationless transitions from E_{lower} to E_{upper} , although less likely, may also occur.

5. CONCLUSIONS

The topography of potential energy surfaces in the immediate vicinity of a crossing with another surface can have two main patterns - a peaked (P) pattern or a sloped (S) pattern. For S patterns, both PES's have downhill slopes and touch each other at the crossing points in the branching space. For P patterns, both PES's are elliptical cones pointing against each other with a common tip. A limiting pattern, called R, intermediate between the P and S patterns, is also possible where there exists a line along which E_1 has zero slope on one side of the intersection and E_2 has zero slope on the other side of the intersection. A considerable variety of patterns can occur for the steepest descent lines. In some, but not in all cases, infinitely many steepest descent lines enter or leave the intersection in certain, but not necessarily in all directions.

The overall character of the steepest-descent lines is such that on the lower PES, reaction paths will be steered away from the crossing and tend to bifurcate in its vicinity, whereas on the upper surface, they will tend to be funnelled towards the intersection with a strong probability for a dynamic transition from one state to the other because the two states exchange character (continuity of energy slope and of wave function from one state to the other) on *any* straight path through the intersection. It can therefore be

inferred that intersections are preferred locations for radiationless transitions from the higher state to the lower state. For S patterns, radiationless transitions from the lower state to the higher state are also conceivable on the downhill slope of both energy surfaces.

ACKNOWLEDGMENT

The Ames Laboratory is operated for the U.S. Department of Energy by Iowa State University under contract No. W-7405-Eng-82. This work was supported by the Division of Chemical Sciences, Office of Basic Energy Sciences.

REFERENCES

1. S. Xantheas, G. J. Atchity, S. T. Elbert, and K. Ruedenberg, *J. Chem. Phys.*, **94**, 8054 (1991).
2. S. Xantheas, S.T. Elbert, K. Ruedenberg, *Theor. Chim. Acta* **78**, 365 (1991).
3. F. Hund, *Z. Physik* **40**, 742 (1927);
J. von Neumann, E. Wigner, *Physik. Z.* **30**, 467 (1929);
E. Teller, *J. Phys. Chem.* **41**, 109 (1937).
4. G. Herzberg and H.C. Longuet-Higgins, *Discuss. Faraday Soc.* **35**, 77 (1963).
See also M.V. Berry, *Proc. Roy. Soc. Lond. A* **392**, 45 (1984).
5. H.C. Longuet-Higgins, *Proc. Roy. Soc. London A* **344**, 147 (1975);
C.A. Mead, *J. Chem. Phys.* **70**, 2276 (1979);
C.A. Mead and D.G. Truhlar, *J. Chem. Phys.* **70**, 2284 (1979).
6. A.J-C. Varandas, J. Tennyson, J.N. Murrell, *Chem. Phys. Lett.* **61**, 431 (1979);
J. Katriel and E.R. Davidson, *Chem. Phys. Letters* **76**, 259 (1980).
7. P. Valtazanos and K. Ruedenberg, *Theor. Chim. Acta* **69**, 281 (1986).

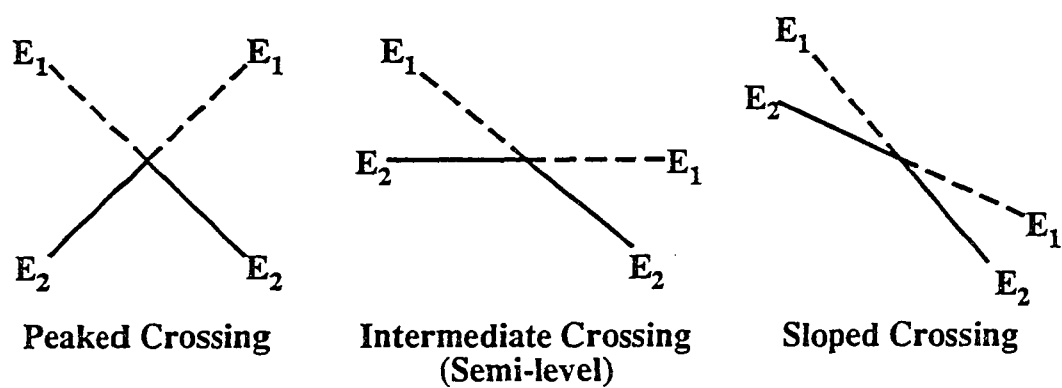


Figure 1. The "exchange of slopes" between two potential energy surfaces and the three basic patterns at an intersection

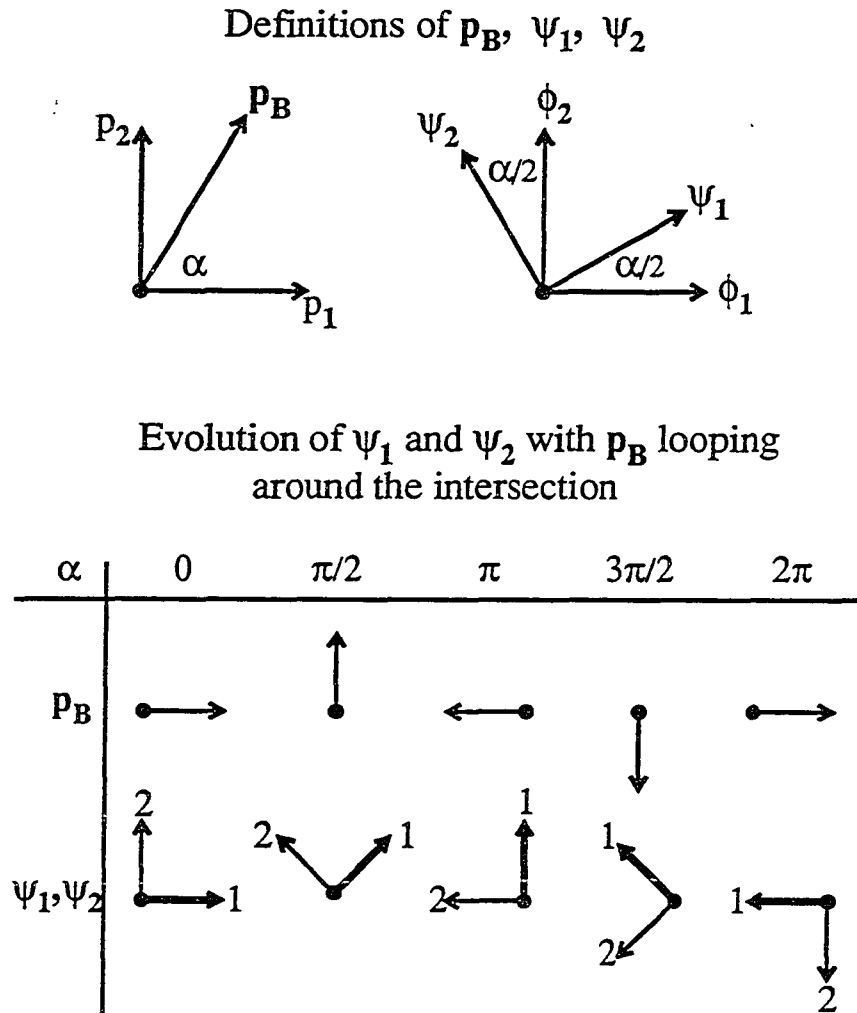


Figure 2. The evolution of the two eigenfunctions ψ_1 , ψ_2 in function space along an internal coordinate loop around the intersection. \mathbf{P}_B = Projection of the intersection-adapted internal coordinate vector in the branching plane p_1 , p_2

$c=1.00$, Increment=0.30

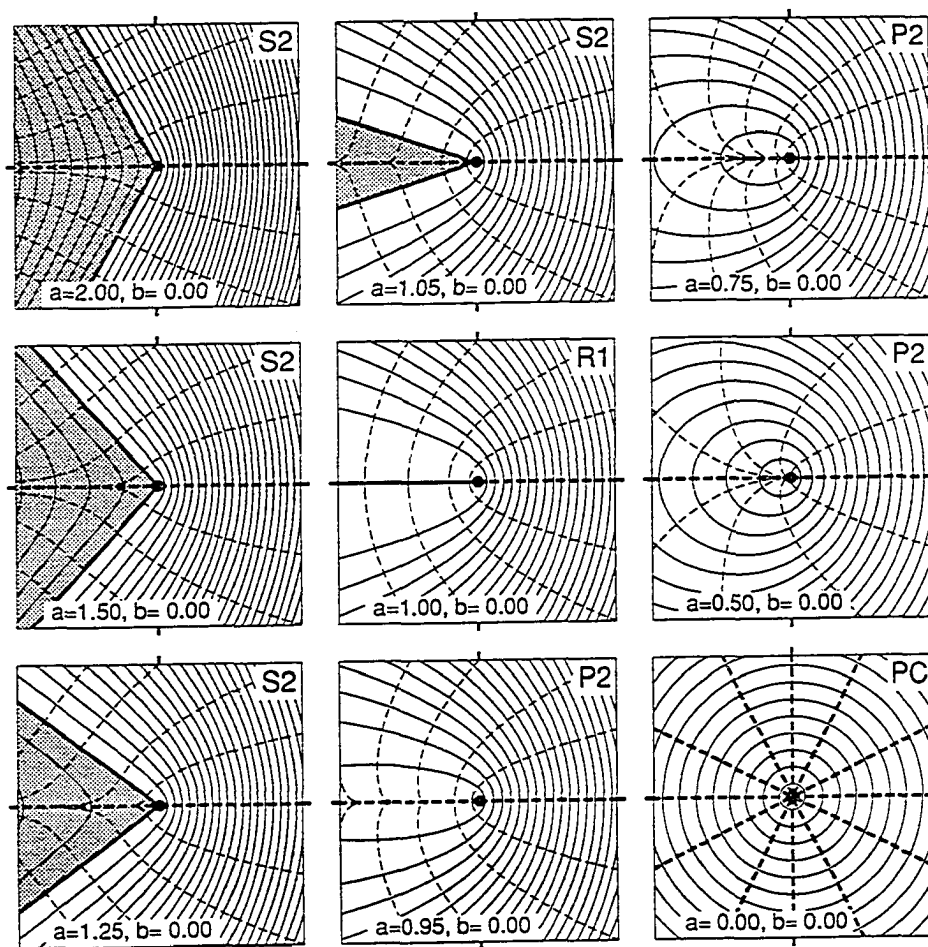


Figure 3. Potential energy surface patterns near an intersection for the case $c=1$, $b=0$. Intersection = heavy dot at center. Ranges of abscissa and ordinate: $-2.5 < x < 2.5$, $-2.5 < y < 2.5$; solid lines: contour lines; bold-faced solid lines: $E-E_0=0$; shaded area: $E-E_0>0$; contour increment=0.3.; dashed lines: orthogonal trajectories; bold-faced dashed lines: orthogonal trajectories which are straight lines

$c=0.50$, Increment=0.30

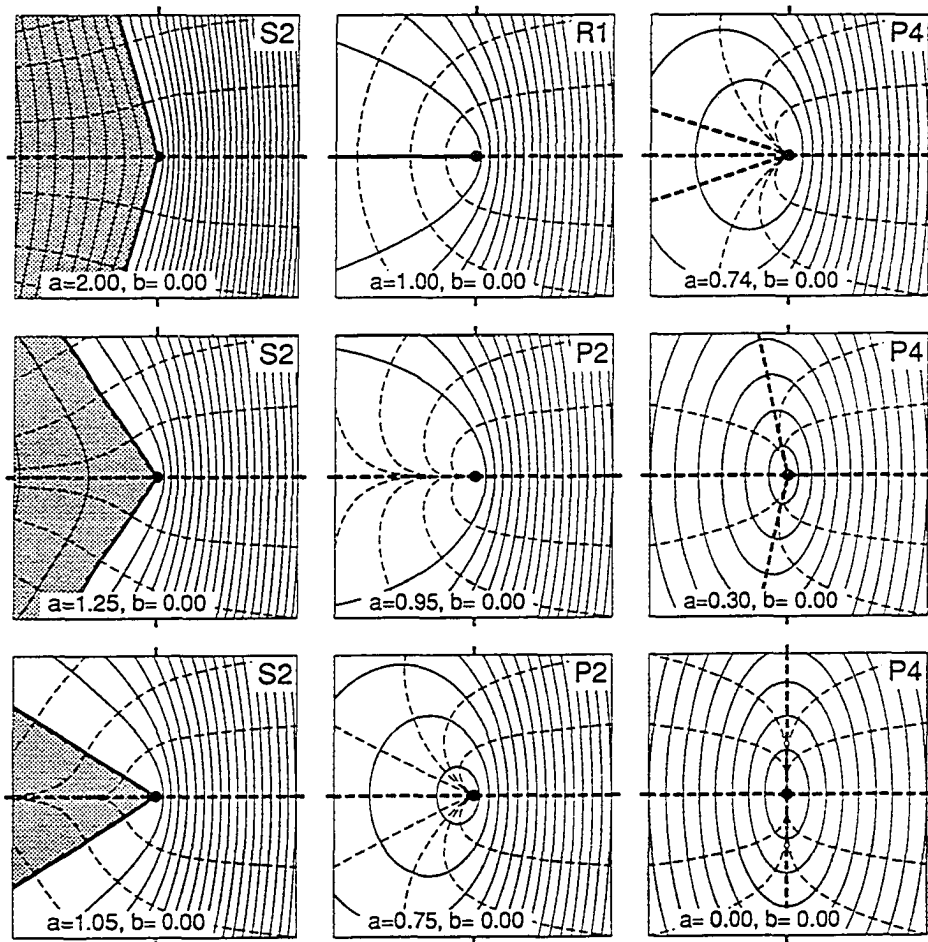


Figure 4. Potential energy surface patterns near an intersection for the case $c=0.5$, $b=0$. For explanations of curves see caption of Fig. 3

$c=1.25$, increment=0.30

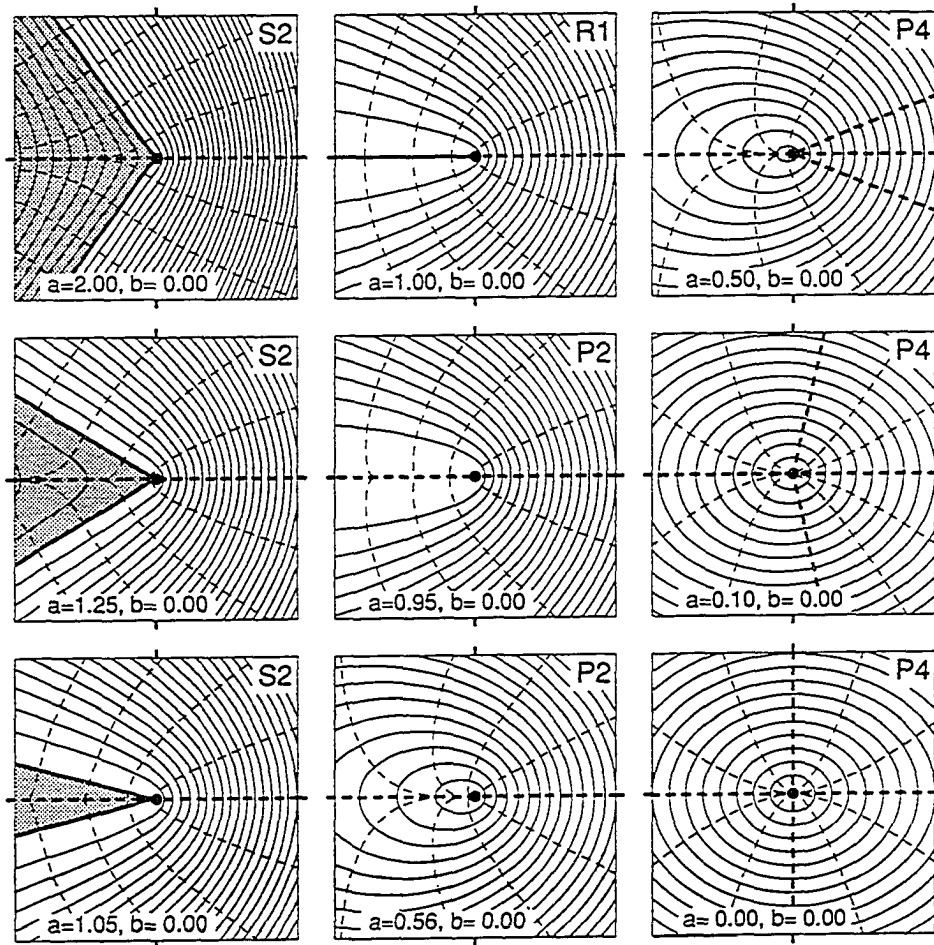


Figure 5. Potential energy surface patterns near an intersection for the case $c=1.25, b=0$. For explanations of curves see caption of Fig.

$c=1.70$, increment=0.45

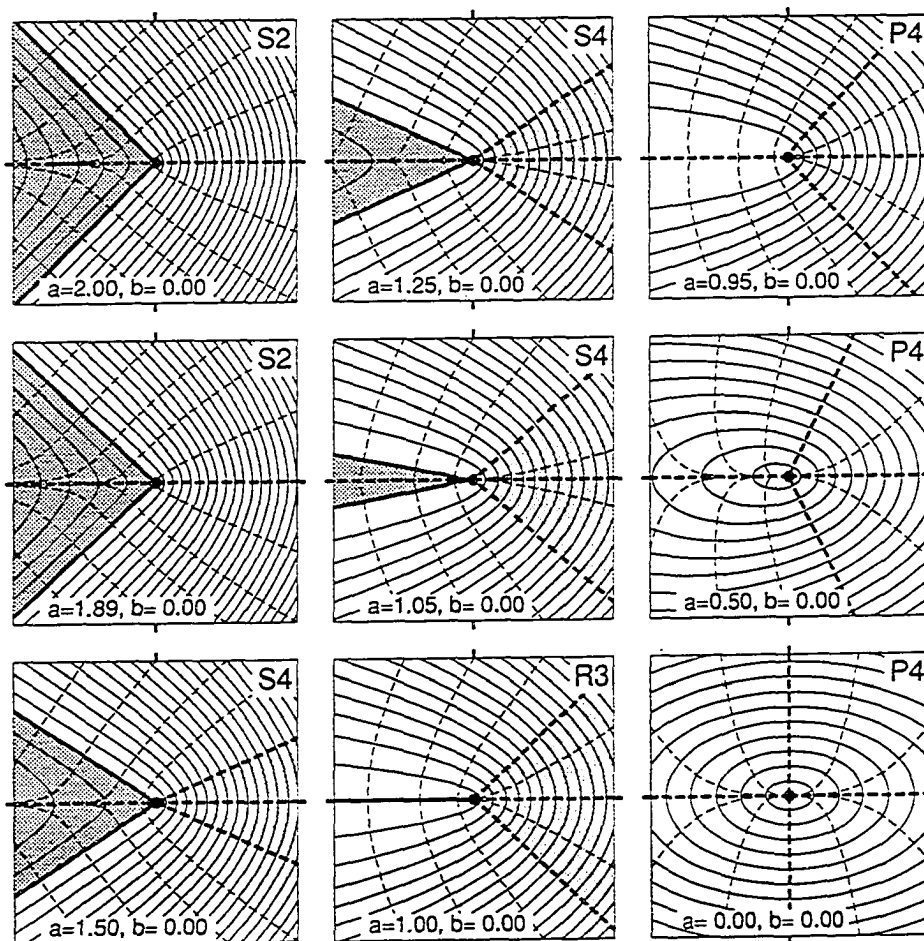


Figure 6. Potential energy surface patterns near an intersection for the case $c=1.70$, $b=0$. For explanations of curves see caption of Fig. 3, except that the increment between contours is 0.45 in this figure

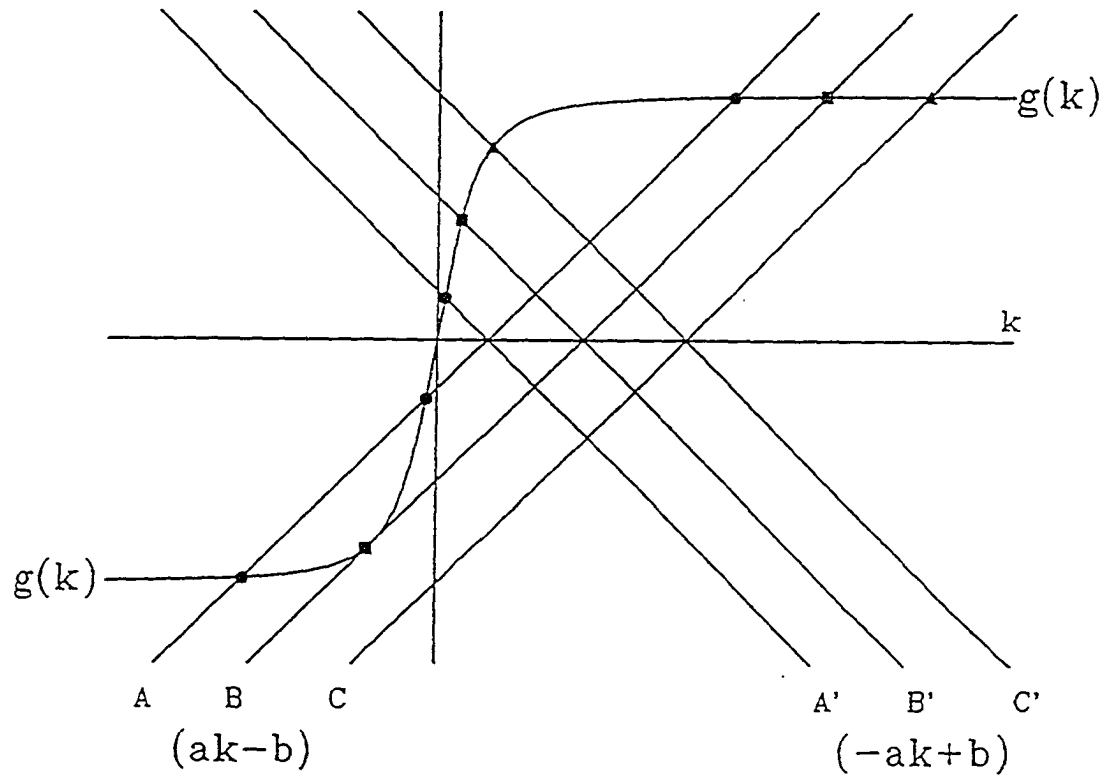


Figure 7. A plot of the function $g(k)$ defined in Eq.(3.25), of three lines $(ak-b)$ and three lines $(-ak+b)$, where $a, b > 0$. The intersections yield solutions of Eq.(3.24)

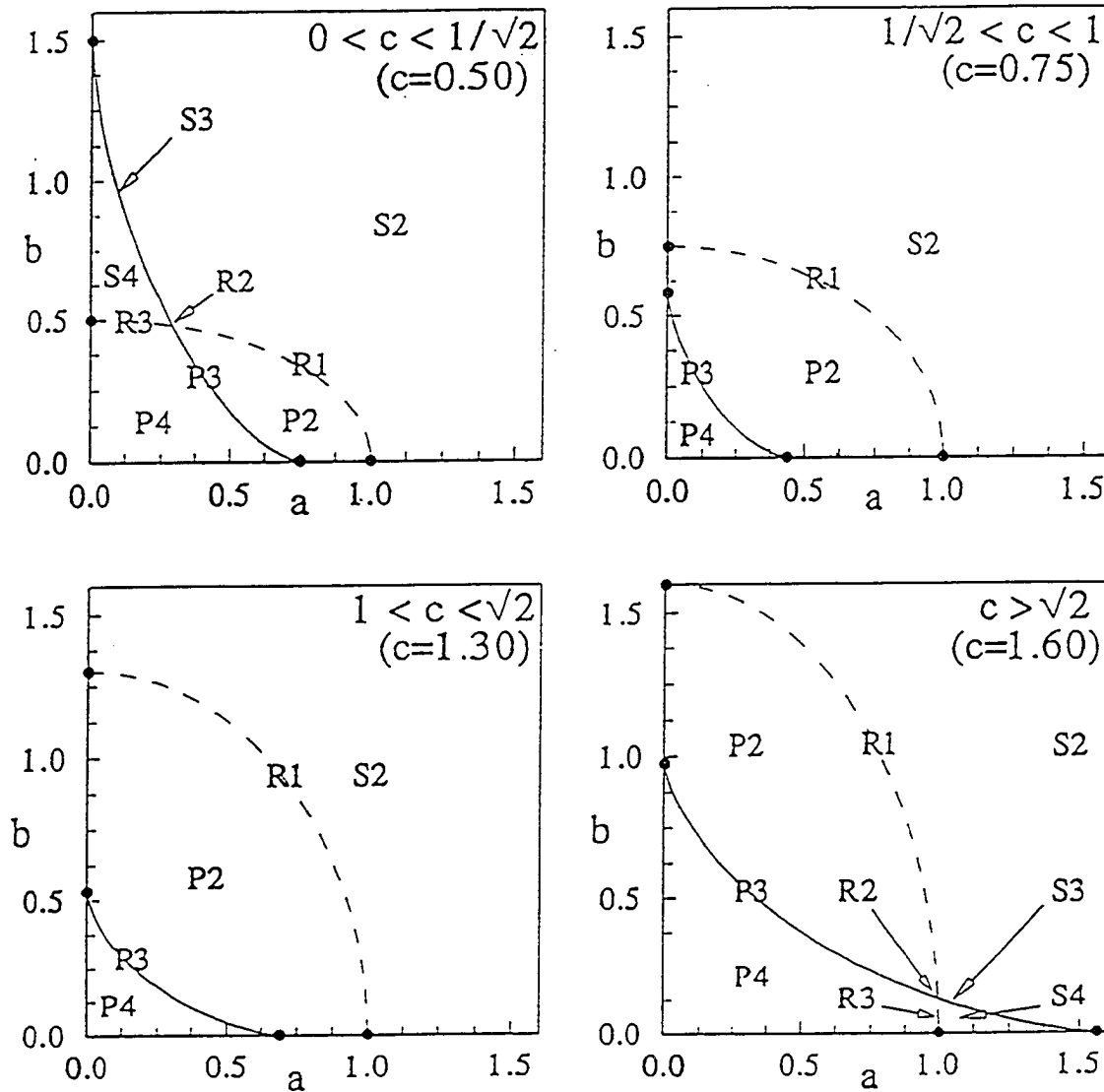


Figure 8. Graphs in the a - b plane for the classification of potential energy surface patterns near an intersection. Solid curves: plots of Eq.(3.32). Dashed curves: plots of Eq.(3.31). The symbols in various regions of the quadrant are defined in Table 1. Symbols on curves refer to those curves

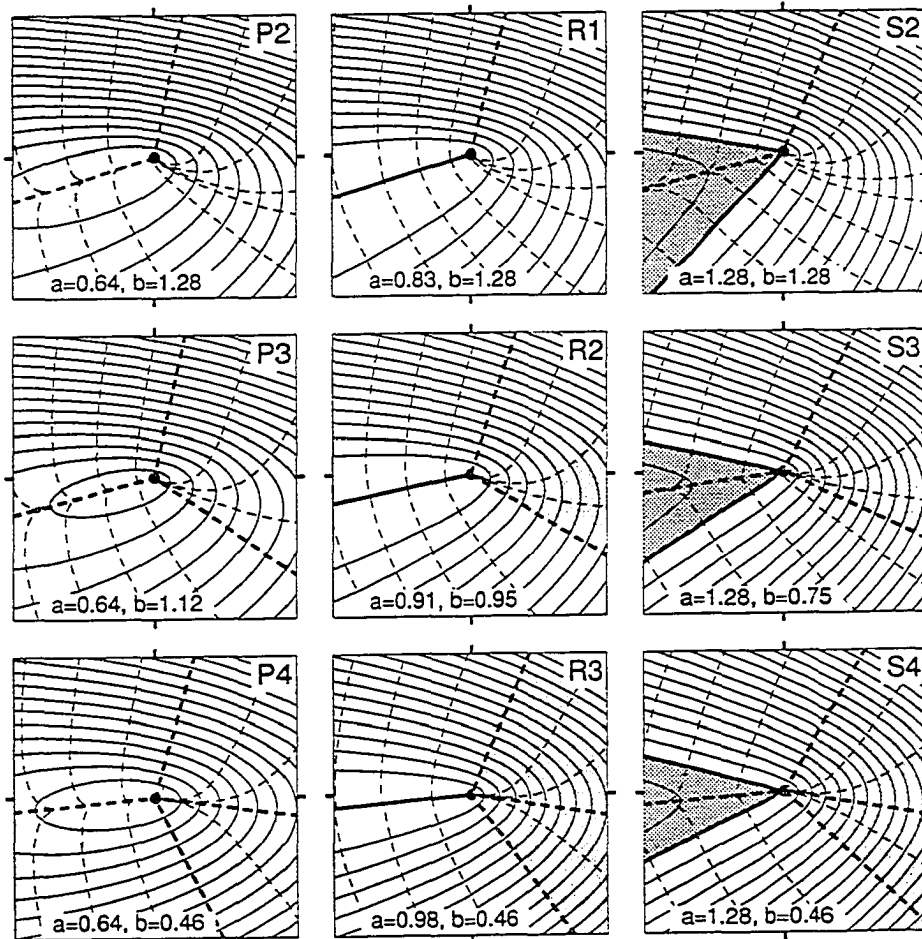
$c=2.29$, increment=0.60


Figure 9. Potential energy surface patterns near an intersection for the case $c=2.29$, $a \neq 0$, $b \neq 0$. For explanations of curves see caption of Fig. 3, except that the increment between contours is 0.6 in this figure

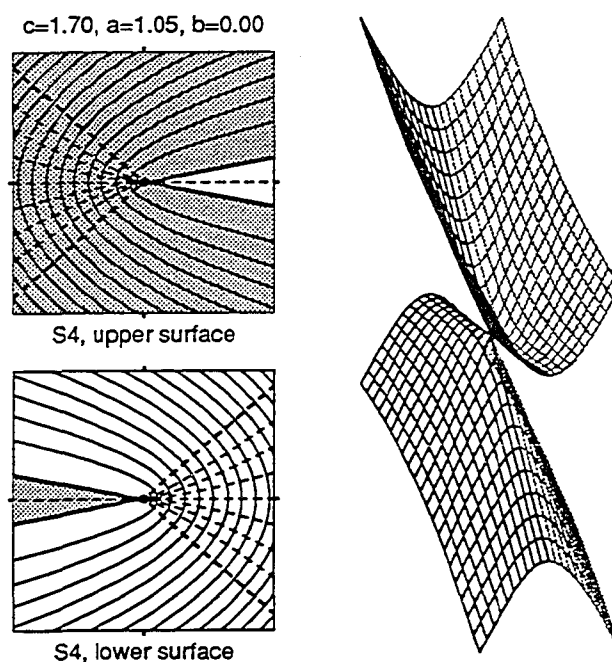


Figure 10. Contour maps (left) and perspective representation (right) of potential energy surfaces of two states in the vicinity of their intersection (Pattern S4). Left figures: solid lines = contours; increment = 0.55. On both panels the contour values decrease from left to right. The bold-faced solid straight lines are the contours $E=E_{\text{intersection}}$. Shaded areas = regions where $E>E_{\text{intersection}}$. Dashed lines = steepest descent curves passing through the intersection. Only the bold-faced dashed lines and the x-axis are straight; all other orthogonal trajectories become tangent to the x axis at the intersection. The x axis goes from left to right on the contour maps and from back left to front right on the perspective figure

PAPER III. A QUANTUM CHEMICAL CONSTRUCTION
OF DIABATIC STATES

A QUANTUM CHEMICAL CONSTRUCTION
OF DIABATIC STATES

Ames Laboratory USDOE and Department of Chemistry

Iowa State University

Ames, IA 50011

ABSTRACT

An electronic-structure-based construction of diabatic states from two adiabatic states is formulated. It is accomplished by maximizing the configurational uniformity of the diabatic states with respect to the dominant configurations throughout the entire coordinate space. No configurational constraints are introduced. The matrix elements between the diabatic states are simply expressible in terms of the adiabatic energies and wavefunction coefficients.

1. INTRODUCTION

Over large regions of the internal coordinate space, adiabatic molecular potential energy surfaces can vary in very complex fashions. Many of these contortions arise from avoided and real crossings of these surfaces and, in almost all such cases, the physical and chemical understanding is greatly helped by expressing the adiabatic states in terms of diabatic states. This is because diabatic states typically exhibit simpler energy surfaces as well as less complex electronic structures in terms of dominant configurations. Notwithstanding this gain in simplicity, the definition of diabatic states has turned out to be a non-trivial problem.

The interest in diabatic states has its origin in work on *dynamical* problems in regions where two potential energy surfaces cross or barely avoid crossing. Under such conditions, the Born-Oppenheimer approximation is inadequate and couplings *between* different adiabatic wavefunctions must be taken into account. Since they are mediated through matrix elements between nuclear derivative operators which become very large and very difficult to calculate, the "dynamic construction" of "diabatic" states [1] has been guided by the goal of reducing these coupling terms to a minimum. In general, they cannot, however, be made to vanish altogether and, as yet, there exists no unique standard definition of such states [2]. The extensive

work in this area has been described in recent papers by Pacher, Köppel and Cederbaum [3] where further references can be found.

From a *quantum chemical point of view*, the *electronic structure* aspects of diabatic states are more immediately apparent, namely that in regions of real and avoided crossings there occurs a manifest *switch* in the configurational composition of the *adiabatic* states, whereas this does *not* seem to be the case for *diabatic* states. This observation suggests an "electronic-structure approach" to the problem of defining and determining diabatic states, namely as states which do not change their configurational character when the system passes through the region of a real or avoided crossing. We are aware of the following proposals to construct diabatic states in this manner. Hendekovic et. al. suggested two methods, one based on the maximization of the sum of squares of natural spin orbital occupation numbers [4] and another based on an interpolation of one-electron densities [5]. Werner, et. al. used a weighted sum of squares of adiabatic configurational coefficients for special types of wavefunctions [6]. Pacher, Köppel and Cederbaum introduced a "minimal block diagonalization" to deduce diabatic states from adiabatic states [3].

In the present investigation, we present a new quantum chemical procedure for deriving diabatic states from adiabatic states. It is based on the configurational expansion of the electronic wavefunctions of the adiabatic

states. It generates diabatic states which span *exactly* the same function space as the adiabatic states and it *maximizes the configurational uniformity throughout the coordinate space for both diabatic states*. No restrictive configurational bias is introduced which would prevent full freedom for the determination of the adiabatic or diabatic states. The algorithm is uncomplicated and straightforward.

Our interest in this subject was motivated by the intention to use the interaction matrix between the diabatic states in order to elucidate the electronic causes for the conical intersection between the two lowest 1A_1 states of ozone. The method outlined below proved simple and effective in its application to this problem. The latter reported in an accompanying paper [1].

We have not examined the magnitudes of the dynamical coupling matrix elements between the diabatic states. But from the shapes of the diabatic potential energy surfaces obtained by this method in the mentioned application (see Figure 5 of reference [1]), it is apparent that they will be small.

2. CONSTRUCTION OF DIABATIC STATES

2.1 Premises

We start from the premise that MCSCF optimized wavefunctions are available over a region of the internal coordinate space for two orthogonal adiabatic states ψ_1 , ψ_2 and that these wavefunctions are expressed in terms of a common set of configurations χ_α ($\alpha=1,2,\dots,A$) generated from a common set of optimized orbitals. Normally, such wavefunctions would result from state-averaged calculations.

We furthermore assume that the orbitals can be unambiguously defined in such a manner that it is possible to follow each of them along a continuous path in the coordinate region of interest. That is to say, each optimized orbital evolves through a sequence of continuous deformations along any continuous path in coordinate space. By virtue of orbital occupations and spin structures, the unambiguous identification of *orbitals* yields then an unambiguous and coherent identification of deforming *configurations* χ_α in the entire coordinate region of interest.

Finally, it is assumed that one can identify a number of *dominant configurations* which determine the character of the two adiabatic states and, furthermore, that the orbitals have been defined in such a manner that, for any one molecular geometry, *different adiabatic states are dominated by*

different dominant configurations. Appropriate orbitals to accomplish this may be natural orbitals, localized orbitals, or orbitals uniformly determined by some other criterion.

Our interest focusses, then, on those regions in coordinate space where there occurs a *switch* in the dominance of configurations between the adiabatic states ψ_1, ψ_2 , as shown by the following scheme:

Dominant Configurations	----- Adiabatic States -----	
	Region I	Region II
$\chi_1 \cdots \chi_a$	dominant in ψ_1	dominant in ψ_2
$\chi_{a+1} \cdots \chi_{a+b}$	dominant in ψ_2	dominant in ψ_1

It would seem that the aforementioned premises are required by any method for deducing diabatic states from the electronic structures of adiabatic states.

2.2 Diabatic States

The purpose of "electronic-structure-based diabatic states" is to simplify the structure of the electronic wavefunctions. To this end, we look for two diabatic wavefunctions ϕ_1, ϕ_2 which have the following attributes:

- (i) The two adiabatic states ψ_1, ψ_2 can be decomposed into , or constructed from the two diabatic states ϕ_1, ϕ_2 by a linear

transformation \mathbf{T} , i.e.,

$$\begin{aligned}\psi_1 &= T_{11}\phi_1 + T_{12}\phi_2 \\ \psi_2 &= T_{21}\phi_1 + T_{22}\phi_2.\end{aligned}\tag{1}$$

(ii) The diabatic states are orthogonal, as are the adiabatic states.

Hence, \mathbf{T} is orthogonal:

$$\mathbf{T}\mathbf{T}^\dagger = \mathbf{T}^\dagger\mathbf{T} = \mathbf{I}\tag{2}$$

whence

$$\mathbf{T} = \begin{pmatrix} T_{11} & T_{12} \\ T_{21} & T_{22} \end{pmatrix} = \begin{pmatrix} \cos\gamma & -\sin\gamma \\ \sin\gamma & \cos\gamma \end{pmatrix}.\tag{3}$$

(iii) Any one of the diabatic states is dominated by one and the same set of configurations throughout the *entire* coordinate space of interest, as shown by the following scheme:

Dominant Configurations	----- Diabatic States -----
	Region I Region II
$\chi_1 \cdots \chi_a$	----- Dominant in ϕ_1 -----
$\chi_{a+1} \cdots \chi_{a+b}$	----- Dominant in ϕ_2 -----

It is in this sense that the diabatic states are "simpler".

In the sequel, we shall describe a method for deducing such diabatic states from the known adiabatic states. It is evident that the transformation \mathbf{T} must be coordinate dependent.

The adiabatic states are expressed, through coefficients $C_{\alpha m}$, in terms

of a large number of given configurations χ_α ($\alpha=1,2,\dots,A$), spanning the configuration space, *viz.*,

$$\Psi_n = \sum_{\alpha}^A \chi_{\alpha} C_{\alpha n} \quad n=1,2. \quad (4)$$

Because of the orthogonalities

$$\langle \chi_{\alpha} | \chi_{\beta} \rangle = \delta_{\alpha\beta}, \quad \langle \phi_n | \phi_m \rangle = \delta_{nm}, \quad (5)$$

one has

$$\mathbf{C}^{\dagger} \mathbf{C} = \sum_{\alpha} (\mathbf{C}_{\alpha n} \mathbf{C}_{\alpha m}) = \mathbf{I}. \quad (6)$$

By virtue of Eqs. (4), (5), (6), the diabatic states are given by

$$\phi_i = \sum_{n=1}^2 \psi_n T_{ni}, \quad i=1,2, \quad (7)$$

whence,

$$\phi_i = \sum_{\alpha}^A \chi_{\alpha} F_{\alpha i} \quad (8)$$

where

$$\mathbf{F}_{\alpha i} = \sum_n^2 \mathbf{C}_{\alpha n} T_{ni} = (\mathbf{C}\mathbf{T})_{\alpha i}. \quad (9)$$

Orthogonality yields

$$\langle \phi_i | \phi_j \rangle = \sum_{\alpha} F_{\alpha i} F_{\alpha j} = (\mathbf{F}^{\dagger} \mathbf{F})_{ij} = (\mathbf{T}^{\dagger} \mathbf{C}^{\dagger} \mathbf{C} \mathbf{T})_{ij} = (\mathbf{T}^{\dagger} \mathbf{T})_{ij} = \delta_{ij} \quad (10)$$

In the following, it is assumed that the dominant configurations are listed *first*, as $\chi_1 \chi_2 \dots \chi_a \chi_{a+1} \dots \chi_{a+b}$, so that the remaining configurations follow as $\chi_{a+b+1} \dots \chi_A$. Typically, $a+b$ is a relatively small number, whereas A , the dimension of the entire configuration space, is a large number.

2.3 Diabaticity Criterion

Our objective, then, is to determine the 2×2 transformation such that, *throughout*, ϕ_1 is dominated by $\chi_1 \dots \chi_a$ and ϕ_2 is dominated by $\chi_{a+1} \dots \chi_{a+b}$. To accomplish this, we demand that, in Eq. (9), the transformation \mathbf{T} be determined such that the quantity

$$\mathbf{F} = \mathbf{F}_a + \mathbf{F}_b = \sum_{\alpha=1}^a \mathbf{F}_{\alpha 1}^2 + \sum_{\beta=a+1}^{a+b} \mathbf{F}_{\beta 2}^2 \quad (11)$$

becomes maximal. From Eq. (9) one obtains

$$\mathbf{F}_a = (\mathbf{T}^+ \mathbf{P} \mathbf{T})_{11} \quad (12a)$$

with

$$\mathbf{P}_{nm} = \sum_{\alpha=1}^a C_{\alpha n} C_{\alpha m} = \mathbf{P}_{mn}, \quad n, m = 1, 2 \quad (12b)$$

and similarly:

$$\mathbf{F}_b = (\mathbf{T}^+ \mathbf{Q} \mathbf{T})_{22} \quad (13a)$$

with

$$\mathbf{Q}_{nm} = \sum_{\beta=a+1}^{a+b} C_{\beta n} C_{\beta m} = \mathbf{Q}_{mn}, \quad n, m = 1, 2. \quad (13b)$$

By virtue of Eq. (3) we can rewrite Eq. (13a) as

$$\mathbf{F}_b = (\mathbf{T}^+ \mathbf{Q} \mathbf{T})_{11} \quad \text{with} \quad \mathbf{Q} = \begin{pmatrix} \mathbf{Q}_{22} & -\mathbf{Q}_{12} \\ -\mathbf{Q}_{21} & \mathbf{Q}_{11} \end{pmatrix} \quad (14)$$

Combining the expressions (12a) and (14) we obtain therefore for \mathbf{F} of Eq.

(11):

$$\mathbf{F} = (\mathbf{T}^+ \mathbf{R} \mathbf{T})_{11} \quad (15)$$

where

$$R_{11} = P_{11} + Q_{22} = \sum_{\alpha=1}^a C_{\alpha 1}^2 + \sum_{\beta=a+1}^{a+b} C_{\beta 2}^2 \quad (16a)$$

$$R_{22} = P_{22} + Q_{11} = \sum_{\alpha=1}^a C_{\alpha 2}^2 + \sum_{\beta=a+1}^{a+b} C_{\beta 1}^2 \quad (16b)$$

$$R_{12} = R_{21} = P_{12} - Q_{12} = \sum_{\alpha=1}^a C_{\alpha 1} C_{\alpha 2} - \sum_{\beta=a+1}^{a+b} C_{\beta 1} C_{\beta 2} \quad (16c)$$

A slight modification of the described method would be as follows.

First, the dominant parts of the adiabatic wavefunctions are renormalized, to give

$$\Psi_n = \sum_{\alpha}^{a+b} \chi_{\alpha} \hat{C}_{\alpha n}, \quad n=1,2 \quad (17a)$$

$$\hat{C}_{\alpha n} = C_{\alpha n} / \left(\sum_{\alpha=1}^{a+b} C_{\alpha n}^2 \right)^{1/2} \quad (17b)$$

and then, the maximization algorithm is applied to the quantity

$$F = F_a + F_b = \sum_{\alpha=1}^a F_{\alpha 1}^2 + \sum_{\beta=a+1}^{a+b} F_{\beta 2}^2. \quad (18)$$

The difference between the two procedures should be small.

2.4 The Transformation Matrix

From the expression (15), it is apparent that the maximization of F is accomplished by *diagonalizing* the matrix \mathbf{R} . The eigenvector with the larger eigenvalue yields (T_{11}, T_{21}) which determines ϕ_1 , whereas the eigenvector with the smaller eigenvalue yields (T_{12}, T_{22}) which determines ϕ_2 . The solutions of

this eigenvalue problem can be expressed in the well-known form

$$\lambda_1 = \bar{R} + \sqrt{(\Delta R)^2 + R_{12}^2} \quad (19a)$$

$$\lambda_2 = \bar{R} - \sqrt{(\Delta R)^2 + R_{12}^2} \quad (19b)$$

$$\begin{pmatrix} T_{11} & T_{12} \\ T_{21} & T_{22} \end{pmatrix} = \begin{pmatrix} \cos\beta/2 & -\sin\beta/2 \\ \sin\beta/2 & \cos\beta/2 \end{pmatrix} \quad (20)$$

where

$$\bar{R} = (R_{11} + R_{22})/2, \quad \Delta R = (R_{11} - R_{22})/2 \quad (21)$$

$$\cos\beta = \Delta R / \sqrt{(\Delta R)^2 + R_{12}^2}, \quad \sin\beta = R_{12} / \sqrt{(\Delta R)^2 + R_{12}^2} \quad (22)$$

It is understood, of course, that the transformation T of Eq. (20) is used to transform the *full expansion* of ψ_1 and ψ_2 as indicated in Section 2.2.

3. CALCULATION OF ΔH AND H_{12}

The hamiltonian matrix elements between the diabatic states are helpful in analyzing the physics determining the adiabatic states (see, e.g., ref [1]) as well as the character of the dynamics. By virtue of Eq. (7) these matrix elements are given by

$$H_{ij} = \langle \phi_i | H | \phi_j \rangle = \sum_{n,m} \langle \psi_n | H | \psi_m \rangle T_{ni} T_{mj} \quad (23)$$

$$H_{ij} = E_1 T_{1i} T_{1j} + E_2 T_{2i} T_{2j}$$

Expressing E_1 and E_2 in terms of

$$\bar{E} = (E_1 + E_2)/2, \quad \Delta E = (E_1 - E_2)/2, \quad (24)$$

one obtains

$$H_{ij} = \bar{E} \delta_{ij} + \Delta E (T_{1i} T_{1j} - T_{2i} T_{2j}) \quad (25)$$

which, with the representation of Eq. (20) becomes

$$H_{11} = \bar{E} + \Delta E \cos \beta \quad (26a)$$

$$H_{22} = \bar{E} - \Delta E \cos \beta \quad (26b)$$

$$H_{12} = -\Delta E \sin \beta \quad (26c)$$

If we now insert the values obtained for $\cos \beta$ and $\sin \beta$ by the maximization procedure of the preceding section, we finally obtain

$$H_{11} = \bar{E} + \Delta E \cdot \Delta R / \sqrt{\Delta R^2 + R_{12}^2} \quad (27a)$$

$$H_{22} = \bar{E} - \Delta E \cdot \Delta R / \sqrt{\Delta R^2 + R_{12}^2} \quad (27b)$$

$$H_{12} = -\Delta E \cdot R_{12} / \sqrt{\Delta R^2 + R_{12}^2}. \quad (27c)$$

4. COMMENT

A particular numerical aspect deserves careful attention in order to insure that ϕ_1 and ϕ_2 as well as ΔH and H_{12} vary continuously in the coordinate range of interest. There are two circumstances which can lead to *apparent* discontinuities in the diabatic states ϕ_1, ϕ_2 . One is the fact that the numerical calculation of the adiabatic states ψ_1, ψ_2 can yield accidental arbitrary jumps in their signs in going from one point to a neighboring point. It is evident from Eqs. (16c) and (27c) that R_{12} and, hence, H_{12} change sign if only one of the adiabatic states ψ_1, ψ_2 change sign (ΔH is insensitive to it). Secondly, even if the two adiabatic states are carefully adjusted not to change sign from one point to the next, a sign change *must* occur in both in case one completes a closed path encircling an intersection point, in accordance with the Herzberg-Longuet-Higgins-Berry theorem [2]. The diabatic states ϕ_1, ϕ_2 , on the other hand, do not have this complication. They can be assumed to be continuous everywhere, and the discontinuity in the sign of ψ_1, ψ_2 can be considered as arising from the fact that the angle γ in the 2×2 transformation from (ϕ_1, ϕ_2) to (ψ_1, ψ_2) [See Eq.(3)] is in fact $1/2$ of an angle varying between $-\pi$ and π . In our reconstruction of (ϕ_1, ϕ_2) from (ψ_1, ψ_2) , this half-angle effect is, in principle, compensated by the half-angle $(\beta/2)$ in Eq. (20). A wrong sign of ψ_1 or ψ_2 , combined with a wrong choice of the principal

value of β , can result in uncontrolled jumps in sign for ϕ_1 or ϕ_2 , and also in an interchange of ϕ_1 and ϕ_2 . The simplest way to avoid this numerical confusion is to monitor both, ϕ_1 and ϕ_2 , and, if necessary, to make the necessary changes in sign and/or interchanges of ϕ_1 and ϕ_2 , such that the configuration coefficients of both diabatic wavefunctions vary continuously over the entire region of interest. This is simpler than trying to make equivalent changes in the signs of ψ_1 and/or ψ_2 or adjustments of the principal value of β .

REFERENCES

1. W. Lichten, *Phys. Rev.* **131**, 229 (1963); F. Smith, *ibid.* **179**, 111 (1969)
2. C. A. Mead, D. G. Truhlar, *J. Chem. Phys.* **77**, 6090 (1982); M. Desouter, D. Dehareng, J. C. Lorquet, *J. Chem. Phys.* **86**, 1429 (1987);
3. T. Pacher, H. Köppel, L. S. Cederbaum, *J. Chem. Phys.* **95**, 6668 (1991) and **89**, 7367 (1988)
4. J. Hendeković, *Chem. Phys. Lett.* **90**, 193 (1982)
5. J. Kučar, M. Pavlović, J. Hendeković, *Int. J. Quant. Chem.* **32**, 699 (1987)
6. H. J. Werner, B. Follmeg, M. Alexander, *J. Chem. Phys.* **89**, 3139 (1988)
7. G. Atchity and K. Ruedenberg, to be submitted.

PAPER IV. ELECTRONIC STRUCTURE BASIS FOR THE CONICAL
INTERSECTION BETWEEN THE LOWEST TWO 1A_1 STATES OF OZONE

ELECTRONIC STRUCTURE BASIS FOR THE CONICAL
INTERSECTION BETWEEN THE LOWEST TWO 1A_1 STATES OF OZONE

Ames Laboratory USDOE and Department of Chemistry

Iowa State University

Ames, IA 50011

ABSTRACT

The quantum chemical construction of diabatic states from adiabatic states formulated in a preceding paper is used to express the lowest two 1A_1 states of ozone in terms of its diabatic components and to determine the interaction matrix H_{ij} between them. An analysis of the electronic structure of the diabatic states leads to an understanding of the reasons for the sign changes in ΔH and H_{12} and, hence, for the conical intersection between these two adiabatic states of like symmetry.

1. INTRODUCTION

The two lowest 1A_1 potential energy surfaces of ozone, which we have mapped out in C_{2v} symmetry in previous investigations [1], are notable for several reasons. First, the ground state surface has *two minima*: the experimentally observed open structure, with a angle of 116° and the, as yet, experimentally unobserved equilateral triangle ring structure. The ring minimum lies about 30 kcal/mol above the open minimum and slightly above the dissociated species O_2+O . Secondly, less than 0.04\AA away from the *transition state* between the ring and open structures of the ground state, the *second* 1A_1 state has a *minimum*. Finally, these two states of like symmetry were found to *cross in a conical intersection* within 0.04\AA of the aforementioned upper state minimum and the ground state transition state. Since this seems to be the first instance of an intersection between the two lowest states of like symmetry near the groundstate minimum in a common molecule, it is of interest to explore the causes for such a crossing. In the present investigation we look, therefore, for those features of the electronic structures of this molecule which lead to the discovered intersection.

The existence of the two minima is a consequence of the fact that there exist two electronic structures, A and B, with different stabilities in different parts of the internal coordinate space. For the equilateral minimum,

structure A is more stable than structure B whereas, for the open minimum, structure B is more stable than structure A. Under such conditions, one usually encounters an avoided crossing near the transition state. In the case at hand, the two states become, however, degenerate at the crossing point.

In the language of the fundamental analysis of surface crossings [2], the two electronic structures A and B correspond to two *diabatic* states ϕ_1 and ϕ_2 from which the two adiabatic states ψ_1 and ψ_2 can be constructed. The change in stability between ϕ_1 and ϕ_2 implies that, near the ridge of the potential energy surface, which separates the catchment basins of the two minima in the C_{2v} restricted two-dimensional coordinate space, the energy difference

$$\Delta H = H_{11} - H_{22} = \langle \phi_1 | H | \phi_1 \rangle - \langle \phi_2 | H | \phi_2 \rangle \quad (1)$$

changes sign. Along this ridge, the two adiabatic states are close in energy. A true intersection will occur if, someplace along the line $\Delta H=0$, the additional condition,

$$H_{12} = \langle \psi_1 | H | \psi_2 \rangle = 0 \quad (2)$$

is also satisfied. That is, the off-diagonal element H_{12} must change sign as well and the degeneracy of the two states occurs where the curves $H_{12}=0$ and $\Delta H=0$ intersect.

In view of these fundamental connections, it seems likely that an understanding of the factors that can lead to an intersection between states of like symmetry can be expected from a closer look at the energetics of the

diabatic states. This approach is chosen in the present investigation. The adiabatic 1^1A_1 and 2^1A_1 states of ozone are decomposed in terms of two diabatic states, which are determined by the method described in the preceding paper [3], and the critical quantities ΔH and H_{12} are calculated over the entire region of interest in coordinate space. An examination of the electronic structures of the diabatic states, then, leads to an appreciation of the reasons for the sign changes of ΔH and H_{12} which are so intimately tied to the conical intersection.

2. THE ADIABATIC AND DIABATIC POTENTIAL ENERGY SURFACES

2.1 Coordinate Space

We choose the coordinates x and y defined through Figure 1 as the two internal coordinates for the C_{2v} restricted deformations of ozone. The center atom is at the origin and the two end-atoms are at mirror image positions with respect to the y -axis.

The potential energy surfaces were calculated at the approximately 500 points shown as dots in Figure 2. Special symbols in the figure mark the various critical points of the two surfaces. A particular sequence of dots marks the line from one ground state minimum to the other through the intersection point. Also shown are the curves $\Delta H=0$ and $H_{12}=0$, which we shall determine in the sequel (solid line and dashed line).

2.2 Orbital Space

The Full Optimized Reaction Space (FORS) is the configuration space spanned by all configurations that can be formed from the set of 12 orbitals which can be perceived as molecule-deformed minimal basis orbitals ("quasi-atomic orbitals") on the three oxygens. They are depicted schematically in Figure 3. Nine of them are symmetric with respect to the molecular plane (" σ -type", A' irrep in C_s symmetry). From them one obtains the bonding-

adapted σ molecular orbitals

$$\begin{aligned} h_{01} &\approx N_+(h_0' + h_1''), & h_{01}^* &\approx N_-(h_0' - h_1'') \\ h_{12} &\approx N_+(h_1' + h_2''), & h_{12}^* &\approx N_-(h_1' - h_2'') \\ h_{02} &\approx N_+(h_2' + h_0''), & h_{02}^* &\approx N_-(h_2' - h_0'') \end{aligned} \quad (3)$$

The remaining three quasi-atomic orbitals are antisymmetric with respect to the molecular plane (" π -type", A'' irrep in C_s).

Appropriate linear combinations of the quasi-atomic orbitals belong to irreps of C_{2v} ($A' \rightarrow A_1, B_2$; $A'' \rightarrow A_2, B_1$). For the σ orbitals one has in particular

$$h_{12} = \sigma_+ \quad : A_1 \qquad h_{12}^* = \sigma_- \quad : B_2. \quad (4)$$

The symmetry and bonding adapted π -type orbitals are of the form:

$$\begin{aligned} \pi &= c_0 \pi_0 + c_+(\pi_1 + \pi_2) & : B_1 \\ \pi_- &= c_-(\pi_1 - \pi_2) & : A_2 \\ \pi_+ &= c_0' \pi_0 - c_+'(\pi_1 + \pi_2) & : B_1 \end{aligned} \quad (5)$$

Figure 4 displays contour plots of the natural orbitals of the actual MCSCF calculations which correspond to the orbitals σ_+ , σ_- , π_+ , π_- discussed above, for three points on the line leading from one minimum to the other (See Figure 2). One can see that the character of these orbitals changes very little along this entire path so that they remain clearly identifiable along the entire path.

2.3 Configuration Space

In the entire region around the intersection as well as the open minimum, the orbitals h_{01}^* and h_{02}^* are found to have very small occupations

and all other orbitals are doubly occupied, except the orbitals σ_+ , σ_- , π_+ , π_- which have changing occupations in the region of interest. This distribution of occupation numbers arises from the fact that, in this region, the wavefunction is dominated by the following four configurations (the entire FORS space is spanned by A=4067 configurations):

$$\begin{aligned}
 |14,4,+ \rangle &= |\sigma^{14}\pi^4 + \rangle = \langle \sigma^{10}\pi^2 \sigma_+^2 \sigma_-^2 \pi^2 \rangle \\
 |14,4,- \rangle &= |\sigma^{14}\pi^4 - \rangle = \langle \sigma^{10}\pi^2 \sigma_+^2 \sigma_-^2 \pi^2 \rangle \\
 |12,6,+ \rangle &= |\sigma^{12}\pi^6 + \rangle = \langle \sigma^{10}\pi^2 \pi_+^2 \pi_-^2 \sigma_+^2 \rangle \\
 |12,6,- \rangle &= |\sigma^{12}\pi^6 - \rangle = \langle \sigma^{10}\pi^2 \pi_+^2 \pi_-^2 \sigma_-^2 \rangle
 \end{aligned} \tag{6}$$

where

$$\sigma^{10} = (h_0''')^2 (h_1''')^2 (h_2''')^2 (h_{01})^2 (h_{02})^2 \tag{7}$$

It is obvious that for the ring minimum, where the symmetry is D_{3h} , six additional configurations will have comparable weight, namely those obtained by the following substitutions:

$$\begin{aligned}
 (i) \quad \sigma_- &= h_{12}^* \rightarrow h_{01}^* \text{ or } h_{02}^* && \text{in } |14,4,+ \rangle \text{ and } |14,4,- \rangle \\
 (ii) \quad h_{01} &\rightarrow h_{01}^* \text{ or } h_{02} \rightarrow h_{02}^* && \text{in } |12,6,+ \rangle.
 \end{aligned} \tag{8}$$

Since our objective is the elucidation of the intersection, we choose as the dominant configurations of the adiabatic states only the four listed in Eq. (6). The dominance of these configurations in ψ_1 and ψ_2 is shown in Table 1. In each of the four cases, the first listed configuration is the one with the lower energy, which survives in the SCF approximation, whereas the configuration listed second provides correlation to the first.

Table 1. Dominant Configurations in the 1^1A_1 and the 2^1A_1 states

	Open Basin	Ring Basin
Ground state 1^1A_1	$ \sigma^{14}\pi^4-\rangle$, $ \sigma^{14}\pi^4+\rangle$	$ \sigma^{12}\pi^6+\rangle$, $ \sigma^{12}\pi^6-\rangle$
Excited state 2^1A_1	$ \sigma^{12}\pi^6+\rangle$, $ \sigma^{12}\pi^6-\rangle$	$ \sigma^{14}\pi^4-\rangle$, $ \sigma^{14}\pi^4+\rangle$

We anticipated that the implementation of the methodology proposed in the preceding paper [3] had to be elaborated in detail and required considerable testing as we went along and, hence, that wavefunctions would have to be evaluated at many points. We therefore decided to begin by carrying through the procedure in a configuration space of a dimension less than 4067. In fact, we limited the configuration space to the four configurations given in Eq. (6). It should be noted that the determination of the matrix \mathbf{T} which yields the diabatic states would proceed no differently than in the present calculations and the numerical values obtained for the T_{ij} would be very little different if the calculations were based on the corresponding four dominant configurations of the *full* FORS wavefunction. The main difference would be that, in the end, the transformation \mathbf{T} would be applied to the adiabatic states ψ_1 , ψ_2 expanded in terms of 4067 configurations.

2.4 Potential Energy Surfaces

The adiabatic states 1^1A_1 and 2^1A_1 were determined by two-state-averaged MCSCF calculation in the space of the four configurations of Eq. (6). The orbitals were expanded in terms of a Dunning-Hay (9s5p1d/3s2p1d) basis of 45 segmented contracted atomic orbitals [4]. (The d-orbitals were of the cartesian type with $\zeta_d=0.85$). The calculations were performed with the program MOLPRO of Werner and Knowles [5].

Contours of the two surfaces are displayed in the upper two panels of Figure 5. These surfaces qualitatively reproduce all features of the FORS potential energy surfaces with one exception: The ring minimum does not have D_{3h} symmetry. This is, of course, due the fact that we have omitted the six correlating configurations mentioned in the preceding section. Table 2 compares the critical points of the two surfaces obtained by the present wavefunction with those of the FORS wavefunction. The good qualitative agreement is a consequence of the dominance of the four configurations in the FORS wavefunction.

From the adiabatic states, we determined the diabatic states by the procedure described in the preceding paper [3]. From the dominance table 1, it is apparent that one of the diabatic states must be dominated by the two ($\sigma^{14}\pi^4$) configurations throughout, whereas the other diabatic state must be dominated by the two ($\sigma^{12}\pi^6$) configurations everywhere. Thus, in Eq. (10) of

the preceding paper, the index α was taken to cover the two ($\sigma^{14}\pi^4$) configurations and the index β to cover the two ($\sigma^{12}\pi^6$) configurations. The quantities R_{ij} were evaluated, $\cos\beta$ and $\sin\beta$ were calculated and the elements of the transformation matrix \mathbf{T} were determined. We discussed in Section 2.4 of the preceding paper the precautions that must be taken in order to obtain continuous diabatic states. Contours of the surfaces of the diabatic states are displayed in the lower panels of Figure 5. It is apparent that each of the two

Table 2. Comparison of geometries of critical points determined with 4 configuration MCSCF wavefunctions to those determined with FORS wavefunctions

	4 Config MCSCF		FORS (4067 configs)	
	θ	R	θ	R
Open Minimum	114.69	1.265	116.32	1.298
Ring Minimum	68.10	1.366	60.00	1.470
Upper Minimum	88.43	1.370	83.59	1.441
Transition State	86.40	1.351	83.86	1.431
Intersection	88.38	1.375	83.18	1.476

diabatic states has a minimum which coincides with one of the two minima of the adiabatic ground state.

On all four panels of Figure 5, all critical points are marked. (On the first one, the lines $\Delta H=0$ and $H_{12}=0$ to be discussed below are also shown).

The difference ΔE between the two adiabatic state energies is displayed in Figure 6. The difference is seen to be very small all along the groundstate ridge separating the basins of the two minima which as we shall see in the sequel, is in fact the line given by $\Delta H=0$. The graph at lower right, plotting ΔE along this line, shows the typical pattern of the conical intersection at the point marked by a cross on the enlarged panel at the lower left.

3. QUANTITATIVE ANALYSIS OF THE INTERSECTION

3.1 The Surfaces of $\Delta H(x,y)$ and $H_{12}(x,y)$

The crucial quantities for the elucidation of the intersection are the functions $\Delta H(x,y)$ and $H_{12}(x,y)$ as defined by Eqs. (1) and (2). As a first step in our analysis, we examine the contour maps of ΔH and H_{12} in order to establish where they change sign. The contours are displayed on the two panels on the left hand side of Figure 7 where negative values are indicated by broken lines, positive values by solid lines, and zero contours by bold-faced solid lines. Both contours $\Delta H=0$ and $H_{12}=0$, are shown on both panels in order to identify the intersection. They were also shown on Figure 2 and on the upper left panels of Figures 5 and 6 so as to show that this intersection coincides indeed with the surface crossing, as required by theory. The upper left panel of Figure 5 shows that the line $\Delta H=0$ is a straight line following the ridge separating the ring minimum basin from the open minimum basin of the ground state. Figure 6 shows that the two adiabatic states are very close along this entire line.

As a further illustration, the graph at the lower right of Figure 7 displays a quantitative plot of ΔH and H_{12} along the dotted line which connects the two minima and passes through the intersection (see Figure 2). In the subsequent sections, we shall address the question how the variation

of ΔH and H_{12} along the line connecting the two minima, as displayed by this graph, can be related to the electronic structures of the diabatic states.

A comparison of Figure 8 with Figure 6 illustrates the fact that an accurate determination of the intersection point is in fact more efficiently accomplished through the intersection of $\Delta H=0$ and $H_{12}=0$, than by finding the point where ΔE vanishes.

3.2 The Wavefunctions

We begin by examining the configurational expansions of the two diabatic states which we denote as

$$\phi_1 = |\sigma^{14}\pi^4\rangle = |14,4\rangle \quad \text{and} \quad \phi_2 = |\sigma^{12}\pi^6\rangle = |12,6\rangle.$$

Both of them are linear combinations of all four configurations. However, we expect that $|14,4,+ \rangle$, $|14,4,- \rangle$ dominate in $|14,4\rangle$ and that $|12,6,+ \rangle$, $|12,6,- \rangle$ dominate in $|12,6\rangle$. This is indeed borne out by Figure 9 which exhibits plots of the four coefficients of the two states along the line connecting the minima. Note the difference in the ordinate scale between the dominant and the minor coefficients!

Of great relevance to the question to be discussed here is, however, the following additional observation:

Within each diabatic state the relative weight of the two dominant configurations changes significantly.

Examination of the left hand side of Figure 9 reveals indeed the pattern formulated in Table 3. The coefficient relationships implied by this Table can be readily understood. At the ring structure, the configurations $|14,4,+\rangle$ and $|14,4,-\rangle$ have approximately equal weight because the MO's π_+ and π_- would be degenerate for D_{3h} symmetry. However, for the open structure, π_- is a nonbonding orbital whereas π_+ is an antibonding orbital so that $|14,4,-\rangle$ is more stable than $|14,4,+\rangle$. On the other hand, the configurations $|12,6,+\rangle$ and $|12,6,-\rangle$ have approximately equal weight for the open structure since, here, the MO's σ_+ and σ_- are almost degenerate because, due to the distance between the end atoms, the bonding-antibonding effect is small. For the ring

Table 3. Relative weights of the two dominant configurations in the diabatic states $|14,4\rangle$ and $|12,6\rangle$.

Configurations in diabatic states	Ring Minimum	Open Minimum
$ 14,14,+\rangle$ in $ 14,4\rangle$	approximately	small
$ 14,4,-\rangle$ in $ 14,4\rangle$	equal weights	large
$ 12,6,+\rangle$ in $ 12,6\rangle$	large	approximately
$ 12,6,-\rangle$ in $ 12,6\rangle$	small	equal weights

structure, however, the two end atoms have come close together so that σ_+ is a bonding MO and σ_- is an antibonding MO. Hence, $|12,6,+ \rangle$ is more stable than $|12,6,- \rangle$.

The adiabatic states are expressed in terms of the diabatic states by a transformation matrix \mathbf{T} , given by the rotation angle γ , as formulated in Eqs. (1) and (3) of the preceding paper. The calculated variation of this angle along the line connecting the two minima is shown in Figure 10. The graph at the lower left displays the overall variation of $(\gamma/2\pi)$. The other graphs display enlarged presentations for three different regions. The plots exhibit the change in dominance of the two diabatic states in the two adiabatic states upon crossing the ridge between the two ground state basins. They show that this change is extremely sudden. The changeover would be discontinuous if the line connecting the minima would pass *exactly* through the intersection point. In fact, it misses this point by a little, and, it is therefore possible to establish the displayed continuous variation within a range of 0.0002\AA from the ridge.

If one substitutes the expansion of the diabatic states (as given by Figure 9) in the transformation to the adiabatic states (as given by Figure 10), then one obtains the expansions of the adiabatic states in terms of the four configurations. The resulting coefficients are displayed in Figure 11. These coefficients were, in fact, the starting point of our calculations from

which the data of Figures 9 and 10 were deduced by the method of Section 2.

3.3 Configurational Analysis of ΔH and H_{12} Along the Line Connecting the Two Minima

Analysis of ΔH

The upper panel of Figure 12 contains plots of the energies of the four configurations as dotted lines. Round symbols denote the two configurations that would appear in an SCF calculation, diamond symbols indicate the two configurations that are the dominant correlation-type configurations.

The solid symbols correspond to the $|12,6\rangle$ configurations. At the ring structure $|12,6,+ \rangle$ is much more stable than $|12,6,- \rangle$. This is because, here, σ_+ is a bonding MO whereas σ_- is antibonding. At the open structure, the configurations have, however, almost equal energies, since at that distance of the end-atoms from each other, σ_+ and σ_- are both non-bonding MO's.

The open symbols correspond to the $|14,4\rangle$ configurations. At the open structure $|14,4,- \rangle$ is more stable than $|14,4,+ \rangle$ because, here, π_- is a non-bonding MO, whereas π_+ is an antibonding MO. However, at the ring structure, the energies of the two configurations are quite close to each other, since for exact D_{3h} symmetry, the orbitals π_+ and π_- would be degenerate.

It is also apparent that, for the ring structure, the configuration $|12,6,+ \rangle$ is much lower in energy than both $|14,4\rangle$ configurations whereas,

for the open structure, the configuration $|14,4,-\rangle$ is much lower in energy than both $|12,6\rangle$ configurations. *Thus, the bonding/non-bonding/antibonding effects of the four molecular orbitals for the various geometries straightforwardly explain the crossover of the energies of the diabatic states which are displayed by the two solid lines.*

The lower panel of Figure 12 exhibits the values obtained for ΔH by (i) using the full four-configuration expression; (ii) using only the two dominant configurations in each diabatic wavefunction; (iii) using only the SCF determinants $|12,6,+\rangle$ and $|12,6,-\rangle$ in the calculation. It shows that the dominant configurations determine the overall character of the ΔH curve.

Analysis of H_{12}

We saw that the sign change in ΔH can be easily related to changes in orbital stabilities caused by changing bonding/nonbonding/antibonding interactions. Such changes of $(H_{11}-H_{22})$ with changing molecular geometries are extremely common. Sign changes in H_{12} , on the other hand, are more difficult to understand. But, here, they are crucial: Wherever H_{12} is nonzero, an *avoided* crossing occurs when ΔH changes sign. *The occurrence of a true crossing hinges on H_{12} changing sign in addition to ΔH doing so.*

For an explanation of the behavior of H_{12} , it is sufficient to use the expansion of the diabatic states in terms of their respective two dominant

configurations, *viz.*,

$$\begin{aligned} |12,6\rangle &= a_+|12,6,+ \rangle + a_-|12,6,- \rangle \\ |14,4\rangle &= b_+|14,4,+ \rangle + b_-|14,4,- \rangle \end{aligned} \quad (9)$$

The values for the coefficients in these equations are obtained from those on the left-hand graphs of Figure 9 by renormalization. It is apparent that a_+ and b_- are positive, whereas a_- and b_+ are negative. With these (approximate) expansions the off-diagonal hamiltonian matrix element becomes a sum of four terms:

$$\begin{aligned} H_{12} &\approx \langle 12,6|H|14,4\rangle \\ &\approx a_+b_+\langle 12,6,+|H|14,4,+ \rangle + a_+b_-\langle 12,6,+|H|14,4,- \rangle \\ &\quad + a_-b_+\langle 12,6,-|H|14,4,+ \rangle + a_-b_-\langle 12,6,-|H|14,4,- \rangle \end{aligned} \quad (10)$$

The solid lines in the top panel of Figure 13 displays the quantitative values of the four terms in Eq. (34) along the line connecting the two minima. The values plotted are the matrix elements multiplied by the coefficients. The sum of the four contributions is the dotted curve which is practically identical with the exact H_{12} curve in the lower right panel of Figure (7). It is apparent that the reason for the sign change in the H_{12} curve is the fact that *the negative contributions change significantly in magnitude along the path.*

The lower two panels provide the decomposition of the contributions shown in the top panel in terms of the orbital coefficient products and the matrix elements between the configurations. The former are displayed in the middle panel, the latter are exhibited in the bottom panel. An examination of these two panels reveals that the variations of the contributions on the top

panel are due to the variation of the coefficient products and not to those of the matrix elements between the configurations. (note that the negative contributions on the top and middle panels change by factors of 2 to 3, whereas the matrix elements in the bottom panel vary only by about 10%). The matrix elements are all positive because all four configurations differ from each other in doubly occupied orbitals so that all matrix elements are exchange integrals.

The sign change of H_{12} is thus related to the changes in the negative coefficient products in the middle panel. The latter are however, a direct consequence of the *changes in the relative weights of the dominant configurations within each diabatic state* which we discussed in detail in Section 3.2. There exist many examples of *two* diabatic state exchanging dominance in *two* adiabatic states, where each diabatic state contains only *one* dominant configuration and where these two dominant configurations differ (as in the case here) by a doubly occupied orbital. In these common cases, the matrix element H_{12} is approximately the exchange integral $\langle uv | r_{12}^{-1} | uv \rangle$ between those orbitals in which the two dominant configurations differ. Since such integrals are always positive *they cannot change signs*. Consequently, the reason for the possibility of a conical intersection in the present case is *the presence of more than one dominant configuration in each diabatic state* and the fact that, on the path from one minimum basin to

another, *not only do the diabatic states exchange dominance in the adiabatic states but, moreover, that there occurs an internal exchange of dominance between configurations within each diabatic state.* The reasons for these changes in the weights of the configurations were explained in Section 3.2.

4. CONCLUSION

The quantum chemical definition and construction procedure of diabatic states, formulated in the preceding paper [3], has been applied to the decomposition of the two lowest 1A_1 states of ozone (the lower one being the ground state) in terms of diabatic states.

Through an examination of the configurational expansions of these diabatic states, it proved possible to identify those features of the electronic structure which are related to the occurrence of a conical intersection between these two states.

It is concluded that, in cases where the dominant configurations of the diabatic states consist of doubly occupied orbitals only (as is common for ground states), an intersection can occur only if each diabatic state itself contains more than one dominant configuration and if the weights of these configurations within the diabatic states change significantly in the region of the coordinate space where the intersection occurs. Such changes can happen as the result of changing bonding interactions.

REFERENCES

1. S. Xantheas, G. J. Atchity, S. T. Elbert, and K. Ruedenberg, *J. Chem. Phys.*, **94**, 8054 (1991).
2. a. G. Herzberg and H. C. Longuet-Higgins, *Discuss. Faraday Soc.* **35**, 77 (1963); see also M. V. Berry, *Proc. R. Soc. London, Ser. A* **344**, 147 (1975); C. A. Mead, *J. Chem. Phys.* **70**, 2276 (1979); C. A. Mead and D. G. Truhlar, *ibid.* **70**, 2284 (1979).
b. G. J. Atchity, S. S. Xantheas, and K. Ruedenberg, *J. Chem. Phys.* **95**, 1862 (1991).
3. G. Atchity and K. Ruedenberg, to be submitted.
4. T. H. Dunning and P. J. Hay, in *Methods of Electronic Structure Theory*, edited by H. F. Schaefer (Plenum, New York, 1977), Vol. III, p. 1.
5. H.-J. Werner and P. J. Knowles, *J. Chem. Phys.* **82**, 5053 (1985); *Chem. Phys. Lett.* **115**, 259 (1985).

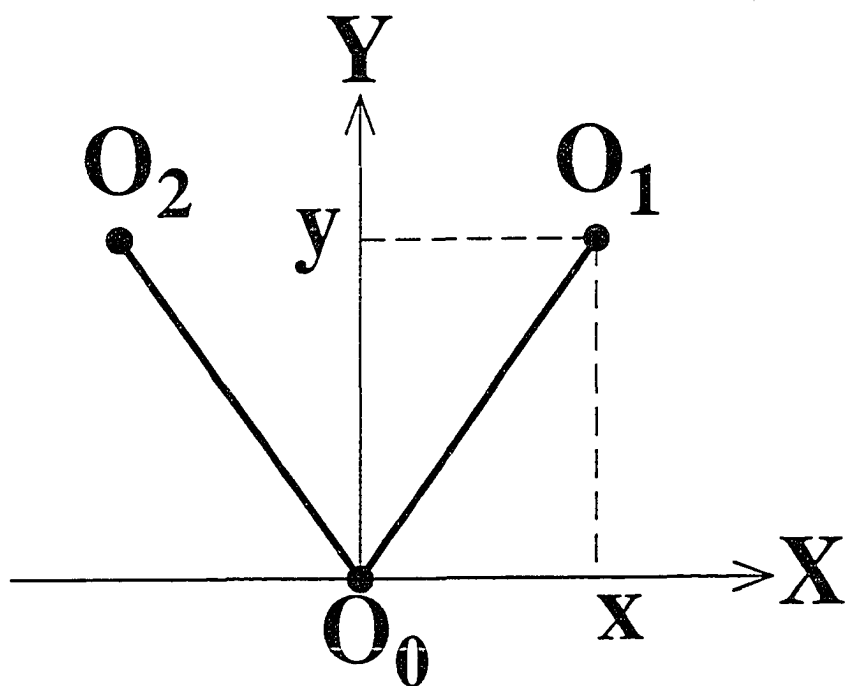


Figure 1. Internal coordinates for ozone in C_{2v}

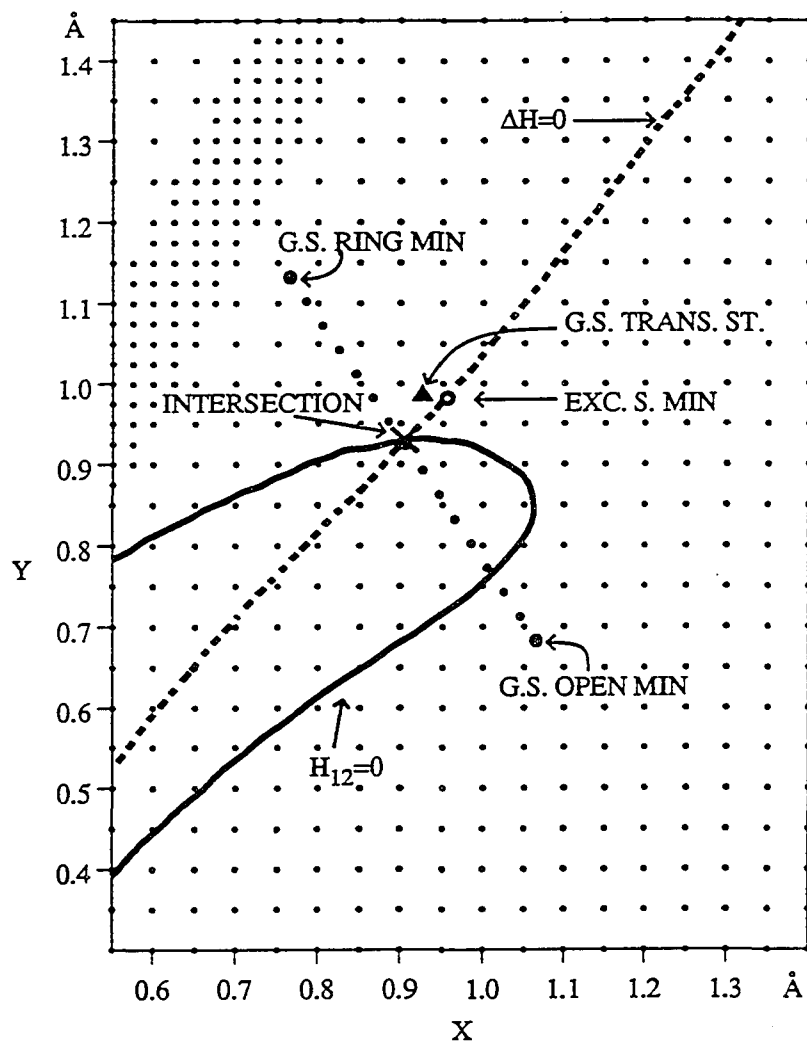


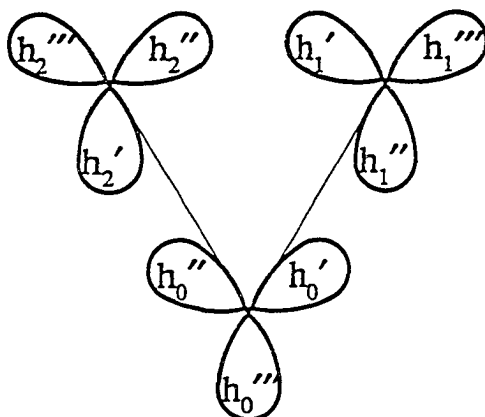
Figure 2. Data points calculated in C_{2v}

Dots mark the points at which energies were calculated.

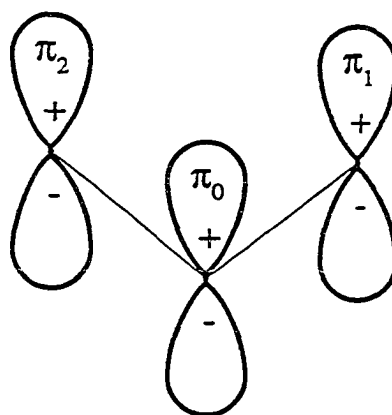
Medium size dots: path between lower surface minima. Large dots: lower surface minima. Empty dot: upper surface minima.

Triangle: ring-opening transition state. \times = intersection between the surfaces. Solid line: $H_{12}=0$. Dashed line: $\Delta H=0$

σ valence atomic hybrid orbitals



π valence atomic orbitals



Minimal Basis Valence Orbitals in O_3

Figure 3. Schematic drawing of the active orbitals of ozone

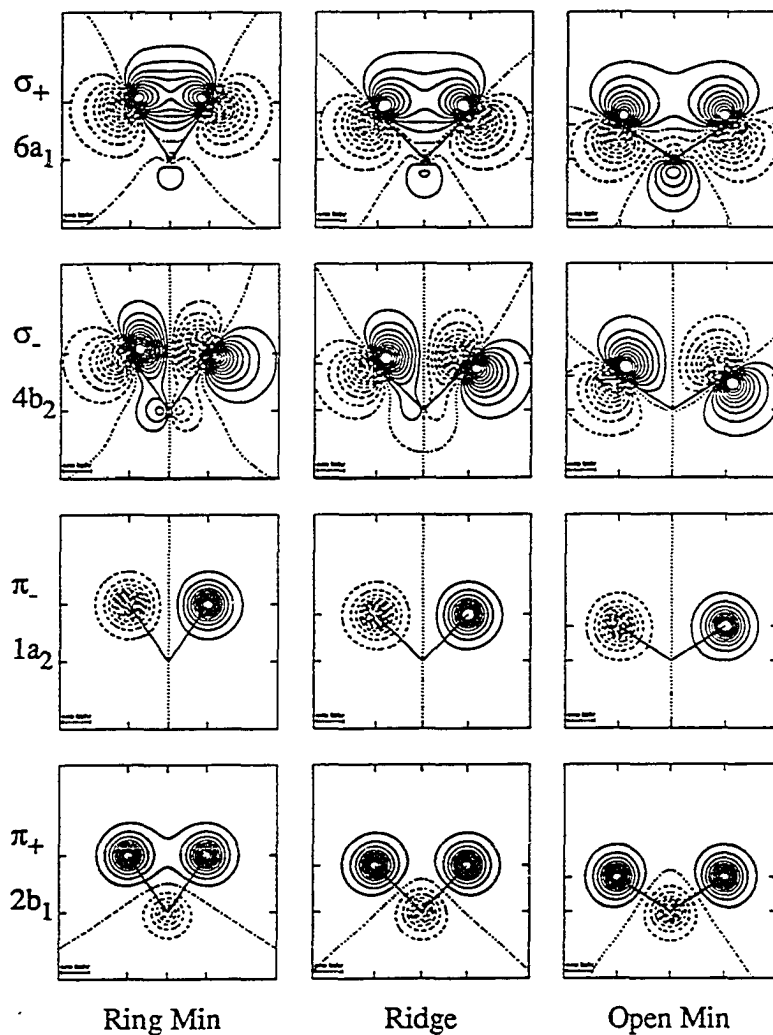


Figure 4. The molecular orbitals of ozone at the three critical points on the path between the two ground state minima

Solid lines: positive contours. Dashed lines: negative contours.

Dotted lines: zero contours. The σ orbitals are plotted in the plane of the molecule. The π orbitals are plotted in a plane slightly above the plane of the molecule

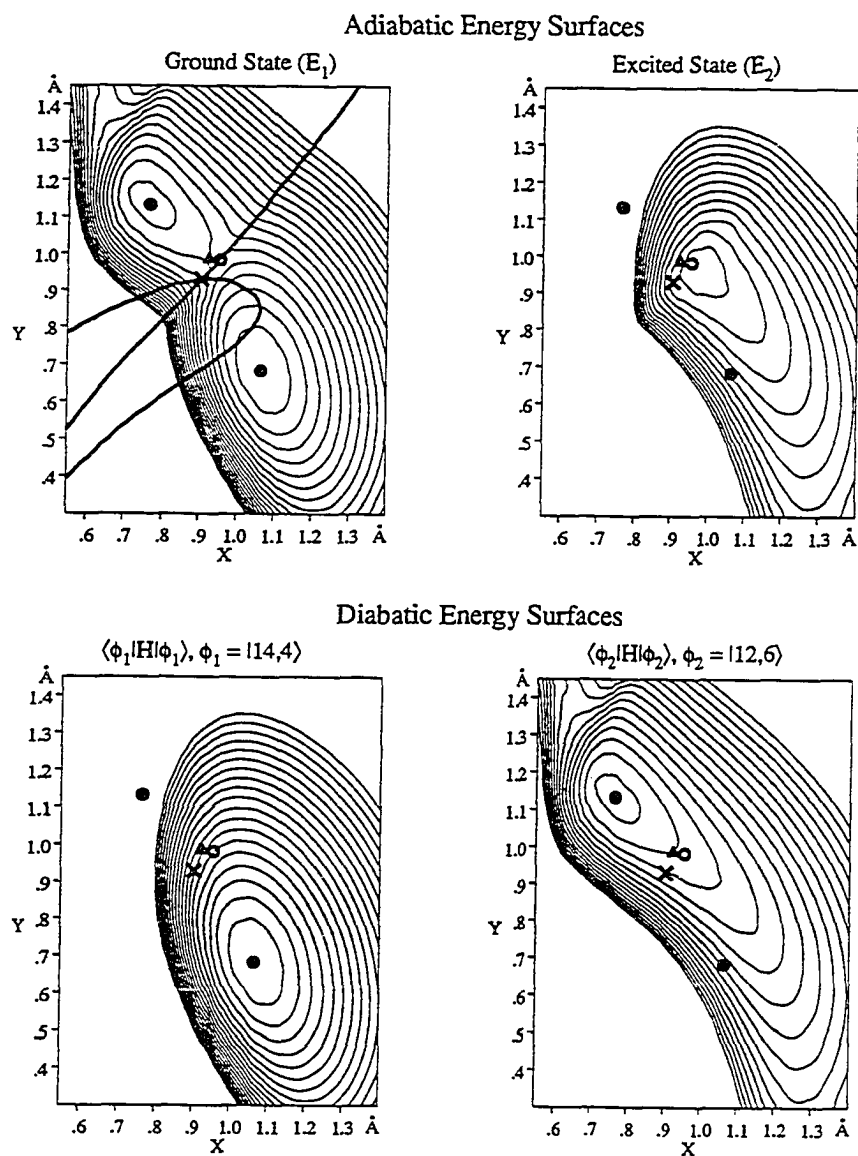


Figure 5. Energy surfaces of the lowest two 1A_1 states of ozone in C_{2v} . Solid dots: minima of the lower surface. Empty dots: minima of upper surface. Triangle: ring-opening transition state. \times : intersection between the surfaces. Solid lines mark $H_{12}=0$ and $\Delta H=0$. Contour increment: 10 millihartree.

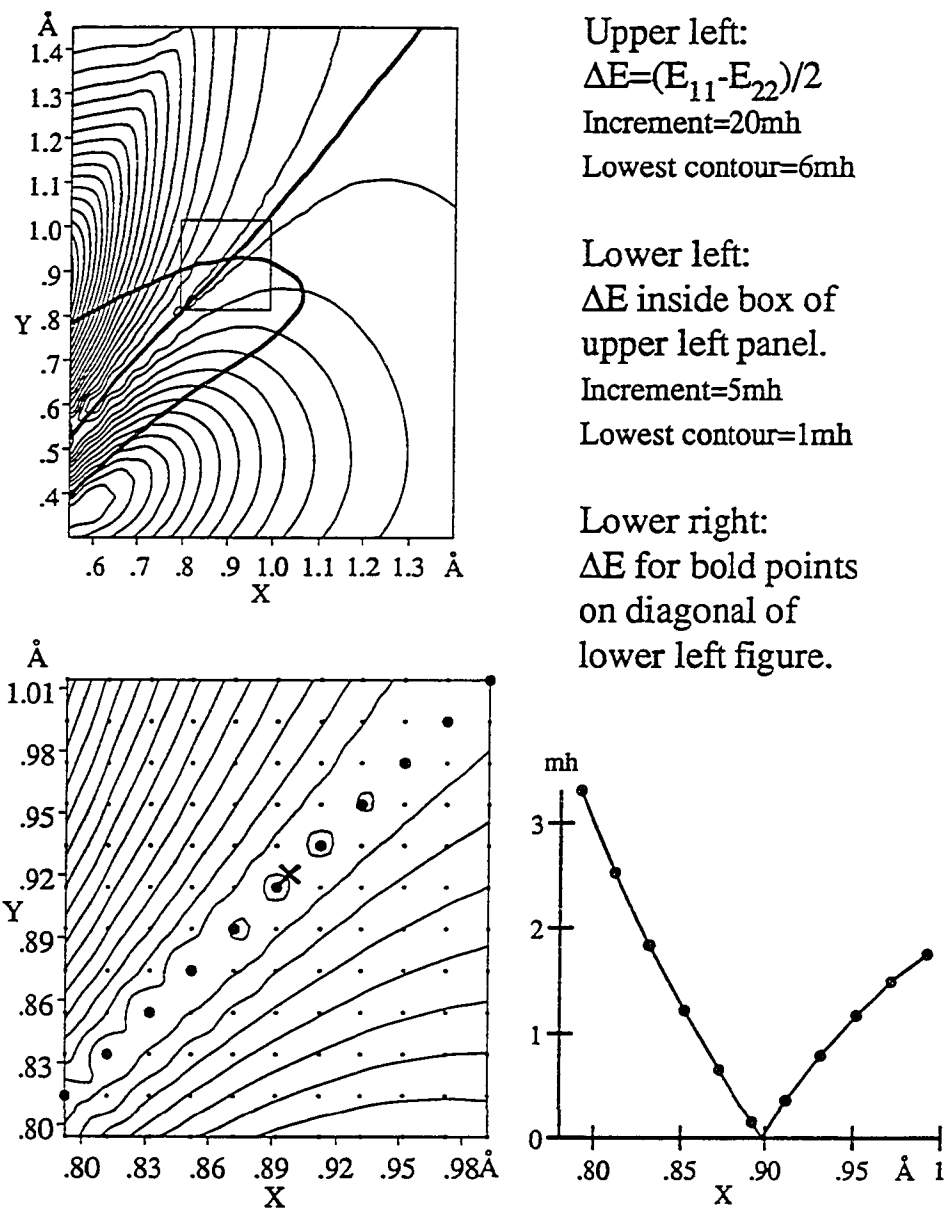


Figure 6. The energy difference $\Delta E = (E_1 - E_2)/2$

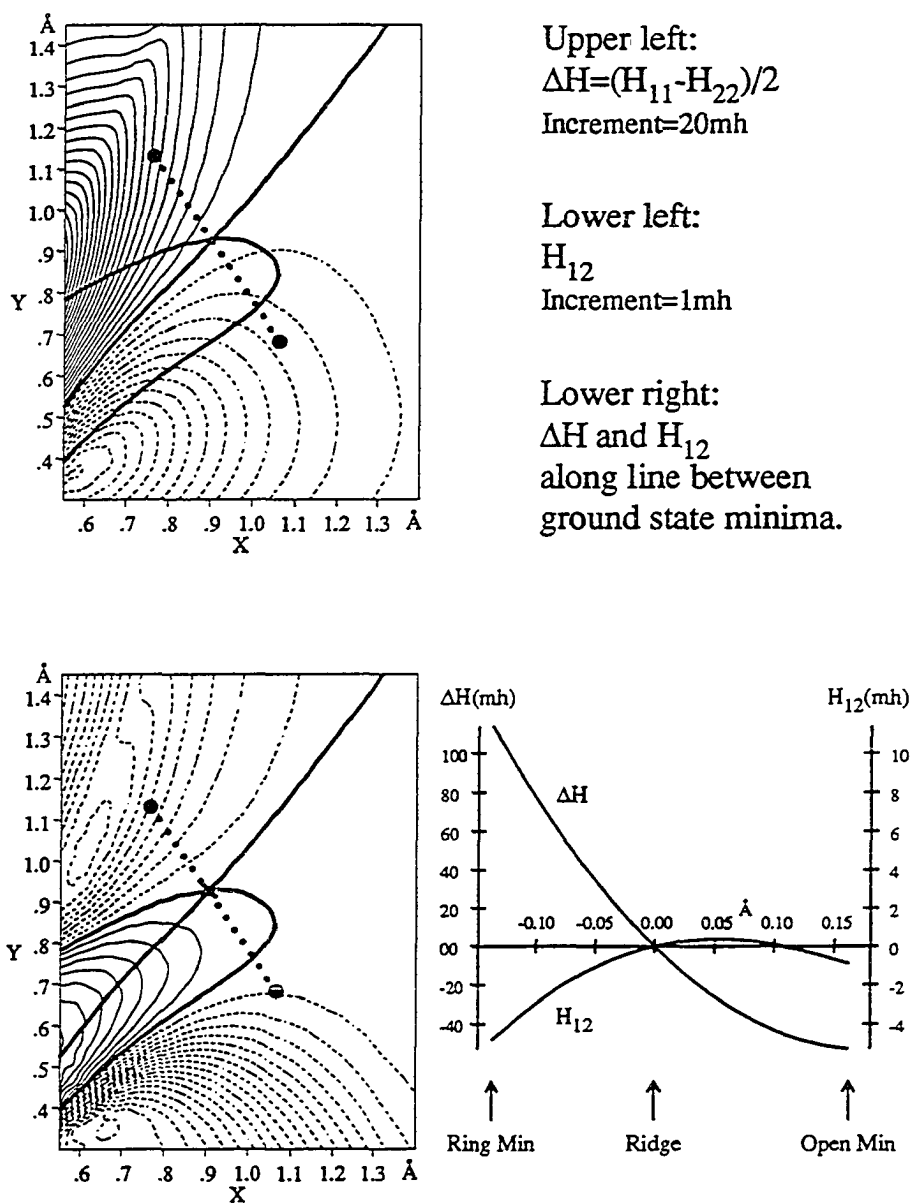


Figure 7. The surfaces of ΔH and H_{12} . Large dots: minima of the lower surface. Small dots: path between the minima. Solid lines: $\Delta H=0$ and $H_{12}=0$. Negative contours are dashed. Positive contours are solid. Zero contours are bold and solid

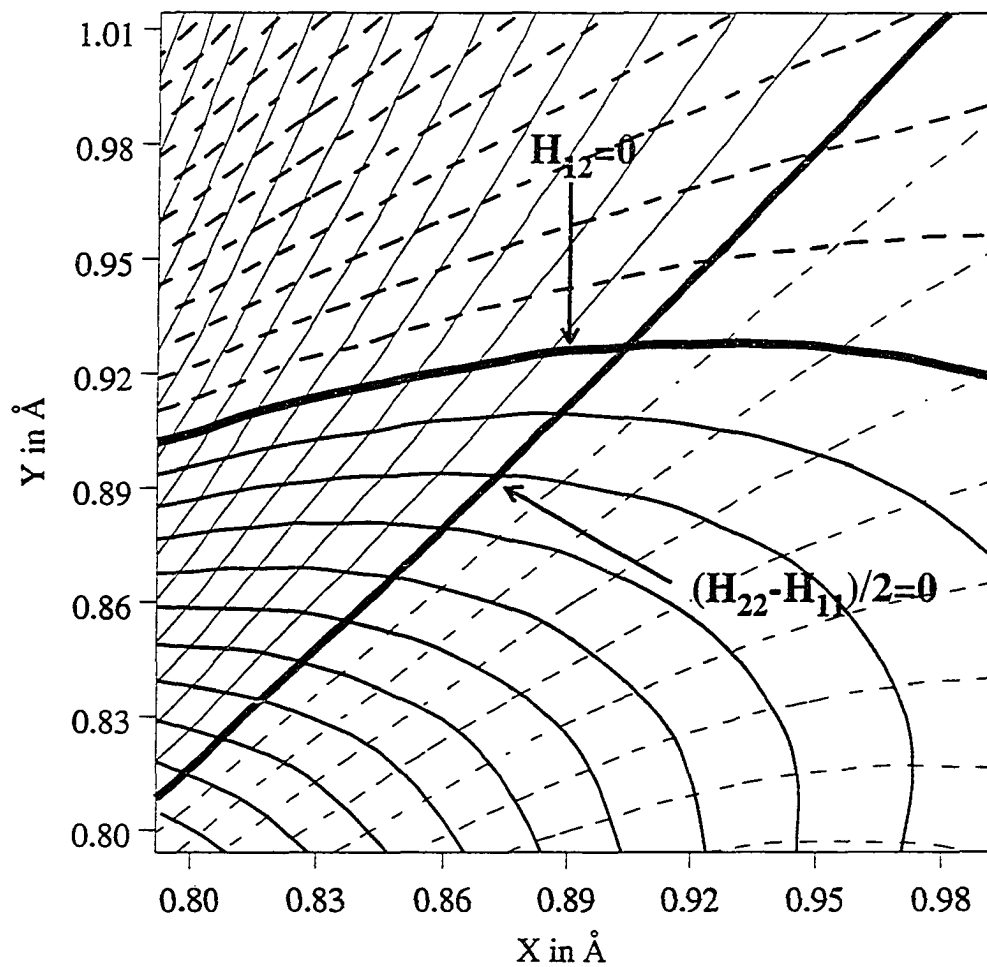


Figure 8. Contours of ΔH and H_{12} near the intersection

Solid lines: positive contours. Dashed lines: negative contours.

Bold solid lines: zero contours

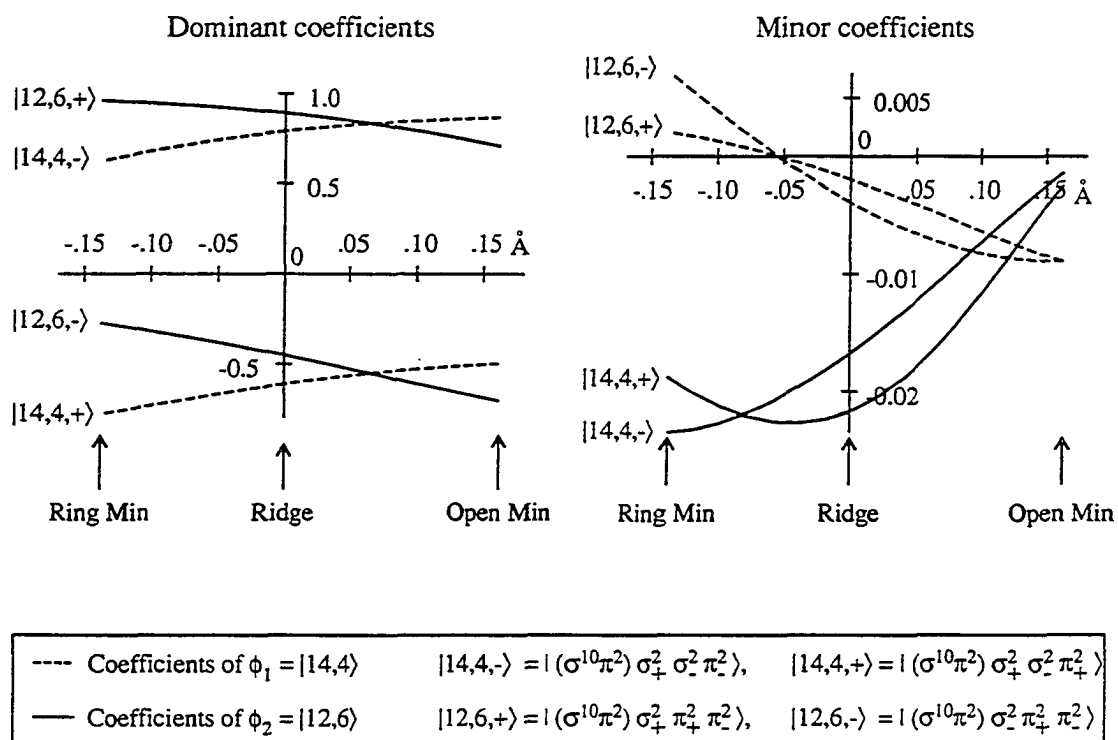


Figure 9. Variation of the coefficients of the diabatic states along the path between the ground state minima

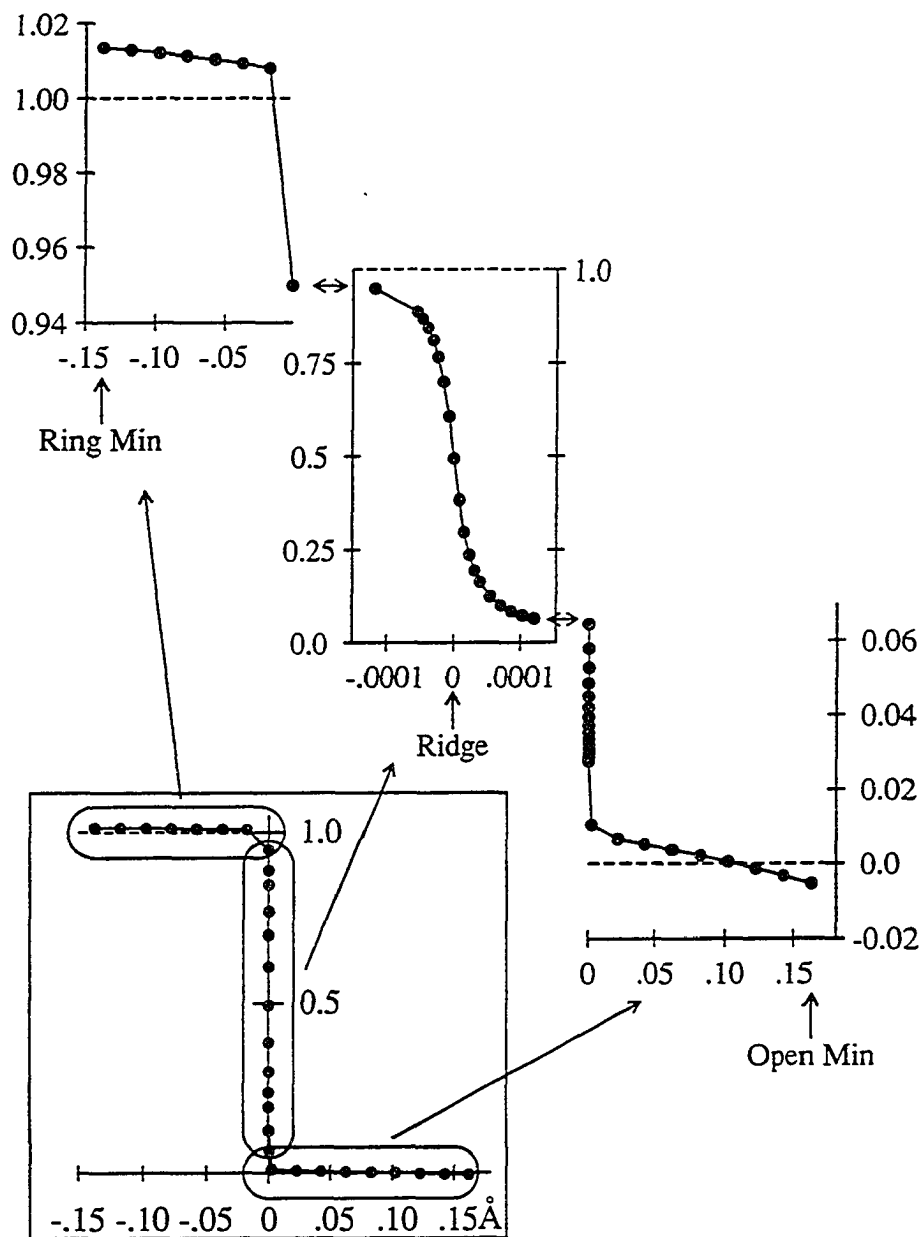


Figure 10. Angle of rotation from diabatic to adiabatic states along path between the ground state minima. Angles are in units of $\pi/2$. Distances from ridge are \AA .

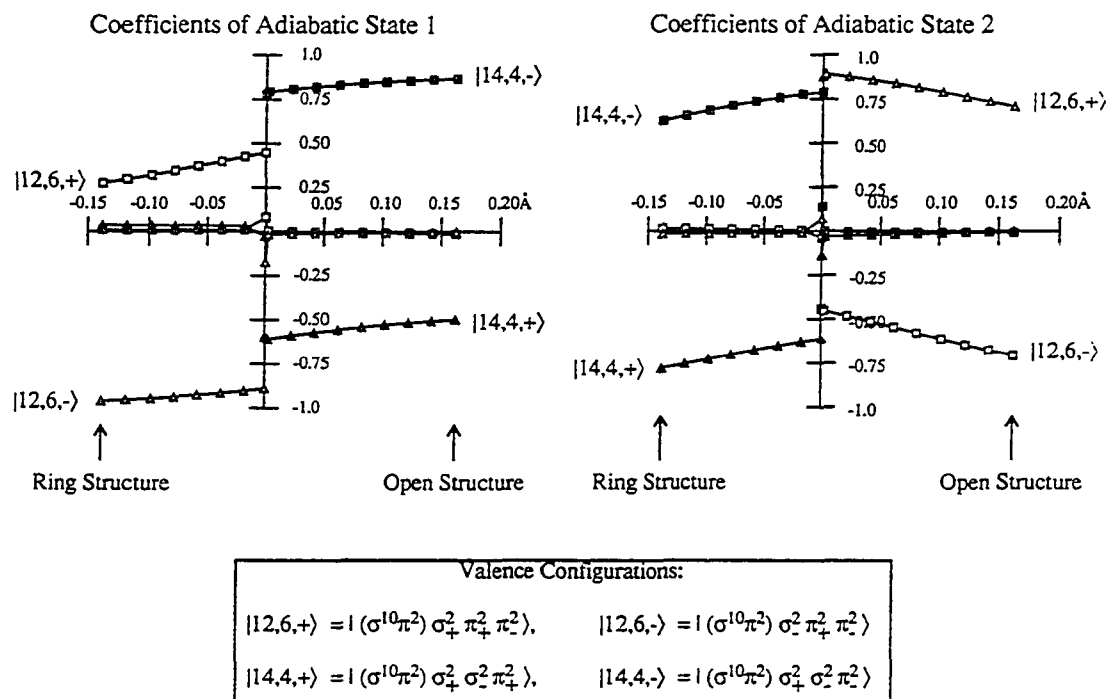


Figure 11. Variation of the coefficients of the adiabatic states along the path between the ground state minima

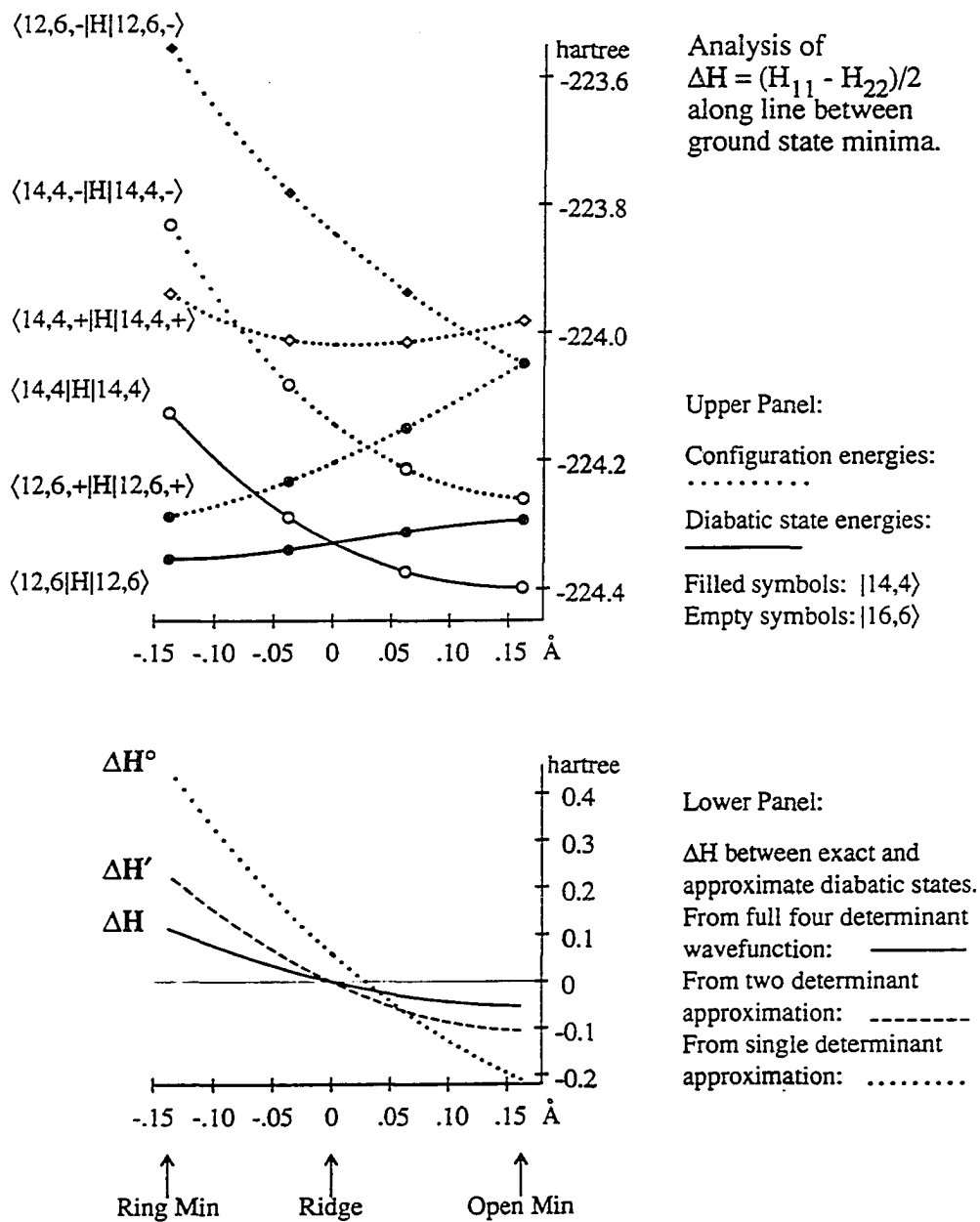


Figure 12. Decomposition of ΔH in terms of configurational contributions

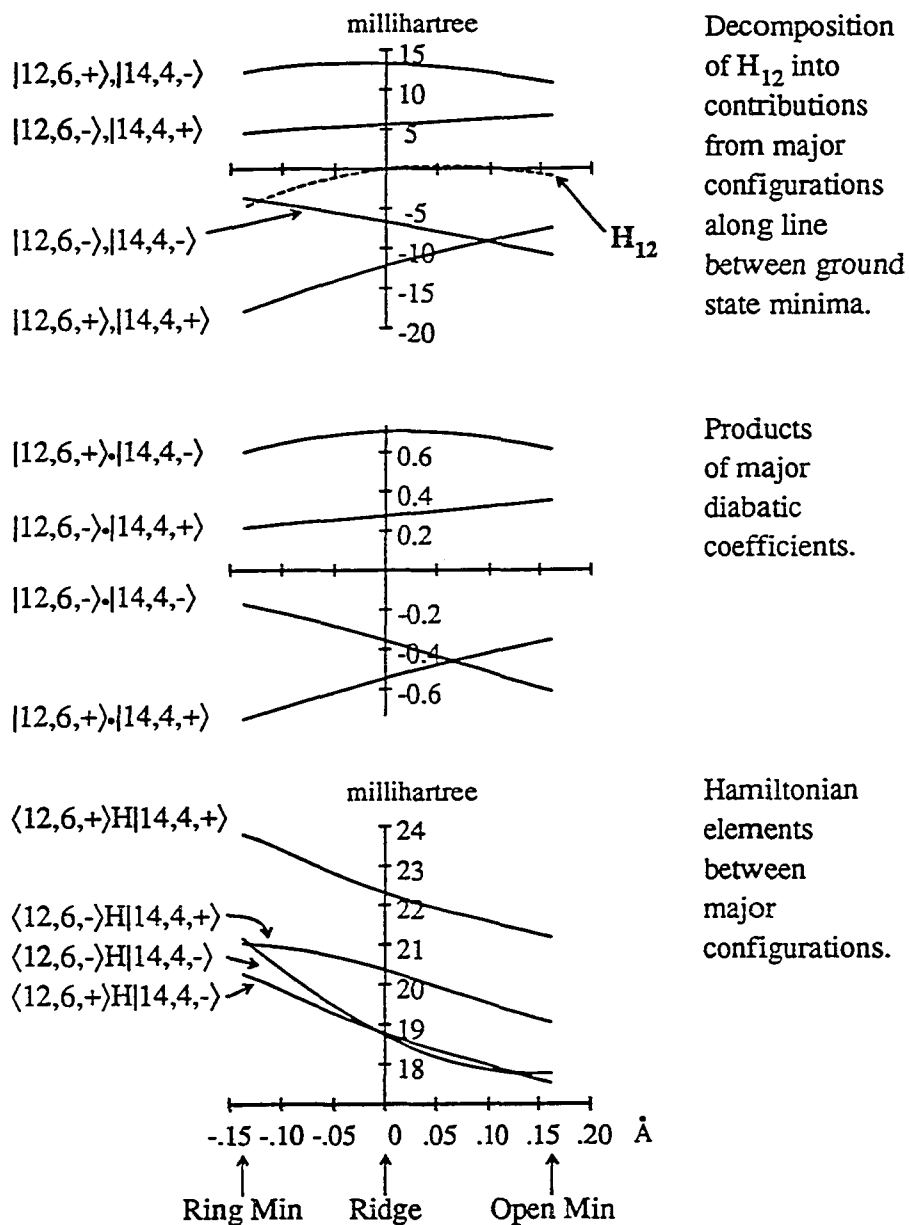


Figure 13. Decomposition of H_{12} in terms of configurational contributions

PAPER V. THE INTERSECTION SEAM BETWEEN THE $1^1A'$ AND $2^1A'$
STATES OF OZONE

THE INTERSECTION SEAM BETWEEN THE $1^1A'$ AND $2^1A'$
STATES OF OZONE

Ames Laboratory USDOE and Department of Chemistry
Iowa State University
Ames, IA 50011

ABSTRACT

The intersection seam between the two lowest ${}^1A'$ states of ozone has been determined in full. The potential energy surfaces and the seam are calculated and discussed in perimetric coordinates which exhibit the full three-dimensional symmetry. The seam is shown to form a closed curve which crosses the C_{2v} restricted coordinate planes at six points. Three of these correspond to the previously determined intersection, the starting point of the present search. The other three correspond to highly repulsive regions on the potential energy surface where two atoms approach each other to within $2/3$ of the O_2 bond length. At the former three points, both states have 1A_1 symmetry but, at the latter three points, one state has 1A_1 symmetry whereas the other has 1B_2 symmetry. Consequently, there exist three additional branches of the intersection seam between these two states. Each of these branches lies entirely in one C_{2v} restricted coordinate plane and connects to the aforesaid C_s -seam in one point. The existence of a further intersection seam is established. A novel method for determining intersection points is described.

1. INTRODUCTION

In recent investigations [1], we have found that the ground state of ozone has a point of degeneracy, a conical intersection, with the first excited state of like symmetry (1A_1) in the C_{2v} restricted two-dimensional internal coordinate space between the two ground state minima. We have also identified those features of the electronic structure which are responsible for this somewhat unusual phenomenon [2].

In view of the fundamental theory pertaining to conical intersections [3], it was apparent from the beginning that the point found would have to be a point on *a one-dimensional curve* along which the two states remain degenerate in the full three-dimensional internal coordinate space: *an intersection seam between the 1^1A_1 and the 2^1A_1 states*. Since, to our knowledge, there exist no previous examples of ab-initio determined *full* intersection seams, it seemed of general interest to map out this particular seam rather carefully in the full internal coordinate space of C_s symmetry. It was also an intriguing question whether the seam would be a closed curve or move out toward the dissociated species without closing.

In what follows we shall describe the methods we developed for following an intersection seam and the characteristics of the seam which was established.

2. ENERGY FUNCTIONS IN TERMS OF PERIMETRIC COORDINATES

2.1 Coordinate Space

For the present investigation, it is essential that all three nuclei be treated on an equal footing. To this end, we shall use *perimetric coordinates* which, previously, have been used by James and Coolidge [4], Pekeris [5], and Davidson [6]. We discuss relevant elements of these coordinates in some detail in a companion paper [7].

If r_{12} , r_{23} , r_{31} are the three internuclear distances, then the perimetric coordinates s_1 , s_2 , s_3 are defined by the formulas

$$s_i + r_{jk} = s = r/2 \quad (1)$$

$$s = s_1 + s_2 + s_3 \quad (2)$$

$$r = r_{12} + r_{23} + r_{31}. \quad (3)$$

They can be separated into the scale coordinate s and the angle-dependent, but scale-independent shape-coordinates ξ_1 , ξ_2 which are related to (s_1, s_2, s_3) by

$$\begin{aligned} s_1 &= s (-\xi_1/\sqrt{2} - \xi_2/\sqrt{6} + 1/3) \\ s_2 &= s (\xi_1/\sqrt{2} - \xi_2/\sqrt{6} + 1/3) \\ s_3 &= s (\quad \quad \quad 2\xi_2/\sqrt{6} + 1/3) \end{aligned} \quad (4)$$

The parameter space of the shape coordinates (ξ_1, ξ_2) covers an equilateral triangle whose dimensions are displayed in Figure 1, where some special points and regions are indicated as well. Also useful are the coordinates

$$x_1 = s\xi_1, \quad x_2 = s\xi_2, \quad x_3 = s/\sqrt{3} \quad (5)$$

which, by virtue of Eq. (4), are related to (s_1, s_2, s_3) through an orthogonal transformation that places the x_3 -axis along the first-octant diagonal of the s_1, s_2, s_3 axis system. In order to fully appreciate and visualize the meaning of these coordinates, the reader should consult the explicit discussion in reference [7] which also clarifies the following statements.

When the shape coordinates fall on one of the perpendiculars from one corner of the triangle in Figure 1, through the center, on to the opposite side, then two internuclear distances are equal and this remains true in the entire plane spanned by this perpendicular line and the x_3 axis. E.g., for all points with $\xi_1=0$, be they on the ξ_2 axis in Figure 1 or in the plane spanned by x_2 and x_3 , the molecule is isosceles, with nucleus 3 at the apex. The center point, $\xi_1=\xi_2=0$, as well as all points on the x_3 axis, correspond to equilateral molecules.

Two points in the shape-coordinate triangle, which are related to each other by reflection with respect to the perpendicular from corner (i) in Figure 1 to the opposite side ($j-k$), describe two molecules which are obtained from each other by permuting atoms j and k and, hence, their shapes are each other's mirror images with respect to any reflection plane normal to the line connecting nuclei j and k .

2.2 Energy Surfaces for Homonuclear Triatomic Molecules

Since ozone is a homonuclear molecule, its potential energy surface (PES) must be invariant with respect to all permutations of its nuclei. By virtue of what has been said in the preceding section, it is readily seen that this invariance implies the invariance of the potential energy surfaces with respect to the symmetry operation of the group C_{3v} , *if applied in the parameter space of the perimetric coordinates*, with the C_3 axis along the x_3 coordinate axis and the three planes of symmetry being the planes spanned by the x_3 axis and the normals from the corners of the shape-coordinate triangle of Figure 1 on to the opposite sides. Each PES can therefore be generated from its values in 1/6 of the entire coordinate space. The projection of this part onto the shape coordinate plane is shaded in Figure 1. It follows, furthermore, that the planes spanned by the x_3 axis and the normals from the corners of the coordinate triangle of Figure 1 on to the opposite sides, i.e. the symmetry planes of C_{3v} in the parameter space, contain the coordinates of all those molecules which possess C_{2v} symmetry. We shall therefore call these planes the C_{2v} -restricted coordinate spaces. The x_3 axis, i.e. the C_3 axis of C_{3v} in parameter space, corresponds to all molecules with D_{3h} symmetry.

The intersection seam is a curve in the three-dimensional coordinate space. Since it runs on potential energy surfaces, it too is invariant under the

operations of C_{3v} in the parameter space and it, too, can be generated in full after having found 1/6 of it. It also follows from this symmetry that such a seam must penetrate each of the symmetry planes of the C_{3v} group in the parameter space at right angles.

We shall display the intersection seam by exhibiting (i) a plot of its projection in the (ξ_1, ξ_2) -plane inside the triangle of Figure 1, (ii) a plot graphing the variation of $s=x_3\sqrt{3}$ along the just mentioned projection curve, and (iii) a plot of the intersection energy E along the same curve. By virtue of the discussed symmetry properties, the projection in the (ξ_1, ξ_2) plane must perpendicularly cross the normals from the corners of the triangle in Figure 1 onto the opposite sides, and the plots of s and E must have horizontal slopes at the points of crossing these C_{2v} restricted coordinate spaces. These symmetry properties apply regardless of whether the intersection seam is a closed or an open curve.

3. DETERMINATION OF THE SEAM

3.1 Point to Point Extrapolation

In the previous investigations [1], [2] we had established the intersection point in C_{2v} symmetry. Because of the three-fold symmetry of the PES, this result yields in fact three intersection points in the coordinate space which are shown in Figure 1 as I_1, I_2, I_3 . Also shown are the positions of the four minima M_0, M_1, M_2, M_3 . The x_3 coordinates, which are not shown, are given by the scale parameters with the values

$$s(I_1) = 2.456\text{\AA}, \quad s(M_0) = 2.214\text{\AA}, \quad s(M_i) = 2.412\text{\AA}, \quad (i \neq 0).$$

We started the determination of the intersection seam at the point I_3 , which has the coordinates

$$x_1^{(0)} = 0, \quad x_2^{(0)} = -0.392\text{\AA}, \quad x_3^{(0)} = 1.418\text{\AA}.$$

Since, as explained above, the seam must cross the x_2 - x_3 plane at a right angle, a reasonable first guess for the next point on the seam is

$$x_1^{(1)} = \varepsilon, \quad x_2^{(1)} \approx x_2^{(0)}, \quad x_3^{(1)} \approx x_2^{(0)},$$

and a reasonable search surface for the *exact* next seam point is the plane $x_1^{(1)} = \varepsilon = \text{constant}$. A search, to be described below, on this plane around the predicted guess yielded then the actual intersection point $(x_1^{(1)}, x_2^{(1)}, x_3^{(1)})$. Because of the symmetry of the seam with respect to the plane $x_1 = 0$, this calculation also yielded a third intersection point, namely:

$$x_1^{(-1)} = -\varepsilon, \quad x_2^{(-1)} = x_1^{(1)}, \quad x_3^{(-1)} = x_3^{(1)}.$$

From here on, the initial guess for each additional seam point was determined by a quadratic extrapolation from the preceding three seam points. The coefficients a to f in the expressions

$$x_2 = a + bx_1 + cx_1^2$$

$$x_3 = d + ex_1 + fx_1^2$$

were determined by a fit to the points (n), (n-1), (n-2) of the seam and then used to predict the values of $x_2^{(n+1)}$ and $x_3^{(n+1)}$ for $x_1^{(n+1)} = x_1^{(n)} + \varepsilon$. The *exact* values of $x_2^{(n+1)}$ and $x_3^{(n+1)}$ were then again determined by searching for the intersection point in the plane $x_1^{(n+1)} = x_1^{(n)} + \varepsilon = \text{constant}$.

Approximately, the same value of about $\varepsilon = 0.02 \text{ \AA}$ was used for the increments at the various points unless difficulty was encountered. We were prepared to change the extrapolation variable from x_1 to some linear combination of x_1 , x_2 , x_3 , and, correspondingly, the choice of the search plane, in case that the intersection seam should curve away significantly from the x_1 direction. Such a change proved however unnecessary because the seam was found to stay remarkably close to parallel to the x_1 axis.

While the initial point of the seam corresponds to a molecule with C_{2v} symmetry, the molecular symmetry is lowered to C_s for the new points on the seam so that the calculations involve more work. However, after having passed through the shaded region of Figure 1, the seam reaches again a point

where the molecule has C_{2v} symmetry. This endpoint can therefore be rechecked by an independent calculation using C_{2v} symmetry.

3.2 Planar Search by Minimizing $(E_2-E_1)^2$

Because of the conical nature of the intersection [3], the difference between the two potential energy surfaces, (E_2-E_1) , cannot be fit by a quadratic, but its square, $(\Delta E)^2$, can. We therefore calculated E_1 and E_2 on each plane $x_1=\text{constant}$ for a grid around the initial guess, fit a quadratic to the $(\Delta E)^2$ values on this grid, determined the minimum, recalculated E_1 and E_2 on a finer grid around this minimum, and proceeded in the same manner until the energy separation at the minimum was reduced to less than half a microhartree.

This procedure, which is analogous to the one used in our previous work [1] to determine the initial point I_3 , proved quite straightforward. It is not overly efficient regarding the number of energy calculations needed and could be considerably improved by using a quasi-Newton procedure with the analytical gradients $\nabla(E_1-E_2)^2 = 2(E_1-E_2)(\nabla E_1-\nabla E_2)$. Such algorithms have been employed by Yarkony [8]. However, the procedure *cannot* prove *conclusively* that the two surfaces, in fact, do become *exactly* degenerate. This shortcoming is overcome by the following method which has not been used previously.

3.3 Corralling an Intersection Point

According to the phase theorem of Herzberg-Longuet-Higgins-Berry [3], both wavefunctions ψ_1 and ψ_2 change sign when deformed continuously on a closed path looping around an intersection. In our previous investigation [1], we used this theorem as a test to prove the existence of a true intersection between the two 1^1A_1 states in C_{2v} : if there were no true intersection, neither function would change sign. We shall now show how this approach can be adapted for the accurate determination of the location of an intersection once its approximate position is known.

An obvious approach is as follows. First, calculate ψ_1 and ψ_2 on a closed path around the suspected point of intersection. If the wavefunctions do not change sign, find another guess at the intersection until the wavefunctions do change sign. Next calculate ψ_1 and ψ_2 along a line connecting opposite sides of the loop, thereby in effect creating two loops each containing about half the area of the original loop. One of the two loops created will contain the intersection and, hence, exhibit the sign changes in ψ_1 and ψ_2 . The other will not. Then, proceed to cut the loop with the intersection in half and repeat the procedure. Successive repetitions of this bisection will decrease the size of the loops until the desired accuracy is reached.

This approach can, however, be considerably refined by a closer

analysis of the phase change. It is known [3] that the adiabatic states ψ_1, ψ_2 can be expressed in terms of two diabatic states ϕ_1, ϕ_2 by the orthogonal transformation

$$\begin{aligned}\psi_1 &= \phi_1 \cos(\alpha/2) + \phi_2 \sin(\alpha/2) \\ \psi_2 &= -\phi_1 \sin(\alpha/2) + \phi_2 \cos(\alpha/2)\end{aligned}\tag{6}$$

where the angle α is obtained from the diabatic matrix elements $H_{ij} = \langle \phi_i | H | \phi_j \rangle$ and $\Delta H = H_{11} - H_{22}$, by the equations

$$\cos(\alpha) = \Delta H / (\Delta H^2 + H_{12}^2)^{1/2}\tag{7}$$

$$\sin(\alpha) = H_{12} / (\Delta H^2 + H_{12}^2)^{1/2}\tag{8}$$

An intersection occurs when ΔH and H_{12} both change signs [3]. Figure 2 exhibits a schematic diagram of the coordinate space near an intersection. The difference ΔH changes sign along the curve $\Delta H=0$, the off-diagonal element H_{12} changes sign along the curve $H_{12}=0$. Also shown is a closed path looping around the intersection of these two curves, which is, in fact, the point of degeneracy between the two energy surfaces.

It is known that, in regions I and II, the diabatic state ϕ_1 dominates in ψ_1 , and the diabatic state ϕ_2 dominates in ψ_2 , whereas the reverse is true in regions III and IV. (Concomitantly $\Delta H=0$ is a line of avoided crossings, except that at the intersection one has a real crossing). Consequently, and in agreement with Eq. (7), one observes a *changeover in the dominant configurations* in ψ_1 and in ψ_2 along the closed path *whenever it crosses the curve $\Delta H=0$* . On the other hand, it follows from Eq. (8) that $\sin\alpha$ will change

sign whenever H_{12} changes sign. It follows then from Eq. (6) that the *small coefficients* in the adiabatic states, i.e. those which are *not* dominant in ψ_1 and ψ_2 , change sign where H_{12} changes sign. We have observed these connections explicitly in a previous paper [1].

By virtue of these relationships, the overall sign change in the wavefunction ψ_1 , say, comes about as a result of the individual changes illustrated in the following scheme:

	Region I	Region II	Region III	Region IV	Region I
Coeffs. of ϕ_1 in ψ_1	Large	Large	Small	-Small	-Large
Coeffs. of ϕ_2 in ψ_1	Small	-Small	-Large	-Large	-Small
	$H_{12}=0$	$\Delta H=0$	$H_{12}=0$	$\Delta H=0$	

By carefully monitoring the major and the minor configurations, it is therefore possible to obtain an approximate idea where the loop around the intersection crosses the lines $\Delta H=0$ and $H_{12}=0$. The intersection of the lines connecting these opposite points on the loop will then yield an approximation to the intersection.

The case at hand is a particularly favorable one, since ϕ_1 and ϕ_2 contain doubly occupied dominant configurations so that the sign changes of

the diabatic as well as the adiabatic wavefunctions are identical with the sign changes in the *coefficients of these configurations* [1] and, hence, are easy to spot.

The method is illustrated in Figure 3 for the determination of the intersection point in C_{2v} symmetry. The *left* hand panels of each figure display increasingly smaller paths in coordinate space looping around the intersection point in C_{2v} symmetry. The coordinates in the upper left hand panel of Figure 3a are the cartesian x,y internal coordinates used previously (Figure 3 of reference [1]), while the coordinates on the other two left hand panels on Figure 3a have been rotated by 31° . The coordinates of the top left panel of Figure 3b have been rotated by 32° and the other two panels at left were rotated by 33° . The solid dots in each left hand panel mark the points on the loops where the wavefunctions were calculated. The *right* hand panels show the magnitudes of the coefficients of the three configurations which are dominant in one state or the other, calculated *at the points marked at left*. The abscissa of each panel at right simply numbers the points on the corresponding panel at left sequentially. The points where the loop crosses the line $\Delta H=0$ can be identified as the regions where the large coefficients exchange dominance with the small ones and the crossing of the loop with the line $H_{12}=0$ occurs where the small coefficients change sign. The boundaries of these crossings are marked by pairs of small tick marks on the

abscissas of the right panels (with generous room for error). The numbered points on the left panels correspond to these tick marks. These points, on opposite parts of the loop, are connected by straight lines. The lines going more or less vertically are expected to bracket the curve $\Delta H=0$ whereas the lines going more or less horizontally are expected to bracket the curve $H_{12}=0$. Guided by these lines, the corners for a smaller loop are estimated and indicated by letters inside each panel. These letters appear then at the corners of the loop on the next panel. In 6 iterations, the loop has been reduced from a $0.2\text{\AA}\times 0.2\text{\AA}$ box to a $0.0004\text{\AA}\times 0.00003\text{\AA}$ box (in the rotated coordinates), whereas, using the divide-by-2 method, six iterations would only reduce the size of the box to $0.2/2^5=0.00625\text{\AA}$. There exist various ways in which the convergence of this procedure could be accelerated.

4. THE INTERSECTION SEAM OF THE $1^1A'$ AND THE $2^1A'$ STATES

4.1 Ab-Initio Procedure

The full intersection seam of the two lowest $1^1A'$ states of ozone in C_s symmetry was determined using a two-state-averaged FORS wavefunctions, with the active space consisting of all 2p orbitals on all three oxygen atoms, giving 1292 configurations of symmetry C_s . The two states were given equal weight in the averaging procedure. The basis set was of the generally-contracted double-zeta type, *viz.* (11s6p1d/3s2p1d). The s and p exponents were taken from Dunning's VQZ basis set [9]. The 1s, 2s, and 2p contractions were the SCF orbitals, while the 3s and 3p orbitals were simply the most diffuse gaussians of each set. The d orbital set had an exponent of 1.185, the one used by Dunning in his VDZ basis set. All calculations were made with the program MOLPRO of Werner and Knowles [10].

4.2 The Intersection Seam in C_s Symmetry

The intersection seam is depicted in Figures 4 and 5. Figure 4 displays the projection of the seam path on the plane of the shape coordinate ξ_1, ξ_2 . Figure 5 shows the variation along the seam for the molecular circumference (r) which is related to x_3 according to Eqs. (1) and (5). The points A through C on Figure 4 are the uniquely calculated points, the rest of

the seam was generated by symmetry. The point marked C is the actual starting point in the calculations. It is the location of the previously reported intersection point I_3 in C_{2v} symmetry, very near the transition point between the two minima on the lower surface (marked M_0 and M_1 in the figure). *It is apparent from Figure 4 that the seam is a closed path.* It intersects each of the three C_{2v} lines in two points: The points C, F, H are the originally known points I_1, I_2, I_3 ; the points A, E, G are the new points. Figure 6 illustrates the variation of the molecular shape along the seam path. Point C is in the center, with the 116° apex angle of the isosceles molecules at the top. As the molecule moves along the path toward point A the top atom moves down and to the right, closing in on the lower right hand atom until a new C_{2v} axis appears, now bisecting the two atoms at right. Table 2 lists the bond lengths for the points M, C, and A. Because of the very short bondlength of r_{23} at point A and the correspondingly small bond angle at atom 1 (about 35°), the

Table 2. Bond Lengths of Ozone at Various Geometries

	r_{13}	r_{23}	r_{12}
Point M	1.305	1.305	2.214
Point C	1.477	1.477	1.957
Point A	1.563	0.940	1.563

molecule is obviously very unstable at this geometry. The energy along the seam is displayed in Figure 7. It confirms that the C_{2v} intersections A, E, G lie in a highly repulsive region of the PES. The repulsive character in the region of point A is also illustrated by Figure 8 which shows a projection of the intersection seam on the PES contour map for the circumference $r=4.6\text{\AA}$, which is about midway on the seam. Even for this constant value of r , the energy difference between the two different C_{2v} points is about 2.2eV. Because of the variation in r , shown in Figure 5, the difference between points A and C in Figure 7 is in fact about 12eV.

The points at which the intersection seam is actually determined are marked by dots on the abscissa of Figure 7.

4.3 The Intersection Seam in C_{2v} Symmetry

In C_s symmetry there are two irreps: A' (symmetric with respect to the molecular plane) and A'' (antisymmetric with respect to the molecular plane). The two irreps of C_{2v} , labelled A_1 and B_2 are compatible with the A' irrep of C_s while the A_2 and B_1 irreps of C_{2v} correspond to the A'' irrep on C_s . Since the original crossing at point C, in C_{2v} symmetry, was between the 1^1A_1 and 2^1A_1 states, these two states become the states $1^1A'$ and $2^1A'$ when the seam enters C_s symmetry. However, upon return to C_{2v} symmetry at point A, *only one of the two states is found to return to 1A_1 , the other turns out*

to become 1B_2 . At this point A, the intersection is thus *not* between two states of *like* symmetry, but between two states of *different* symmetry.

Because the off-diagonal element H_{12} between the diabatic states vanishes automatically between two such states, there exists only *one* crossing condition, namely $\Delta H=0$ (see text after Eq (8) above). Since the C_{2v} restricted molecule has two degrees of freedom, the intersection subspace between 1A_1 and 1B_2 in C_{2v} is therefore of dimension $2-1=1$ (see reference [3]). Hence, there exists *another one-dimensional intersection seam* between the states we are considering, one which is constrained to lie entirely in C_{2v} , and which also passes through point A. The seam in C_s which was displayed in Figure 4 must then connect with this C_{2v} constrained seam at right angles at point A. This is confirmed by Figure 9 which shows contours of the energy difference between the 1A_1 and the 1B_2 states in the C_{2v} plane near point A. The dashed contours indicate where 1B_2 is lower in energy and the solid contours indicate where 1A_1 is lower. The solid line is the intersection seam between the two states in C_{2v} . The large dot marks the point A where the intersection seam, which we determined in C_s , extrapolates to the C_{2v} coordinate plane. It is seen to fall exactly on the independently determined 1A_1 - 1B_1 intersection seam.

It is obvious that entirely equivalent situations must exist in the other two C_{2v} restricted coordinate spaces which are obtained through rotations by

$\pm 120^\circ$ around the x_3 axis. We have not explored the full extent of the intersection seam between the 1^1A_1 and 1^1B_2 states since it lies in a dynamically rather inaccessible region of the C_{2v} coordinate space. Two possibilities for these additional seams are schematically sketched in Figure 10, an open seam and a closed seam. This figure displays all four branches of the entire seam: The branch in C_s is denoted by S_0 , the three C_{2v} branches are denoted by S_1, S_2, S_3 .

4.4 Orbital Interpretation of the Symmetry Change

The symmetry change of one of the two states from A_1 at point A of Figure 4 to B_2 at point C can be understood by the following reasoning in terms of orbital stabilities.

In C_s , the FORS wavefunction is constructed from 12 σ -type MO's, belonging to the irrep A' and 3 π -type MO's, belonging to the irrep A'' . It is found that, along the entire seam and for both states, 9 natural orbitals of A' symmetry (three core and six valence orbitals) maintain near-constant double occupancy, whereas two natural orbitals of this symmetry remain effectively empty throughout. In addition, one natural orbital of A'' symmetry maintains near-double occupancy along the entire seam. This leaves three orbitals whose occupancies vary significantly in going from point C to point A, namely

$$\sigma = |10a'\rangle, \pi_1 = |2a''\rangle, \pi_2 = |3a''\rangle$$

Figure 11 exhibits plots of the three orbitals for three points along the seam. The σ orbitals are plotted in the molecular plane, the π orbitals are plotted in a plane above and parallel to the molecular plane. At further intermediate points, the analogous plots look similar. The orbital symmetries are also given in these plots. It may be noted that, because of a degeneracy in the occupation numbers in both states at point A (see below), the two π orbitals can be arbitrarily superimposed and, thereby, two orbitals similar to those at the intermediate point can be generated. The orbitals plotted are the MCSCF optimized orbitals.

In Figure 12, we show the variations of natural orbitals (which are almost identical with the plotted MCSCF optimized orbitals) along the seam in going from point C to point A. The label INT indicates the point on the seam to which the intermediate orbitals of Figure 11 belong. The solid lines represent the occupations of state 1, the dashed lines those of state 2. As was mentioned earlier, the calculated states are not exactly degenerate, but differ by about 0.5 microhartree. This difference is sufficient to maintain the character of the two wavefunctions so that the orbital occupations do follow non-erratic, continuous curves. We denote the lower state as "state 1" and the higher state as "state 2".

For state 1, one recognizes the following occupation changes. In going

from point C to point A, the orbitals π_1 and π_2 each lose one electron and both electrons go into the orbital σ . The presumed reason is that σ manifestly changes from an antibonding to a bonding orbital whereas the π_1, π_2 set changes from slightly anti-bonding to more strongly anti-bonding. State 2 exhibits a compensating charge shift in the opposite direction which is attributable to the maintenance of orthogonality between the two states.

The dominant configuration of both states are listed in Table 3. It is

Table 3. Dominant configurations of the $1^1A'$ and $2^1A'$ states

Configuration	Point C		Point A	
	State 1	State 2	State 1	State 2
(core) $\sigma^0 \pi_1^2 \pi_2^2$	-0.85	-0.02	-0.16	0.93
(core) $\sigma^2 \pi_1^2 \pi_2^0$	0.01	0.75	0.00	0.00
(core) $\sigma^2 \pi_1^0 \pi_2^2$	0.04	-0.54	0.00	0.00
(core)* $\sigma^2 \pi_1^2 \pi_2^2$	0.41	0.00	0.00	0.00
(core) $\sigma^2 \pi_1^1 \pi_2^1$	0.00	0.00	0.91	0.16

(core) = eleven doubly occupied σ -type orbitals and one doubly occupied π -type orbital.

(core)* = ten doubly occupied σ -type orbitals and one doubly occupied π -type orbital.

seen that the single occupation of orbitals π_1 and π_2 in state 1 at point A result from a configuration in which both these orbitals are singly occupied so that the wavefunction of state 1 belongs indeed to the irrep $A_2 \otimes B_1 = B_2$. At point C it manifestly belongs to the irrep A_1 . State 2, however, has only

dominant configurations with doubly occupied orbitals throughout, so that it always belongs to the irrep A_1 .

4.5 Another Intersection Seam of the 1^1A_1 state

In the course of the present work, it was noticed that, in the C_{2v} restricted space near the point A, the state 1^1A_1 comes very close to *another* 1^1A_1 state ($3^1A_1'$). Minimization of ΔE^2 and use of the phase-change theorem of Herzberg-Longuet-Higgins-Berry proved that these two states of like symmetry also intersect in C_{2v} symmetry. This point is marked with an asterisk in Figure 5. It lies approximately 25 millihartree higher in energy than the intersection point A. From the general dimensionality rules follows that there may exist another 1-dimensional intersection seam involving the $1^1A_1'$ state, leading into C_s symmetry from this new intersection point.

5. CONCLUSIONS

The intersection seam between the lowest two ${}^1A'$ states of ozone has a multi-connected structure. It consists of four branches S_0, S_1, S_2, S_3 which are connected through four knots as illustrated in Figure 11. The knots and the three C_{2v} restricted branches S_1, S_2, S_3 lie, however, in a highly repulsive part of the potential energy surface. On the other hand, a large part of the branch S_0 , in C_s symmetry, lies at relatively low energies and offers opportunities for radiationless transitions. The S_0 branch cuts through C_{2v} symmetry at two kinds of points. At the low energy C_{2v} points, both states have 1A_1 symmetry but, at the high-energy C_{2v} points (the knots), one state has 1A_1 symmetry whereas the other has 1B_2 symmetry. This change is due to changes in orbital stabilities along the seam.

Intersections with further surfaces exist.

The method of "corralling an intersection", by identifying the curves on which the diabatic ΔH and H_{12} vanish, through monitoring the sign and magnitude changes of the dominant coefficients of the adiabatic states, deserves further attention.

REFERENCES

1. S. Xantheas, G. J. Atchity, S. T. Elbert, and K. Ruedenberg, *J. Chem. Phys.*, **94**, 8054 (1991).
2. G. Atchity and K. Ruedenberg, to be submitted.
3. a. G. Herzberg and H. C. Longuet-Higgins, *Discuss. Faraday Soc.* **35**, 77 (1963); see also M. V. Berry, *Proc. R. Soc. London, Ser. A* **344**, 147 (1975); C. A. Mead, *J. Chem. Phys.* **70**, 2276 (1979); C. A. Mead and D. G. Truhlar, *ibid.* **70**, 2284 (1979).
b. G. J. Atchity, S. S. Xantheas, and K. Ruedenberg, *J. Chem. Phys.* **95**, 1862 (1991).
4. A. S. Coolidge and H. M. James, *Phys. Rev.* **51** 855 (1937).
5. C. L. Pekeris, *Phys. Rev.* **112** 1649 (1958).
6. E. R. Davidson, *J. Am. Chem. Soc.* **99** 397 (1977).
7. G. Atchity and K. Ruedenberg, to be submitted.
8. M. R. Manaa and D. R. Yarkony, *J. Chem. Phys.* **93** 4473 (1990); see also N. Joga and K. Morokuma, *Chem. Phys. Lett.* **119** 371 (1985).
9. T. H. Dunning, Jr., *J. Chem. Phys.* **90**, 1007 (1989).
10. H.-J. Werner and P. J. Knowles, *J. Chem. Phys.* **82**, 5053 (1985); *Chem. Phys. Lett.* **115**, 259 (1985).

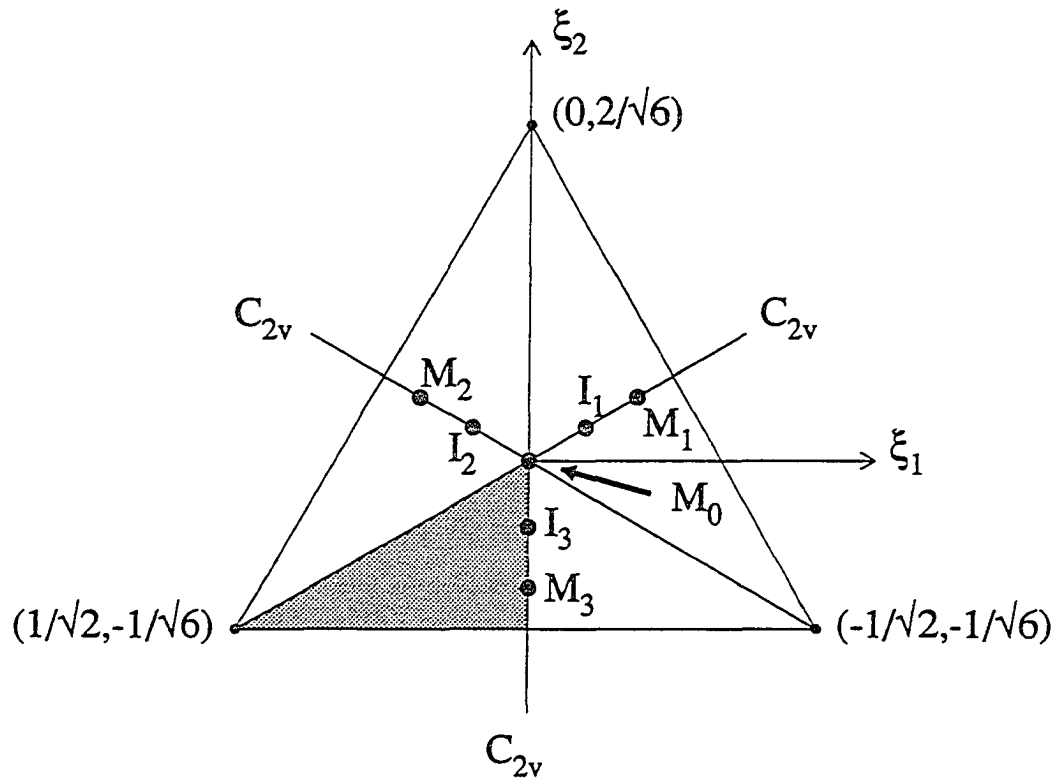


Figure 1. Parameter space of the scale-independent shape coordinates

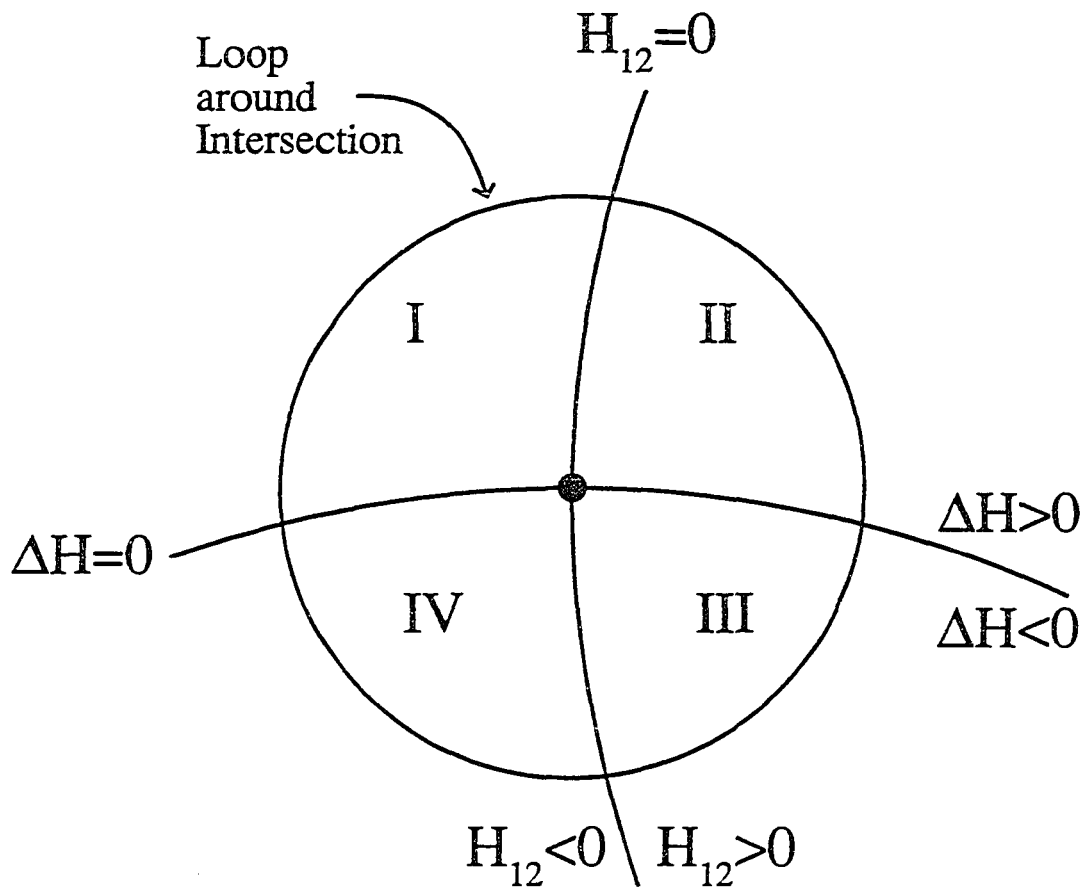


Figure 2. Schematic diagram of branching coordinate space near an intersection

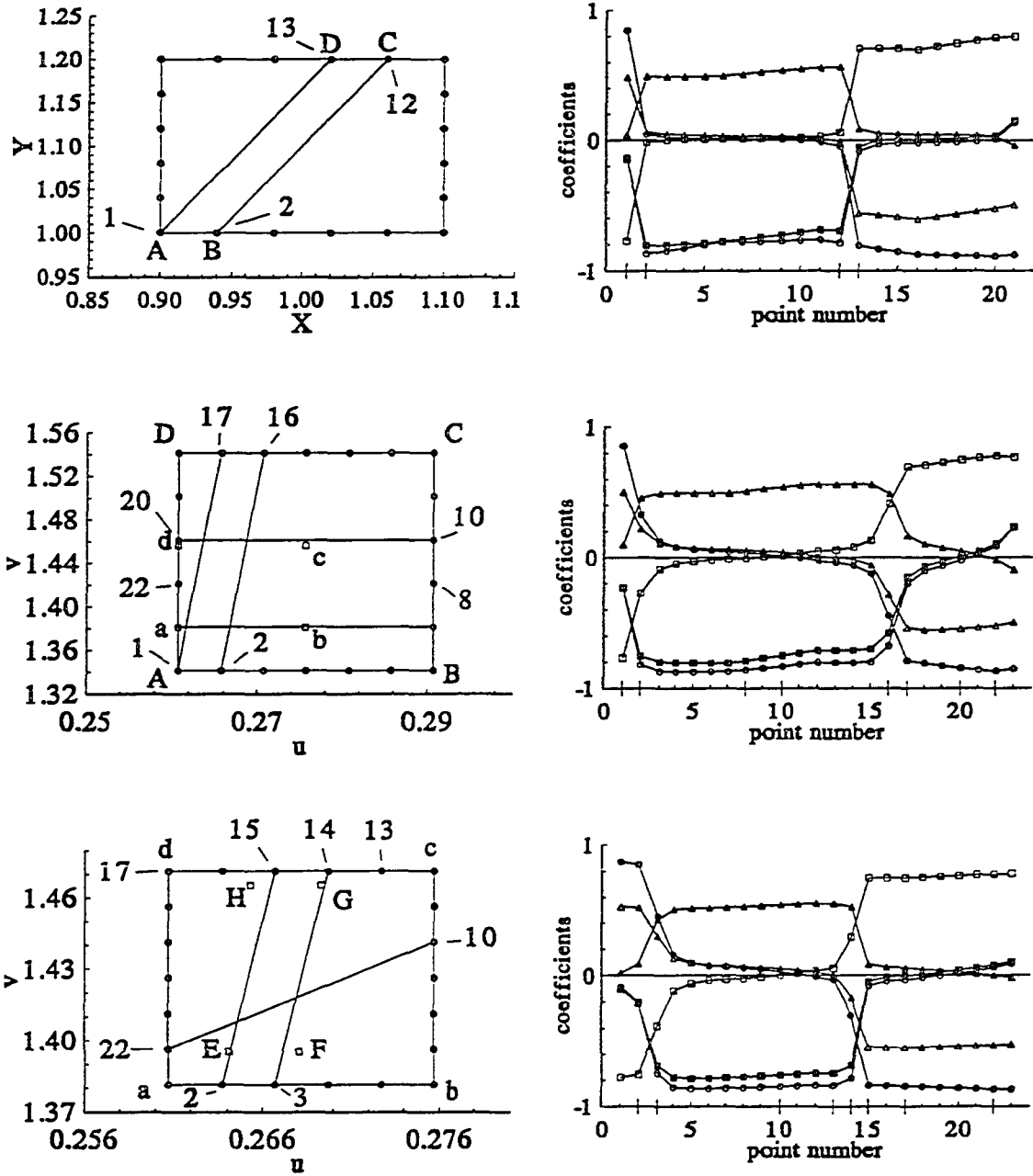


Figure 3. Corraling an intersection. a) the first three loops

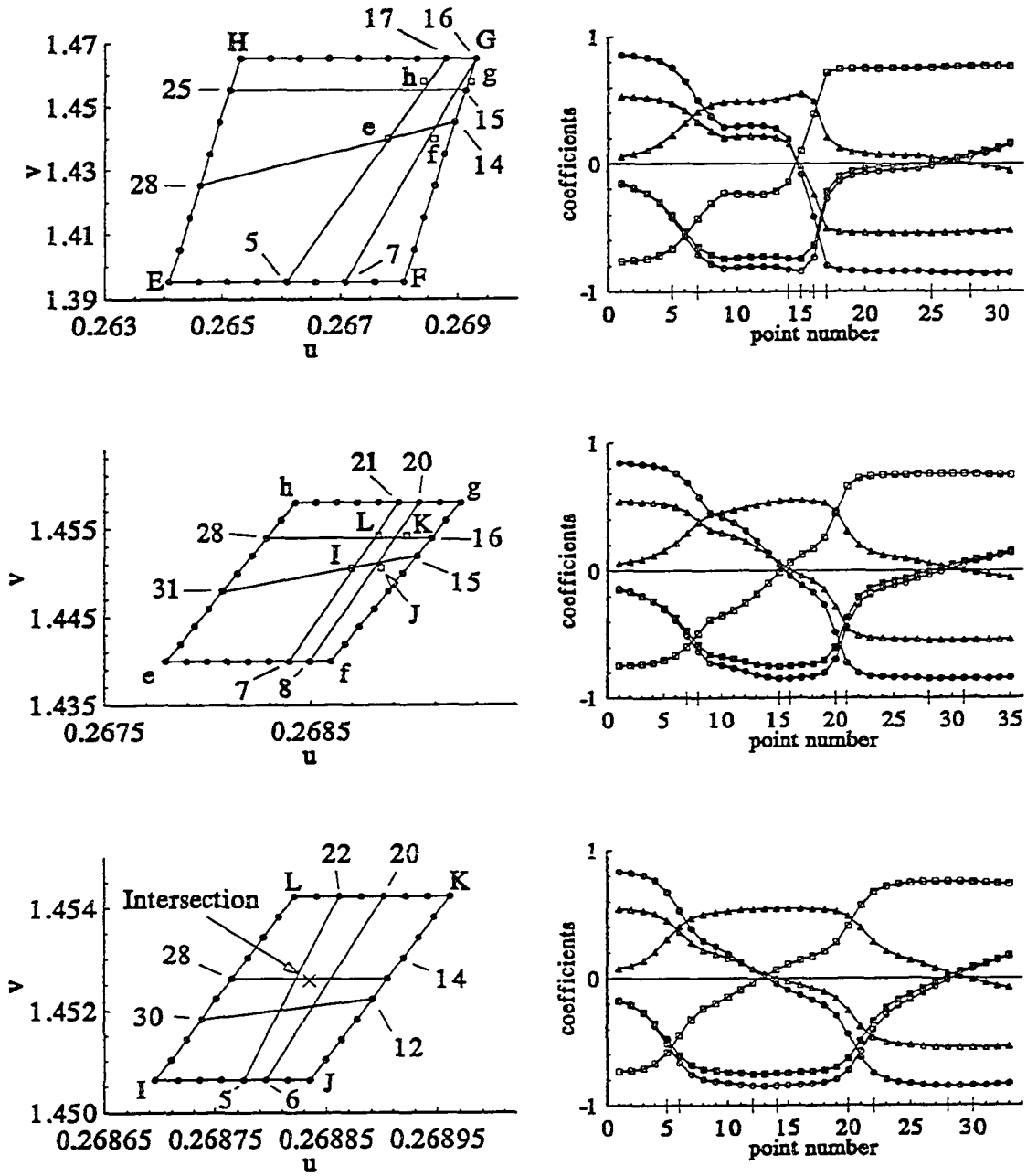


Figure 3. continued; b) the last three loops

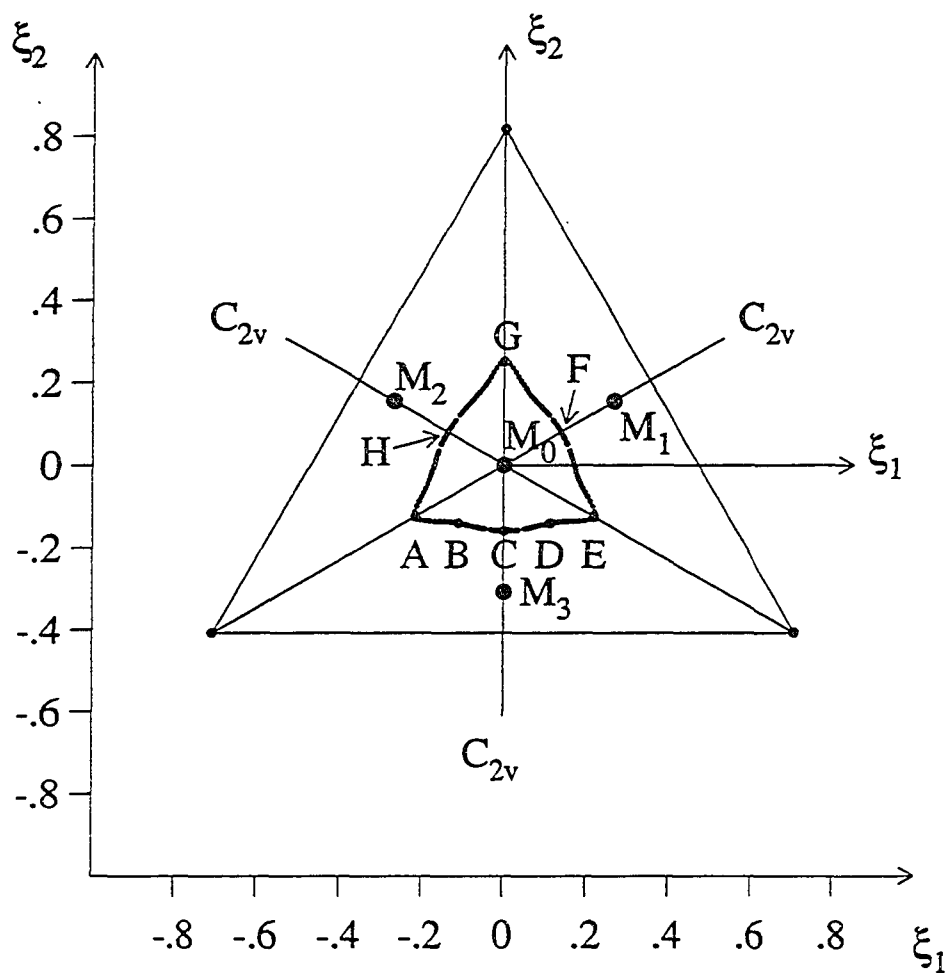


Figure 4. Projection of the intersection seam onto the scale-independent shape coordinate space

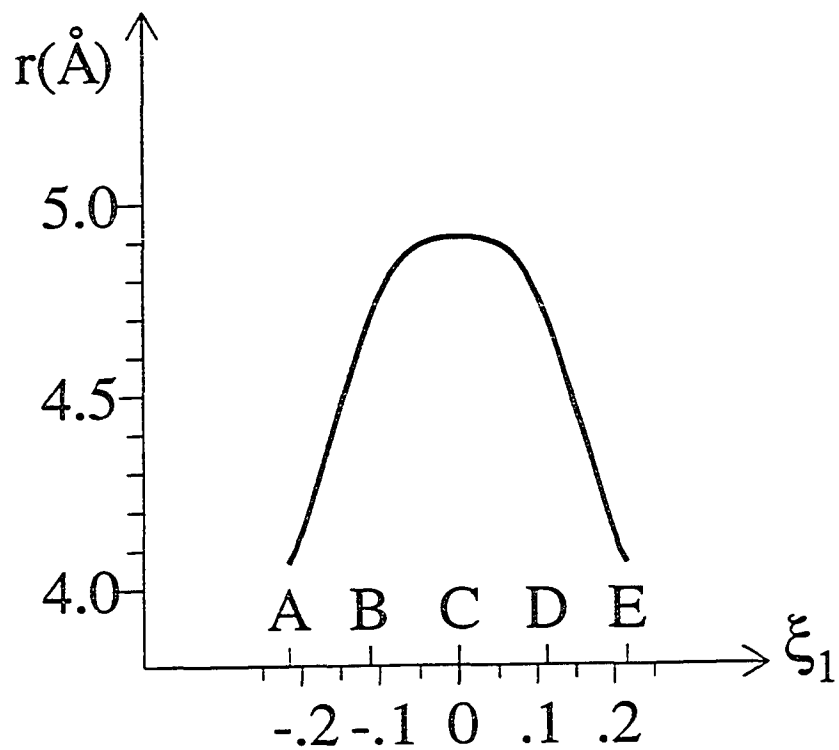


Figure 5. Variation of molecular circumference along the seam

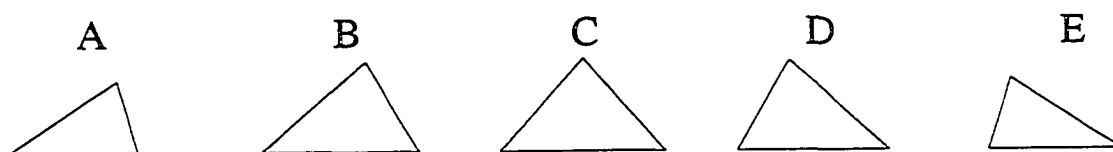


Figure 6. Variation of molecular shape along the seam

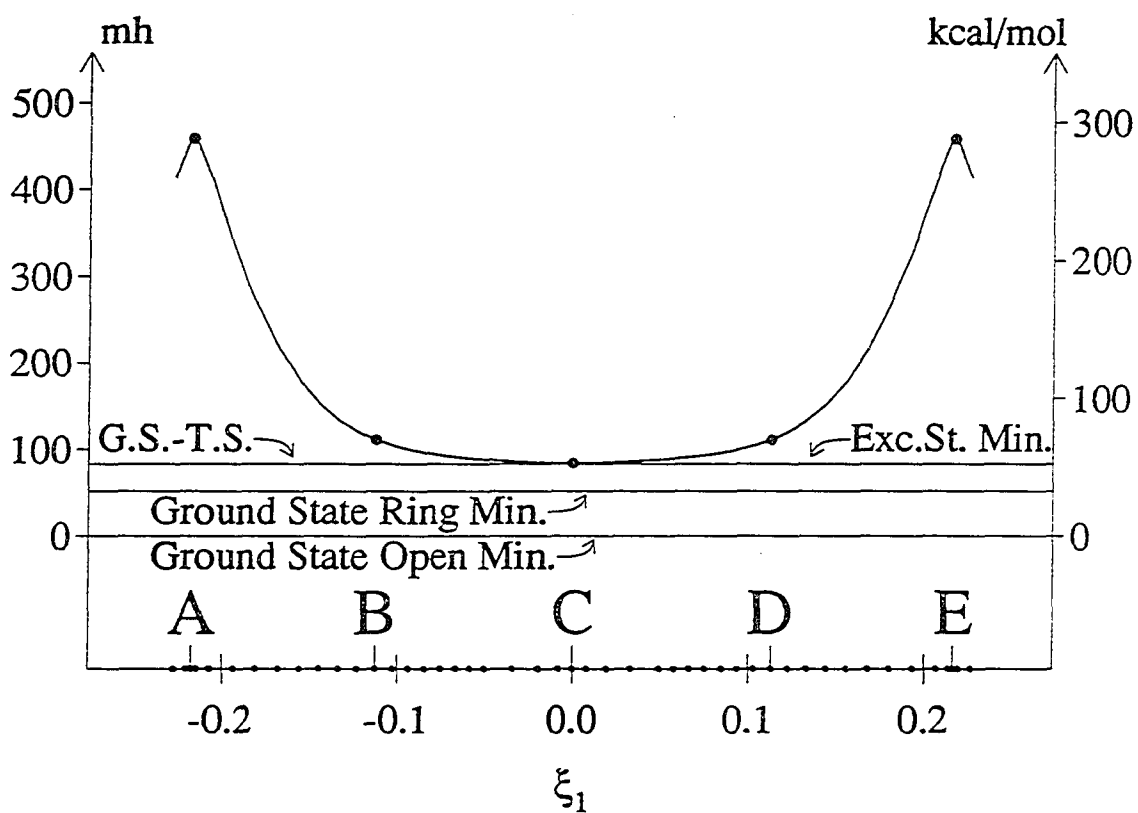


Figure 7. Variation of molecular energy of the $1^1A'$ and $2^1A'$ states along the intersection seam. Energies are relative to the ground state minimum

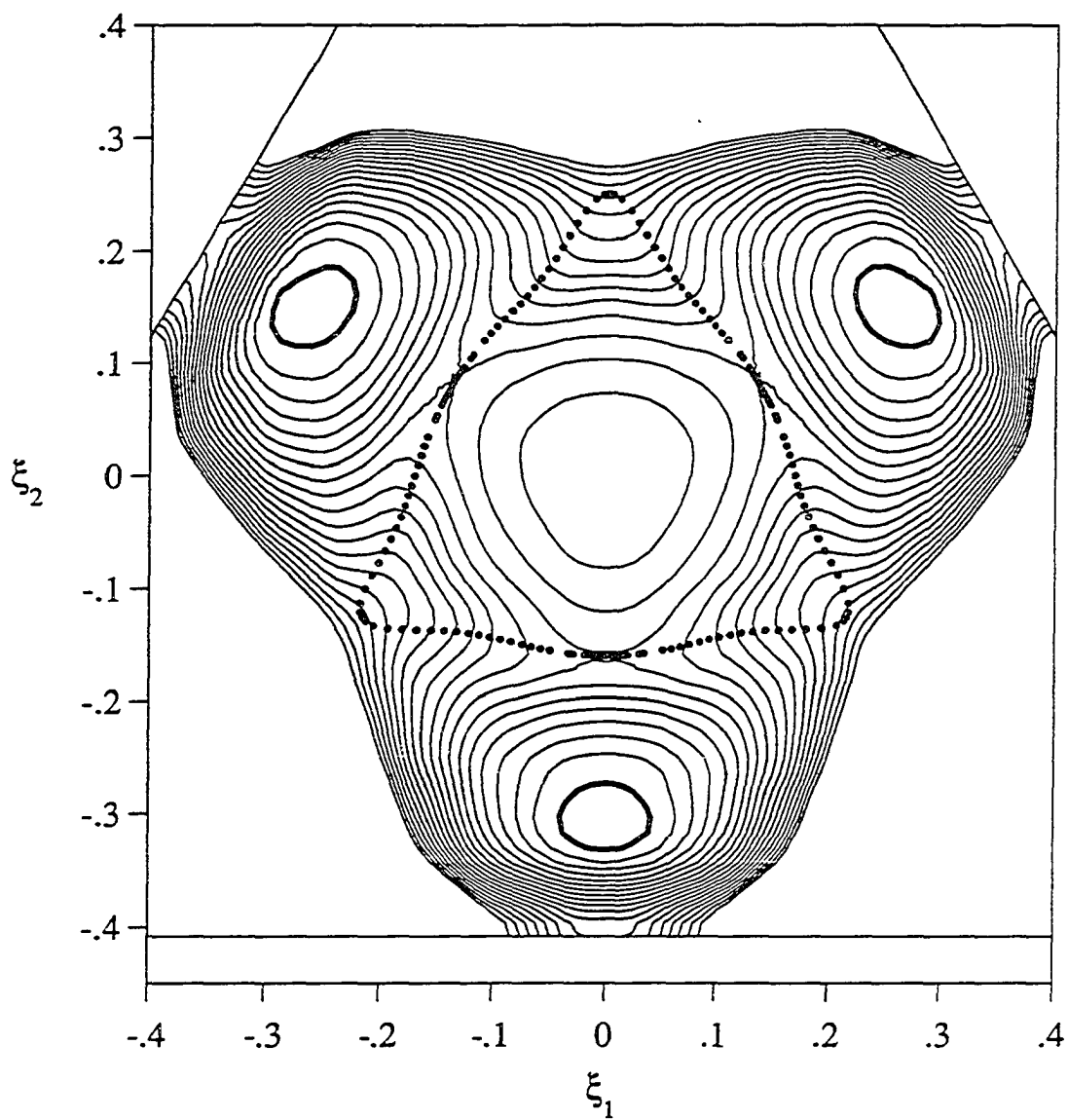


Figure 8. Projection of intersection seam onto contours of ground state for $s=2.3$

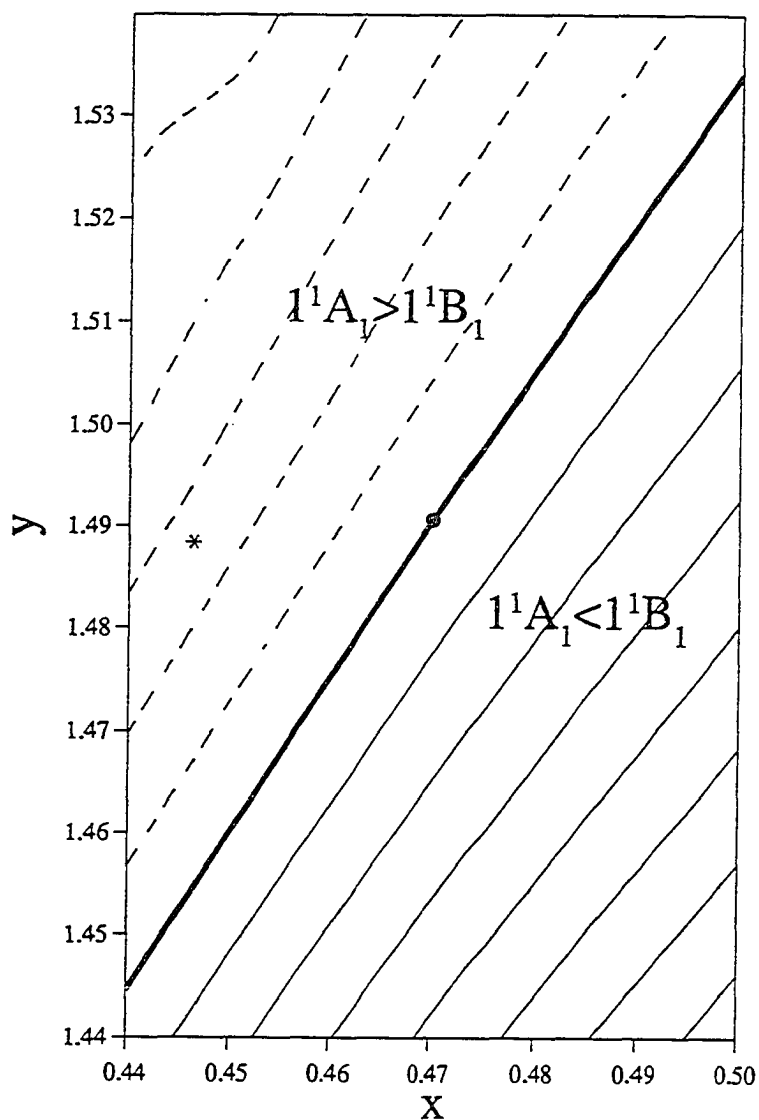


Figure 9. Contours of the energy difference $[E(1^1B_1) - E(1^1A_1)]$ states in the C_{2v} restricted coordinate space near point A. Coordinates are x, y cartesian coordinates of end atom (see Figure 3 of reference [1]). Solid lines: >0 , dashed lines: <0 , bold contour = 0. Increment = 10mh

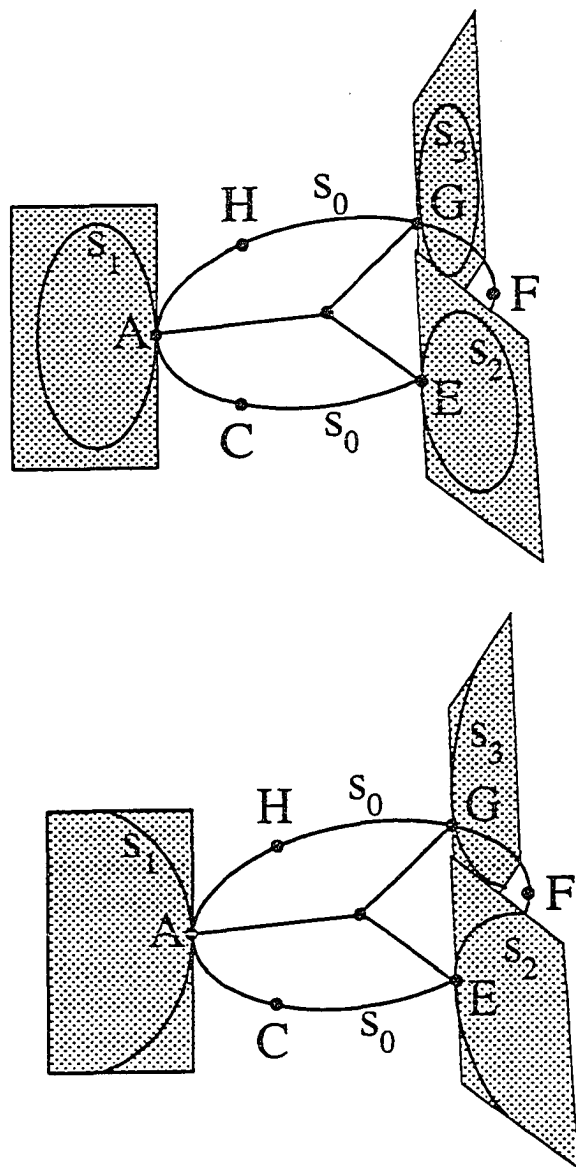


Figure 10. Two possibilities for the four branches of the intersection seam in the shape-scale coordinate space. Shaded planes: C_{2v} restricted spaces

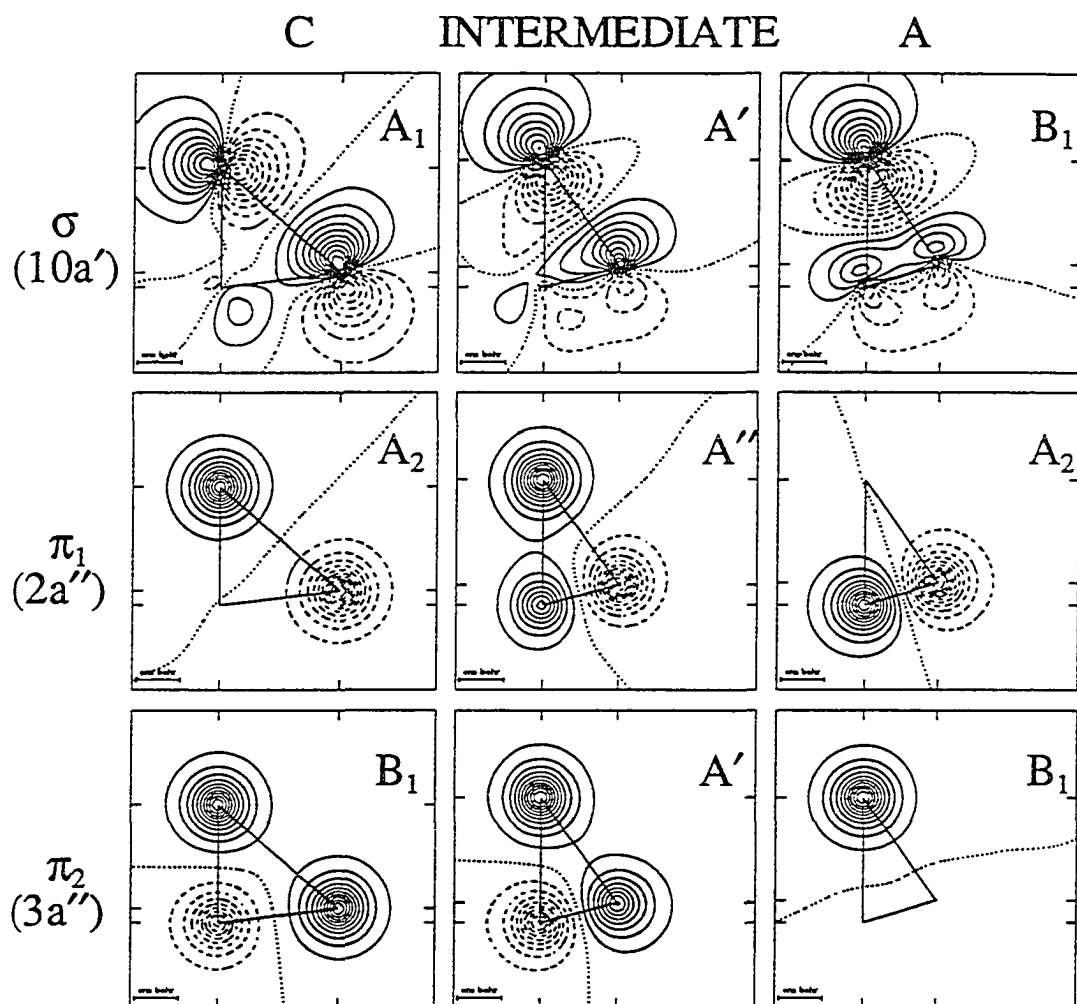


Figure 11. Shapes of the three natural orbitals σ , π_1 , and π_2 , at three points along seam from point C to point A

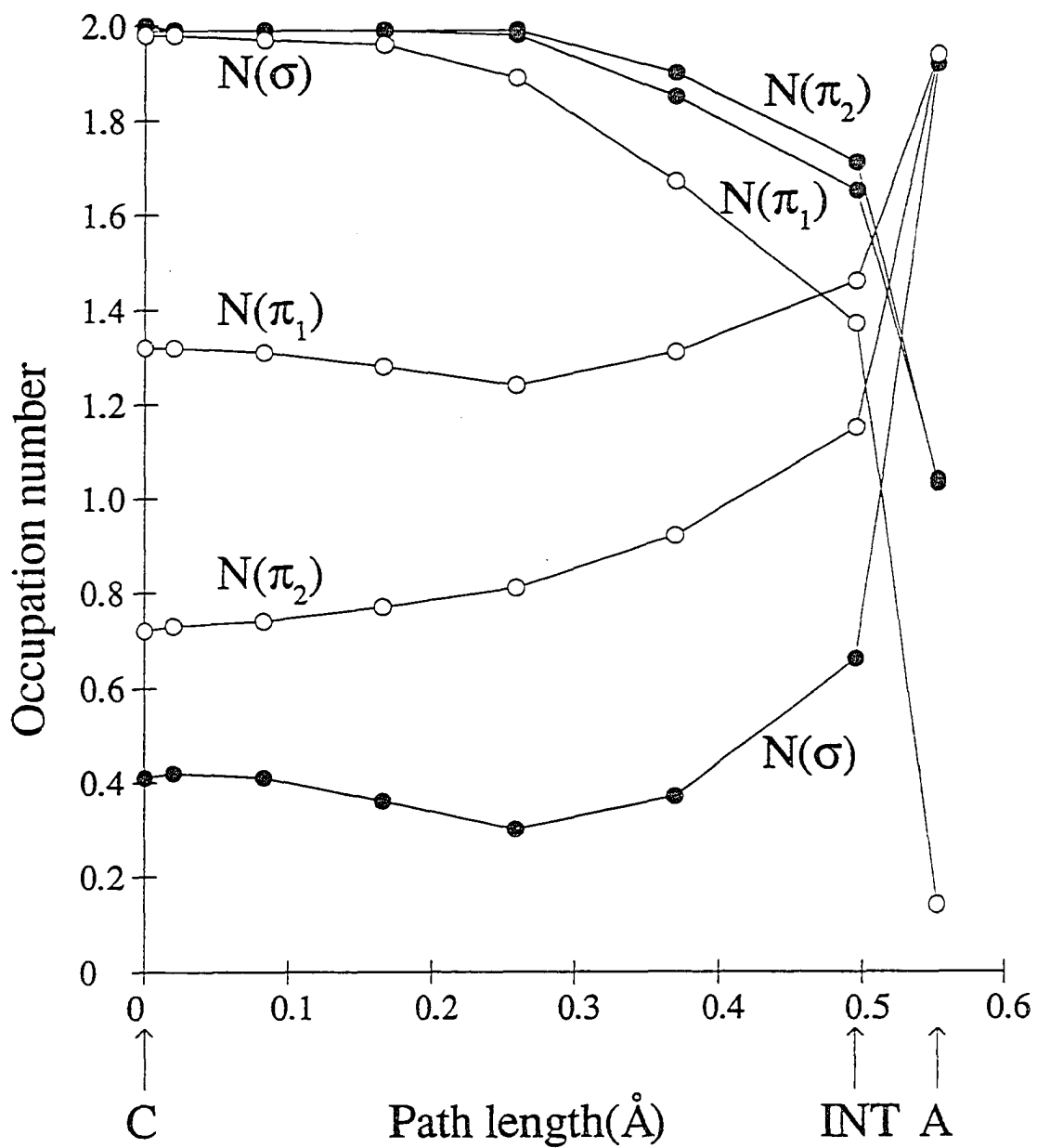


Figure 12. Plots of occupation numbers of the three natural orbitals σ , π_1 , and π_2 , on path from point C to point A

PAPER VI. GLOBAL POTENTIAL ENERGY SURFACES FOR
THE LOWEST TWO $^1A'$ STATES OF OZONE

GLOBAL POTENTIAL ENERGY SURFACES FOR
THE LOWEST TWO $^1A'$ STATES OF OZONE

Ames Laboratory USDOE and Department of Chemistry

Iowa State University

Ames, IA 50011

ABSTRACT

The global features of the potential energy surfaces of the lowest two $^1A'$ states of ozone have been established and detailed information has been determined for the critical regions. Contour maps are generated on a variety of planes and curved surfaces cutting through the two energy surfaces in various directions to obtain a full understanding of the three-dimensional characteristics of both surfaces. Perimetric internal coordinates are used so that the three atoms are treated on an equal footing.

The $1^1A'$ state, the groundstate, has a ring minimum and three equivalent open minima, all in C_{2v} . Direct dissociation to O_2+O is only possible from the open minima. The lowest energy path from the ring minimum first leads to an open minimum before going to dissociation. The transition states between the ring minimum and the open minima also have C_{2v} symmetry. Close to these transition states lie the three open minima of the $2^1A'$ state which has no ring minimum. Isomerization between the open minima is highly unlikely in the groundstate, but not entirely excluded in the excited state. Both states dissociate into the same state of O_2+O , namely the groundstate whose energy lies between those of the open minima of the two O_3 states. There exists an extended, interestingly shaped region in coordinate space in which the two states come very close to each other.

Indeed, it contains an intersection seam between the two states which consists of four branches which are connected by three knots. Radiationless transitions between the two states can be expected.

1. INTRODUCTION

Ozone has become particularly important because of its life protecting ultra-violet absorption in the upper atmosphere. But it has also attracted attention because of its toxicity in big-city smog and its potential as high-energy-density material. Not too much is known, however, about even the lower potential energy surfaces of this molecule.

The ground state equilibrium structure of ozone is an isosceles triangle with an apex angle of 113° . Since each of the three oxygen atoms can be at the apex, there are three equivalent such minima. Near each of these geometries, the molecule has four excited singlet states within about 6eV of the ground state energy. Under the restriction of C_{2v} symmetry (which is that of the groundstate minima) the excited states belong to the irreducible representations 1A_1 , 1A_2 , 1B_1 , 1B_2 . The groundstate belongs to 1A_1 . When the molecule distorts to C_s symmetry, the A_1 and B_2 irreps become A' (symmetric with respect to the molecular plane) whereas A_2 and B_1 become A'' (antisymmetric with respect to the molecular plane). Upon removal of one oxygen, all of these states dissociate into two states of the O_2+O system, namely $[O_2({}^3\Sigma_g^-) + O({}^3P)]$ and $[O_2({}^1\Delta_g) + O({}^1D)]$. These relationships are schematically illustrated by the correlation diagram in Figure 1. It accounts for all three singlet states arising from the lowest dissociated configuration

(which also yields an equal number of triplet states and quintuplet states). The dissociated configuration [$O_2(^1\Delta_g) + O(^3P)$], on the other hand, yields eight additional singlet states of O_3 , all at higher energies.

Upon deformation of the molecule to an equilateral triangle, all singlet states become very high in energy, except one, a 1A_1 state (in C_{2v} labelling). This 1A_1 state in D_{3h} symmetry is, of course, part of the groundstate potential energy surface (1^1A_1). It is in fact a fourth minimum on this surface. Its electronic structure is, however, related to that of the *excited* 2^1A_1 state at the groundstate minimum geometry. Indeed, we have shown in previous investigations [1] that these two 1A_1 surfaces intersect each other in C_{2v} symmetry at a point very close to the transition state from the ring minimum to the open minimum and that, in C_s symmetry, the corresponding $^1A'$ states intersect along a closed one-dimensional seam. Experimentally, nothing is known about the 2^1A_1 state [2].

In view of these findings, an elucidation of the PES of these two states, $1^1A'$ and $2^1A'$, over larger regions of the internal coordinate space seemed to be called for. The present investigation contributes such a study. Our aim is twofold, namely to obtain a credible picture of the global features within a reasonable approximation and to obtain more accurate data for the critical regions.

The time seems ripe for in-depth global examinations of actual triatomic *ab-initio* potential energy surfaces.

2. METHOD

2.1 Wavefunctions

The quality of any calculation, i.e. the reliability of the theoretical predictions, depends on the quality of the determined wavefunctions. At this time, it is still necessary to strike a compromise between various competing desired objectives. In the present context, they are: (i) sufficient accuracy for credible experimental predictions, (ii) sufficient flexibility for an unbiased description in different regions of the global internal coordinate space, (iii) computational feasibility. Regarding the last objective, it has to be kept in mind that several hundred energy values may have to be determined on each two-dimensional cross section through the PES in order to obtain the global features, and that the clarification of the critical regions may increase the effort by a substantial additional fraction. In the present case, about 2000 energies were determined on fifteen coordinate planes for both surfaces.

Basis Sets

Dunning's correlation-consistent VDZ (10s5p1d/3s2p1d) basis sets [3] were used for the three oxygen atoms. In section 3, we shall see that multi-reference SDCI calculations yield reasonable values for the dissociation energies of $O_3 \rightarrow O_2 + O$ and $O_2 \rightarrow 2O$ which are notorious for being difficult to reproduce. We therefore believe this basis to be capable of generating

credible results for the investigated potential energy surfaces. For higher excited states, complementation by diffuse orbitals will probably be called for.

Configuration Space

In order to guarantee the necessary flexibility over the various regions of the coordinate space we chose to determine the PES within the full-valence-space-MCSCF approximation (FORS, Valence CASSCF [4]). For ozone, these wavefunctions contain 4067 CSFs in C_{2v} symmetry and 8027 CSFs in C_s symmetry. Moreover, since two states of the same symmetry are to be determined, the calculations were based on state-averaged energy minimizations (SA-FORS calculations), giving equal weights to both states and using the same orbitals for them. In section 3, we shall compare the results obtained from these wavefunctions with those of more elaborate wavefunctions. It will be seen that the FORS wavefunctions yield the energy differences between the ring minimum, the open minimum, and the transition states with sufficient accuracy to be able to provide a credible elucidation of the PES.

The full valence space MCSCF wavefunction does not yield good quantitative values for the dissociation energies $O_3 \rightarrow O_2 + O$ and $O_2 \rightarrow 2O$ which, so far, have not been reproduced well with any medium size configuration expansion. The corresponding points require therefore correction along the

lines discussed in Section 3. We shall come back to this problem in future investigations.

All calculations were performed with the MOLPRO program of Werner and Knowles [5].

2.2 Energy Surface in Coordinate Space

In order to draw meaningful conclusions from energy surfaces, one requires internal coordinates which can be straightforwardly related to the molecular shape and an intelligible visualization of the surfaces in the internal coordinate space.

Coordinate Space

In order to obtain a presentation which exhibits the equivalent roles of the three nuclei, we chose perimetric coordinates, in particular, in scale-shape-adapted form. We have defined these coordinates and described them in detail in a preceding paper [6] and it is therefore not necessary to discuss them again here. Figure 2 exhibits the x_1 - x_2 -plane of these coordinates, perpendicular to the x_3 axis. In addition to the axes (x_1, x_2) , additional axes (x_1', x_2') and (x_1'', x_2'') are also indicated which are obtained from (x_1, x_2) by rotations through $+120^\circ$ and -120° respectively.

Since all three nuclei are identical, the PES have C_{3v} symmetry with

the x_3 axis being the three-fold axis [6]. The entire PES can therefore be obtained from the section in the area that is shaded in Figure 2 (between the negative x_2 and the positive x_2'' axes) by applying the symmetry operations of C_{3v} . Hence, energies have to be calculated only in one-sixth of the global internal coordinate space.

In order to visualize the dependence on the three nuclear positions equivalently, we decided to determine cross-sections through the PES on planes $x_3 = s/\sqrt{3} = r/(2\sqrt{3}) = \text{constant}$ (corresponding to molecules with fixed circumference) which cover the region of interest. Calculations were made on fifteen such planes defined by the values of r going from 4\AA to 6.8\AA in steps of 0.2\AA . The relation of these values to relevant molecular conformations is seen from Table 1. The fifteen coordinate planes correspond thus to the s -values

$$s = 2(0.1) 3.4 \text{ \AA}. \quad (2.1)$$

Table 1. Molecular circumference (\AA) for some geometries of O_3

Conformation	r_{12}	r_{13}	r_{23}	r
Ground State Open Minimum	2.214	1.305	1.305	4.824
Ground State Ring Minimum	1.476	1.476	1.476	4.428
Transition State between the above	1.916	1.438	1.438	4.792
(O_2+O) in C_{2v}	1.208 ^a	2.796	2.796	6.800

^aequilibrium bondlength of O_2 .

Four of these planes are illustrated on Figure 3 with respect to the perimetric coordinates s_1 , s_2 , s_3 .

On each of the fifteen planes, energies were calculated on a grid of points located at distances of 0.1Å in each direction - and confined to the unique shaded area indicated on Figure 2. Only few calculations were made, however, in the corners of the coordinate triangles where two atoms approach each other closer than about 80% of the O₂ bondlength ($\approx 0.96\text{Å}$) and the energy becomes correspondingly high. The larger the value $s=\text{const}$, the smaller is, of course, the fraction of the entire coordinate triangle taken up by these difficult-to-access corners. The number of points at which energies were calculated varied from 55 for $s=2\text{Å}$ to 158 for $s=3.4\text{Å}$. Approximately 1500 energies were determined in total for this global scan. The closer examination of the various critical regions required energies at about an additional 500 points.

Interpolation

Interpolation of the calculated energy values is a necessity for the graphical depiction and analysis of the PES. There are at least two essential reasons for this. One is the preparation of energy contours in a coordinate plane. Contouring algorithms are routinely predicated upon the function values to be plotted being offered on a rectangular grid which is equidistant

along each coordinate axis. Moreover, in order to obtain good, smooth contours, the grid has to be quite a bit denser than the pristine grid mentioned above on which energies were actually evaluated. The contouring grid has therefore to be derived from the pristine grid by interpolation. Another need for interpolation arises when one wishes to determine energy values and contours on planes or surfaces other than $x_3=\text{constant}$. Such a change in the viewing directions is an important tool for fully visualizing the three-dimensional behavior of a PES. To cut across the PES at various inclinations and with various origin displacements appears to be the only way to gain a complete understanding of the global character of a PES. (Only limited insight can be obtained by generating three dimensional energy contour surfaces perspectively). In fact, it is for this reason that energies were calculated on 15 planes $x_3=\text{constant}$, so that a grid with elementary displacements of 0.1\AA was available for interpolation in all three coordinate directions.

The triangular coordinate space covered by the coordinates (x_1, x_2) terminates along the sides of the triangles as shown in Figures 2 and 3 and the problem arises how to interpolate successfully near these borders. This task was accomplished by extending the pristine data beyond these borders through reflections into additional neighboring triangle spaces, as explained in [6]. Interpolation and contouring was then performed over the entire

enlarged region. Only the central part of this larger contour map, covering the original coordinate triangle, was then used and is displayed in the figures of this paper.

Bivariate interpolation techniques are still evolving and an ideal "method for all seasons" is still outstanding [7]. Different methods are useful under different conditions. If the pristine data are given on a rectangular grid that is equidistant in each coordinate direction, then cubic B-spline procedures are applicable and usually do a fine job [8]. This is useful for limited areas of the coordinate space. However, since we obtain data points in the full coordinate space by means of the C_{3v} operations, applied to one sixth of the data, we do not have such a grid for the global coordinate space. Moreover, it is often desirable to augment the original data set by additional denser grids in critical regions of the PES. For a pristine data set of this kind, one must use "scattered data interpolation" methods [9] which are still topics of research. We have used several methods: a triangulation method by Akima [10] and two methods based on the weighted superposition of local interpolation functions, one based upon the method of Shepard [11], another by Franke [12]. The performance of the various procedures depended upon the distribution and the homogeneity of the data.

The bivariate interpolation methods rarely reproduced the exact pristine data and, not infrequently, had problems in generating smoothly

curved contours when plotted. It must however be acknowledged that quantum chemical potential energy surfaces have a tendency to change their geometric characteristics very rapidly in the regions of greatest interest and are therefore not easy objects for interpolation. The development of bivariate and, subsequently, multi-variate interpolation algorithms optimally suited for molecular potential energy surfaces would seem to be a subject deserving further investigative attention.

3. CRITICAL FEATURES OF THE POTENTIAL ENERGY SURFACES

Before proceeding to a close global examination of the PES of the $1^1A'$ and $2^1A'$ states, it is expedient to discuss the critical features of the two surfaces found by our calculations.

The groundstate $1^1A'$ has four minima: three open minima, each of C_{2v} symmetry and belonging to the $1A_1$ irrep, with the apex angle of 116° located at one of the three oxygen nuclei, and one ring minimum with D_{3h} symmetry. To each of the open minima, there leads a transition state from the ring minimum, with an apex angle of about 85° . Near each of these transition states, the excited 2^1A_1 state has a minimum and, in the immediate vicinity, is part of an intersection seam in C_s symmetry. The groundstate dissociation can occur along six pathways, two from each of the open minima, with one of the end atoms moving away under approximate preservation of the apex angle. The dissociation from an excited state minimum occurs in a somewhat similar fashion. Both, the $1^1A'$ and the $2^1A'$ states, have the same dissociation limit [$O_2(^3\Sigma_g^-) + O(^3P)$] (see Figure 1) whose energy lies between those of the $1^1A'$ and the $2^1A'$ minima. There exists therefore, a barrier along the dissociation path on the $2^1A'$ surface. The calculations also reveal a barrier to dissociation on the $1^1A'$ surface. This, we feel, is an artifact of the calculations, and will be elaborated below.

These energetic relationships are represented quantitatively in Figure 4. Figure 4a exhibits the results of Internally Contracted Multi-Reference Singles and Doubles CI (ICMRSDCI) calculations where the FORS space was complemented by all internally contracted single and double excitations within the (3s2p1d) basis mentioned in Section 2.1 [13]. This configuration space is of dimension 446,977 (the dimension of the uncontracted SDCI space is about 21×10^6). Figure 4b exhibits the analogous energetic results from the full Valence State MCSCF (FORS) calculations. The full quantitative data of the various calculations are listed in Table 2. Table 3 lists the parameters of the various optimized geometries.

It is seen from Table 2 and Figure 4 that the energy differences between the groundstate minima and the transition state between them are reproduced equally well by both the FORS wavefunctions and the ICMRSDCI wavefunctions. However, the dissociation energy of the FORS wavefunction is only 20% of the experimental value, compared to the ICMRSDCI value that is 60% experiment. While the ICMRSDCI value may appear to be less than satisfactory, it should be noted that a much larger ICMRSDCI calculation involving 165 orbitals and almost 3 million contracted configurations generates a dissociation value that is still only 88% of the experimental value [14].

Table 2. Comparison of ground state energy differences obtained from various configurational approximations^a.

	Ring - Open	R-O TS ^b - Ring	(O ₂ +C) - Open	Dissoc TS ^c - (O ₂ +O)	2O - O ₂
FORS	51.03	33.82	8.46	13.46	141.66
SA FORS	50.64	31.09			
ICMRSDCI ^d	52.84	33.73	24.83	4.98	165.06
SA ICMRSDCI ^e	52.69	35.26			
Experiment			41.43	41.43	191.65
ICMRSDCI - FORS	1.81	-0.08	16.37	16.37	23.40
SA ICMRSDCI - SA FORS	2.05	4.18			
FORS - SA FORS	0.39	2.73			
ICMRSDCI - SA ICMRSDCI	0.15	-1.53			

^aAll energies in millihartree. 1 millihartree=0.6kcal/mol.

^bRing-opening transition state.

^cCalculated transition state to dissociation.

^dICMRSDCI wavefunction using FORS reference and FORS optimized orbitals.

^eICMRSDCI wavefunction using FORS reference and SA-FORS optimized orbitals.

Table 3. Geometry parameters of critical points of the ground state of ozone^a

	O-O Bond Length	O-O-O angle
Open Min.	1.298Å	116.32°
Ring-opening T.S.	1.431Å	83.86°
Ring Min.	1.470Å	60.0°
Dissociation T.S.	1.211Å, 1.720Å	113.59°
O ₂	1.2075Å	-

^aAll critical points except the dissociation transition state possess C_{2v} symmetry.

As mentioned earlier, the FORS wavefunction yields a barrier to dissociation on the 1¹A' surface. However, an ICMRSDCI calculation at this FORS determined geometry, which is likely to be different from the ICMRSDCI transition state geometry (if there is a transition state this surface), yields a much smaller barrier. We believe, therefore, that further examination at this or a slightly higher level of theory will reveal no barrier to dissociation on the 1¹A' surface.

4. GLOBAL FEATURES OF THE $1^1A'$ AND THE $2^1A'$ POTENTIAL ENERGY SURFACES

As mentioned in Section 2.2, energies of the two states were calculated on the fifteen planes $s=x_3/\sqrt{3} = r/2 = 2.0(0.1)3.4$ in the perimetric coordinate space, four of which were shown in Figure 2b.

4.1 PES of the $1^1A'$ state

Minima and Transition State

Contours of the lower state $1^1A'$ on twelve of the above mentioned planes are exhibited in Figure 5. All features of this PES can be deduced from the following markings. Since the global (open) minima are reached for $s=2.412A$, they are indicated on the panel for $s=2.4\text{\AA}$. Their energy is $E_0=-224.501h$. All contours on all panels correspond to energy values $E_0+k\times 20mh$ ($k=\text{integer}$, $20mh=0.54eV\approx 12\text{kcal/mol}$). They can be related to each other by reference to the bold contours which correspond to the energy E_0+60mh on all panels. The shaded areas denote regions within which the energy goes downhill to local minima *on that panel* ("basins") and all contours which are boundaries of basins have the same energy value *on any one panel*. The energy values go up for the contours in the unshaded regions. No contours are drawn for energy values larger than $E_0+200mh$ since they are getting too dense. This occurs when two atoms get substantially closer to each other

than the O₂ equilibrium distance of 1.21Å. These regions are indicated as dotted areas on all panels.

It is seen that, for s values $\leq 2.5\text{\AA}$, each PES cross-section has one ring minimum in the center, three equivalent open minima, and three saddlepoints leading from the ring minimum to the open minima. The minimum (as a function of s) of each of the three open minima occurs for $s=2.412\text{\AA}$ with an energy of $E=E_0$; they represent the equivalent global equilibrium structures. The minimum of the ring minima (as a function of s) occurs for $s=2.214\text{\AA}$ with an energy of $E=E_0+51\text{mh}$; it is the metastable ring equilibrium structure. The minima of the saddlepoints occur for $s=2.396\text{\AA}$ with an energy of $E=E_0+82\text{mh}$; they are the transition states from the ring structure to the open structures. For a value of s between 2.5\AA and 2.6\AA , the ring minimum disappears and, for all larger s values, the PES has a dome in the center region.

Dissociation

At about $s=2.6\text{\AA}$, one can see the onset of dissociation: each of the open minima splits into two, moving away from the original C_{2v} position, under approximate preservation of the apex angle (See Figure 6 of reference 6). For large s values, the dissociated system [(O⁽¹⁾-O⁽²⁾) + O⁽³⁾] corresponds to the line

$$x_2 = (-s_1 - s_2 + 2s_3)/\sqrt{6} = s\sqrt{2/3} - r_{12}\sqrt{3/2} \quad (4.1)$$

where $r_{12} = R(\text{O}_2) = 1.21\text{\AA}$. For $s=3.4\text{\AA}$, this yields $x_2=1.29\text{\AA}$ which is not too different from the minima on the panel for $s=3.4\text{\AA}$. A counting of contours on panels $s=-2.6\text{\AA}$ to 3.0\AA reveals the existence of a barrier with respect to dissociation on this surface, at about $s=2.7\text{\AA}$ with a barrier height of about 16mh. This is in agreement with diagram B on Figure 4 and with Table 2. Most likely, this barrier is due to the failure of this wavefunction in predicting the dissociation energy $\text{O}_3 \rightarrow \text{O}_2 + \text{O}$ correctly, as was discussed in Section 3. On Figure 4A and Table 2, we saw indeed that no barrier is found with the ICMRSDCI calculations. Nonetheless, the barrier found by the full valence MCSCF calculation is useful in that it provides a reasonable indication of the reaction path.

A better view of this reaction channel is obtained by looking at the contours on a surface in coordinate space which approximately contains the dissociative reaction path. Such a surface is defined in Figure 6. Figure 6A shows the s_1, s_2 coordinates of several critical points of the $1^1\text{A}'$ surface in the s_1 - s_2 coordinate plane. Namely: the (s_1, s_2) -values for two open minima and the corresponding transition states, as well as the line $s_1 + s_2 = R(\text{O}_2) = 1.21\text{\AA}$ for the dissociated system $\text{O}_2 + \text{O}$ (with nucleus $\text{O}^{(3)}$ being removed). Figure 6A furthermore shows a parabola drawn in a least-mean-square fashion through these critical point projections. As a surface on which to plot PES contours, we now choose the parabolic cylinder section which is parallel to the x_3 axis,

perpendicular to the x_1 - x_2 plane, and intersecting the x_1 - x_2 plane in the just described parabola. Such a cylinder is shown in Figure 6B which also illustrates the intersection of this cylinder section with two planes $s=\text{constant}$.

The contours of the $1^1A'$ PES on this cylinder section are shown on the upper panel of Figure 7. As on Figure 5, the bold lines indicate the contours $E_0+60\text{mh}$ and the shaded areas indicate basins. The increment between contours is, however, only 5mh and the dotted area covers the region $E>E_0+100\text{mh}$. The intersections with four planes $s=\text{constant}$ are indicated by dashed lines and the same intersection lines are shown on the smaller, lower panels, representing contours on corresponding planes $s=\text{constant}$ taken from Figure 5.

The dissociation channel from the two open minima are quite apparent. The most important inference from this plot is probably that there exists no realistic option of avoiding dissociation in favor of isomerization from one open minimum to another.

Is dissociation from the ring minimum into O_2+O possible without passing through an open minimum?

The contours of Figure 5 are somewhat awkward for recognizing whether or not a direct dissociative reaction path exists from the ring minimum without first going to an open minimum, e.g. by abstraction of the

central oxygen. In order to answer this question, we determined PES contours on three planes *containing the x_3 axis, i.e. perpendicular to the planes $s=\text{constant}$* . These planes, called A,B,C, are shown perspectively on Figure 8, where the axes ($x_1, x_2, x_1', x_2', x_1'', x_2''$) are those defined on Figure 2. The PES contours on these planes are exhibited on Figure 9, where the markings have the same meanings as those on Figure 5. The panels A and C correspond to two different C_{2v} subspaces and, hence, show equivalent contours. On these two panels, one sees one of the open minima, the ring minimum and the saddlepoint between them. (This part of the plot is equivalent to Figure 4 of reference [1a]). Comparison of panel C of Figure 9 and panel $s=2.4\text{\AA}$ of Figure 5 at this saddlepoint, shows that the C_{2v} conserving normal mode pointing to the two minima is the *only* downhill mode in all three dimensions and that there exist *two* uphill normal modes, one C_{2v} conserving (on Figure 9) and another C_{2v} symmetry breaking (on Figure 5, panel $s=2.4\text{\AA}$). This saddlepoint is therefore indeed a transition state.

Figure 9C exhibits, however, another saddlepoint, namely towards positive x_2 values, whose steepest descent line leads to a dissociation corresponding to abstraction of the central atom in a C_{2v} conserving subspace. In addition to this C_{2v} conserving downhill mode at this saddlepoint, which occurs at about $s=2.6\text{\AA}$ on Figure 9C, one finds however a *second*, C_{2v}

symmetry breaking, downhill mode, on the panel for $s=2.6\text{\AA}$ of Figure 5, heading towards two open minima. This saddlepoint is therefore not a transition state. Moreover, it is almost 20mh higher than the transition states towards the open minima. One must therefore conclude that most reaction trajectories which might start out towards a C_{2v} conserving abstraction of a central oxygen will turn around and end up in one of the open minima. Hence, dissociation from the ring structure goes through one of the open minima.

The contours on panel B of Figure 9 are intermediate between panels A and C. They give an indication how these contours deform into each other if one slowly rotates the plotting plane around the x_3 axis from A to C. The saddlepoints on plane B of Figure 9 are not saddle points on Figure 5.

Linear Structures

Linear arrangements of the three atoms correspond to the sides of the coordinate triangles of Figure 5. It is seen that, for $s \leq 2.6\text{\AA}$, the *isosceles* linear structure, corresponding to the midpoints of the triangle sides, are the ones with the lowest energies and represent saddlepoints with respect to inversion of the molecule under constant circumference. For panels with $s \geq 3\text{\AA}$, where we approach dissociation, the lowest energy occurs for two atoms at the O_2 equilibrium distance and the third, collinearly, a long distance

away.

On Figure 9, the linear molecules are represented by the lines marked $s_1=0$ (corresponding to $O^{(1)}$ lying between $O^{(2)}$ and $O^{(3)}$) and $s_2=0$ (corresponding to $O^{(2)}$ lying between $O^{(1)}$ and $O^{(3)}$). Panels A and C are C_{2v} preserving planes and, therefore, the lines $s_1=0$, $s_2=0$ correspond to the *isosceles* linear molecules which, as noted above, are saddlepoints on the panels for $s \leq 2.6 \text{ \AA}$ on Figure 5. It is seen from Figures 9A,C that the saddlepoints with the lowest energy occur at about $s=2.5 \text{ \AA}$. These points are therefore transition states with respect to inversion, with a barrier of about 60-70mh and bond lengths of about 1.25 \AA .

On the other hand, it is apparent from Figure 8 that the lines $s_1=0$ and $s_2=0$ on panel B correspond to linear molecules where the distances between the central atom and the two end atoms are in a ratio of 2:1. (See Section 4.2 of reference [6]). When the shorter of these distances is equal to the O_2 bondlength of 1.21 \AA , then the larger one will be 2.42 \AA and s =half the circumference will be 3.63 \AA . It is apparent that the (extrapolated) minima on the lines $s_1=0$ and $s_2=0$ of panel B occur just about for this value of s . The similarity of these minima for large s values with those on panels A and C reflects the independence of the dissociated system upon the location of the oxygen atom. The near dissociation minimum on the lines $s_1=0$ of panel B is reached from the global open minimum of panel A by a path penetrating

panels intermediate between A and B in agreement with the earlier discussion of this dissociation.

4.2 PES of the $2^1A'$ State

The contours of the $2^1A'$ state on planes $s=\text{constant}$ are displayed on Figure 10. The *method* of marking is the same as that for the $1^1A'$ state on Figure 5. In fact, the energy increment between contours (20mh) is the same on both figures and some contours on Figure 10 have the same energy as some contours on Figure 5. However, the bold contours on Figure 10 correspond to the energy $E_0+100\text{mh}$, i.e., they are 40mh higher than the bold contours on Figure 5. Similarly the dotted region starts at a higher energy ($E_0+500\text{mh}$ as compared to $E_0+200\text{mh}$ in Figure 5).

Minima

On all panels $s=2.0\text{\AA}$ to 2.7\AA , the PES cross-sections exhibit three minima corresponding to open structures, i.e. obtuse molecular triangles. The minimum (as a function of s) of these minima occurs for $s=2.421\text{\AA}$ with an energy of $E_0+82\text{mh}$ (E_0 still denotes the energy of the global ground state minimum). These global minima of the $2^1A'$ state are indicated on the panel for $s=2.4\text{\AA}$. As mentioned earlier, their locations are very close to the groundstate transition states between the groundstate ring minimum and

open minima.

In contrast to the ground state, the $2^1A'$ has no ring minimum, its energy is quite high for conformations near the equilateral triangle structure.

Dissociation

On the panel $s=2.4\text{\AA}$ one notices the appearance of a second set of three minima, corresponding to *acute* molecular triangles with C_{2v} symmetry. These minima become more pronounced on the panels $s=2.5\text{\AA}$ and 2.6\AA . The transition, on a panel $s=\text{const}$, from one of the previous minima (open triangle structures) to one of the presently considered minima (acute triangle structures) corresponds to a change in electronic structure. Indeed, for the acute triangle minima, the electronic wavefunction belongs to the irreducible representation 1B_2 . With increasing values of s , corresponding to one oxygen further and further away from the O_2 left behind, these minima steadily decrease in energy and reach their lowest value for $s=\infty$, where they end up with the same (O_2+O) configuration as the groundstate (see Figure 1). (For $s=3.4\text{\AA}$, this state is, however, less close to being a dissociated system than $1^1A'$ was, in as much as the minimum energies are not yet constant along lines parallel to the triangle sides.) The minima for the open triangle structure, on the other hand, become less and less deep with increasing s and finally disappear. Consequently, there exists a dissociation path from the

global minimum of the $2^1A'$ PES for $s=2.421\text{\AA}$ to the near dissociated system for $s=3.4\text{\AA}$. The transition state for this path occurs for $s=2.6\text{\AA}$ where the saddlepoint between the two types of minima (for $s=\text{const}$) reaches its minimum, with a barrier of $(104\text{mh}-82\text{mh})=22\text{mh}$.

Two successive enlargements of the panel for $s=2.6$ in the region around this transition state are shown on Figure 11, where the energy contour increments are 1mh and 0.5mh respectively and the shadings indicate basins with energy values $E \leq E_0 + 103\text{mh}$. It can be seen that the two transition states lie within 0.2\AA from each other. If both would move by 0.1\AA towards each other, then they would coalesce into one, on the x_2 axis with C_{2v} symmetry at the position marked by an asterisk on Figure 11, and it would become a transition state for isomerization between two equivalent minimum structures rather than for dissociation. It would seem that, even with the critical region as it is in Figure 11, there is some probability for the molecule to undergo isomerization from one open minimum to another when starting out on this reaction path.

As in the case of the $1^1A'$ PES, this dissociation channel can be better recognized by contours on a parabolic cylinder perpendicular to the s_1 - s_2 plane. On Figure 6a, we also showed the s_1, s_2 coordinates of the critical points of the $2^1A'$ state as well as a least mean squares parabola through these points. Again we consider contours on a parabolic cylinder, such as

shown in Figure 6B, but now intersecting the s_1 - s_2 plane in the new parabola. It should be noted that, on it, the dissociated system has an O_2 bondlength of 1.37\AA , i.e. somewhat larger than the O_2 equilibrium bondlength of 1.21\AA . The contours on this cylinder section are displayed on Figure 12 where the markings are very similar to those on the analogous Figure 7 for the $1^1A'$ surface. The contours confirm that the two transition states are close to having the characteristics of *one* transition state in C_{2v} with a third downhill branch going off at a right angle toward the dissociated system. This latter, C_{2v} conserving, downhill steepest descent path originates on a *ridge* from the center of the coordinate plane (corresponding to the high-energy ring geometries) and *changes into a valley* very close to the aforementioned transition states. At this valley-ridge inflection point [15] the second derivative of the energy vanishes in the C_{2v} symmetry breaking x_1 direction.

The actual downhill path in C_{2v} symmetry can be seen on panels A and C of Figure 13, which displays cross-sections of the $2^1A'$ PES in the planes containing the x_3 axis which were specified on Figure 8. The contours of Figure 13 are analogous to those shown on Figure 9 for the $1^1A'$ state and have similar markings. An entirely congruent C_{2v} preserving plane with identical contours would be the x_2 - x_3 plane. That plane intersects the cylinder section defined in Figure 6 (on which the contours of Figure 12 are plotted) in a line that is indicated as a dotted line on Figure 12. On the C_{2v}

conserving x_2 - x_3 plane, this intersection line is found to be

$$s = 3 \cdot (1.37/2) + x_2 \sqrt{3/2} = 2.055 + 1.225x_2 \quad (4.2)$$

(See Eq. (15) of reference [6]) and the analogous line is shown as a dotted line on panel A of Figure 13. From Figure 11, one finds the coordinates

$$x_1 = 0, \quad x_2 = 0.442\text{\AA}, \quad s = \sqrt{3}x_2 = 2.6\text{\AA} \quad (4.3)$$

for the point midway between the two transition states, which is marked by an asterisk on that Figure. The same point is also marked by asterisks on Figure 12 and on panel A of Figure 13. It can now be seen that the steepest descent reaction path from this point to dissociation on Figure 13 does not deviate too much from the cylinder constructed in Figure 6.

Linear Structures

An examination of the triangle sides on Figure 10 and of the lines $s_1=0$ and $s_2=0$ on Figure 13 leads to conclusions regarding the linear structures of the $2^1A'$ state which are similar to those found for the $1^1A'$ state. Namely, there exist linear isosceles transition states with respect to inversions from one minimum to another at about $s=2.8\text{\AA}$, corresponding to two equal bond lengths of 1.4\AA , with a barrier of about 65mh. For large values of s ($s \geq 3\text{\AA}$), the minimum of the linear molecules corresponds to an oxygen molecule in its groundstate and an oxygen atom at a large distance.

4.3 Energy Difference Between the Two States

We know from previous investigations [1b] that the $1^1A'$ state and the $2^1A'$ state intersect along a seam which forms a closed curve looping around the x_3 axis in our coordinate system. We have also shown [1a] that, at least in C_{2v} , the intersection is of the sloped type [16] and that the two surfaces seem to stay close to each other over a somewhat extended range near the C_{2v} intersection point. Since, in such regions, there exists a high probability for radiationless transitions, it is of interest to know the actual *global extent* of the part of coordinate space where the energy difference between the two states is small.

Contours of the energy difference $\Delta E = [E(2^1A') - E(1^1A')]$ on panels $s = \text{constant}$ are exhibited on Figure 14. Note that, here, the markings are very different from those on the analogous Figures 5 and 10 for the separate surfaces. Now, the light areas denote the regions of *low* ΔE values, namely $\Delta E < 20 \text{mh}$. In this area, there can lie one more contour, namely $\Delta E = 5 \text{mh}$. Shaded is the area where $\Delta E > 20 \text{mh}$. The increment between contours is 15mh . The bold contour corresponds to $\Delta E = 95 \text{mh}$. The dotted corner regions correspond to molecular geometries where two oxygen atoms approach each other closer than $0.8 \text{\AA} = 66\%$ of the O_2 bondlength, where the energies of both states become extremely high.

An examination of all panels reveals that the shape of the region where

the two states come close remains remarkably similar for practically all values of s . In the three dimensional coordinate space, it represents a volume which is schematically drawn on Figure 15. It is approximately the volume between two cylinders with radii 0.4\AA and 0.5\AA , the x_3 axis being the cylinder axis, and, joined to it, three sheet-like volumes within about $0.1\text{-}0.2\text{\AA}$ of those sections of the three C_{2v} conserving planes which, starting at the aforementioned cylinder, go outward to the corners of the coordinate triangles.

How the two states approach each other can be seen on Figure 16 which plots the energies of both states as functions of the radial distance

$$(x_1^2 + x_2^2)^{1/2} = (r_{12}^2 + r_{23}^2 + r_{13}^2) - (r_{12} + r_{23} + r_{13})^2/3 \quad (4.4)$$

where r_{ij} are the molecular bondlengths (Eq. (4.4) follows from Eqs. (17), (3), and (15) of reference [6]). Plots are given for various values of the angle ω , as explained in Figure 17a. It is seen that the radius of closest approach remains remarkably close to $(x_1^2 + x_2^2)^{1/2} \approx 0.4\text{\AA}$.

From the exact points of closest approach we determined accurate functions $(x_1^2 + x_2^2)^{1/2} = f(\omega)$ for various values of s , some of which are shown in Figure 17b. In Figure 18, we display the energies of the two states along these lines for various s -values.

The intersecting seam between the two states, which was a partial stimulus for the present investigation, must lie in the volume of close approach depicted in Figure 15. In reference [1b] we determined explicitly

the intersection seam which loops around the x_3 axis, i.e. which runs in the cylinder section of Figure 15. The exact points where this seam intersects various PES cross-sections discussed above are indicated by heavy dots on Figures 5,10,14,16,18. We had also found in reference [1b], however, that the intersection in fact consists of four connected branches S_0, S_1, S_2, S_3 . The branch S_0 is the one just discussed which lies in the cylinder section of Figure 15. In addition, there is one branch in each of the three C_{2v} conserving planes. These branches (S_1, S_2, S_3) lie in the sheetlike volumes of Figure 15 which are fanning out from the cylinder to the triangle corners (see Figure 10 of reference [1b]). The somewhat surprising form of Figure 15 is thus confirmed by the results of reference [1b]. Finally, it was also found in reference [1b] that, on the branches S_1, S_2, S_3 , the two states belong to different irreps of C_{2v} , namely 1A_1 and 1B_2 , and this is presumably also the case for the entire sheet-like parts of Figure 15.

5. CONCLUSIONS

The global features of the potential energy surfaces and detailed information regarding their critical points have been established for the lowest two $^1A'$ states of ozone.

The ground state has a D_{3h} ring minimum and three equivalent open C_{2v} minima. A lowest-energy path leads from the ring minimum over a transition state to each open minimum and from there, under approximate preservation of the apex angle, to dissociation into O_2+O . The excited state has three open minima, whose geometries are close to those of the aforementioned transition states between the ground state minima. Dissociation of the excited state follows similar paths as for the ground state. The path towards isomerization between the open minima would start out close to the dissociative path and then split off from it. This is highly unlikely on the ground state surface, but not entirely improbable on the excited state surface. Both states dissociate into the same state of O_2+O , viz. the ground state, whose energy lies in between the energies of the open minima of the $1^1A'$ and $2^1A'$ PES of O_3 . The excited state is therefore metastable with a dissociation barrier of about 13kcal/mol. The groundstate has no barrier towards dissociation.

There exists an extended region in coordinate space, of a somewhat

peculiar shape, where the two states come very close. In fact, the two states intersect in this region along a seam which consists of four branches which are connected in three knots. Radiationless transitions can therefore be expected.

For isosceles conformations with obtuse apex angles, both states belong to the same irreducible representation in C_{2v} , viz. 1A_1 . However, for isosceles conformations with very acute angles, the two states belong to different C_{2v} irreps, namely 1A_1 and 1B_2 . A complete elucidation in C_{2v} requires therefore the simultaneous consideration of the three states 1^1A_1 , 2^1A_1 , and 1^1B_2 , all of which become ${}^1A'$ states when the symmetry is lowered to C_s .

REFERENCES

1. a. S. Xantheas, G. J. Atchity, S. T. Elbert, and K. Ruedenberg, *J. Chem. Phys.*, **94**, 8054 (1991).
b. G. Atchity and K. Ruedenberg, to be submitted.
2. J. I. Steinfeld, S. M. Adler-Golden, and J. W. Gallagher, *J. Phys. Chem. Ref. Data* (Am. Chem. Soc. and Am. Inst. Phys. for U. S. Nat. Bur. Standards), Vol. 16, No. 4, p. 911 (1987).
3. T. H. Dunning, Jr., *J. Chem. Phys.* **90**, 1007 (1989).
4. A good review of MCSCF methods is by R. Shepard in *Ab Initio Methods in Quantum Chemistry-II* (John Wiley & Sons, Great Britain, 1978), pp. 63-200. See also *B. O. Roos, ibid*, pp. 399-445.
5. H.-J. Werner and P. J. Knowles, *J. Chem. Phys.* **82**, 5053 (1985); *Chem. Phys. Lett.* **115**, 259 (1985).
6. G. Atchity and K. Ruedenberg, to be submitted.
7. R. Franke and G. M. Nielson, in *Scattered Data Interpolation and Applications: A Tutorial and Survey*.
8. C. de Boor, in *A Practical Guide to Splines* (Springer Verlag, New York, 1978).
9. R. Franke, *Math. Comp.* **38** 181 (1982).
10. H. Akima, Algorithm 526 in *ACM TOMS*, **4**, 160 (1978).

11. R. Renka, Algorithm 660 in ACM TOMS, **14**, 149 (1988).
12. R. Franke, Comp. Maths. Appls. **8**, 273 (1982).
13. H.-J. Werner and E. A. Reinsch, J. Chem. Phys, **76**, 3144 (1982);
H.-J. Werner, Adv. Chem. Phys. **59** 1 (1987).
14. G. J. Atchity and K. Rudenberg, to be submitted.
15. P. Valtazanos and K. Ruedenberg, Theor. Chim. Acta **69** 281 (1986).
16. G. J. Atchity, S. S. Xantheas, and K. Ruedenberg, J. Chem. Phys. **95**,
1862 (1991).

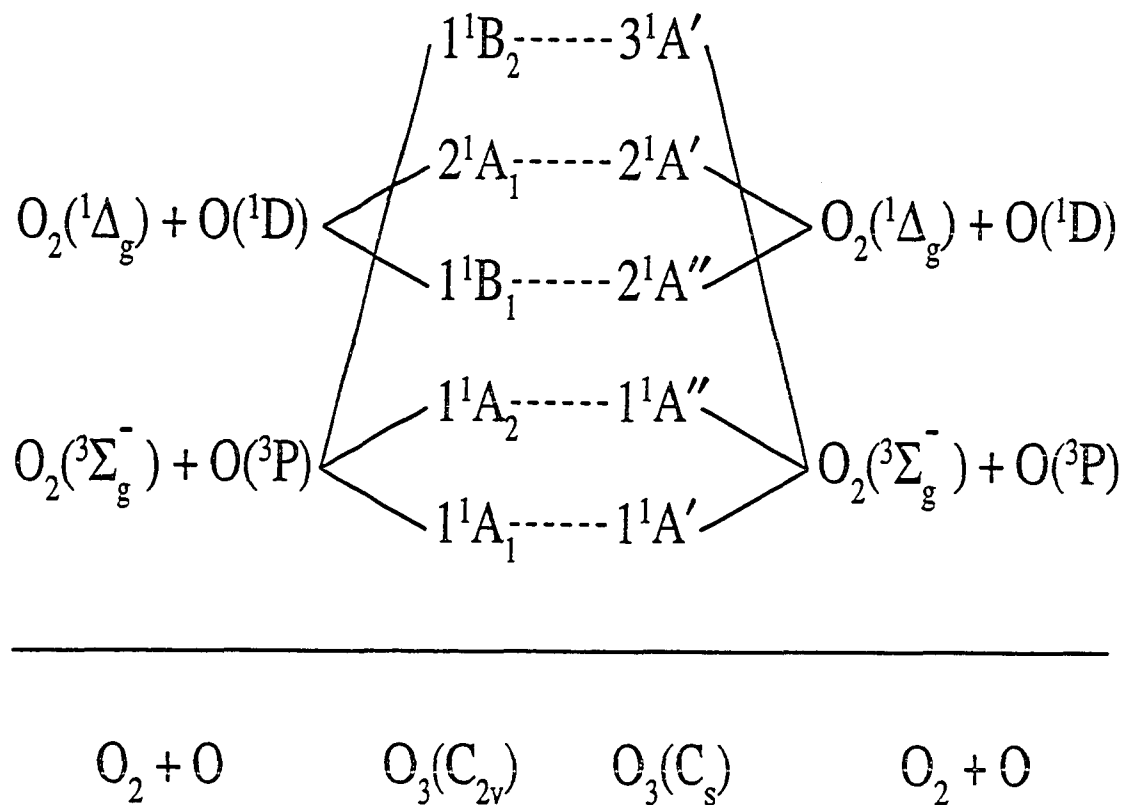


Figure 1. Correlation of lowest singlet states of ozone

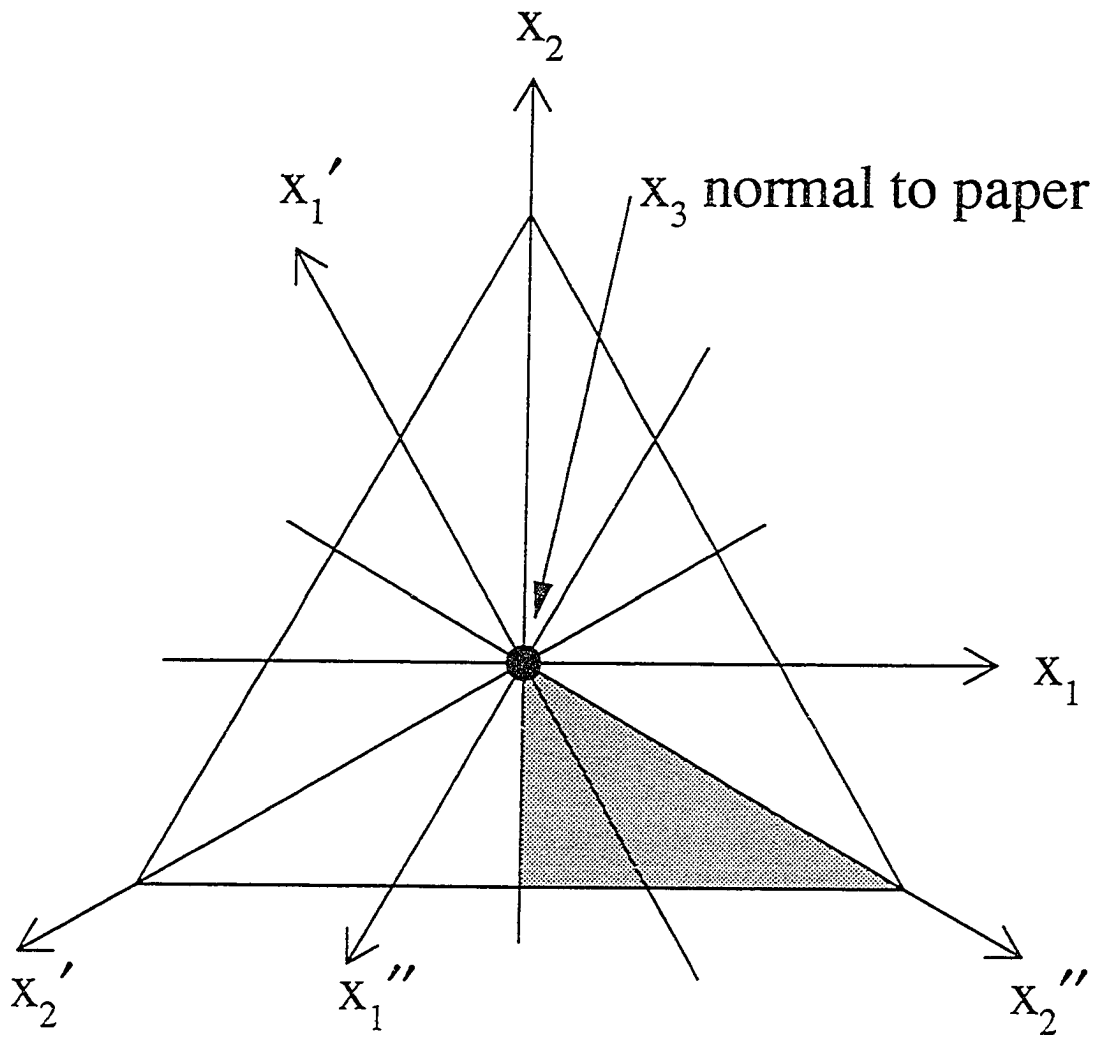


Figure 2. Scale-shape adapted perimetric coordinates (x_1, x_2, x_3). Shaded area: region of independent energy values in ozone

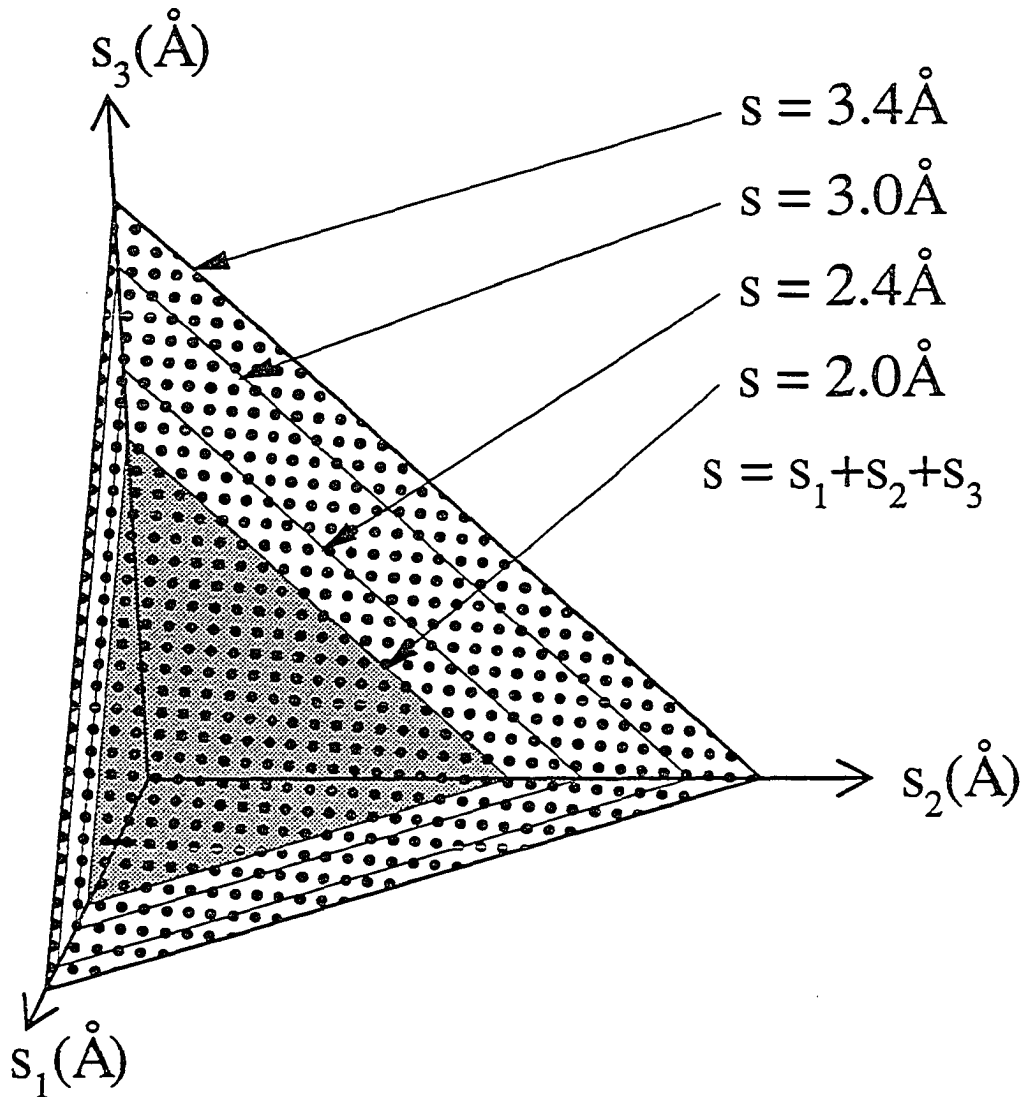


Figure 3. Four planes $s=\text{constant}$ in the perimetric coordinate system.

Shaded: $s=2.0\text{Å}$. Dotted: $s=3.4\text{Å}$

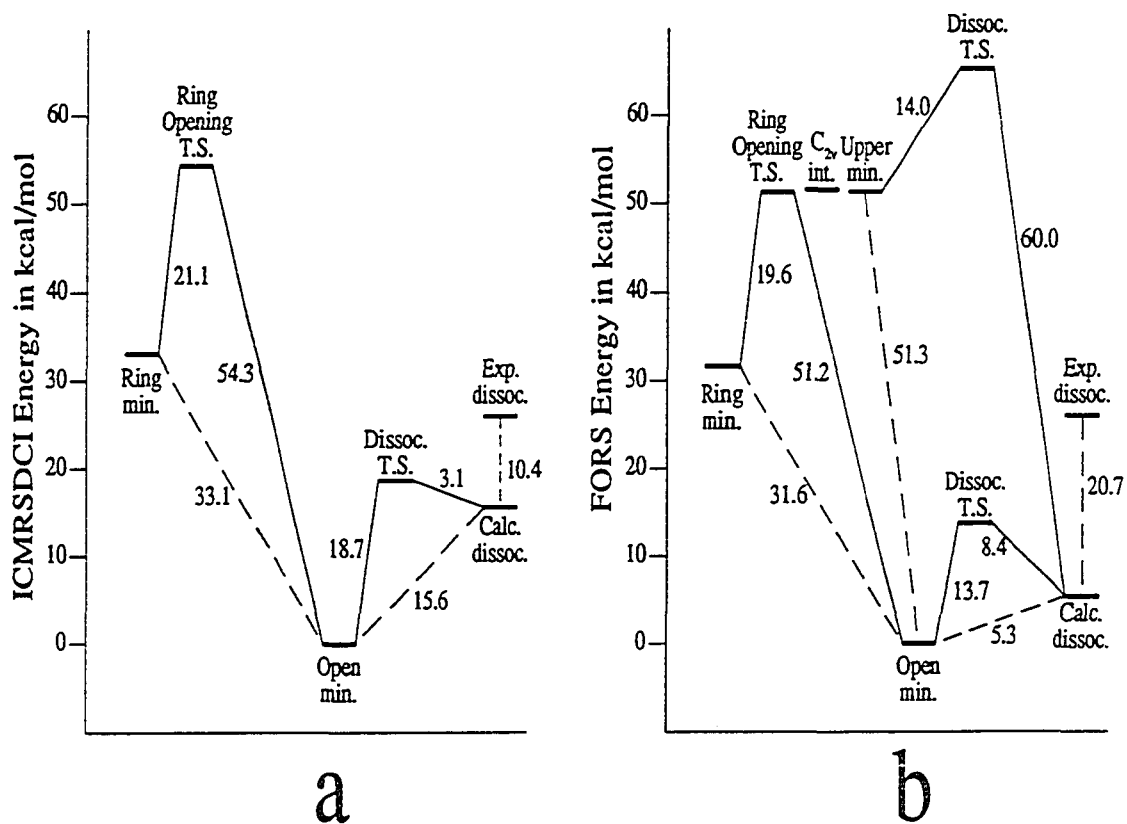


Figure 4. Critical energy differences for the $1^1A'$ and the $2^1A'$ states of ozone. A: ICMRSDCI calculations. B: FORS calculations

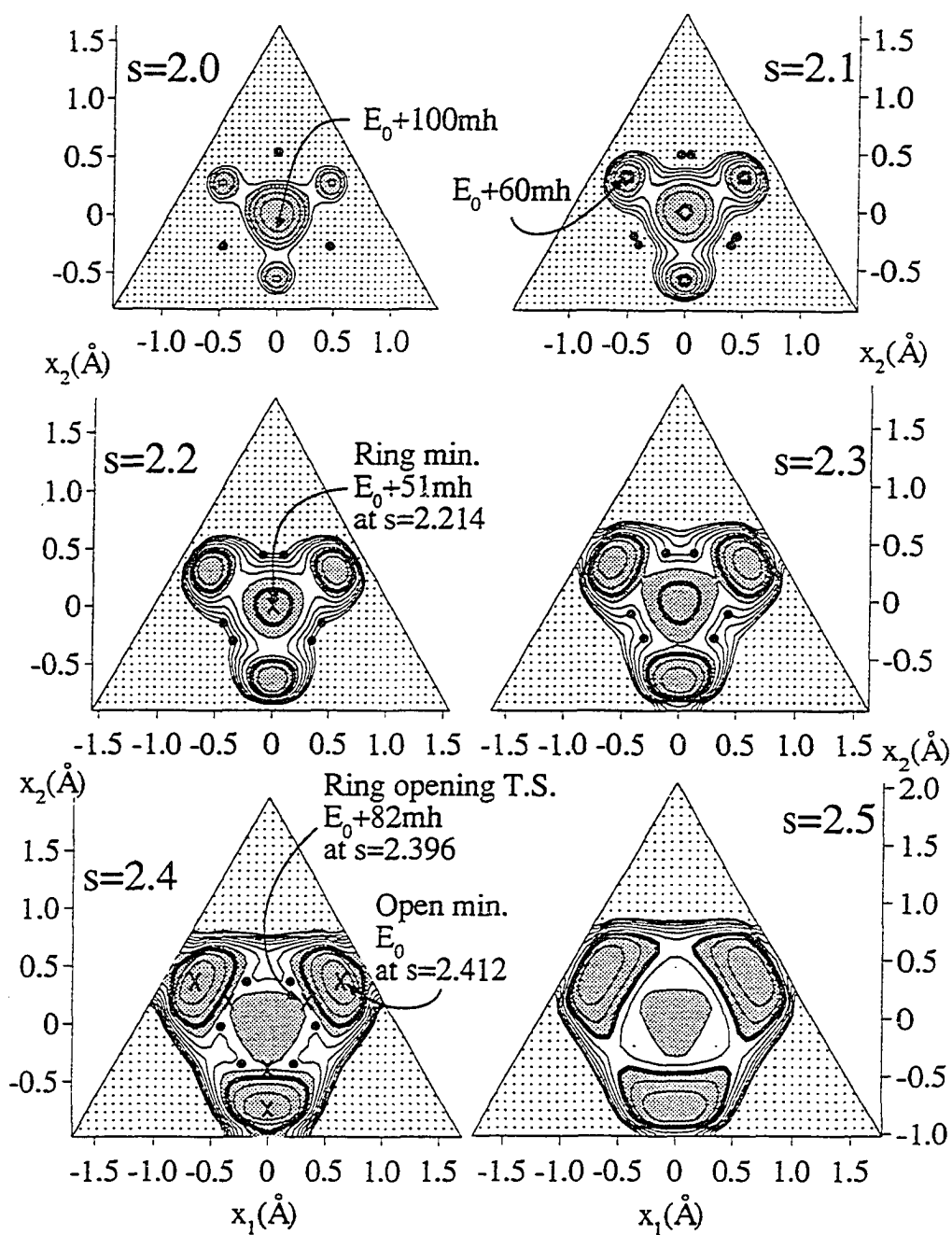


Figure 5. $1^1A'$ state PES contours in planes normal to the x_3 axis. a) $s=2.0\text{\AA}$ to $s=2.5\text{\AA}$. Bold= $E_0+60\text{mh}$. Dotted> $>E_0+200\text{mh}$. Shaded: basins. Increment= 20mh

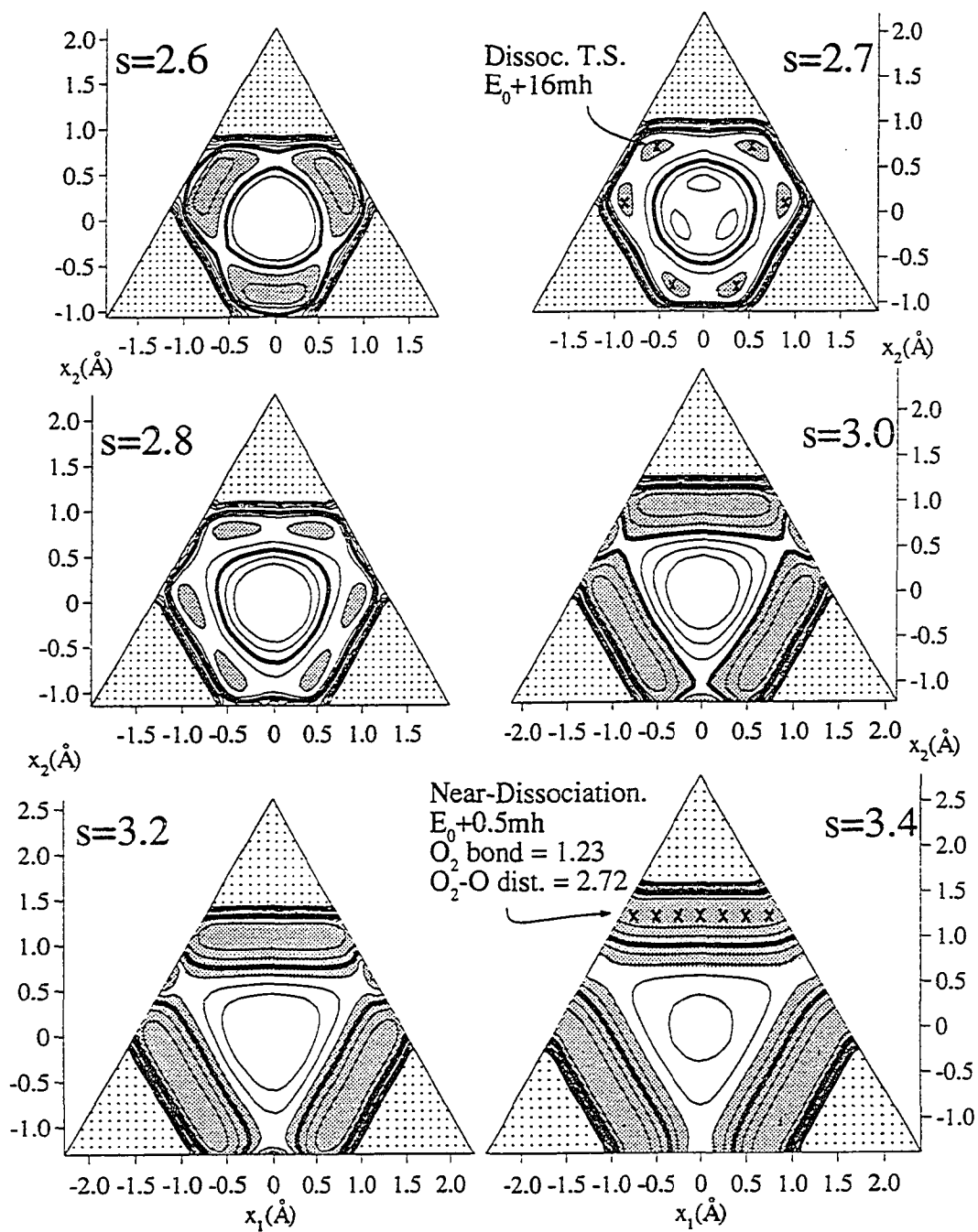


Figure 5. continued; b) $s=2.6\text{\AA}$ to $s=3.4\text{\AA}$. Bold= E_0+60mh .

Dotted $>E_0+200mh$. Shaded: basins. Increment= $20mh$

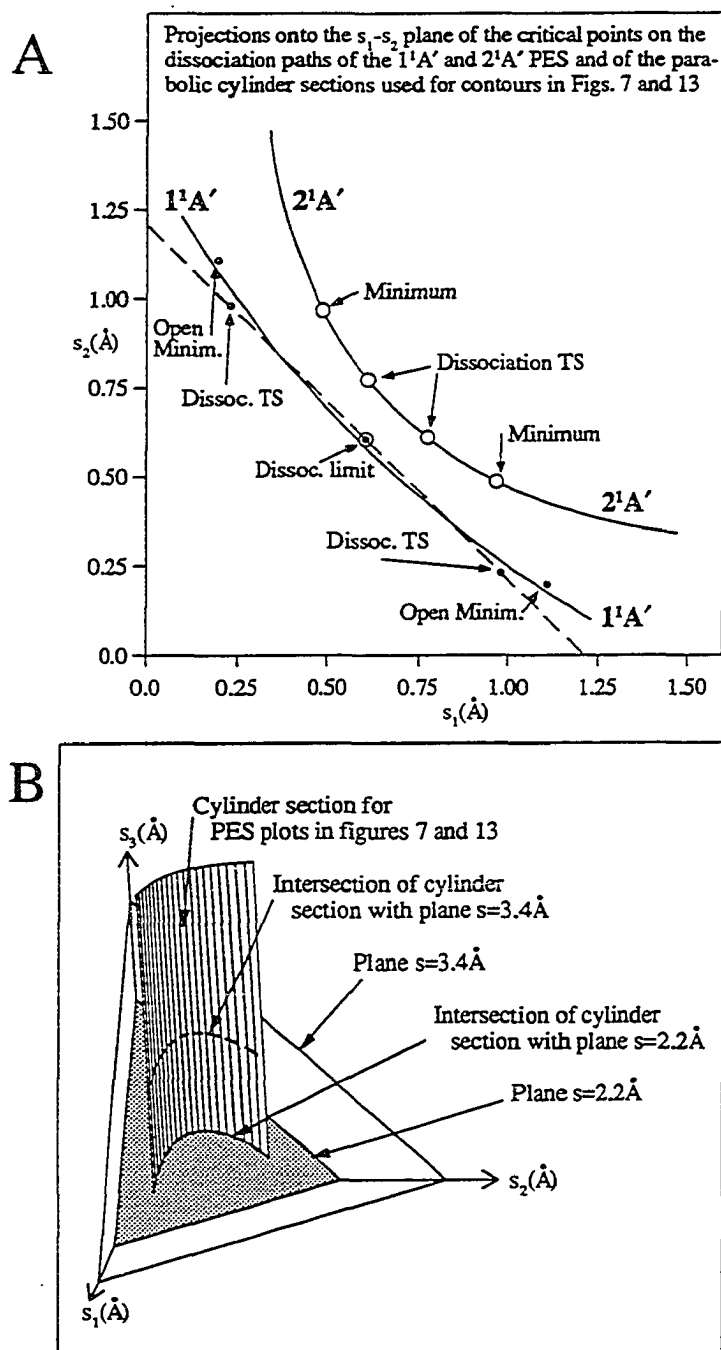


Figure 6. Cylinder sections in perimetric coordinate space for dissociative contour plots considered in Figures 7 and 13

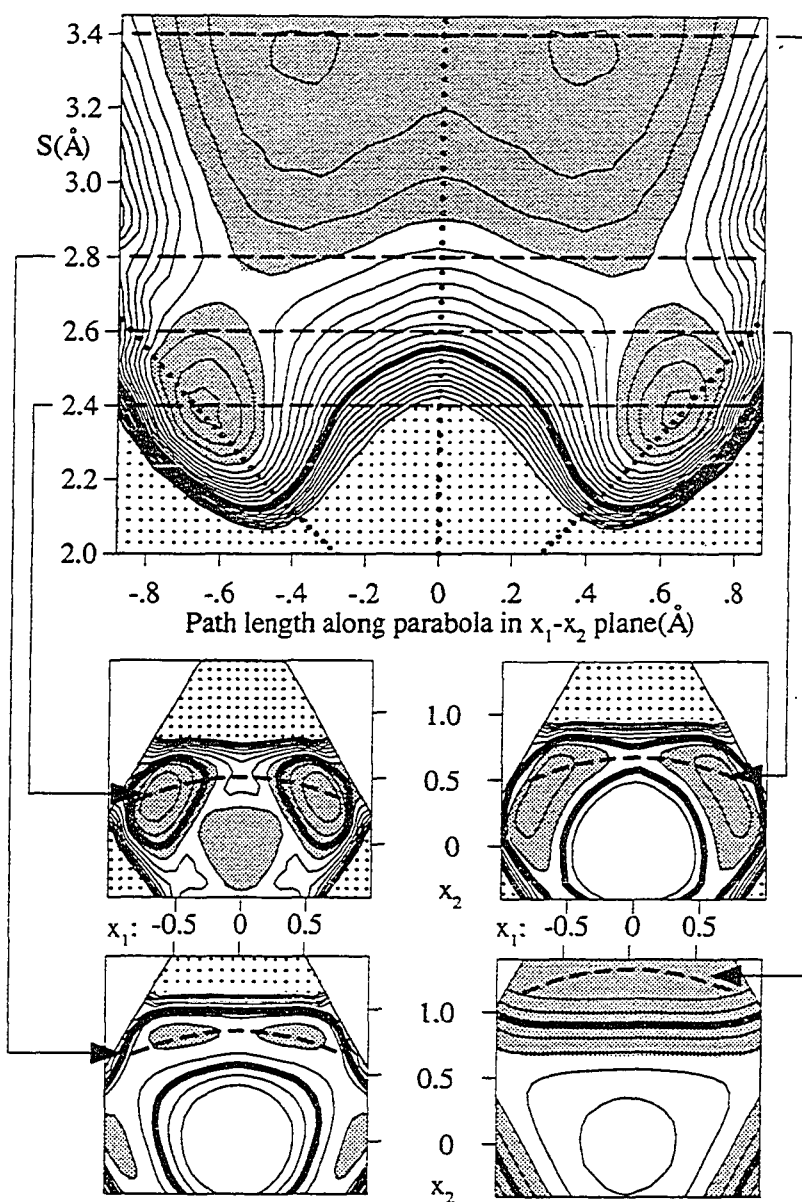


Figure 7. Contours of $1^1A'$ PES on cylinder defined in Figure 6 for this state. Upper panel: Dots $E_0+100mh$. Shaded: basins. Bold= E_0+60mh . $Incr.=5mh$. Lines of heavier dots: C_{2v} conserving. Lower panel: as in Figure 5

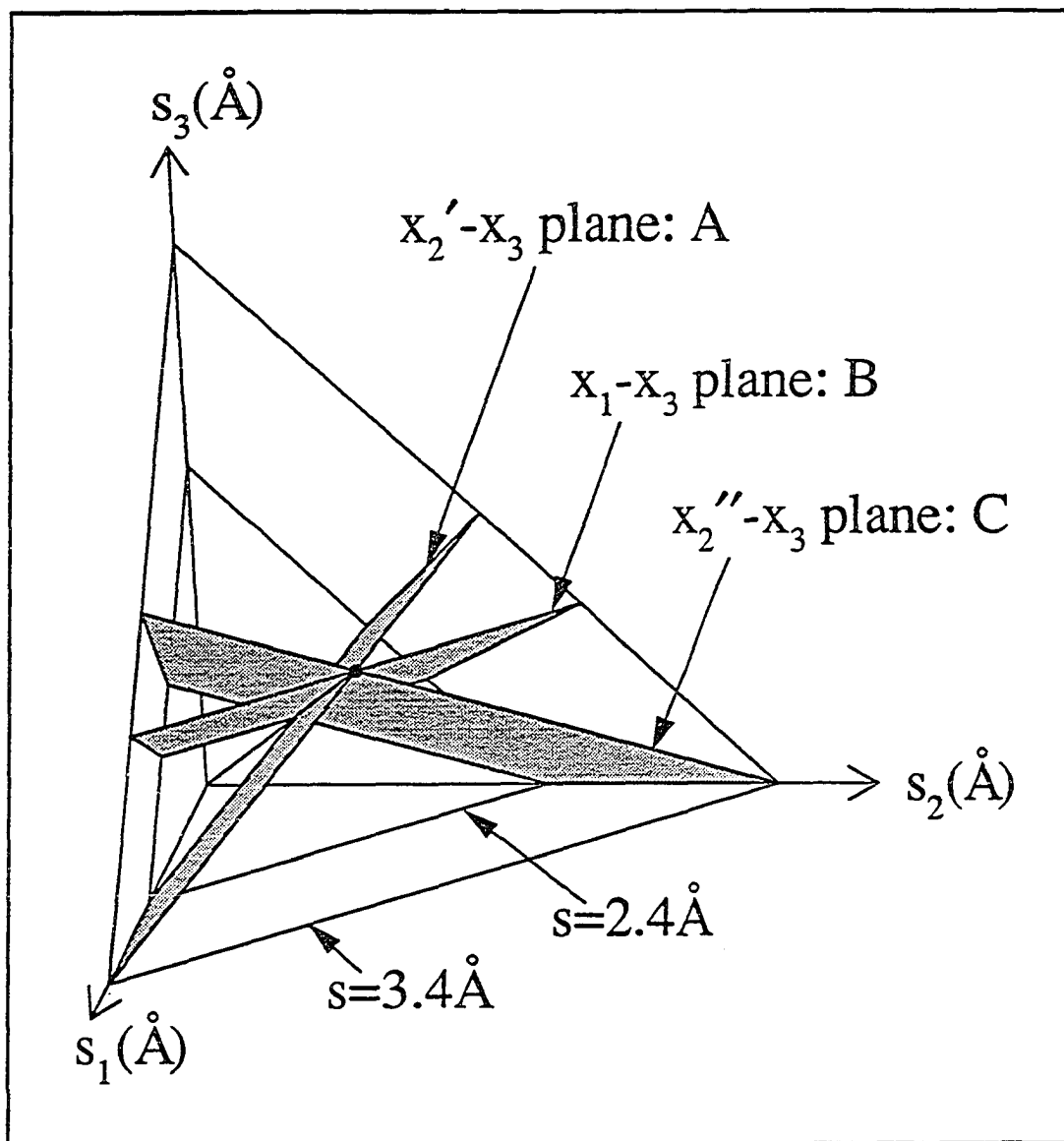


Figure 8. Planes $ax_1 + bx_2 = 0$ in perimetric coordinate space used for contour plots in Figure 9

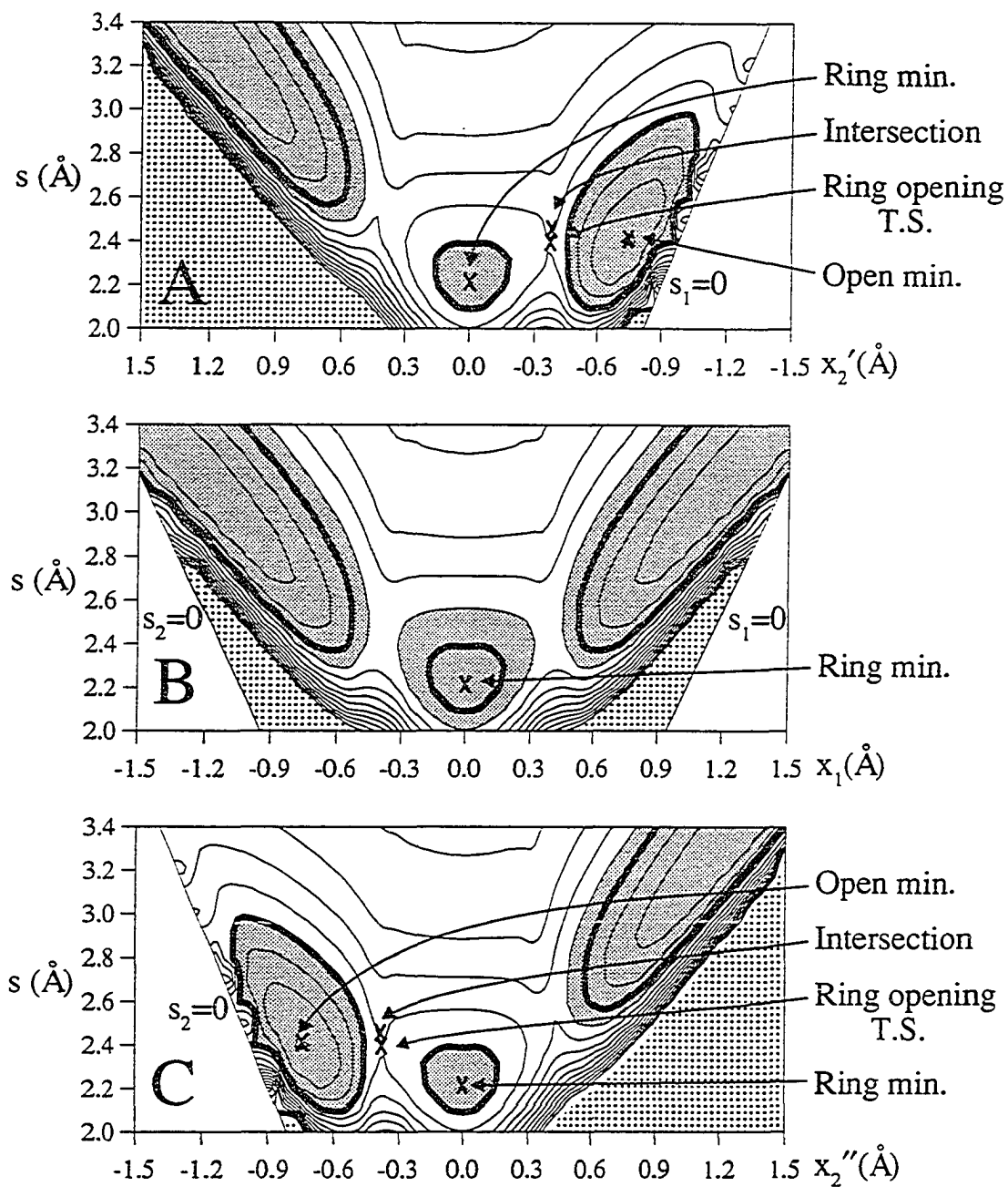


Figure 9. $1^1A'$ state PES contours in planes containing the x_3 axis, defined in Figure 8. Bold= E_0+60 mh. Dotted> $>E_0+200$ mh. Shaded: basins. Increment=20mh

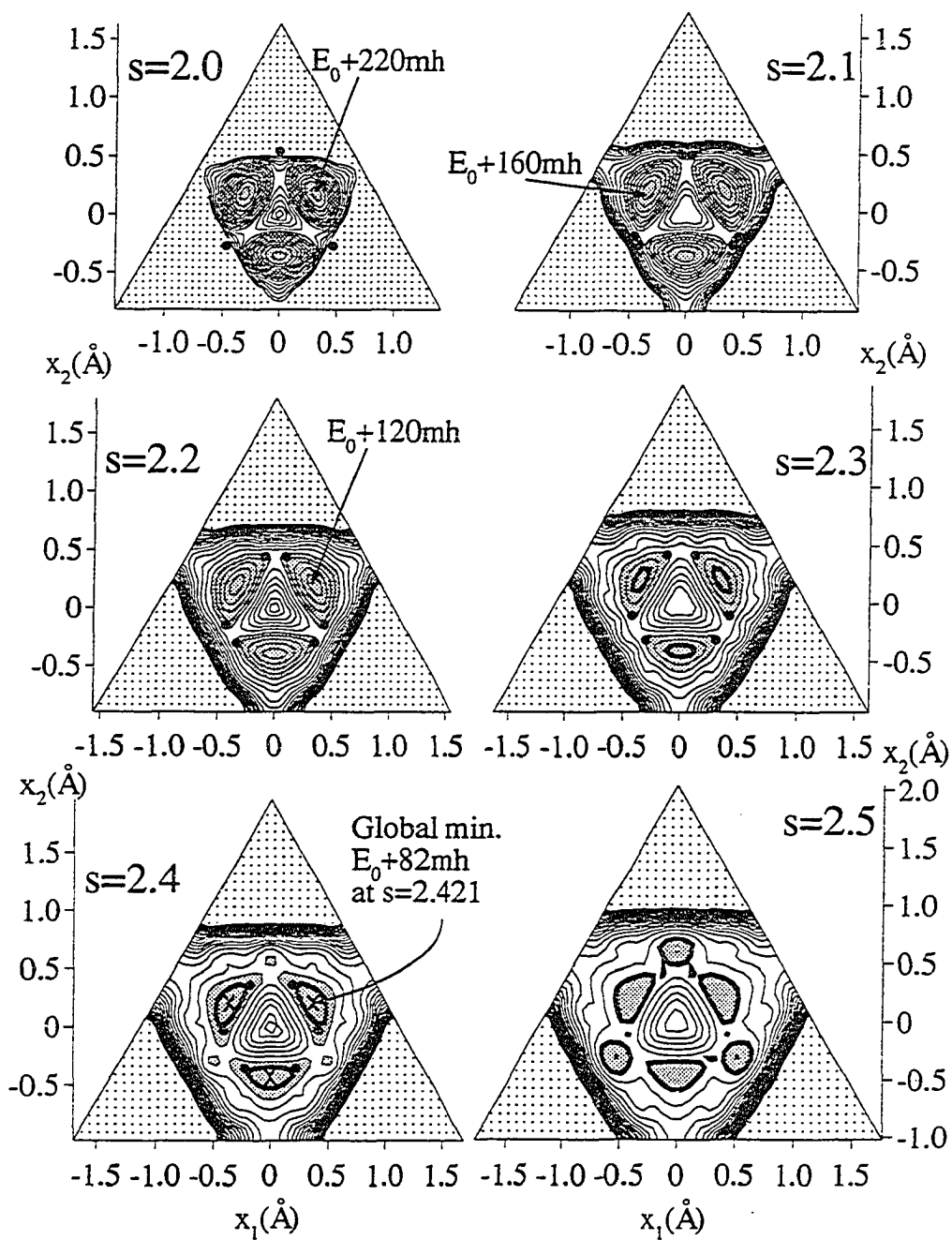


Figure 10. $2^1A'$ state PES contours in planes normal to the x_3 axis. a) $s=2.0\text{Å}$ to $s=2.5\text{Å}$. Bold= $E_0+100\text{mh}$. Dotted= $E_0+500\text{mh}$. Shaded: basins. Increment=20mh

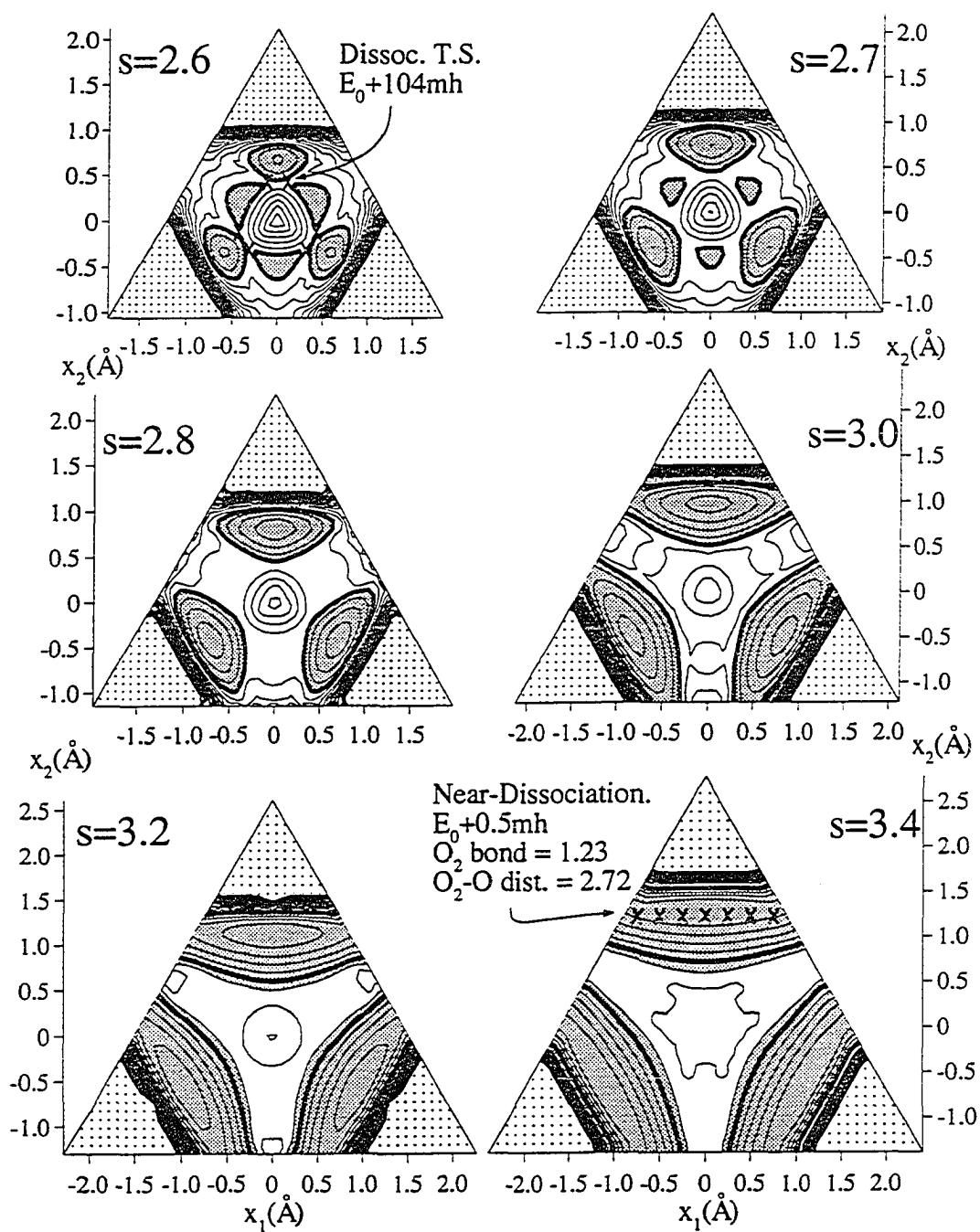


Figure 10. continued; b) $s=2.6\text{\AA}$ to $s=3.4\text{\AA}$. Bold= $E_0+100mh$.

Dotted= $E_0+500mh$. Shaded: basins. Increment=20mh

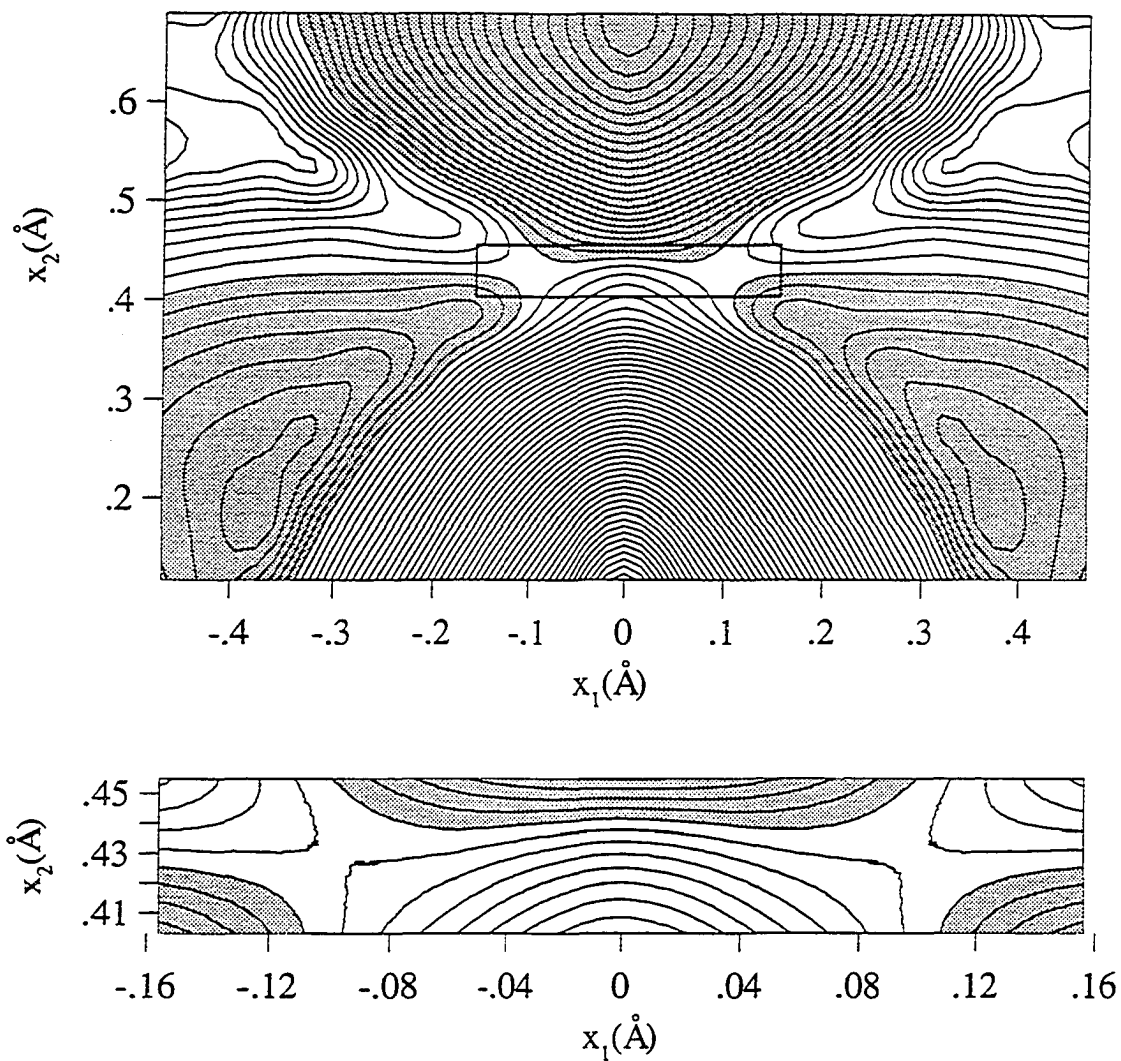


Figure 11. Enlargement of the $2^1A'$ state PES near the dissociative transition state in the plane $s=2.6\text{\AA}$. Lower panel: magnified view of region inside rectangle in upper panel. Upper panel increment= 2mh . Lower panel increment= 1mh . Shaded region: $E < E_0 + 103\text{mh}$

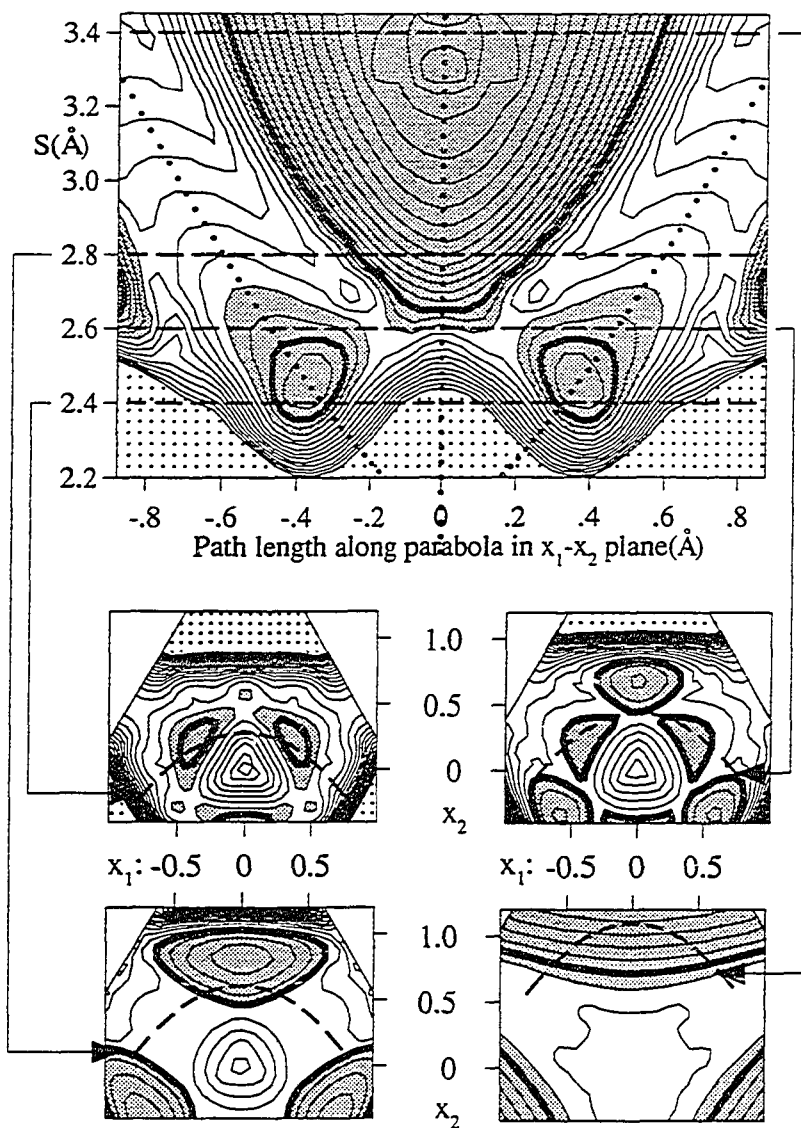


Figure 12. Contours of $2^1A'$ PES on cylinder defined in Figure 6 for this state. Upper panel: Dots: $E_0+160mh$. Shaded: basins. Bold: E_0+60mh . Increment = $5mh$. Lines of heavier dots: C_{2v} conserving. Lower panel: as in Figure 10

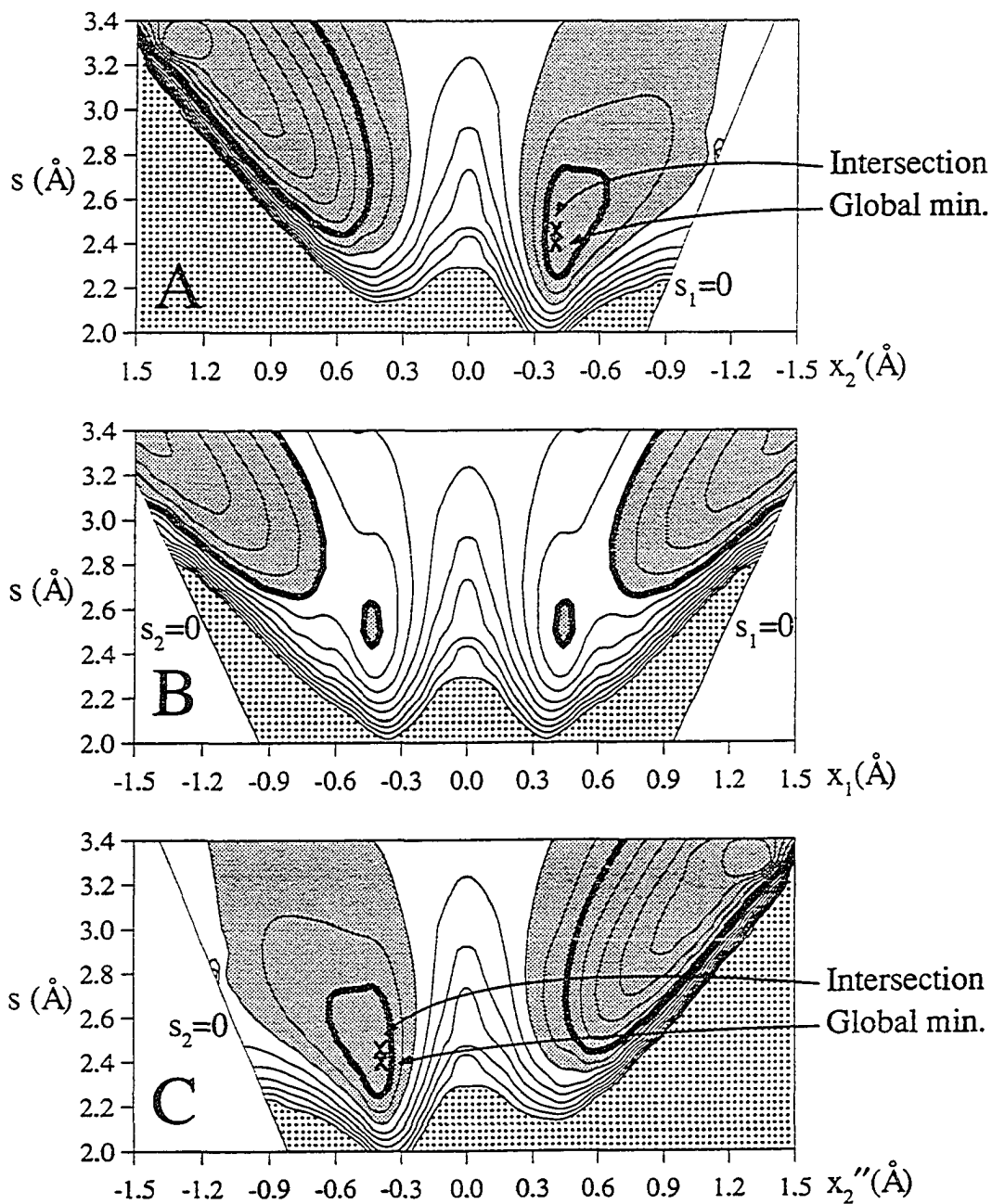


Figure 13. $2^1A'$ state PES contours in planes containing the x_3 axis defined in Figure 8. Bold= E_0+100 mh. Dotted> $>E_0+360$ mh. Shaded: basins. Increment= 20 mh

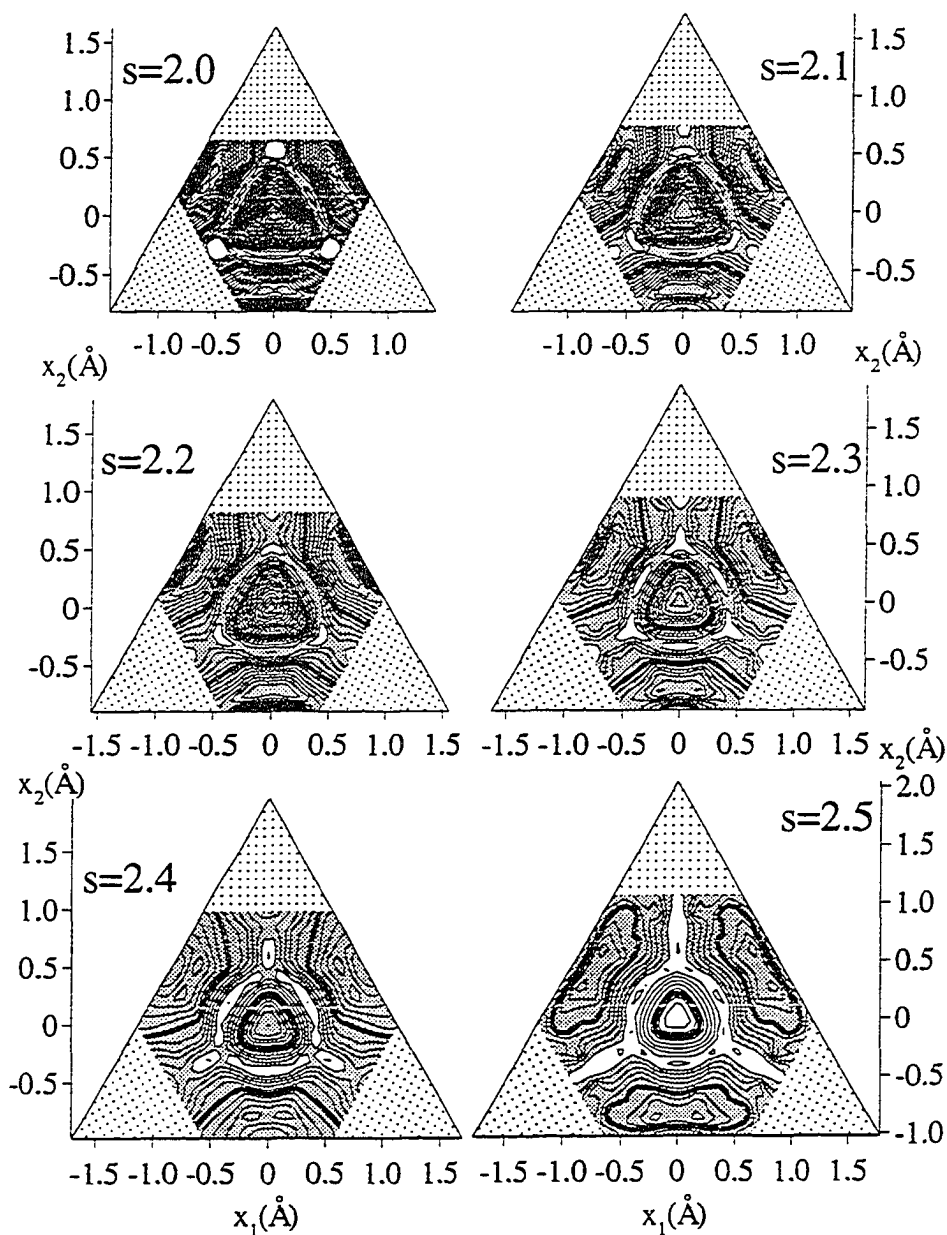


Figure 14. Contours of the energy differences between the $1^1A'$ PES and $2^1A'$ PES in planes normal to the x_3 axis. a) $s=2.0\text{\AA}$ to $s=2.5\text{\AA}$.
 Contours: Lowest=5mh. Increment=15mh. Bold=95mh.
 Shaded:>20mh. Dotted: one bond length<0.8Å

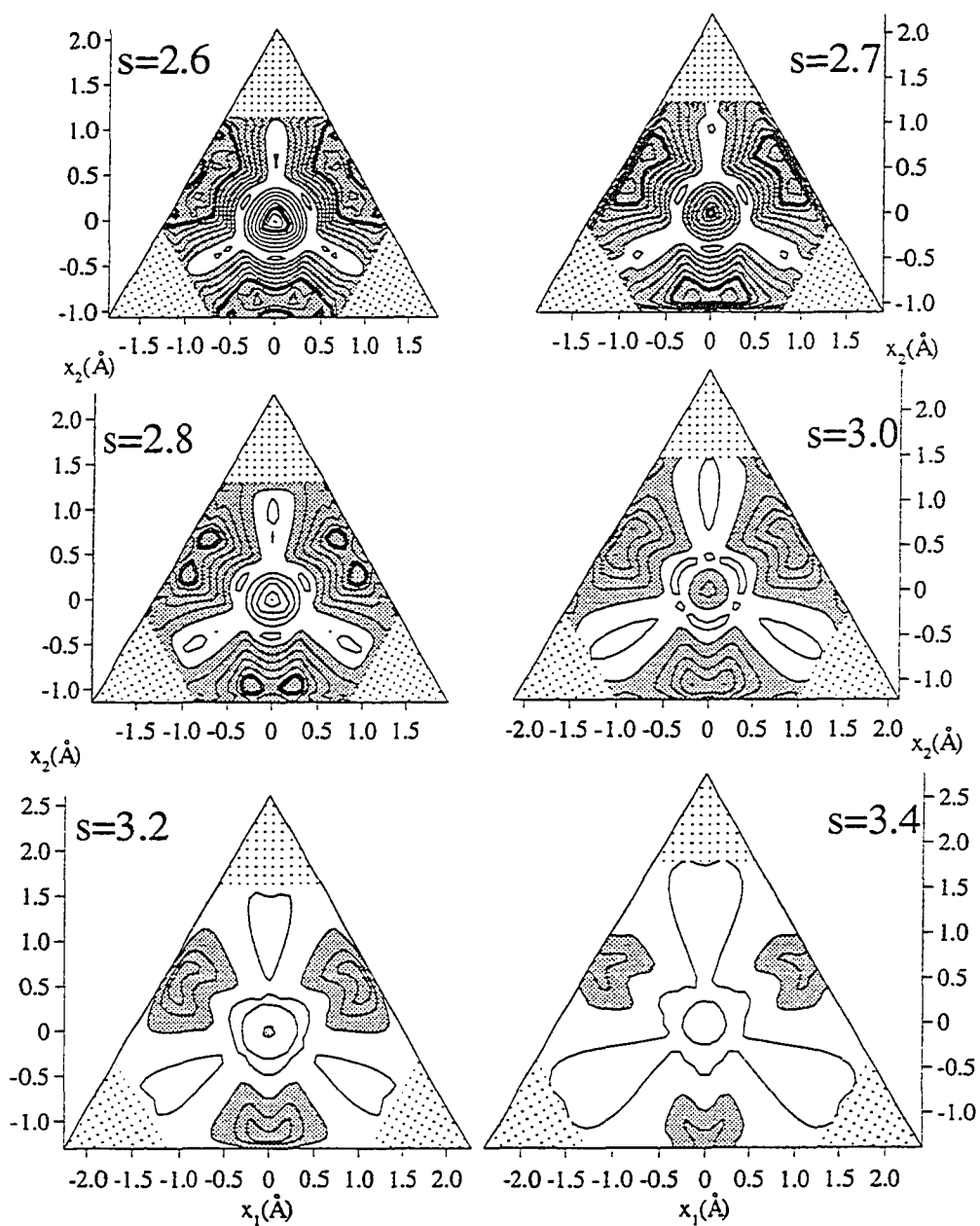


Figure 14. continued; b) $s=2.6\text{\AA}$ to $s=3.4\text{\AA}$. Contours: Lowest=5mh. Increment=15mh. Bold=95mh. Shaded:>20mh. Dotted: one bond length<0.8Å

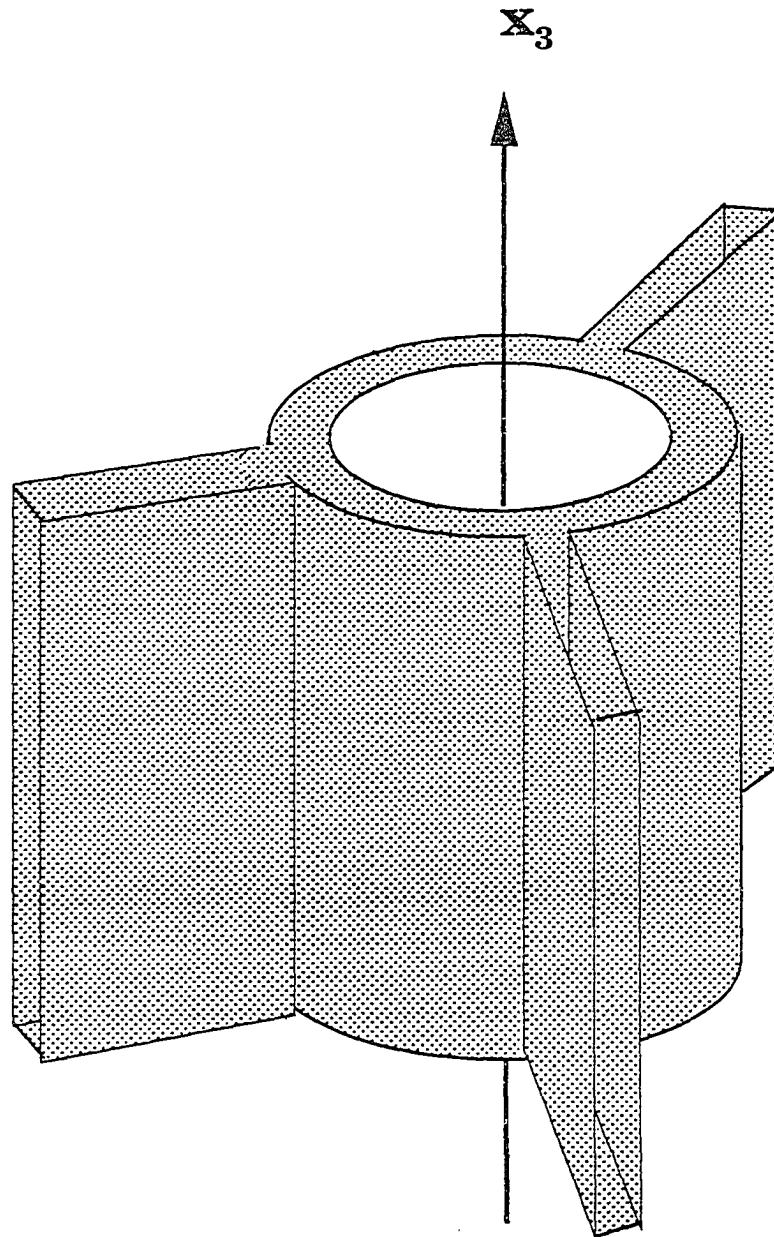


Figure 15. Schematic diagram of the volume in the perimetric coordinate space along which the $1^1A'$ and $2^1A'$ states are close to each other

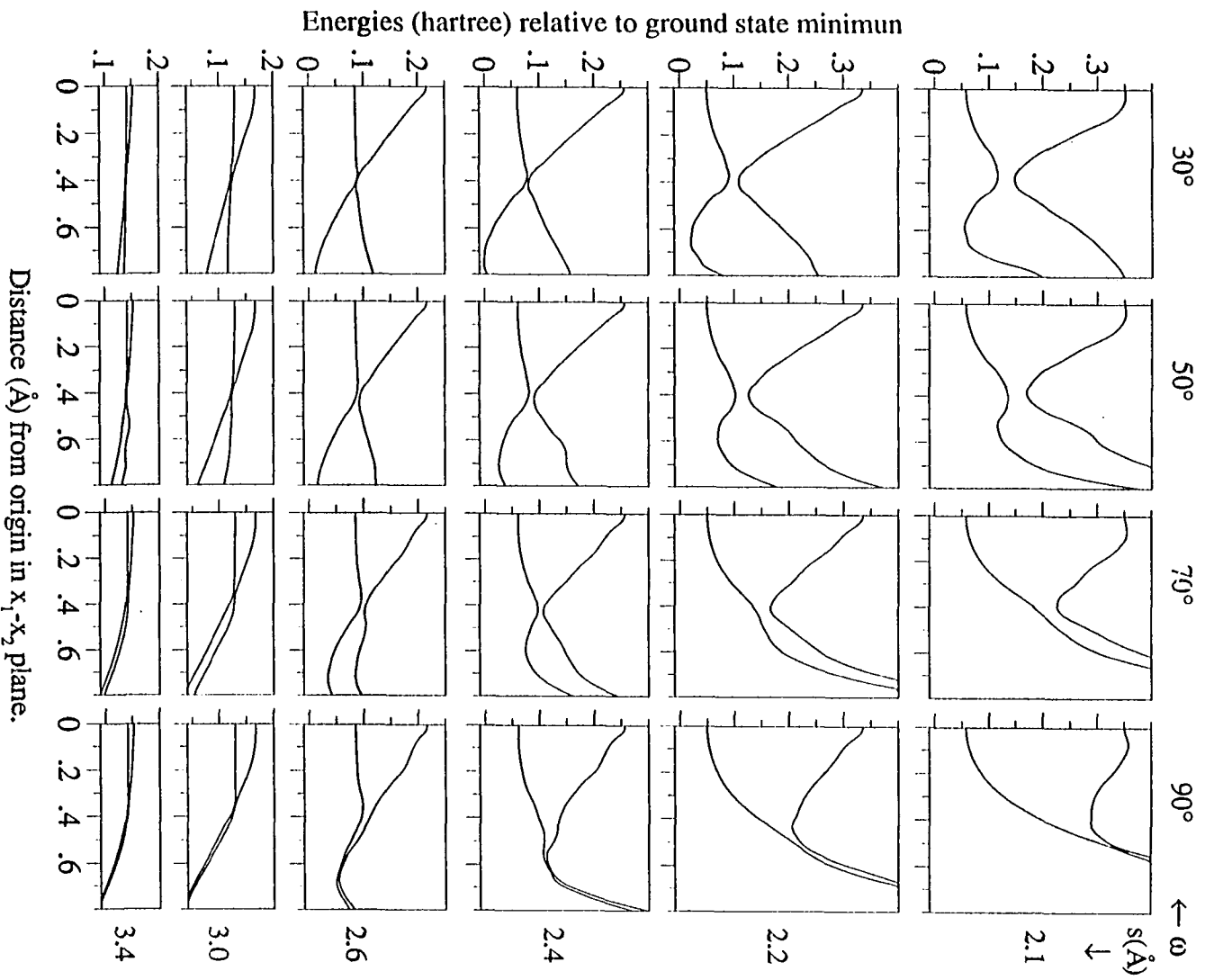


Figure 16. Energies of the $1^1A'$ and $2^1A'$ states along lines

$x_2/x_1 = \tan\omega + \text{constant}$. For definition of angle ω , see Figure 17

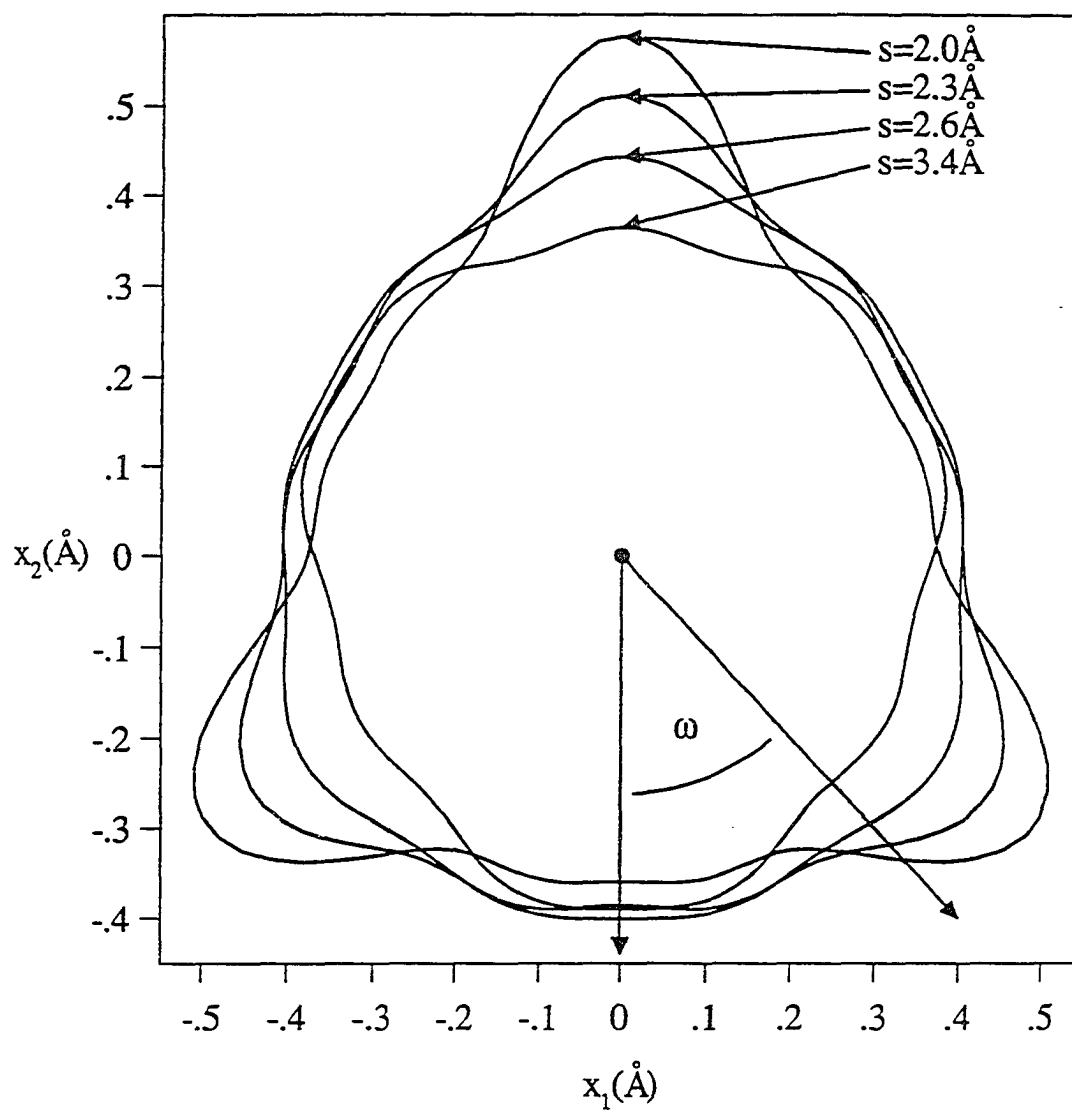


Figure 17. Curves of closest approach between $1^1A'$ and $2^1A'$ states in the cylinder section. The curves are defined by $(x_1^2+x_2^2)^{1/2}=a(s) + b(s)\sin 3\omega + c(s)\sin 6\omega + d(s)\sin 9\omega$

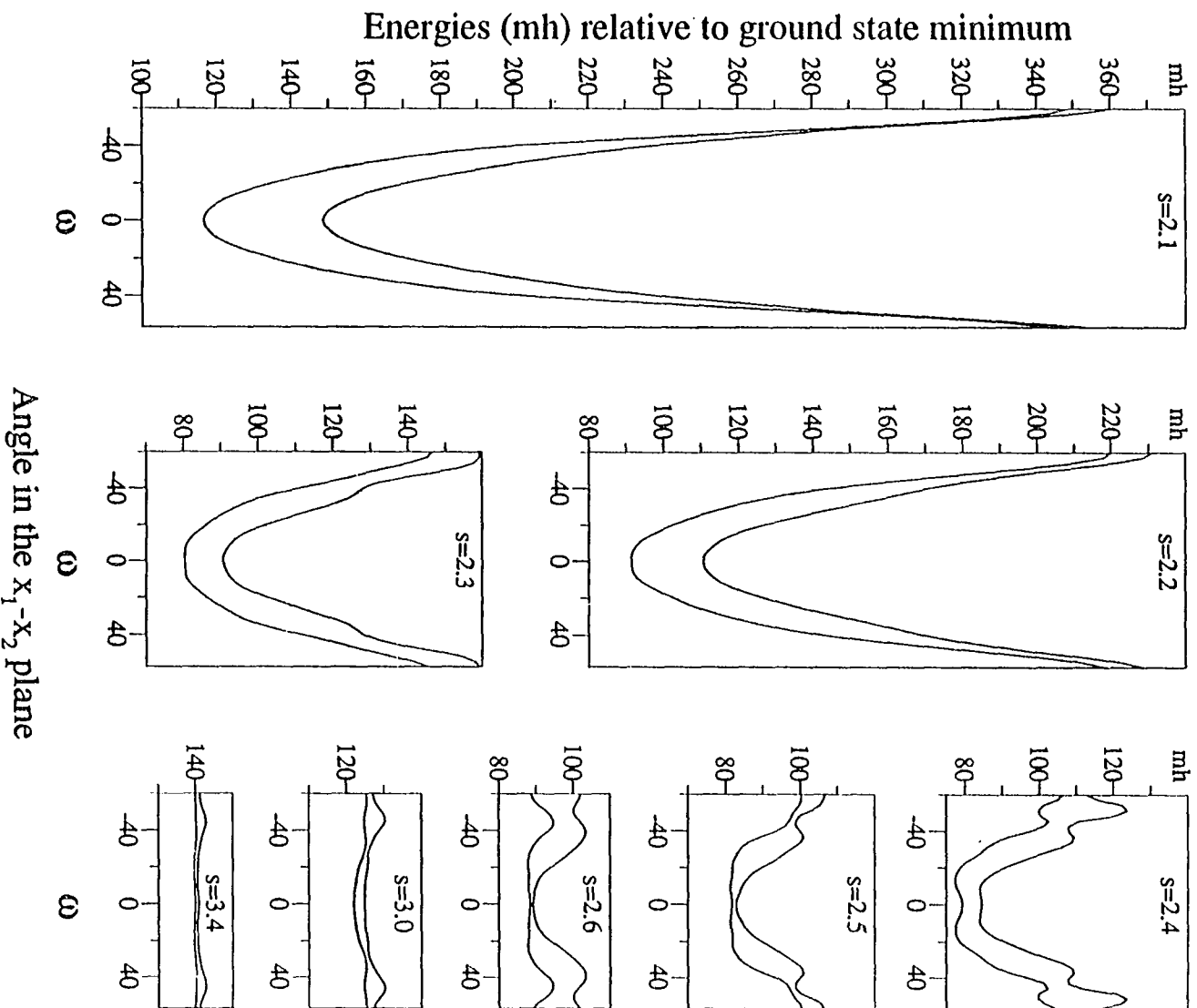


Figure 18. Energies of $1A'$ and $2^1A'$ states along the lines shown in Figure

17

SUMMARY AND CONCLUSIONS

The first part of this dissertation dealt with strictly theoretical material necessary for an in-depth investigation of the two potential energy surfaces. It covered background material on intersections of potential energy surfaces, on the construction of diabatic states, and on the internal coordinates for triatomic molecules.

Paper I presented a set of symmetric, *perimetric*, scale-shape internal coordinates for triatomic molecules. The *perimetric* coordinates of James and Coolidge, first used in the 1930's [4], are advantageous for use with triatomic molecules because they treat all three atoms equivalently. Each of these coordinates is a distance that varies from zero to infinity. This paper introduced *shape-scale perimetric coordinates* in which the size of the molecule is defined by one coordinate, and the shape by another pair of coordinates. In these coordinates, all molecules of constant size lie in the same angular parameter plane. The coordinates are particularly useful for the visualization of properties of triatomic molecules where many two dimensional contour maps can be generated in parallel planes containing molecules of constant size. Furthermore, the C_{3v} symmetry exhibited by the PES and other properties of homonuclear triatomic molecules is particularly clearly displayed in these coordinates, a fact which is advantageous for the

study of the rearrangements of ozone. This paper also discussed in detail the relation between the scale-shape symmetry coordinates and the molecular shape.

Paper II provided the theoretical background necessary for understanding conical intersections. The "crossing conditions", $H_{12}=0$ and $\Delta H=0$, were derived and examined. The topography of the two crossing surfaces was examined in the neighborhood of the intersection. Within a certain domain, the dimensionality of the *intersection crossing space* (ICS) was discussed and shown, in general, to be $N-2$ where N is the number of internal coordinates of the molecule. Within this ICS the two states in question are exactly degenerate. The two-dimensional *branching space* is the coordinate space in which the degeneracy between the two states is lifted. In the branching space, the two surfaces E_1 and E_2 were shown to have the function form

$$E_{1,2}=E^{\circ}+b_1x+b_2y\pm\sqrt{c_1^2x^2+c_2^2y^2}$$

where E° is the intersection energy. These surfaces were illustrated and characterized for the entire range of parameters b_1 , b_2 , c_1 , and c_2 . The steepest descent lines of these surfaces were also discussed and characterized. It was noted that conical intersections are preferred locations for radiationless transitions from the higher state to the lower state, but that in some instances transitions from the lower state to the upper state are also

conceivable.

Paper III presented a new method based on quantum chemical algorithms for the construction of diabatic states from adiabatic states. The method is founded on the idea that a diabatic state is *dominated throughout coordinate space by a single set of configurations*. The transformation to diabatic states is therefore derived by maximizing the contribution of these configurations to their respective states.

The second part of the dissertation contained investigations of the two lowest ${}^1A'$ potential energy surfaces of ozone. The intersection between them is covered in detail in the first of these papers.

Paper IV applied the construction procedure of diabatic states, formulated in Paper III, to the two lowest 1A_1 states of ozone in C_{2v} symmetry. Careful examination of the configurational expansions of these two states yielded an understanding of the causes of the intersection between them. It was concluded that, in cases where the dominant configurations consist entirely of doubly occupied orbitals, an intersection between two states can occur only if each *diabatic* state consists of more than one dominant configuration, and if the weights of the dominant configurations in the diabatic states changes significantly in the region where the crossing occurs. These changes in the weights of dominant configurations can occur in

the case of changing bonding interactions, as is the case with ozone.

Paper V examined the intersection of these two states of ozone in the full C_s coordinate space. Because the C_s coordinate space has three internal coordinates, the intersection crossing space (from Paper II) is of dimension $3-2=1$, i.e. a one dimensional seam. This intersection seam was mapped out in its entirety in the scale-shape symmetry coordinates of paper I. It was shown to consist of four branches, one of which is a closed loop. The three other branches lie entirely in C_{2v} restricted subspaces and connect to the first branch at points. The change in symmetry of one of the states from A_1 to B_2 along a segment of the closed branch from one point of C_{2v} , into C_s symmetry, and back to C_{2v} was discussed in detail. It was concluded that this change in symmetry was driven by changing bonding and anti-bonding character of the molecular orbitals due to the close approach of two of the atoms in the molecule as the geometry varies along the seam. A novel method for determining an intersection point in a two-dimensional coordinate space was also presented. Based on the wavefunction phase-change theorem of Herzberg-Longuet-Higgins [5], using this method one "corrals" an intersection by examining the phase of the wavefunction on successively smaller and smaller loops around a point of intersection. Finally, a new, high-energy intersection point was found between the 1^1A_1 and 2^1A_1 states in the C_{2v} restricted coordinate space, implying yet another one-dimensional

intersection seam between the lowest two ${}^1A'$ states in the full C_s coordinate space.

In paper VI, we finally presented a global mapping of the two potential energy surfaces in the scale-shape perimetric coordinates. It was shown that the only minimum energy path from the ground state ring structure leads directly to the open structure, making direct formation of the ring structure from O_2 and O improbable. It was also shown that there is no rearrangement pathway on the ground state representing the interchange of two atoms. The global minimum of the $2^1A'$ surface was shown to be in C_{2v} , and the dissociation pathways of the two surfaces were also discussed. Finally, the difference between the two surfaces was examined and discussed. The peculiar shape of the intersection seam discovered in paper V was confirmed. It was concluded that radiationless transitions between the states can be expected in the region of coordinate space surrounding the intersection seam.

This investigation of the two lowest ${}^1A'$ surfaces of ozone has uncovered a number of novel features and enhanced our understanding, not only of ozone, but of intersections and triatomic molecules in general. The investigations of the intersection point in C_{2v} and the intersection seam in C_s are noteworthy because they are the most careful examinations of

intersections to date. It is hoped that the analysis of the intersection point in C_{2v} will be helpful in the prediction and determination of intersections of other molecules. The shape-scale perimetric coordinates will surely prove useful for future studies of other triatomic molecules besides ozone. The information gained about the global nature of the PES will prove useful in future studies of ozone.

Much work is left to be done with this system. The ring structure of ozone is still undetected by experiment. It should perhaps be possible to realize this configuration using two-photon excitation from the 1^1A_1 ground state to an intermediate low-lying state of different symmetry, followed by immediate excitation to the 2^1A_1 state. Subsequent radiationless transitions through the intersection seam to the ground state should result in some observed occupation of the ring structure. Therefore, accurate calculations of these excitation energies are needed to guide this experiment. Furthermore, determination of the second intersection seam might well reveal a yet unsuspected pathway to the excited states and/or the ring structure.

Further work also needs to be done on the low-lying excited states, especially the triplet states. Detailed information on these surfaces is still lacking, and is essential to our understanding of this important molecule and its role in atmospheric chemistry.

This dissertation has confirmed that basic theoretical work is a

essential for the progress of quantum chemistry. There is a growing tendency in this age of high-performance computing to spend a great deal of time and effort simply computing energies, vibration frequencies, reaction paths, and other properties. While this is an important aspect of quantum chemistry, much may be gained by careful analysis of the results.

The lessons of this work are many. A thorough understanding of the basic theory involved can be an invaluable predictive aid, as was the case of predicting the one-dimensional intersection seam of ozone in the full C_s coordinate space. Careful planning and attention to details, such as the choice of internal coordinates, can greatly aid in the interpretation of the calculations. And although quantitative energy calculations are an essential part of quantum chemistry, they must be coupled with analysis, and with the development of simple qualitative models in order to gain a clear understanding. The wavefunctions generated in such calculations can yield a better understanding of the electronic structure of the molecule of interest, as was the case when examining the causes of the intersection. Furthermore, simply identifying the maxima, minima, and transition states may not be enough to completely understand the potential energy surfaces of the states involved. Although it is quite expensive when there are more than two degrees of freedom, examination of potential energy surfaces on a global scale is the only way to truly understand the PES.

REFERENCES

1. See, for example, Steinfeld, Adler-Golden, and Gallagher, *J. Phys. Chem. Ref. Data* (Am. Chem. Soc. and Am. Inst. Phys. for U.S. Nat. Bur. Standards), Vol. 16, No 4, (1987).
2. S. Xantheas, G. J. Atchity, S. T. Elbert, and K. Ruedenberg, *J. Chem. Phys.*, **94**, 8054 (1991).
3. M. Born and J. R. Oppenheimer, *Ann. Physik* **84**, 457 (1927).
4. A. S. Coolidge and H. M. James, *Phys. Rev.* **51** 855 (1937).
5. G. Herzberg and H. C. Longuet-Higgins, *Discuss. Faraday Soc.* **35**, 77 (1963); see also M. V. Berry, *Proc. R. Soc. London, Ser. A* **344**, 147 (1975); C. A. Mead, *J. Chem. Phys.* **70**, 2276 (1979); C. A. Mead and D. G. Truhlar, *ibid.* **70**, 2284 (1979).

ACKNOWLEDGEMENTS

I would most like to thank my wife and children for the support they provided and the patience they have shown these long years. I would also like to thank my parents without whom my college career would not have been possible.

I would also like to acknowledge Steve Elbert for teaching me most of what I know about computers. Finally, I must thank my major professor, Dr. Ruedenberg, for the extreme patience he has shown with me. I will be struggling to emulate his attention to detail the rest of my life.

This work was performed at Ames Laboratory under contract no. W-7405-eng-82 with the U. S. Department of Energy. The United States government has assigned the DOE Report number IS-T 1217 to this thesis.